AD-A148 524 MLS MULTIPATH STUDIES PHASE 3 VOLUME 3 APPLICATION OF MODELS TO MLS ASSES..(U) MASSACHUSETTS INST OF TECH LEXINGTON LINCOLN LAB J E EVANS ET AL. 08 JUN 81 1/4

UNCLASSIFIED ATC-88-VOL-3-PT-2 FAA-RD-79-21-VOL-3-PT2 F/G 17/7 NL

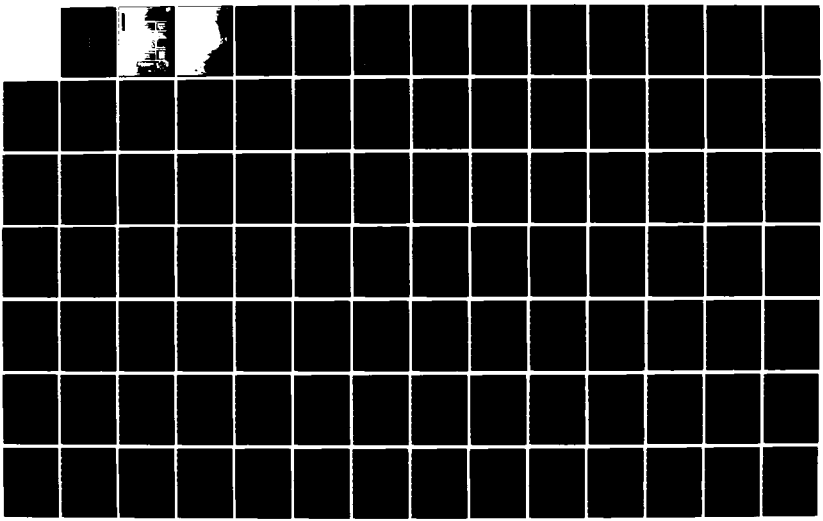

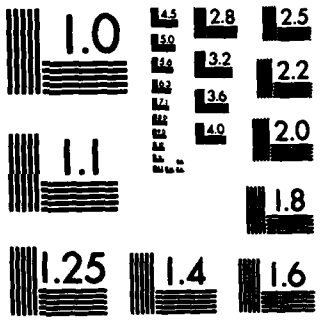

MICROCOPY RESOLUTION TEST CHART
NATIONAL BUREAU OF STANDARDS-1963-A

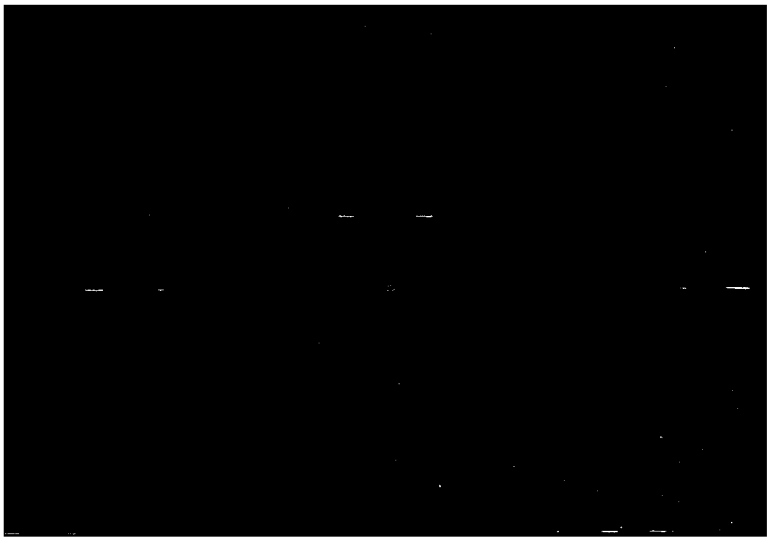

Technical Report Documentation Page

1. Report No.	2. Government Accession No.	3. Recipient's Catalog No.
FAA-RD-79-21	AD-A148 524	

4. Title and Subtitle	5. Report Date
MLS Multipath Studies, Phase 3. Final Report, Volume III: Application of Models to MLS Assessment Issues	8 June 1981
	6. Performing Organization Code
7. Author(s)	8. Performing Organization Report No.
James E. Evans, Samuel J. Dolinar, and David A. Shnidman	ATC-88, Volume III, Part II
9. Performing Organization Name and Address	10. Work Unit No. (TRAIS)
Massachusetts Institute of Technology Lincoln Laboratory P.O. Box 73 Lexington, MA 02173	11. Contract or Grant No. DOT-FA74-WAI-461
12. Sponsoring Agency Name and Address	13. Type of Report and Period Covered
Department of Transportation Federal Aviation Administration System Research and Development Service Washington, DC 20591	Project Report
	14. Sponsoring Agency Code

15. Supplementary Notes

The work reported in this document was performed at Lincoln Laboratory, a center for research operated by Massachusetts Institute of Technology under Air Force Contract F19628-80-C-0002.

16. Abstract

This report presents work done during phase 3 of the US national Microwave Landing System (MLS) program toward developing a computer simulation model of MLS multipath effects, the experimental validation of the model, and the application of the model to investigate multipath performance of ICAO proposals for the new approach and landing guidance system.

The first two volumes of the report presented an overview of the simulation effort as well as describing in detail the propagation and MLS technique mathematical models and their validation by comparison with experimental data. In this volume, we describe the results of comparative simulations for the various MLS techniques in various scenarios and analyze in detail certain multipath performance features which were found to be significant in the scenario simulations.

Simulation results are presented for several scenarios, and shadowing of the MLS azimuth by taxiing and overflying aircraft is analyzed.

The remainder of the report focuses on multipath performance factors specific to various individual techniques. These include:

(1) the effects of angle data outlier tests and filtering in the TRSB receivers,

(2) the effects on the DMLS system due to receiver AGC, receiver motion-induced Doppler shifts, and the use of commutated reference systems, and

(3) acquisition/validation algorithms for all three techniques.

The report concludes with a summary and suggestions for future work.

Part I of this volume consists of Chapters I through IV; Part II contains Chapters V through VIII and the Appendices.

17. Key Words	18. Distribution Statement
Microwave Landing System (MLS) Multipath Doppler MLS (DMLS) Time Reference Scanning Beam (TRSB) DME Based Landing System (DLS)	Document is available to the public through the National Technical Information Service, Springfield, VA 22151.

19. Security Classif. (of this report)	20. Security Classif. (of this page)	21. No. of Pages	22. Price
Unclassified	Unclassified	320	

Form DOT F 1700.7 (8-72) Reproduction of completed page authorized

ABSTRACT

This report presents work done during phase 3 of the US National Microwave Landing System (MLS) program toward developing a computer simulation model of MLS multipath effects, the experimental validation of the model, and the application of the model to investigate the multipath performance of proposals for the new approach and landing guidance system. The model was developed by separately considering the charactertistics of the four basic elements affecting system operation in a multipath environment, i.e., airport, flight profile, propagation, and system elements. This modeling approach permits the examination of the effect on system performance of individual multipath performance factors such as: (a) reflections from terrain, aircraft, buildings with differing orientations; (b) shadowing by aircraft, buildings, and convex runways; (c) aircraft flight profiles and approach speeds; and (d) system design features to combat multipath.

The first two volumes of the report presented an overview of the simulation effort as well as describing in detail the propagation and MLS technique mathematical models and their validation by comparison with experimental data. In this volume, we describe the results of comparative simulations for the various MLS techniques in various scenarios and analyze in detail certain multipath performance features which were found to be significant in the scenario simulations.

Simulation results are presented both for the common comparative scenarios developed by the AWOP Working Group A (WG-A) multipath subgroup and for additional scenarios suggested by individual members of WG-A. Shadowing of the MLS azimuth by taxiing and overflying aircraft is analyzed analytically, by comparison of various field results and by comparative simulations.

The remainder of the report focuses on multipath performance factors specific to various individual techniques. These include:

(1) the effects of angle data outlier tests and filtering in the TRSB receivers

(2) the effects on the DMLS system due to the receiver AGC, receiver motion-induced Doppler shifts, and the use of commutated reference systems, and

(3) acquisition/validation algorithms for all three techniques.

The report concludes with a summary and suggestions for future work.

Part I of this volume consists of Chapters I through IV; Part II contains Chapters V through VIII and the appendices.

ACKNOWLEDGMENTS

The theoretical, simulation result, and field data analyses in this volume had significant contributions from several people in addition to the report authors. R. Orr contributed to the AWOP scenario result analysis as well as the TRSB shadowing and slew limiter studies. D. Shnidman analyzed the AWOP scenario multipath features and features of the DLS system performance. Steve Sussman contributed to the analysis of Doppler reference scalloping effects. Bob Burchsted, Janet Reid, and Bob Moffatt assisted in running many of the scenarios.

The studies on DMLS reference scalloping benefited from work by H. Wheeler of Hazeltine Corporation [11], J. Goodwin of ITT Gilfillan [13], and I. White of Plessey Company [140]. D. Vickers, G. Adams, J. Tracy, and R. Cleary of the Federal Aviation Administration provided the experimental data used in the shadowing studies (this included conducting a series of special field tests to address certain issues).

The AWOP WG-A multipath subgroup chaired by R. Butler was instrumental in the development and use of the comparative multipath scenarios. Other principal contributors from the subgroup included N. Hughes, J. Jones, H. Ecklundt, T. Hagenberg, and D. Cooper.

The encouragement of H. Weiss and I. Stiglitz of Lincoln Laboratory and F. Frisbie of the Federal Aviation Administration for our various studies when considerable controversy arose is gratefully acknowledged.

D. Young and N. Campbell typed the report, while C. Casazza and S. Cormney prepared the bulk of the figures.

Accession For
NTIS GRA&I ☒
DTIC TAB ☐
Unannounced ☐
Justification
By
Distribution/
Availability Codes
Dist | Avail and/or Special
A-1

CONTENTS

Abstract		iii
Acknowledgments		iv
List of Illustrations		vii
V.	EFFECTS OF SLEW RATE LIMITING IN TRSB RECEIVERS	5-1
	A. Introduction	5-1
	B. TRSB Phase II Data Processing	5-4
	C. Single Scan Multipath Error for a TRSB Dwell Gate Processor	5-5
	D. Phase II Slew Limiter Phenomenology	5-7
	E. Slew Rate Limiter at Filter Output	5-20
	F. Conclusions/Extensions	5-31
VI.	UNIQUE DMLS MULTIPATH PERFORMANCE ISSUES	6-1
	A. Effect of Time-Varying AGC Gain on the Effective DMLS Antenna Patterns	6-2
	B. Reference Scalloping	6-31
	C. Array Scalloping	6-88
	D. Lateral Diversity	6-101
	E. Comparative Simulations of Scenarios Related to DMLS Multipath Mechanisms	6-118
	F. Potential Impact of Various DMLS Dynamic Factors on System Implementation	6-154
VII.	ACQUISITION/VALIDATION (ACQ/VAL) STUDIES	7-1
	A. TRSB ACQ/VAL	7-3
	B. DLS ACQ/VAL	7-5
	C. Doppler ACQ/VAL	7-8
	D. TRSB/DMLS Comparative Simulation Results	7-38
	E. Summary	7-53
VIII.	SUMMARY AND RECOMMENDATIONS FOR FUTURE STUDIES	8-1
	A. Summary of Results	8-1
	B. Recommendations for Future Studies	8-5

APPENDIX A	Comparison of "Standard" and "Special" DMLS Simulation Models for a Spatially Homogeneous Building	A-1
APPENDIX B	System Implementations Simulated	B-1
APPENDIX C	Simultaneous Commutation in DMLS Arrays	C-1
References		R-1

LIST OF ILLUSTRATIONS

5-1	Data editing structure employing slew rate limiters.	5-2
5-2	Input-output characteristic for slew limiter.	5-8
5-3	Input-output time waveforms with TRSB Phase II receiver slew limiter.	5-8
5-4	Illustration of determining P_+, P_- and long duration multipath error with slew limiter.	5-14
5-5	Slew bias error vs. separation angle for various multipath amplitudes.	5-16
5-6	Slew bias error vs. multipath amplitude for various separation angles.	5-17
5-7	Slew limiting at filter output or input.	5-20
5-8	Input and output waveforms for case of limiter outside feedback loop.	5-26
5-9	Maximum outlier amplitude for a given maximum output error.	5-28
6-1	Sum filter frequency response for zero scalloping frequency (uniform AGC factors).	6-4
6-2	Difference filter frequency response for zero scalloping frequency (uniform AGC factors).	6-6
6-3	Sum filter frequency response for scalloping frequency of $\frac{1}{2}\frac{2\pi}{16T}$ (210 Hz) and midscan phase of 0°.	6-12
6-4	Difference filter frequency response for scalloping frequency of $\frac{1}{2}\frac{2\pi}{16T}$ (210 Hz) and midscan phase of 0°.	6-13
6-5a	Real part of sum filter frequency response for scalloping frequency of $\frac{1}{2}\frac{2\pi}{16T}$ (210 Hz) and midscan phase of 90°.	6-14
6-5b	Imaginary part of sum filter frequency resonse for scalloping frequency of $\frac{1}{2}\frac{2\pi}{16T}$ (210 Hz) and midscan phase of 90°.	6-15
6-6a	Real part of difference filter frequency response for scalloping frequency of $\frac{1}{2}\frac{2\pi}{16T}$ (210 Hz) and midscan phase of 0°.	6-16
6-6b	Imaginary part of difference filter frequency response for scalloping frequency of $\frac{1}{2}\frac{2\pi}{16T}$ (210 Hz) and midscan phase of 90°.	6-17

6-7	Sum filter frequency response for scalloping frequency of $\frac{1}{2}\frac{2\pi}{16T}$ (210 Hz) and midscan phase of 180°.	6-18
6-8	Difference filter frequency response for scalloping frequency of $\frac{1}{2}\frac{2\pi}{16T}$ (210 Hz) and midscan phase of 180°.	6-19
6-9	Sum filter frequency response for scalloping frequency of $\frac{2\pi}{16T}$ (420 Hz) and midscan phase of 0°.	6-20
6-10	Difference filter frequency response for scalloping frequency of $\frac{2\pi}{16T}$ (420 Hz) and midscan phase of 0°.	6-21
6-11a	Real part of sum filter frequency response for scalloping frequency of $\frac{2\pi}{16T}$ (420 Hz) and midscan phase of 90°.	6-22
6-11b	Imaginary part of sum filter frequency response for scalloping frequency of $\frac{2\pi}{16T}$ (420 Hz) and midscan phase of 90°.	6-23
6-12a	Real part of difference filter frequency response for scalloping frequency of $\frac{2\pi}{16T}$ (420 Hz) and midscan phase of 90°.	6-24
6-12b	Imaginary part of difference frequency response for scalloping frequency of $\frac{2\pi}{16T}$ (420 Hz) and midscan phase of 90°.	6-25
6-13	Sum filter frequency response for scalloping frequency of $\frac{2\pi}{16T}$ (420 Hz) and midscan phase of 180°.	6-26
6-14	Difference filter frequency response for scalloping frequency of $\frac{2\pi}{16T}$ (420 Hz) and midscan phase of 180°.	6-27
6-15	Motion averaging factor for proposed scan sequence $d_p(n)$ (++++++------).	6-44
6-16	Motion averaging factor for alternating scan sequence $d_A(n)$ (+-+-+-+-+-+-).	6-46
6-17	Motion averaging factor for scan sequence #819 (++--++--++--).	6-54
6-18	Motion averaging factor for scan sequence #237 (++++---+--+-).	6-55
6-19	Motion averaging factor for scan sequence #347 (+++-+-+--+--).	6-56
6-20	Motion averaging factor for scan sequence #700 (++-+-+----++).	6-57

6-21	First-order static error characteristic, $\rho H_{\Delta}(\omega_s')$.	6-62
6-22	Motion averaged errors for proposed scan sequence $d_p(n)$ (++++++------).	6-78
6-23	Motion averaged errors for alternating scan sequence $d_A(n)$ (+-+-+-+-+-+-).	6-80
6-24	Motion averaged errors for scan sequence #819 (++--++--++--).	6-81
6-25	Motion averaged errors for scan sequence #237 (++++---+--+-).	6-82
6-26	Motion averaged errors for scan sequence #347 (+++-+-+--+--).	6-83
6-27	Motion averaged errors for scan sequence #700 (++-+-+----++).	6-84
6-28a	Motion averaging factor for proposed scan sequence $d_p(n)$ (++++++------) with zero multipath time delay.	6-88
6-28b	Motion averaging factor for proposed scan sequence $d_p(n)$ (++++++------) with multipath time delay of 6 μsec.	6-90
6-29a	Motion averaging factor for alternating scan sequence $d_A(n)$ (+-+-+-+-+-+) with zero multipath time delay.	6-91
6-29b	Motion averaging factor for alternating scan sequence $d_A(n)$ (+-+-+-+-+-+-) with multipath time delay of 6 μsec.	6-92
6-30	Scalloping frequency geometry.	6-94
6-31	Dynamic DMLS "inbeam" multipath region for reflected array x direct reference component.	6-96
6-32	DMLS single frequency static error vs. separation angle.	6-98
6-33	DMLS dynamic error for out-of-beam azimuth multipath.	6-100
6-34 and 6-35	Dynamic DMLS error vs. scalloping frequency for out-of-beam azimuth multipath.	6-102
6-36	Simple lateral diversity sequence.	6-104
6-37	Error components at Doppler angle decoder input for single multipath reflection.	6-105

6-38	Lateral diversity elevation with reflective object (from [7]).	6-106
6-39	Final UK lateral diversity array concept proposal.	6-112
6-40	Lateral diversity antenna used in initial trials alongside phase 1 antenna.	6-113
6-41	Experimental and simulation results for performance improvement with lateral diversity.	6-116
6-42	Brussels Airport map.	6-120
6-43	Airport map for "system sensitivity" scenario derived from Fig. 6-42.	6-121
6-44	Azimuth multipath characteristics for scenario of Fig. 6-43.	6-122
6-45	DMLS error for Brussels scenario with threshold height of 50 ft.	6-124
6-46	Brussels National Airport.	6-126
6-47	Brussels National landing chart ICAO.	6-128
6-48	Abelag hangar as seen from fuel storage area.	6-129
6-49	Map of Brussels airport fuel storage area.	6-130
6-50	Aerial photograph of Brussels National Airport.	6-132
6-51	Inferred fuel storage area structure locations and heights.	6-134
6-52	Vertical plan view of Abelag Hangar shadowing by fuel storage area structures.	6-135
6-53	Inferred shadowing profile of fuel storage area.	6-136
6-54	Airport map for comparative scenario based on June 1977 Brussels airport environment.	6-140
6-55	Azimuth multipath diagnostics for comparative scenario of Fig. 6-54.	6-141
6-56	Computed raw errors for comparative scenario of Fig. 6-54.	6-142
6-57	Door spacing of hangars for scenario based on Sydney Airport.	6-144
6-58	Airport map for "system sensitivity" scenario derived from Sydney Airport.	6-146

6-59	Azimuth multipath diagnostics for scenario of Fig. 6-58.	6-148
6-60	Azimuth error waveforms for "system sensitivity" scenario based on Sydney Airport.	6-149
6-61	Airport map used to derive array scalloping "system sensitivity" scenario.	6-150
6-62	Airport map for array scalloping scenario.	6-152
6-63	Azimuth multipath characteristics for array scalloping scenario.	6-152
6-64	TRSB and DMLS azimuth multipath errors for array scalloping scenario.	6-153
7-1	DLS time delay discrimination as a function of scatterer location.	7-6
7-2	Summary of DMLS ACQ/VAL.	7-10
7-3	DMLS ACQ/VAL flow chart.	7-11
7-4	Acquisition/validation for correlation processor.	7-12
7-5	Frequency response characteristic of DMLS ordinary" acquisition bins.	7-14
7-6	Output of DMLS pairwise "ordinary" bin summations for single input signal.	7-16
7-7	Airport map for original WP/322 ACQ/VAL scenario.	7-40
7-8	Azimuth multipath characteristics for original WP/322 ACQ/VAL scenario.	7-41
7-9	DMLS and TRSB errors for original WP/322 ACQ/VAL scenario.	7-42
7-10	DMLS and TRSB errors for original WP/322 ACQ/VAL scenario.	7-44
7-11	Long and short term tracked averages time history for original WP/322 ACQ/VAL scenario.	7-46
7-12	Azimuth multipath characteristics for WP/322 scenario at 118 knots ground speed.	7-47
7-13	DMLS and TRSB errors for WP/322 scenario at 118 knots ground speed.	7-48

7-14	Long and short term tracked averages time history for WP/322 scenario at 118 knots.	7-50
7-15	Azimuth multipath characteristics for WP/322 ACQ/VAL scenario at 80 knots.	7-51
7-16	DMLS and TRSB errors for WP/322 ACQ/VAL scenario at 80 knots.	7-52
7-17	Long and short term tracked averages time history for WP/322 scenario at 80 knots.	7-54
A-1	Airport map for test scenario using "special" DMLS simulation model.	A-2
A-2	Azimuth multipath diagnostics for test scenario using "special" DMLS model.	A-3
A-3	Azimuth multipath diagnostics using "standard" DMLS simulation model.	A-4
A-4	Comparison of "standard" and "special" DMLS models for test scenario.	A-5
B-1	DLS azimuth antenna configuration.	B-2
B-2	DLS lateral diversity EL antenna.	B-3
C-1	One argument for increased Doppler resolution via "two source mobility".	C-4
C-2a	Commutated Doppler array.	C-6
C-2b	Ground derived system which is dual to commutated Doppler array.	C-6
C-3	Simultaneous linear two source movement.	C-8
C-4	Sequential linear two source movement.	C-12
C-5	Spectra of various Doppler components.	C-14
C-6	Time waveforms with sequential linear two source movement.	C-16

C-7	Reference/sideband source locations in randomized two source movement.	C-18
C-8	Relation of phase perturbations to sideband/reference separation.	C-22
C-9	Relation of various phasors for "normal" commutated Doppler array at 0.5 BW separation angle.	C-30
C-10	Relation of various phasors for simultaneous two source commutation at separation angle = 0.5 beamwidths.	C-32

V. EFFECTS OF SLEW RATE LIMITING IN TRSB RECEIVERS

A. Introduction

The MLS, as embodied in the various states' system proposals evaluated by ICAO, is an example of a class of systems which is commonly encountered in many areas of communication and control, especially radio-navigation - multirate sampled data system. The multirate property is inherent in the capability of the system to make raw measurements at a rate exceeding the user's requirements for output data. In this situation, it is customary to use techniques of data processing/reduction to refine the raw estimates before the presentation to the user.

In particular, the excess data rate at the input permits incorporation of data editing procedures which can eliminate or otherwise preprocess individual data points which seem to be highly at variance with the character of the adjacent data. In certain statistical literature, these are known as outlier rejection tests. These have had application within the several national MLS programs, and it is within this general context that the specific problem studied in this report is introduced.

Figure 5-1 shows an editing structure representative of those employed in versions of the U.S. TRSB receiver. Possible options for feedback are also indicated. The specific editor used is a slew rate limiter, which is a nonlinear device that truncates a data point at some limiting value if the data deviates sufficiently far from a predicted, or reference, level. In the Phase II receiver, the limiter was placed ahead of the filter; no post-filter processing was performed. The rationale for the limiter-before-filter configuration is primarily to prevent the propagation of anomalous values (resulting

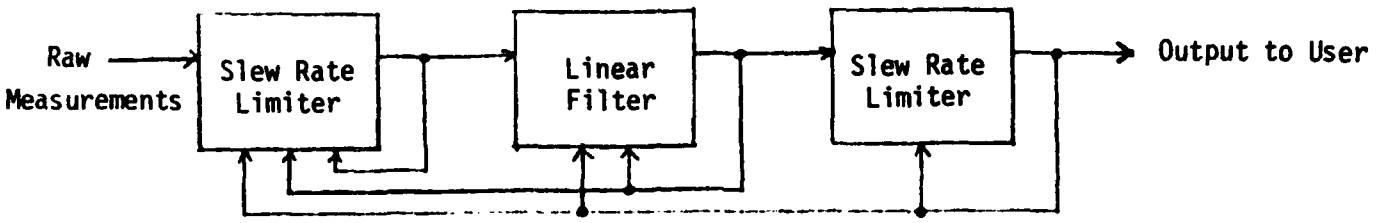

Fig. 5-1. Data editing structure employing slew rate limiters.

from things such as momentary equipment failures or adjacent channel interference, e.g., C-band weather radar pulses) through the relatively narrow-band filter wherein their effects would persist for too long a time. Secondarily, it provides a measure of immunity to short duration, high intensity multipath perturbations ("bright flash"). It is not difficult to design configurations which achieve reasonable success in both objectives; unfortunately, some of these designs also have potentially objectionable susceptibility to bias errors from lower level, persistent multipath returns. In the Phase II receiver, truncation limits were selected in accordance with the maximum rates of air-frame motion over the relatively short (e.g., 25 msec in EL1) raw data period rather than with regard to any multipath-related criteria.

The opposite configuration, limiter-after-filter, represents what has been utilized in the TRSB Phase III receivers. Generally speaking, this arrangement is intended to provide the outlier capability of the former without dragging along its multipath bias susceptibility.

The general data editing structure has not, to our knowledge, undergone any systematic study within the MLS realm. This is unfortunate in that there it probably harbors some reasonable compromise solutions, ones which could be available to virtually all the competing techniques as well as to related non-MLS areas such as landing monitors and surveillance. It is not the purpose of this chapter to fully address that general task; what is presented in the following is a rather detailed investigation of the Phase II slew limiter/filter combination and some of its variants. It is felt that the results have implications reaching beyond the specific designs studied and are, therefore, useful in forming a basis upon which to attack the more general problem.

B. TRSB Phase II Data Processing

Prior studies of the TRSB data processing have concentrated on the multipath performance of the dwell gate processor used for determining beam arrival time. Analytic and experimental studies have produced a reasonably good understanding of the multipath bias and rms errors in the linearly filtered output. Outlier performance is directly deducible from the impulse response of the filter.

The Phase II receiver incorporated a nonlinear slew rate limiter at the input which adjusted the input data in the direction of the most recent filtered output in the event that the two differed sufficiently. The objectives were to largely eliminate outliers before they could propagate through the filter and to attenuate the oscillatory errors associated with high scalloping rate multipath.

The Phase II data confirmed the predicted outlier performance of the slew rate limiter. However, it also became obvious that a second look at multipath performance was needed. Both the experimental and comparable computer simulation data showed error waveforms not explainable by previously known results. In particular, a sizable bias error appeared when (i) the individual elevation scan errors themselves were large (relative to the slew limit), and (ii) the scalloping frequency was well above 5 Hz. In such cases, we have found that single scan static error results together with classic motion averaging theory (see e.g., Chapter 5 of Ref. [28]) cannot adequately describe the overall performance of the highly nonlinear dynamic system composed of the slew rate limiter followed by a low-pass (10 rad/sec cutoff frequency) digital filter.*

A principal objective of this chapter is to explain the error behavior of the Phase II receiver and to quantify the error magnitudes for various multipath conditions. Section B reviews the error behavior of the standard dwell gate processor (without slew limiting), presenting some newly obtained refinements (derived in Volume II of this report) of previous results. Section C describes the Phase II limiter-before-filter configuration and shows that the key to understanding its multipath performance lies in curves of error as a function of rf phase for fixed separation angle and multipath/direct amplitude ratio.

Slew limiting either the state or the output of the first-order linear filter has been proposed as a solution to the bias problem, and some aspects of that arrangement are studied in Section D. Outlier rejection capability of these new configurations is also treated there.

Section F summarizes the conclusions of the study and draws upon them to make some suggestions for studies in the area of raw data editing as it applies to the TRSB Phase III receivers.

C. Single Scan Multipath Error for a TRSB Dwell Gate Processor

For the purpose of studying in-beam multipath error, it is adequate to model the scanning beam antenna pattern as having Gaussian shape, i.e.:

$$P(x) = e^{-kx^2} \quad ; \quad k = 2 \ln 2 = 1.386$$

---

*The MLS Phase III receivers have the slew limiter at the output of a predictive (α,β) low pass filter. Comments on the Phase III receiver are in Section E.

where x is angular displacement in beamwidths. Expressions for mean, rms, and peak-to-peak errors are presented below. These are given as functions of relative multipath amplitude ρ, separation angle θ (BW), and nominal threshold crossing points $\pm v$ (BW).* The derivations, given in Appendix E of Volume II, take into account terms through squared order in the variable $\nu = \rho e^{-k\theta^2}$. Previous results of this type [28] only retained terms through first-order in η and consequently were incapable of obtaining the bias result:

$$\text{(bias):} \quad \bar{e} = \frac{1}{2} k \rho^2 \theta^3 e^{-2k\theta^2} \frac{\sinh kv\theta}{kv\theta} \left[2 \cosh 2kv\theta + 1 - \frac{\sinh 2kv\theta}{2kv\theta}\right] \tag{5-1}$$

$$\text{(rms):} \quad \sigma_e = \frac{1}{\sqrt{2}} \rho \, |\theta| \, e^{-k\theta^2} \frac{\sinh 2kv\theta}{2kv\theta} \tag{5-2}$$

$$\text{(peak-peak):} \quad e_{pp} = 2\rho \, |\theta| \, e^{-k\theta^2} \frac{\sinh 2kv\,\theta}{2kv\theta} \tag{5-3}$$

For small separation angles, the bias term is:

$$\bar{e} \simeq 0.34 \, \rho^2 \, \theta^3 \, e^{-2k\theta^2} \tag{5-4}$$

We note in particular the θ^3 dependence on angle, since this will be contrasted to the result obtained using slew-limiting. The rms error formula is identical to the one obtained from the first-order analysis; no new terms

*Beamwidths (BW) are measured at the -3 dB points in the waveform. Typical values in the MLS application range from 0.5° to 3.0°.

appear in the extension. The same is true of the peak-to-peak error, although with the aid of the higher order error vs. phase formula, more accurate expressions for the positive and negative peak errors have been obtained.

D. Phase II Slew Limiter Phenomenology

First, we briefly review the mode of operation of the Phase II slew rate limiter insofar as it affects the resulting angle estimates.* The procedure is as follows:

(1) the angle estimate, θ_n, for the n-th to-fro scan pair is compared to the last smoothed angle estimate, $\theta_{s,n-1}$:

(2) if the single scan estimate differs from the smoothed estimate by more than the slew limit ε, the single scan estimate is truncated to a value θ_n' which consists of a step of ε in the direction of the difference $(\theta_n - \theta_{s,n-1})$, i.e.,

$$\theta_n' = \begin{cases} \theta_n & ; \ |\theta_n - \theta_{s,n-1}| > \varepsilon \quad (5\text{-}5) \\ \theta_{s,n-1} + \varepsilon \operatorname{sgn}(\theta_n - \theta_{s,n-1}) & ; \ |\theta_n - \theta_{s,n-1}| > \varepsilon \quad (5\text{-}6) \end{cases}$$

(3) the smoothed estimate is updated using $\hat{\theta}_n'$; e.g., for the first-order low-pass filter

$$\theta_{s,n} = (1-\alpha)\,\theta_{s,n-1} + \alpha\theta_n' \qquad (5\text{-}7)$$

---

*We ignore here the confidence counter associated with the slew rate limiter,

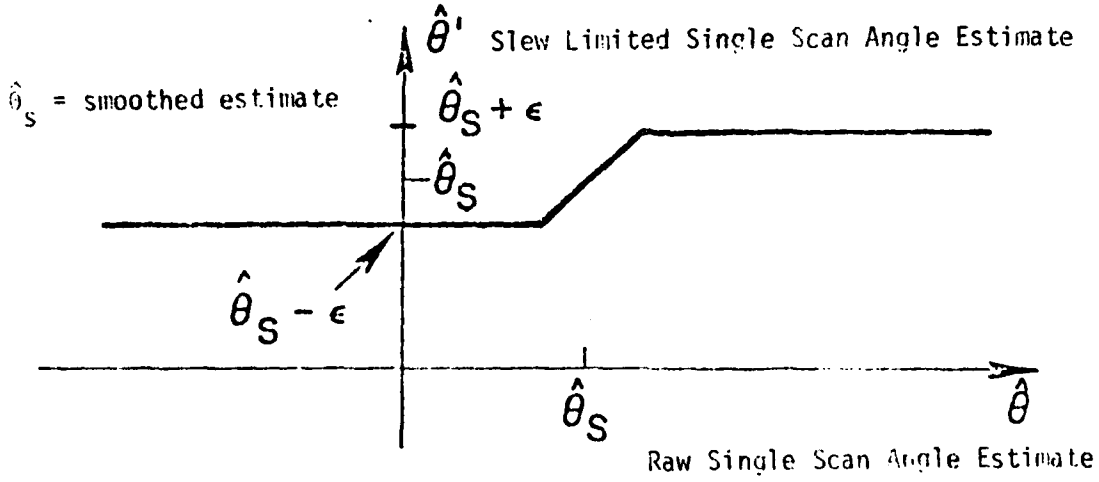

Fig. 5-2. Input-output characteristic for slew limiter.

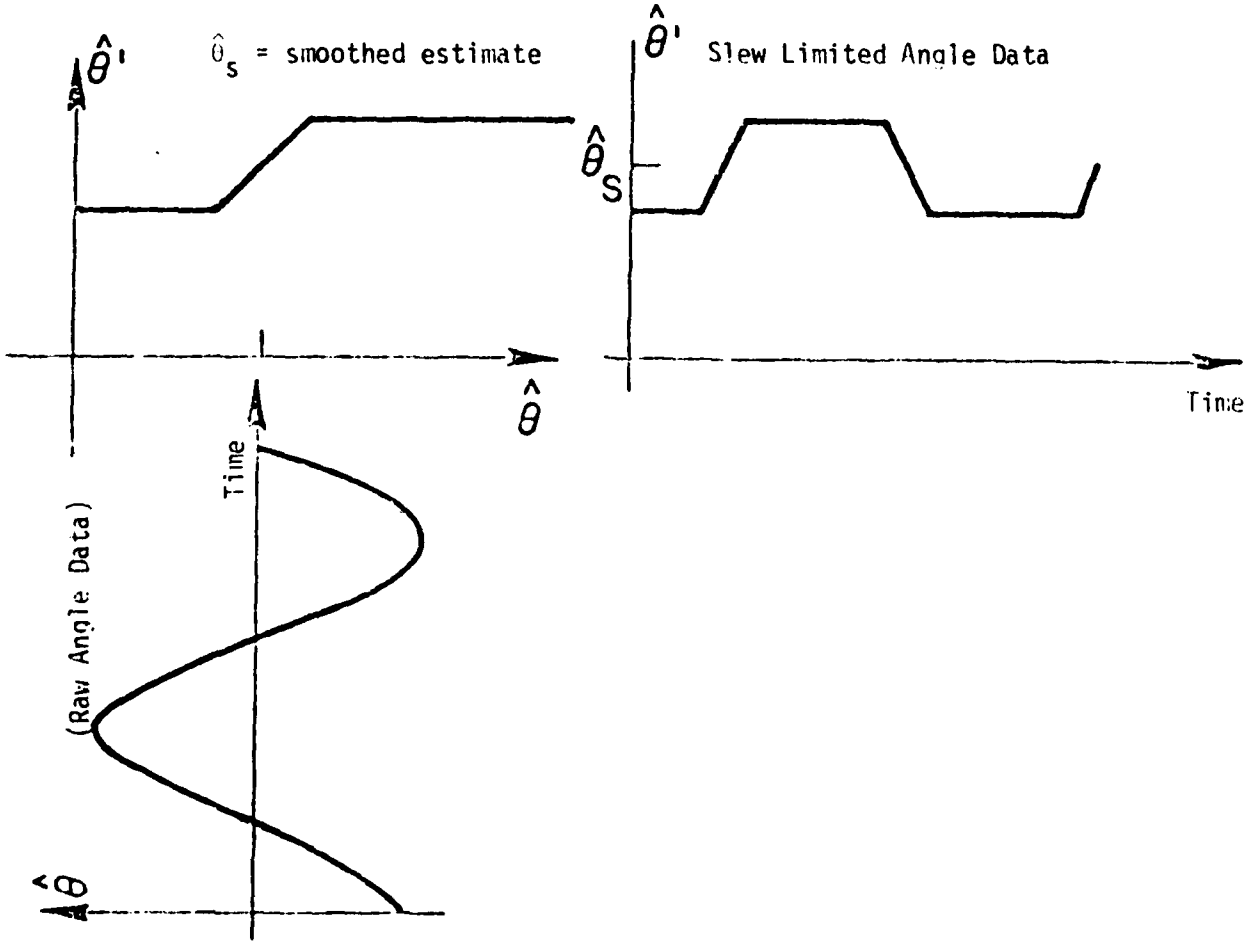

Fig. 5-3. Input-output time waveforms with TRSB Phase II receiver slew limiter.

The truncation level ε is 1°/sec ÷ data rate, for example, 0.025° for elevation.

In Fig. 5-2, we have plotted θ_n' as a function of θ_n. A key to understanding the operation of the slew limiter is to observe that when θ_n has large oscillations (i.e., $\gg \varepsilon$) about θ_s, as illustrated in Fig. 5-3, the slew rate limiter acts very much like hard limiter with output values $\theta_s \pm \varepsilon$.

Note that the dynamics, Eqs. (5-5) through (5-7), can be rewritten in terms of estimation errors rather than the estimates themselves and the form is unchanged. Just define $e_n = \theta_n - \theta_o$, where θ_o is the direct signal angle, and similarly define the other error variables to get

$$e_{s,n} = (1-\alpha)e_{s,n-1} + \alpha \begin{cases} e_n \quad ; \quad |e_n - e_{s,n-1}| < \varepsilon \\ e_{s,n-1} + \varepsilon \operatorname{sgn}(e_n - e_{s,n-1}); \text{ otherwise} \end{cases} \tag{5-8}$$

Thus, the comments made above about the hard limiting of the estimates apply equally well to the errors. If, then, the estimate $\hat{\theta}_s$ <u>were</u> fixed, then the long term statistics of the errors in the slew-limited raw data, under the assumption of large errors ($\gg \varepsilon$), would be

$$\overline{e'} = \overline{\theta'} - \theta_o = e_s + \varepsilon\,(P_+ - P_-) \tag{5-9}$$

$$\sigma_{e'} = \varepsilon \sqrt{1 - (P_+ - P_-)^2} \tag{5-10}$$

where

$$P_+ = \text{fraction of time } e > e_s \tag{5-11}$$

$$P_- = \text{fraction of time } e < e_s \tag{5-12}$$

The direct effect of the slew limiter is evident in that the results do not depend on the magnitude of the deviations of θ_n from $\hat{\theta}_{s,n-1}$, but only on the time exceedance characteristics. In Appendix E of Volume II, it is shown that the time exceedance parameter $(P_+ - P_-)$ can be approximated as follows:

$$P_+ - P_- = \frac{2}{\pi} \sin^{-1} \frac{\rho^2 \theta\, e^{-2k\theta^2} \dfrac{\sinh 4kv\theta}{4kv\theta} - E}{\rho\theta e^{-k\theta^2} \dfrac{\sinh 2kv\theta}{2kv\theta}} \tag{5-13}$$

where E is the comparison level (which is e_s for the slew rate limiter).

If the multipath is of short duration, we may assume that any initial error in the smoothed estimate is negligible ($e_s \simeq 0$), and that the statistics of a single scan slew limited error are [using Eq. (5-13)]

$$\overline{e'} = \frac{2\varepsilon}{\pi} \sin^{-1} \frac{\rho^2 \theta e^{-2k\theta^2} \left(\dfrac{\sinh 4kv\theta}{4kv\theta}\right) - E}{\rho\theta e^{-k\theta^2} \left(\dfrac{\sinh 2kv\theta}{2kv\theta}\right)} \tag{5-14}$$

$$\sigma_{e'} = \varepsilon \sqrt{1 - \left[\frac{2}{\pi} \sin^{-1} \left(\rho e^{-k\theta^2} \cosh 2kv\theta\right)\right]} \tag{5-15}$$

This mean error result can be compared to the bias error given earlier in Eq. (5-4) as follows. Recall that the assumption here is that the raw scan errors are generally >> ε. Then the same must certainly be true of the peak error, which can be approximated by taking half the peak-to-peak error given in Eq. (5-3):

$$\varepsilon \ll e_p \simeq 1/2\ e_{pp} \simeq \rho|\theta|e^{-k\theta^2} \tag{5-16}$$

Using this in Eq. (5-14), linearizing the $\sin^{-1}(\cdot)$ function and overbounding the cosh factor by its small argument Gaussian approximation ($\cosh x \simeq e^{x^2/2}$) yields:

$$|e'| \ll 0.637\ \rho^2|\theta|^{(-2k+4k^2v^2)}\ \theta^2 \tag{5-17}$$

as compared to the bias of

$$\bar{e} = 1.39\ \rho^2\theta^3e^{-2k\theta^2} \tag{5-18}$$

The angle factor in (5-17) is larger than that in (5-18) for $\theta < 1$ and greater for $\theta > 1$, but since (5-17) is an upper bound, it is apparently safe to conclude that there is no great worsening of the bias due to slew limiting short duration multipath.

The standard deviation is greatly decreased from what it would have been without the limiter, as the following shows:

$$\sigma_{e'} < \varepsilon << \rho|\theta|e^{-k\theta^2} \cong \sqrt{2}\,\sigma_e \tag{5-19}$$

For an estimate of what effectively constitutes "short duration," let us look at the tracking equation on the assumption that there is a slew violation on every scan:

$$e_{s,n} = (1-\alpha)\, e_{s,n-1} + \alpha\, [e_{s,n-1} + \varepsilon \operatorname{sgn}(e_n - e_{s,n-1})]$$

$$= e_{s,n-1} + \alpha\, \varepsilon \operatorname{sgn}(e_n - e_{s,n-1}) \tag{5-20}$$

For high enough scalloping rates, $\operatorname{sgn}(e_n - e_{s,n-1})$ will essentially be a sequence of binary random variables with probabilities P_+, P_- (having the statistics derived from Eqs. (5-14) and (5-15)). Then Eq. (5-20) says that the smoothed output is the <u>sum</u> (note, not the average) of the previous scan errors. Thus, if the multipath started at scan 1,

$$\sigma_{e_{s,n}} < \sigma\, \varepsilon \sqrt{n} \tag{5-21}$$

Thus, the "short duration" analysis holds as long as the standard deviation of the smoothed output is still small relative to the peak error, i.e.,

$$n << \left(\frac{e_p}{\alpha\varepsilon}\right)^2 \tag{5-22}$$

Subsequently, we rederive the condition on n by a different means and obtain a more precise result.

From the above, we conclude that the slew rate limiter is quite effective at reducing transient errors due to "bright flash" multipath.

For long duration, high amplitude multipath, the situation is somewhat different. The smoothed output will have time to transition to a steady state mode in which it oscillates about an equilibrium value such that $P_+ - P_- = 0$, that is, the errors exceed the equilibrium value half the time and are less than it half the time. Equation (5-13) directly yields an expression for this slew equilibrium point:

$$\overline{e}_{slew} = \rho^2 \theta e^{-2k\theta^2} \left(\frac{\sinh 4kv\theta}{4kv\theta}\right) \tag{5-23}$$

A second way to obtain this value is to note that since error vs. phase (ϕ) is a function of cos ϕ, it is symmetric about both $\phi = 0°$ and $\phi = 180°$ (see Fig. 5-4). *Further, the function is monotone over (0°, 180°). Then the regions of* "above equilibrium" and "below equilibrium" will be centered around 0° and 180°. Alternatively, the demarcation between them occurs at $\phi = 90°$, 270°, implying that the <u>slew rate limiter equilibrium value</u> is merely the <u>static error evaluated at 90° differential phase</u>. This value can be shown to be identical to (5-23):

$$e(90°) = \rho^2 \theta e^{-2k\theta^2} \left(\frac{\sinh 4kv\theta}{4kv\theta}\right) = \overline{e}_{slew} \tag{5-24}$$

Comparison with the other results is easily made. From Eq. (5-17) we see that the slew equilibrium is much greater than the short multipath bias. Using Eq. (5-4) we see that:

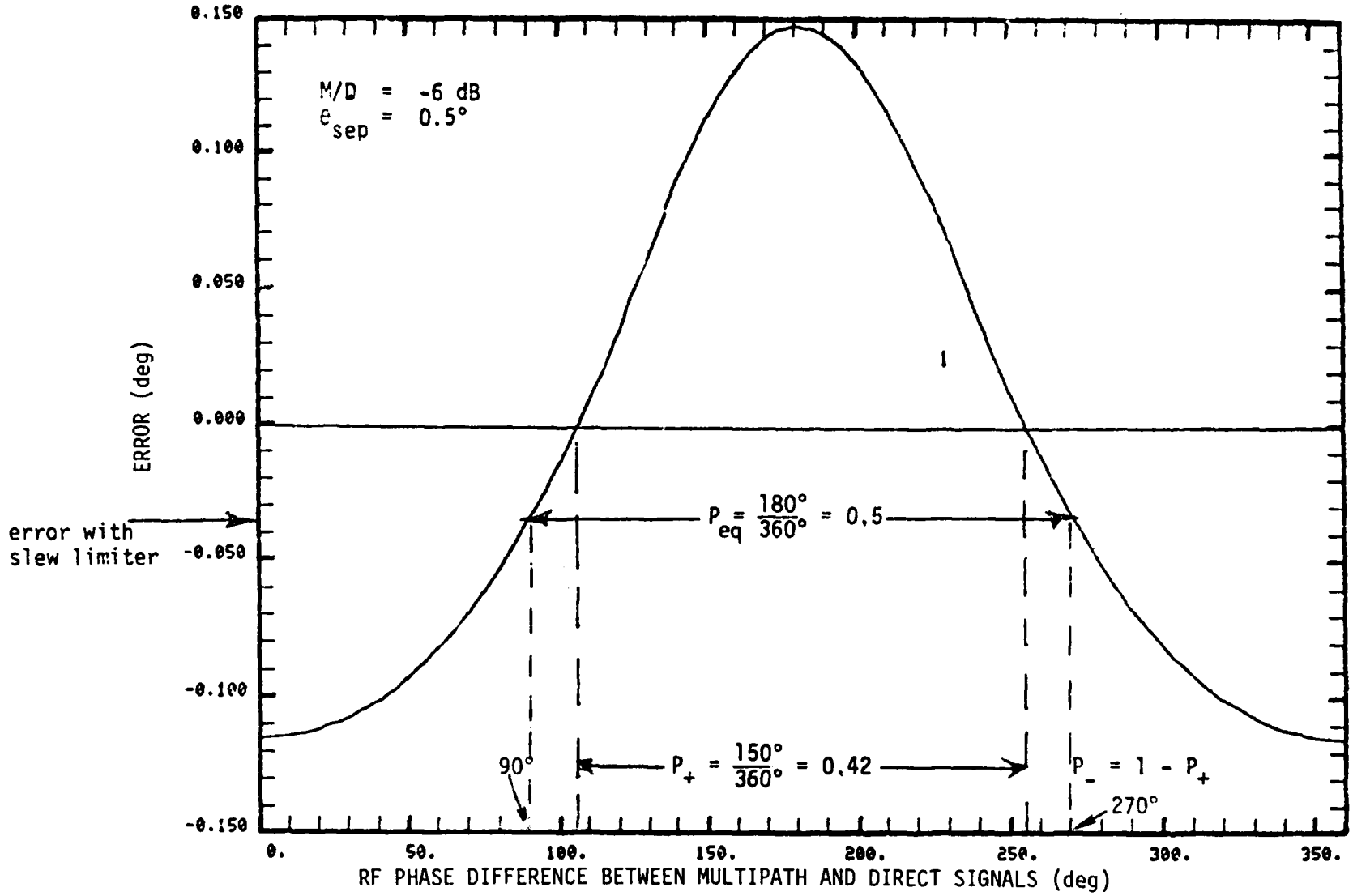

TRS EL1

Fig. 5-4. Illustration of determining P_+, P_-, and long duration multipath error with slew limiter.

$$\bar{e}_{slew} \approx \left(\frac{0.85}{\theta}\right)^2 \bar{e} \tag{5-25}$$

so that for small separation angles there is an appreciable increase in bias.

Figure 5-5 contains plots of the slew equilibrium point vs. separation angle for several multipath levels. The values were obtained from the Lincoln Laboratory TRSB simulation by fixing the multipath phase at 90°. Evaluations of Eq. (5-24) are included to check the accuracy of the formula. It is seen that the formula is quite accurate for all separation angles up to -4 dB multipath. For levels of -3 dB and above, we observe a phenomenon discovered in earlier TRSB studies, which is that the bias error tends to increase almost linearly and suddenly drops rapidly to zero. The explanation is that since the multipath level exceeds the dwell gate threshold level, the trailing edge threshold crossing displaces linearly with separation angle until the separation is large enough to cause a double hump characteristic in the envelope. When the dip in the hump goes low enough to cross the threshold, the trailing edge crossing snaps back to near its nominal value, cutting the error almost to zero.

This same phenomoneon is seen in Fig. 5-6 which plots the above data in the opposite manner, i.e., error vs. multipath amplitude for fixed separation angle. The ρ^2 behavior for small ρ is clearly evident. When the separation angle becomes large (> 1.0°), the slew bias takes a large leap upward at the threshold level, ρ = -3 dB.

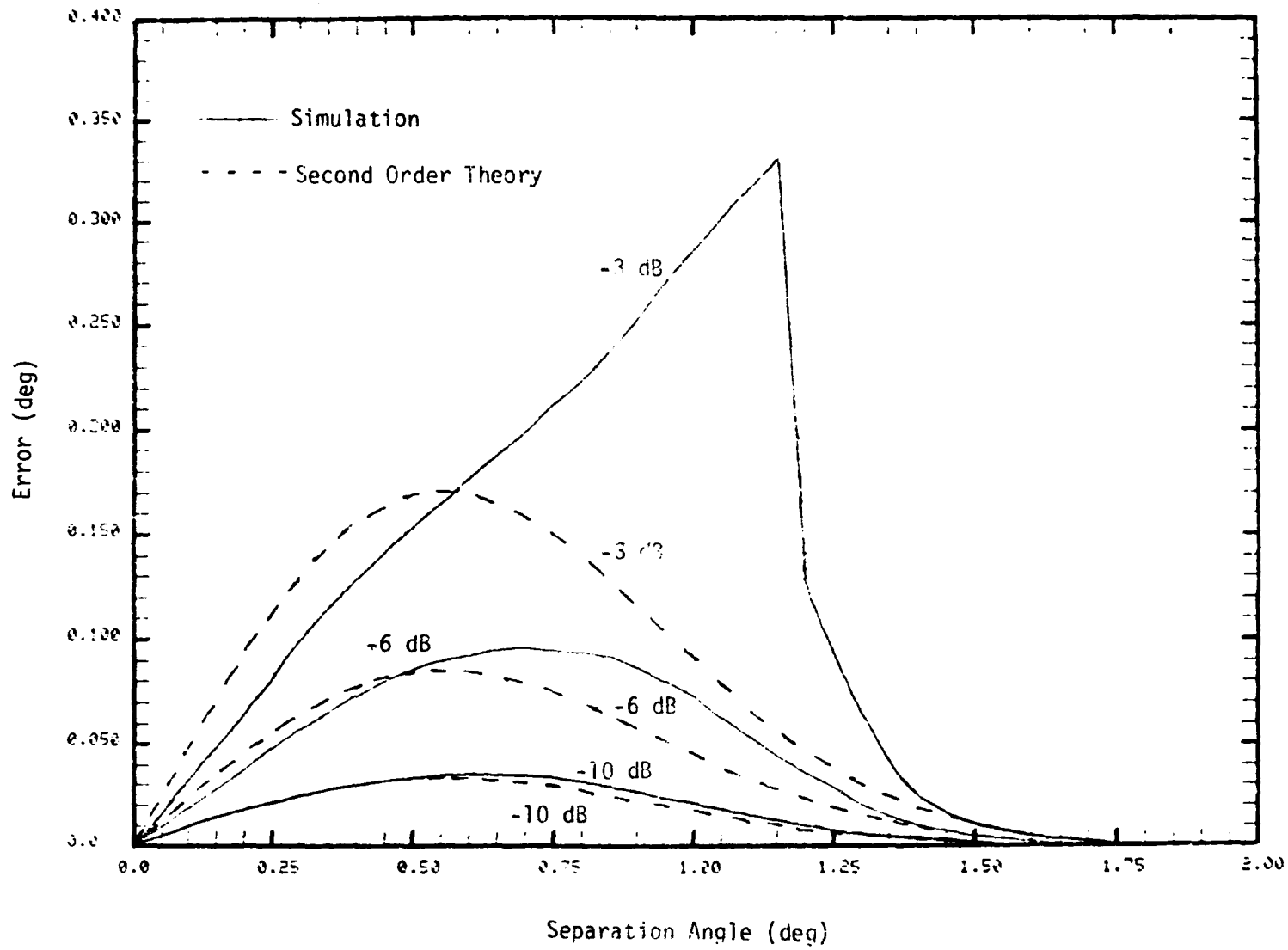

Fig. 5-5. Slew bias error vs. separation angle for various multipath amplitudes.

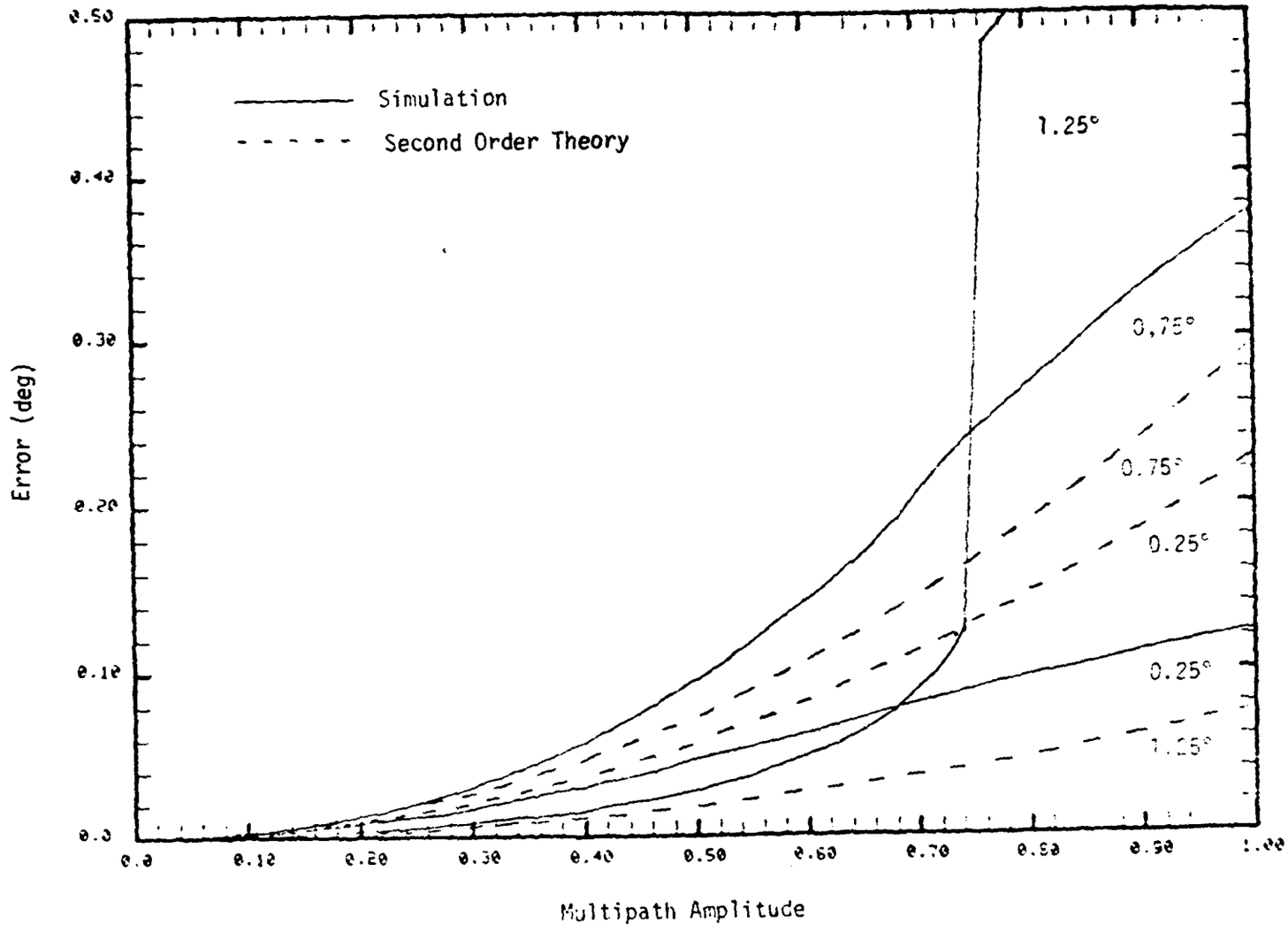

Fig. 5-6. Slew bias error vs. multipath amplitude for various separation angles.

The first and second-order statistics of the filter output errors as a function of time can be found from the procesing equation (5-20). The result for the mean is

$$\bar{e}_{s,n} = \left(1 - \frac{2\alpha\varepsilon}{\pi e_p}\right)^n e_{s,o}$$

$$+ \rho^2 \theta e^{-2k\theta^2} \left(\frac{\sinh 4kv\theta}{4kv\theta}\right) \left[1 - \left(1 - \frac{2\alpha\varepsilon}{\pi e_p}\right)^n\right] \qquad (5\text{-}26)$$

where $e_{s,o}$ is the initial filter state before the onset of multipath (ρ,θ). The equation above shows how the filtered output transitions exponentially from the initial state to the slew bias level, i.e., $\lim \bar{e}_{s,n} \triangleq \overline{e_{s,\infty}} = \overline{e_{slew}}$. The time constant n_o (in scans) of the transition is found by writing the exponential term thus:

$$\left(1 - \frac{2\alpha\varepsilon}{\pi e_p}\right)^n \triangleq e^{-n/n_o} \qquad (5\text{-}27)$$

$$n_o = \frac{1}{-\ln\left(1 - \frac{2\alpha\varepsilon}{\pi e_p}\right)} \simeq \frac{\pi}{2}\left(\frac{e_p}{\alpha\varepsilon}\right) \quad ; \quad \alpha\varepsilon \ll e_p \qquad (5\text{-}28)$$

Compare this with the condition given previously (5-22) for "short duration" multipath and note that the new result yields a smaller time constant. As an example, consider the case $\rho = -10$ dB, $\theta = 0.5°$ for a BW = 1.0° system and -3 dB threshold, i.e., $v = 0.5$. Equation (5-3) predicts a peak error $e_p = 0.12°$. For the elevation slew limit $\varepsilon = 0.025°$ and smoothing parameter $\alpha = 0.22$, corresponding to the 10 rad/sec filter, we get $n_o \simeq 34$ scans = 850 msec. The slew bias for this example is found to be

$$\overline{e_s} = 0.035\ ° \tag{5-29}$$

The equation for the mean squared error is somewhat more complicated. It can be shown by a Markov process analysis* that the steady state value of the error is

$$\overline{\hat{e}^2_{s,\infty}} \triangleq \lim_{n\to\infty} \overline{\hat{e}^2_{s,n}}$$

$$\sigma^2_\infty = \frac{\pi\alpha\varepsilon\ e_p}{4} + \left(\overline{e_{s,\infty}}\right)^2 \tag{5-30}$$

where $\overline{e_{s,\infty}}$ denotes the steady state slew bias error given by (5-23) or (5-24). The first term in (5-30) is the steady state variance:

$$\sigma^2_\infty = \frac{\pi\alpha\varepsilon\ e_p}{4} \tag{5-31}$$

For the numerical example given above

$$\sigma_\infty = 0.023° \tag{5-32}$$

as it does not affect the angle estimates.

*Using the error propagation equation

$$e_{s,n} = e_{s,n-1} + \alpha\ \varepsilon\ Z_n$$

where

$e_{s,n}$ = smoothed estimate, n-th scan
e_n = raw estimate, n-th scan
ε = slew limit (per scan)
α = smoothing constant in the filter
Z_n = sgn $(e_n - e_{s,n-1})$ is at high scalloping rate an independent random

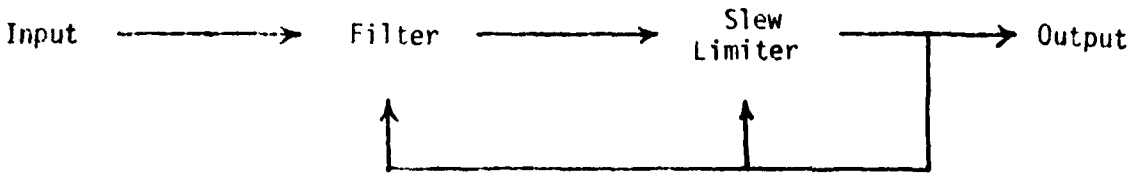

(a) Limiter within feedback loop

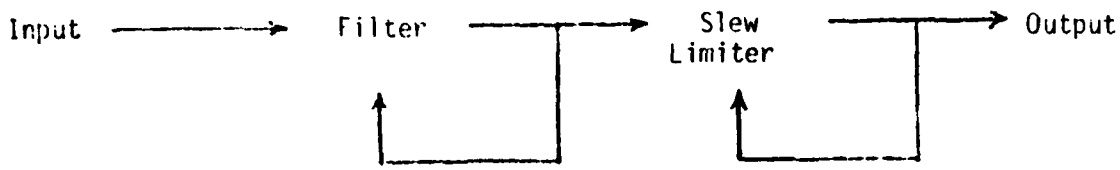

(b) Limiter outside feedback loop

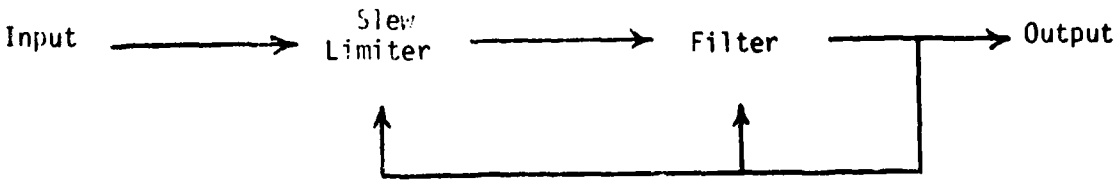

(c) Limiter before filter (ϕII)

Fig. 5-7. Slew limiting at filter output or input.

and the total rms error is 0.042°.

When the slew limiter is not used, then

$$e_{s,n} = (1-\alpha)\, e_{s,n-1} + \alpha\, e_n \tag{5-33}$$

which has the steady state expected values

$$\overline{e_{s,n}} = \bar{e} \triangleq \overline{e_n} \tag{5-34}$$

and

$$\sigma^2 = \overline{\tilde{e}_{s,\infty}} = \frac{\alpha}{2-\alpha}\,\sigma^2 \tag{5-35}$$

i.e., the filter has no effect on the bias.

E. Slew Rate Limiter at Filter Output

In this section, receivers which slew rate limit at the filter output are studied. As before, the analysis here assumes a first-order filter, but it is hoped that the results may provide intuitive insight into the behavior of higher order filter/limiter combinations as well.

Two configurations are possible, depending on whether the internal feedback of the slew-limited variable precedes or follows the limiter. These two options are shown in Fig. 5-7 (along with the limiter-before-filter arrangement) and are considered in turn below.

a. Slew Rate Limiter Within Feedback Loop

Let $e_{s,n-1}$ represent the previous (slew-limited) output or state of the filter. It is determined as follows. The new data input θ_n is linearly filtered to yield a preliminary state estimate $\theta_{s,n}$:

$$\theta_{s,n} = (1 - \alpha)\, \theta_{s,n-1} + \alpha\theta_n \tag{5-36}$$

The final state estimate is found by slew limiting $\theta_{s,n}$:

$$\theta_{s,n} = \begin{cases} \theta_{s,n} \quad : \quad |\theta_{s,n} - \theta'_{s,n-1}| < \varepsilon & (5\text{-}37) \\ \theta'_{s,n-1} + \varepsilon\, \mathrm{sgn}(\theta_{s,n} - \theta'_{s,n-1}) \ ; \text{ otherwise} & (5\text{-}38) \end{cases}$$

If the input variations are sufficiently small, the filter will operate in its linear region as given by (5-37) with $\theta'_{s,n-1} = \theta_{s,n-1}$ for all n. On the contrary, if there is a slew violation on the n-th scan, the output is given by the bottom equation in (5-38).

Note that the slew test can be rewritten as follows, using (5-37):

$$|\theta_{s,n} - \theta'_{s,n-1}| < \varepsilon \longleftrightarrow |\alpha\theta_n - \alpha\theta_{s,n-1}| < \varepsilon \tag{5-39}$$

$$|\theta_n - \theta'_{s,n-1}| < \varepsilon/\alpha$$

The latter form shows that the slew test is identical to the one used when limiting on the raw input data, except that the effective slew limit has become ε/α rather than ε (compare with Eqs. (5-5) and (5-6)). Furthermore, the output equations in the two cases are identical under the same transformation of slew limit. What we have shown is that slew limiting at the output of a first-order filter with limit ε is <u>exactly equivalent</u> to limiting at the

input with the (larger) limit ε/α as long as the slew limited state variable is fed back in the recursive filter equation. The implication is that the smoothing which occurs in the filter permits use of a smaller limit value than would have been required at the input to achieve the same effect. Thus, limiting the state variable amounts to no more than an alternate realization of slew limiting at the input for a first-order filter.

b. Slew Rate Limiter Outside Feedback Loop (as in Phase III TRSB Receiver)

In this configuration, the slew limiting is applied to the linear filter output sequence and its outcome does not influence the filtering. The newly filtered output is compared to the previous output of the slew limiter and the slew test is made on their absolute difference. The equations are

$$\theta_{s,n} = (1 - \alpha)\, \theta_{s,n-1} + \alpha\theta_n \quad : \text{ linear filter output} \tag{5-40}$$

$$\theta'_{s,n} = \begin{cases} \theta_{s,n} & : \text{ no slew} \\ \theta'_{s,n-1} + \varepsilon\, \mathrm{sgn}(\theta_{s,n} - \theta'_{s,n-1}) & : \text{ slew} \end{cases} \tag{5-41}$$

the slew test being

$$|\theta_{s,n} - \theta'_{s,n-1}| \underset{\text{slew}}{\overset{\text{no slew}}{\lessgtr}} \varepsilon \tag{5-42}$$

As was done for the previous case, the slew test equation can be rewritten in another form using (5-40):

$$|\theta_{s,n} - \theta'_{s,n-1}| = |\alpha(\theta_n - \theta'_{s,n-1}) + (1 - \alpha)(\theta_{s,n-1} - \theta'_{s,n-1})| \lessgtr \varepsilon \tag{5-43}$$

Equation (5-43) shows that if there were no slew violation at time (n-1), the test at time n would be

$$|\theta_n - \theta'_{s,n-1}| \lessgtr \varepsilon/\alpha \tag{5-44}$$

which is identical to the slew test derived in Eq. (5-39) for the case in which the limiter is within the feedback loop. If there was a violation at (n-1), there will be a bias applied to the test variable $\alpha(\theta_n - \theta'_{s,n-1})$ which is proportional to the discarded difference in the previous slew truncation. This discarded difference can be expanded further in terms of variables n-2, etc., but the procedure does not seem to lead to a particularly useful expression for the test variable. Just by examining (5-43) above, however, we can clearly see that this slew limiter has behavior different from the other two types considered.

One way to evaluate this limiter is to look at its effectiveness at outlier suppression, which can be done by computing the impulse response. Let the filter input sequence consist of an impulse of magnitude $A\varepsilon$ at n=0 and zeros elsewhere, and assume that A is large, specifically $A \gg \alpha^{-1}$. The filter output sequence [the solution of Eq. (5-40)] will be

$$\theta_{s,n} = A\alpha(1 - \alpha)^n \varepsilon \tag{5-45}$$

The first output will have value $A\alpha\varepsilon$, which generates a slew violation and causes the observed output to be limited to ε (it is assumed that both the filter and slew limiter are quiescent at $n = 0$). The slew limiter output will continue to increase linearly in steps of ε until the exponential series in (5-45) decays to within ε of the limiter output. Let $n = N$ be the time at which this first occurs;

$$0 < A\alpha(1 - \alpha)^N\varepsilon - (N + 1)\varepsilon < \varepsilon \tag{5-46}$$

or

$$0 < A\alpha(1 - \alpha)^N - (N + 1) < 1 \tag{5-47}$$

After time N, the slew limiter will be able to follow the exponential, provided that its slope is small enough. The change in the exponential from time N to N+1 is

$$\hat{\theta}_{s,N+1} - \hat{\theta}_{s,N} = - A\alpha^2(1 - \alpha)\ \varepsilon \approx (N + 1)\ \alpha\varepsilon \tag{5-48}$$

The approximation in (5-48) makes use of the defining relationship for N, (5-46). Evidently, the increment can have magnitude either smaller or greater than ε, depending on the value of A. If the slope magnitude exceeds ε at time N, the negative-going exponential will cause slew violations; the limiter output will decrease linearly until it again catches the exponential a second time. When the slope at the first intersection is small enough, the limiter follows from there on without slew violations. Figure 5-8 illustrates both possibilities.

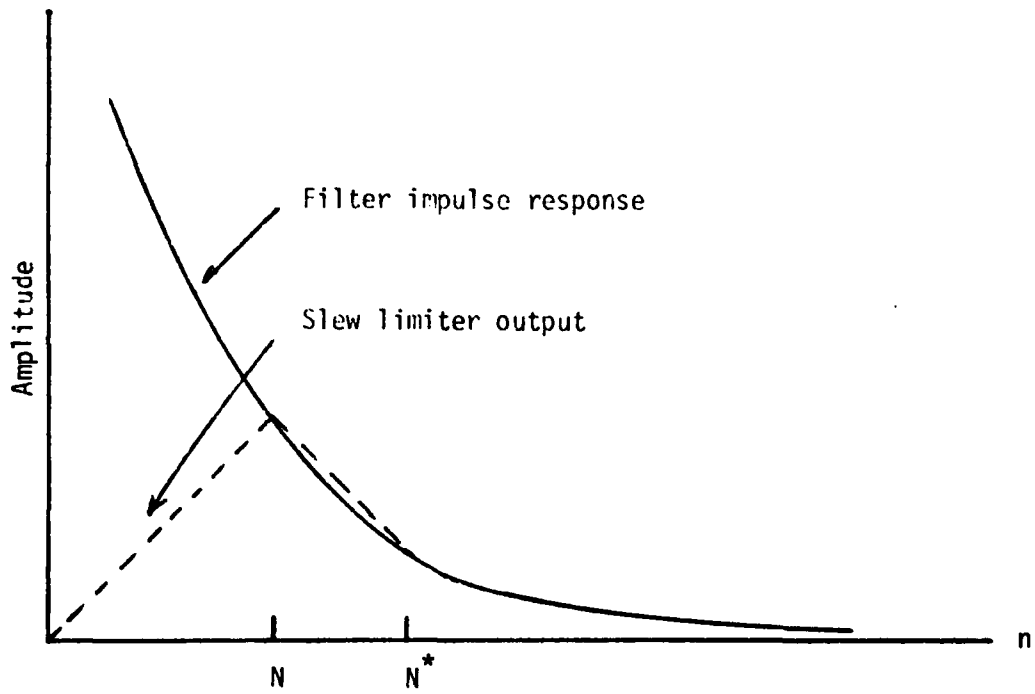

(a) Large slope at intersection

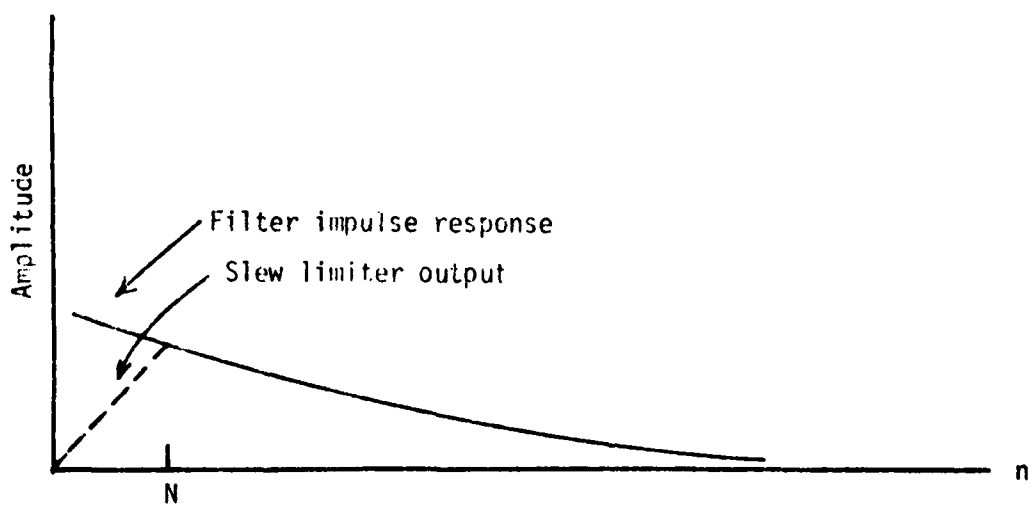

(b) Small slope at intersection

Fig. 5-8. Input and output waveforms for case of limiter outside feedback loop.

A way to calibrate this performance is to answer the following question: For fixed α and ε, what is the largest outlier amplitude that will not cause the slew limiter output to exceed a specified level? Suppose the output is not to exceed $V\varepsilon$. This essentially defines the time point N at which the linear and exponential curves first interact:

$$N = V - 1 \tag{5-49}$$

The outlier amplitude A which causes the intersection at time N is found by solving the approximate intersection equation [obtained from (5-47)]

$$A\alpha(1 - \alpha)^N = (N + 1) \tag{5-50}$$

i.e.,

$$A = \frac{V}{\alpha(1 - \alpha)^{V-1}} \tag{5-51}$$

An outlier of $A\varepsilon$ deg can be tolerated.

Figure 5-9 shows a graph of Eq. (5-51) from which some interesting conclusions can be drawn. For a slew limit $\varepsilon = 0.025°$ (corresponding to the EL system limit rate of 1.0°/sec), the output error will not exceed 0.05° until the outlier amplitude exceeds 0.53°. Decreasing the limit by a factor of 4 (the $\alpha\varepsilon$ "output" value equivalent to $\varepsilon = 0.025°$ at the input for the configuration considered earlier) provides rejection of outliers up to 1.5°. Opening up the limit decreases the outlier rejection capability somewhat. Note that if a larger maximum error (e.g., 0.1°) can be tolerated, the allowable outlier amplitude increases greatly (almost 30° rather than 1.5° for the case just

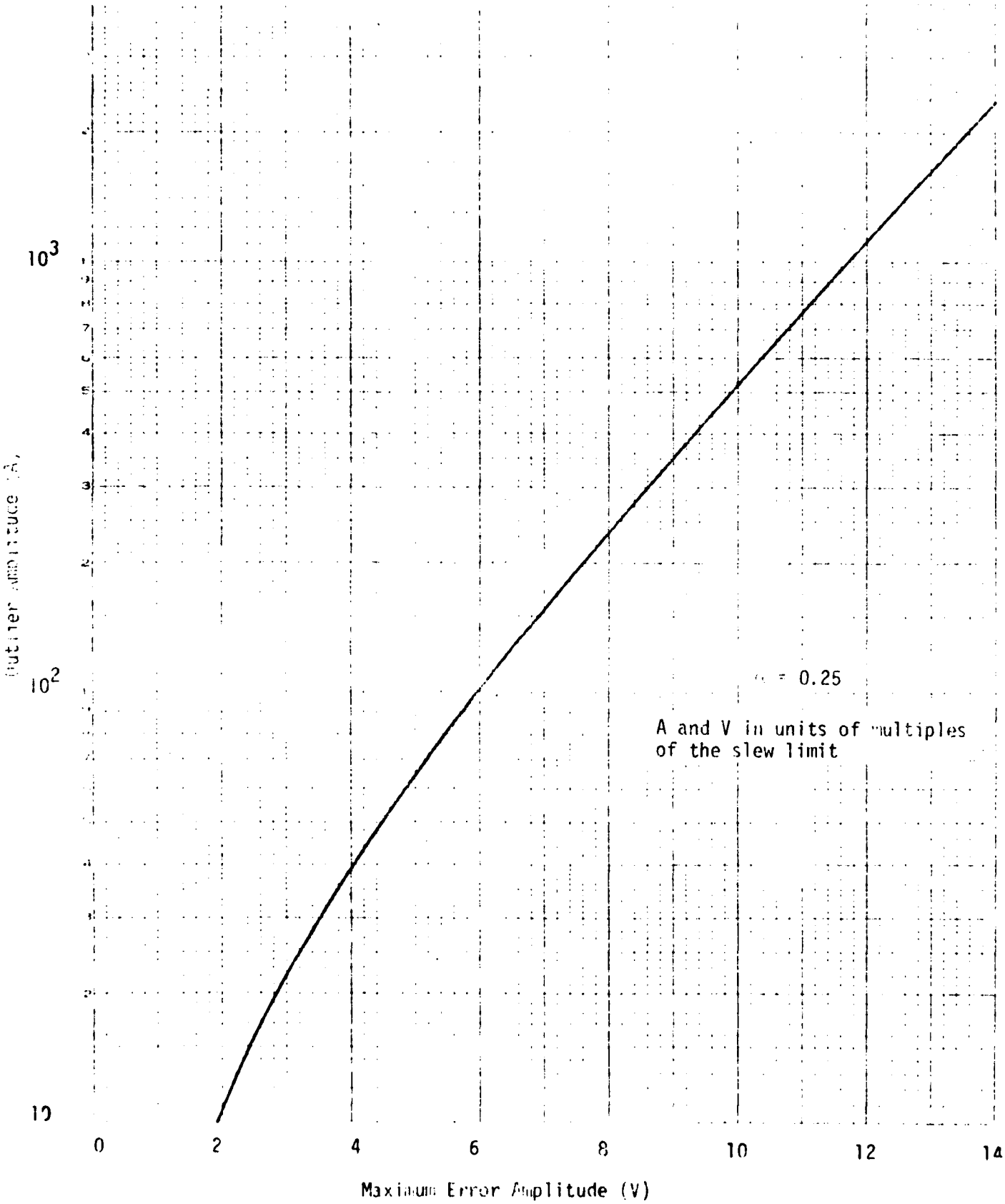

Fig. 5-9. Maximum outlier amplitude for a give maximum output error.

cited). Based on the outlier rejection above, then, one concludes that the use of relatively small slew limits at the output is appropriate.

The smaller the slew limit, however, the longer the strip of slew violations which occur during outlier recovery. It is undesirable to have too many consecutive unidirectional slew violations, which could cause the receiver to lose lock even though the system has almost recovered to accurately tracking the direct signal. We shall demonstrate below that the outlier amplitudes required for unlock are typically far too large to be of any real concern.

The approach in this analysis is similar to that taken above, that is, the smallest outlier amplitude which will cause unlock is calculated. Let N^* be the number of consecutive slews required for unlock. Referring to Fig. 5-8, we see that N^* slews can occur for an exponential which initially crosses the slew output with a slope too steep for the limiter to track and subsequently intersects it again at time N^*. The first intersection occurs at time N, which is determined by noting that the initial and final values of the triangle are 1 and $A\alpha(1 - \alpha)^{N^*}$, respectively, and that its slope (in units of multiples of the slew limit) is ±1 on the two segments. Consequently,

$$N = \frac{1}{2}\left[A\alpha(1 - \alpha)^{N^*} + (N^* - 1)\right] \tag{5-52}$$

Since the final value of the exponential is positive, we can underbound it by zero to get

$$N > \frac{N^* - 1}{2} \tag{5-53}$$

A second bound on N is found from the condition that the slope is too large at time N. From Eq. (5-48), we find that the slope condition is

$$(N + 1)\alpha > 1 \tag{5-54}$$

i.e.,

$$N > \alpha^{-1} - 1 \tag{5-55}$$

For typical values of N^* and α in the MLS application, (5-53) usually represents the tighter constraint. By inspecting the graph, it is easy to see that the smallest amplitude exponential which satisfies the conditions is one for which $N = (N^*-1)/2$. Solving Eq. (5-52) for the amplitude which produces the intersection at time N yields

$$A = \frac{N^*+1}{2\alpha(1-\alpha)^{(N^*-1)/2}} \tag{5-56}$$

It remains to be verified that this amplitude yields a final value for the exponential which is near or below 1, or else the result is not consistent with the assumption that $N \approx \frac{N^*-1}{2}$. The final value corresponding to the choice of A in (5-55) is

$$A\alpha(1 - \alpha)^{N^*} = \frac{N^*+1}{2}(1 - \alpha)^{(N^*+1)/2} \tag{5-57}$$

which has a maximum value of

$$\max_{N^* > 0} \left(\frac{N^*+1}{2}\right)(1-\alpha)^{(N^*+1)/2} = \frac{1}{e \ln\left(\frac{1}{1 - \alpha}\right)} \tag{5-58}$$

For $\alpha > 0.308$, the maximum never exceeds 1, which assures that the approximation is valid for the TRSB azimuth case. For EL ($\alpha = 0.25$), the maximum is 1.28, which is also adequate to verify that (5-53) is a good approximation for the present use.

The TRSB receiver will unlock on one second's worth of consecutive slew violations, which for AZ is essentially $N^* = 13$. For the AZ filter ($\alpha = 0.5$), (5-56) gives $A = 1792$, which is very large (134.4° for $\varepsilon = 0.075°$/scan). In EL, the number is even larger. Thus, the use of small slew limits at the output should not be expected to cause loss of track conditions as a price for good suppression of short transients.

F. Conclusions/Extensions

The analyses and simulation experiments reported in this chapter demonstrate the effect of introducing slew limiting at various points in a first-order tracking filter such as was used in the Phase II TRSB receiver. Two situations are of primary concern: (1) high level multipath reflections which are persistent and have a scalloping frequency well above 5 Hz, and (2) fast outlier transients due either to multipath or equipment malfunction. The major findings about these are summarized below.

1. Persistent Multipath

(i) Slew limiting the raw data at the input to the smoothing filter can introduce a ρ^2 bias error which exceeds the bias error expected from a dwell gate processor.

(ii) Placing the limiter at the filter output (but still within the feedback loop) does not fundamentally change the situation. It is shown that this case is fully equivalent to the configuration discussed in (i), but with a different equivalent slew limit. Specifically, limit ε at the input is equivalent to a (smaller) limit $\alpha\varepsilon$ at the output, where α is the filter constant.

(iii) The multipath performance of slew limiting outside the feedback loop was not evaluated in this study.

2. Outlier Rejection

(i) Slew limiting at the filter input is an effective means of outlier suppression because it eliminates large excursions before they can propagate through the filter.

(ii) The configuration having the limited output feed back into the filter is identical to Case (i) under the same transformation of slew limit stated above. Thus, the two have identical outlier capability.

(iii) If a slew limiter follows the filter and a sufficiently small slew limit is used, the resulting processor can have a good outlier rejection without engendering a receiver unlock due to a long string of slew violations.

None of the techniques under discussion has been exhaustively treated either here or elsewhere in the MLS literature. In this chapter, various problem areas have been discovered, pointing out the need for further work. Based on the present study, the Phase III receiver use of a second-order α-β tracker with slew limiting at the output seems to represent a desirable compromise between multipath bias and outlier rejection.

These results do impact on points raised in the introduction where a more general data processing/reduction problem is considered. The conclusions of the present study suggest that a combination of input and output limiting probably provides the best overall design when both transient and persistent error sources are present.

VI. UNIQUE DMLS MULTIPATH PERFORMANCE ISSUES

Several multipath performance issues were unique to the DMLS technique as a consequence of

(1) multiplicatively combining the array and reference signals to yield the signal analyzed, and

(2) using a frequency code to represent angle.

In this section, we analyze in depth several of these issues which were discussed in Volume II and/or the preceding chapters of this report. The first Section A deals with the effects of a time varying AGC gain on the effective DMLS antenna patterns. It is shown that significant pattern variations do occur, but that the principal angle error effect is to increase the effective sidelobe level.

The next two sections examine the "reference" and array scalloping effects which arise from receiver motion induced Doppler shifts to the reference and array signals, respectively. Section B considers reference scalloping which yields inbeam multipath signals in most situations where multipath is encountered. Previously reported results [41] are extended to consider the impact of scan sequence on the resultant error. Section C considers array scalloping in which the array signal effective multipath angle is altered by receiver motion induced Doppler to such an extent that an angularly out of beam multipath signal becomes inbeam in frequency code.

Section D is concerned with a DMLS growth feature "lateral diversity" which utilizes the multiplicative receiver processing to obtain directivity in the horizontal plane as a means of reducing inbeam elevation multipath from

vertical surfaces (e.g., building walls). Section E presents some comparative scenarios which relate to the issues discussed in the preceding sections. The final discussion considers the potential impact of the various factors on the use of DMLS in the anticipated MLS multipath environment.

A. Effect of Time-Varying AGC Gain on the Effective DMLS Antenna Patterns

The DMLS receiver calculates its angle estimates by forming sum and difference filter outputs and dividing the difference output by the sum output, in a manner similar to radar monopulse processing. The sum and difference filters are realized by digitally correlating the received signal with internally generated sinusoids at the tracked frequency. The correlation products are weighted by Taylor coefficient time tapers which are designed to reduce the effective sidelobes.

At the same time, however, the received signal is passed through an automatic gain conrol (AGC) circuit in order to prevent the incoming signal from lying outside the range of the receiver's A/D converter. The AGC gain can vary significantly during the correlation period, thus imposing an undesired additional time taper on the received data.

In this section, we will look at some of the effects of time-varying AGC gain. The reader is referred extensively to Volume II of this report, Sections III and IV, for the basic equations and notations which we have used to describe the operation of the DMLS receiver.

As shown in Eqs. (II.4-1) to (II.4-11), the sum and difference filter outputs on the nth scan, $\Sigma(n)$, $\Delta(n)$, can be evaluated in the form

$$\Sigma(n) = \frac{1}{4} \sum_{i=0}^{M} \sum_{j=0}^{M} \rho_i R \rho'_j \quad H_\Sigma^n \left[d(n)\ \omega_{ijn} - \omega_t(n) \right] \quad \exp j\left[-d(n)\alpha_{ijn} \right) H(\omega_{ijn}] \tag{6-1}$$

$$\Delta(n) = \frac{1}{4} \sum_{i=0}^{M} \sum_{j=0}^{M} \rho_i R \rho'_j \quad jH_\Delta^n \left[d(n)\omega_{ijn} - \omega_t(n) \right] \exp j\left[-d(n)\alpha_{ijn} \right] H(\omega_{ijn}) \tag{6-2}$$

where the sum and difference filter frequency responses are evaluated as

$$H_\Sigma^n(\omega) = \frac{\sin \omega T}{\omega T} \sum_{k=1}^{8} \frac{\Gamma_\Sigma(k)}{E_n^2(t_k)/R_n} \exp j\ (-\omega t_k) \tag{6-3}$$

$$jH_\Delta^n(\omega) = \frac{\sin \omega T}{\omega T} \sum_{k=1}^{8} \frac{\Gamma_\Delta(k)}{E_n^2(t_k)/R_n} \exp j(-\omega t_k) \tag{6-4}$$

$$t_k = (2k-9)\ T, \qquad k = 1,\ 2, \ldots, 8 \tag{6-5}$$

In these equations, $\Gamma_\Sigma(k)$ and $\Gamma_\Delta(k)$ are the Taylor coefficient time tapers, 16T is the total correlation time, $E_n^2(t_k)/R_n$ are the AGC factors, ρ_i and ρ_j are the angle and reference signal multipath amplitudes, $d(n) = \pm 1$ denotes the scan direction, ω_{ijn} and α_{ijn} are the cross-product frequencies and phases, $\omega_t(n)$ is the tracked frequency, and $H(\cdot)$ is the magnitude of the sector filter frequency response.

We notice that the effect of the time-varying AGC factors is to modify the Taylor weights in the calculation of the filter responses $H_\Sigma^n(\cdot)$, $H_\Delta^n(\cdot)$ to the cross-product frequencies ω_{ijn}. Thus, it is instructive to examine the behavior of these frequency response functions under conditions of constant and varying AGC gain.

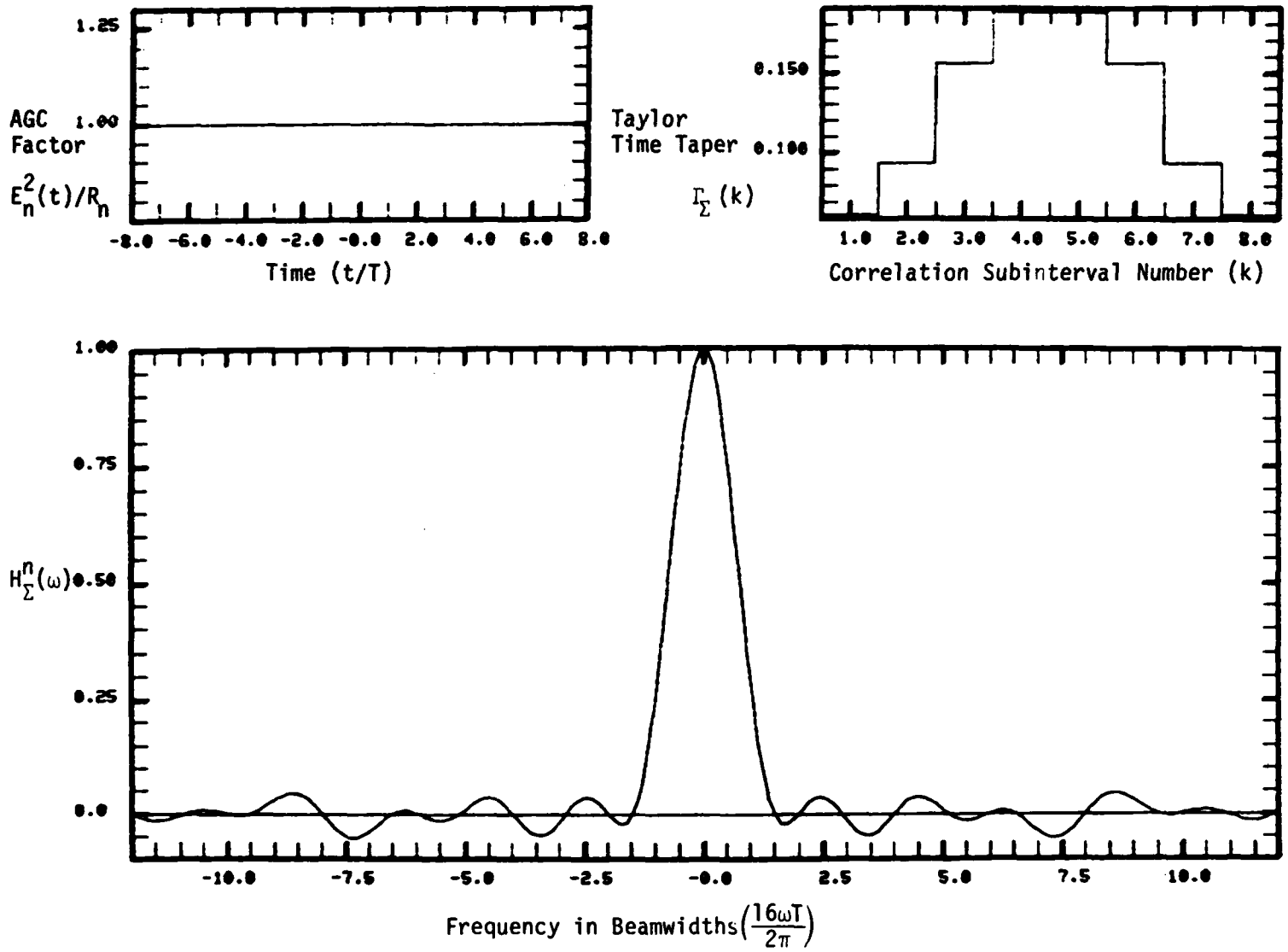

Fig. 6-1. Sum filter frequency response for zero scalloping frequency (uniform AGC factors).

In the absence of AGC variations ($E_n^2(t_k)/R_n = 1$), the sum and difference filter frequency responses are independent of scan number n and may be calculated as

$$H_\Sigma(\omega) = \frac{\sin\omega T}{\omega T} \sum_{k=1}^{8} \Gamma_\Sigma(k)\, e^{-j\omega(2k-9)T} \tag{6-6}$$

$$jH_\Delta(\omega) = \frac{\sin\omega T}{\omega T} \sum_{k=1}^{8} \Gamma_\Delta(k)\, e^{-j\omega(2k-9)T} \tag{6-7}$$

Because the Taylor weights $\Gamma_\Sigma(k)$, $\Lambda_\Delta(k)$ have even and odd symmetry, respectively, around midscan (i.e., $\Gamma_\Sigma(k) = \Gamma_\Sigma(9-k)$, $\Gamma_\Delta(k) = -\Gamma_\Delta(9-k)$), $H_\Sigma(\omega)$ and $H_\Delta(\omega)$ are both real; $H_\Sigma(\omega)$ is even, and $H_\Delta(\omega)$ is odd. Figures 6-1 and 6-2 show the assumed uniform AGC factors, $E_n^2(t_k)/R_n$, the sum and difference Taylor weights $\Gamma_\Sigma(k)$, $\Gamma_\Delta(k)$, and the resulting sum and difference filter frequency responses $H_\Sigma(\omega)$, $H_\Delta(\omega)$. We note that at the highest sidelobes, $H_\Sigma(\omega) = 0.05$ and $|H_\Delta(\omega)| = 0.05$, i.e., -26 dB with respect to $|H_\Sigma(0)| = 1$.

The frequency responses that result from non-uniform AGC gain may be written in the form

$$H_\Sigma^n(\omega) = \frac{\sin\omega T}{\omega T} \sum_{k=1}^{8} \Gamma_\Sigma^n(k)\, e^{-j\omega(2k-9)T} \tag{6-8}$$

$$jH_\Delta^n(\omega) = \frac{\sin\omega T}{\omega T} \sum_{k=1}^{8} \Gamma_\Sigma^n(k)\, e^{-j\omega(2k-9)T} \tag{6-9}$$

where the effective time tapers $\Gamma_\Sigma^n(k)$, $\Gamma_\Delta^n(k)$ are defined by

$$\Gamma_\Sigma^n(k) = \frac{\Gamma_\Sigma(k)}{E_n^2(t_k)/R_n} \tag{6-10}$$

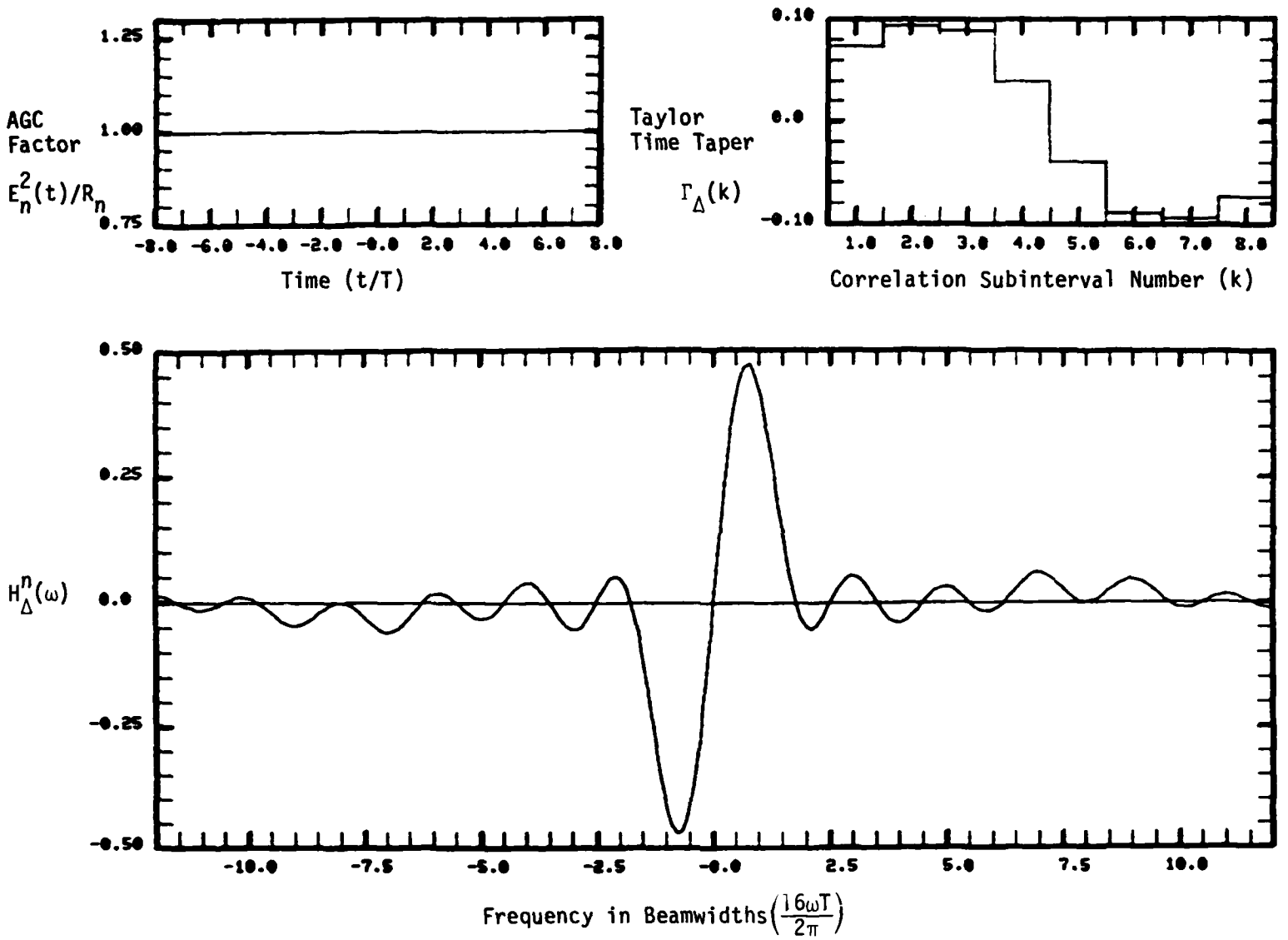

Fig. 6-2. Difference filter frequency response for zero scalloping frequency (uniform AGC factors).

$$\Gamma_\Delta^n(k) = \frac{\Gamma_\Delta(k)}{E_n^2(t_k)/R_n} \tag{6-11}$$

The AGC factors are evaluated from Eq. (II.3-46) as

$$E_n^2(t)/R_n = \frac{1}{2} R_n \left| \, |y_n'(t)|^2 + \sum_\ell |y_n^\ell(t)|^2 \, \right| \tag{6-12}$$

where $y_n'(t)$ is the received reference signal and $\{y_n^\ell(t)\}$ are coherent sums over subgroups of angle signal components with frequency differences clustered within the passband (3 kHz) of the lowpass filter in the AGC feedback loop. Using (II.3-32), (II.3-33), (II.3-39), (II.3-40), and (II.3-43), we evaluate $|y_n'(t)|^2$ and $|y_n^\ell(t)|^2$,

$$y_n'(t)^{\;2} = R^2 \sum_{i=0}^{m} \rho_0' \; e^{j[(\omega_{in}-\omega_{0n})t + (\phi_{in} - \phi_{0n})]^{\;2}} \tag{6-13}$$

$$y_n^\ell(t)^2 = \sum_{i\varepsilon I_n^\ell} \rho_i \; e^{j[(\omega_{in} - \omega_{0n})t + (\phi_{in} - \phi_{0n})]^{\;2}} \tag{6-14}$$

where ω_{in}, ϕ_{in}, ω_{in}', ϕ_{in}', are the frequencies and phases of the ith angle and reference signal components, and I_n^ℓ is the set of angle signal components contributing to $y_n'(t)$. Because of the reference-to-array emphasis factor (R = 2.2 for azimuth, R = 4.47 for elevation), the reference signal term $|y_n(t)|^2$ usually dominates the calculation of $E_n^{\;2}(t)/R_n$, except in the case of a deep reference signal fade under phase conditions which cause the sum of complex exponentials in (6-13) to nearly vanish.

We will now confine our attention to the usual situation for reference scalloping multipath, i.e., a single multipath component which is well out of

beam. In this case, the angle signal components are separated by more than 3 kHz. Thus, each $y_n'(t)$ consists of a single term and the angle signal contribution to the AGC factor is not subject to fading.

$$\left|y_n'(t)\right|^2 = R^2 \left|\rho_o' + \rho_1' \, e^{j\chi_n(t)}\right|^2 \tag{6-17}$$

where the linearly time-varying phase factor $\chi_n(t)$ is defined by

$$\chi_n(t) = (\omega_{1n}' - \omega_{0n})t + (\phi_{1n}' - \phi_{0n}') \tag{6-18}$$

The rate of change of $\chi_n(t)$, $\omega_{1n}' - \omega_{0n}'$, is essentially independent of n (see Eq. (II.3-35)) and is termed the reference scalloping frequency $\omega_1'^s$. Thus, Eq. (6-18) may be re-written in the form

$$\chi_n(t) = \chi_n(0) + \omega_1'^s t \tag{6-19}$$

Finally, by applying (II.3-37) to calculate $(\phi_{0n}' - \phi_{0n}')$, we note that the midscan phase increments from scan to scan according to

$$\chi_n(0) = \chi_{n-1}(0) + \omega_1'^s \, T_s \tag{6-20}$$

where T_s is the total scan time, $0.95\ T_s = 16\ T$.

Collecting terms from (6-15), (6-16), and (6-17), we rewrite (6-12) in the form

$$E_n^2(t)/R_n = A_n(1 + B_n \cos \chi_n(t)) \tag{6-21}$$

where

$$A_n = \frac{1}{2} R_n(\rho_0{}^2 + \rho_1{}^2 + R^2 \rho_1'^2) \tag{6-22}$$

$$B_n = R_n R^2 \rho_0' \rho_1'/A_n \tag{6-23}$$

We shall choose the constant A_n to produce the condition $H_\Sigma^n(0) = 1$, in order that the sum and difference filter frequency response functions may be directly compared under varying AGC conditions. This convention requires a different value of R_n from that defined in Eq. (II.3-47), but such a modification has no effect on receiver performance, because angle estimates are computed from the ratio $\Delta(n)/\Sigma(n)$ and R_n scales $\Sigma(n)$ and $\Delta(n)$ equally.

The effect of increasing (decreasing) the multipath amplitude is to increase (decrease) the sinusoid amplitude modulation factor B_n in the expression (6-21) for the AGC factor. Calculating B_n from (6-23) and assuming that $\rho_0 = \rho_0'$ and $\rho_1/\rho_0 = \rho_1'/\rho_0' = \rho$, we obtain

$$B_n = \frac{R^2}{R^2 + 1} \frac{2\rho}{1 + \rho^2} \tag{6-24}$$

The following table lists the peak-to-peak variation $(1 + B_n)/(1 - B_n)$ in the AGC factor for several values of ρ, under the assumption that $R = 2$ (as it is for azimuth).

TABLE 6-1

PEAK-TO-PEAK AGC VARIATION AS A FUNCTION OF RELATIVE MULTIPATH AMPLTUDE

Multipath Amplitude		AGC Variation	
	ρ $(1+B_n)/(1-B_n)$		
0	(-∞dB)	1	(0 dB)
.1	(-20 dB)	1.38	(3 dB)
.2	(-14 dB)	1.89	(6 dB)
.3	(-10 dB)	2.57	(8 dB)
.4	(-8 dB)	3.46	(11 dB)
.5	(-6 dB)	4.56	(13 dB)
.6	(-4 dB)	5.80	(15 dB)
.7	(-3 dB)	7.05	(17 dB)
.8	(-2 dB)	8.11	(18 dB)
.9	(-1 dB)	8.78	(19 dB)
1.0	(0 dB)	9.00	(19 dB)

We see that there is a sizable peak-to-peak variation in the AGC factor even for moderate multipath levels. The entire peak-to-peak variation will be felt on any given scan if the reference scalloping frequency is high enough to cause the AGC factor to progress through one complete sinusoidal period, i.e., $\omega_1'^s \frac{2\pi}{16T}$. In addition, a scan may be subjected to the entire peak-to-peak AGC variation for scalloping frequencies as low as one-half this value, if the midscan phase condition is unfavorable.

The effective time tapers $\Gamma_\Sigma^n(k)$, $\Gamma_\Delta^n(k)$ are given by

$$\Gamma_\Sigma^n(k) = \frac{1}{A_n} \frac{\Gamma_\Sigma(k)}{1 + B_n \cos[\chi_n(0) + \omega_1'^s(2k-9)T]} \tag{6-25a}$$

$$\Gamma_\Delta^n(k) = \frac{1}{A_n} \frac{\Gamma_\Delta(k)}{1 + B_n \cos[\chi_n(0) + \omega_1'^s(2k-9)T]} \tag{6-25b}$$

We see that, unless the midscan phase $\chi_n(\ )$ is exactly 0° or 180°, the sum/difference time tapers no longer possess even/odd symmetry around midscan.

The resulting frequency response functions $H_{\Sigma}^{n}(\omega)$, $H_{\Delta}^{n}(\omega)$ have nonzero imaginary parts. From (6-8), (6-9), (6-25), and (6-26), we observe the following properties of the frequency response functions:

1) Re $[H_{\Sigma}^{n}(\omega)]$ is even;

2) Im $[H_{\Sigma}^{n}(\omega)]$ is odd;

3) Re $[H_{\Delta}^{n}(\omega)]$ is odd;

4) Im $[H_{\Delta}^{n}(\omega)]$ is even;

5) if the signs of ω and $\chi_n(0)$ are both reversed, $H_{\Sigma}^{n}(\omega)$ (or $H_{\Delta}^{n}(\omega)$) is simply conjugated.

Figures 6-3 to 6-14 depict the time-varying AGC factors $E_n^2(t_k)/R_n$, the effective time tapers $\Gamma_{\Sigma}^{n}(k)$, $\Gamma_{\Delta}^{n}(k)$, and the resulting sum and difference filter frequency responses $H_{\Sigma}^{n}(\omega)$, $H_{\Delta}^{n}(\omega)$, for cases of -6 dB reference scalloping multipath. In the first case, the reference scalloping frequency ω_1's is $\frac{1}{2}\,\frac{2\pi}{16T}$ (210 Hz) for azimuth, and in the second case, it is $\frac{2\pi}{16T}$ (420 Hz) for azimuth; these values cause the cos $\chi_n(t)$ term in the AGC factor expression (6-21) to progress through one-half cycle and one cycle, respectively, sub-cases are considered, corresponding to midscan phases $\chi_n(0)$ = 0°, 90°, 180°. Analysis for midscan phases in the range (-180°, 0°) is superfluous due to property 5) above.

We see from the plots that the sidelobes of the frequency response functions are generally increased by the AGC variations, and the mainlobe peak of $H_{\Delta}^{n}(\omega)$ is often heightened. Tables 6-2 and 6-3 list the characteristics of each frequency response function plotted in Figs. 6-1 to 6-14. The mainlobe width is taken to be twice the value of the first positive zero-crossing point, measured in units of $\frac{2\pi}{16T}$ (beamwidths).

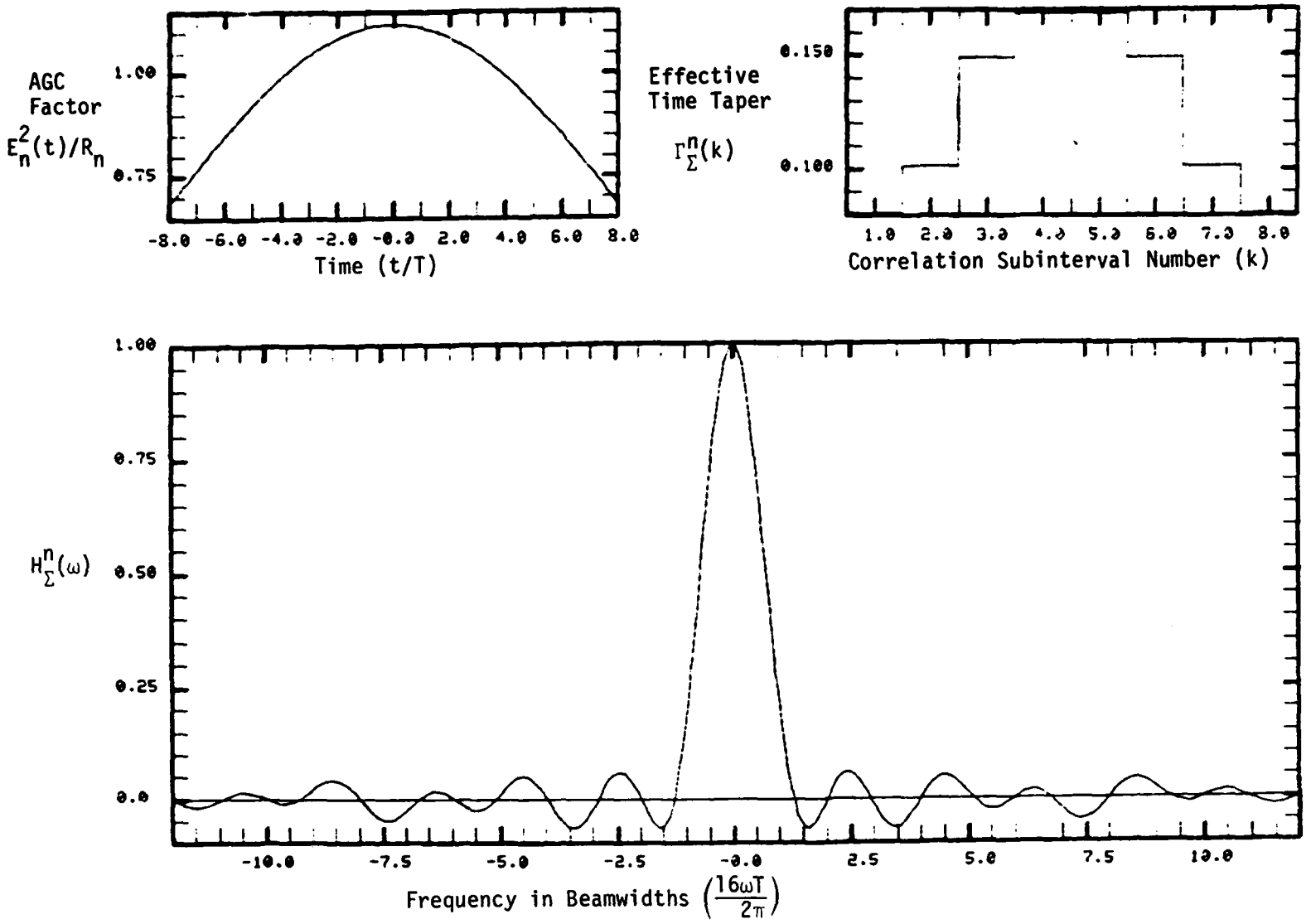

Fig. 6-3. Sum filter frequency response for scalloping frequency of $\frac{1}{2}\frac{2\pi}{16T}$ (210 Hz) and midscan phase of 0°.

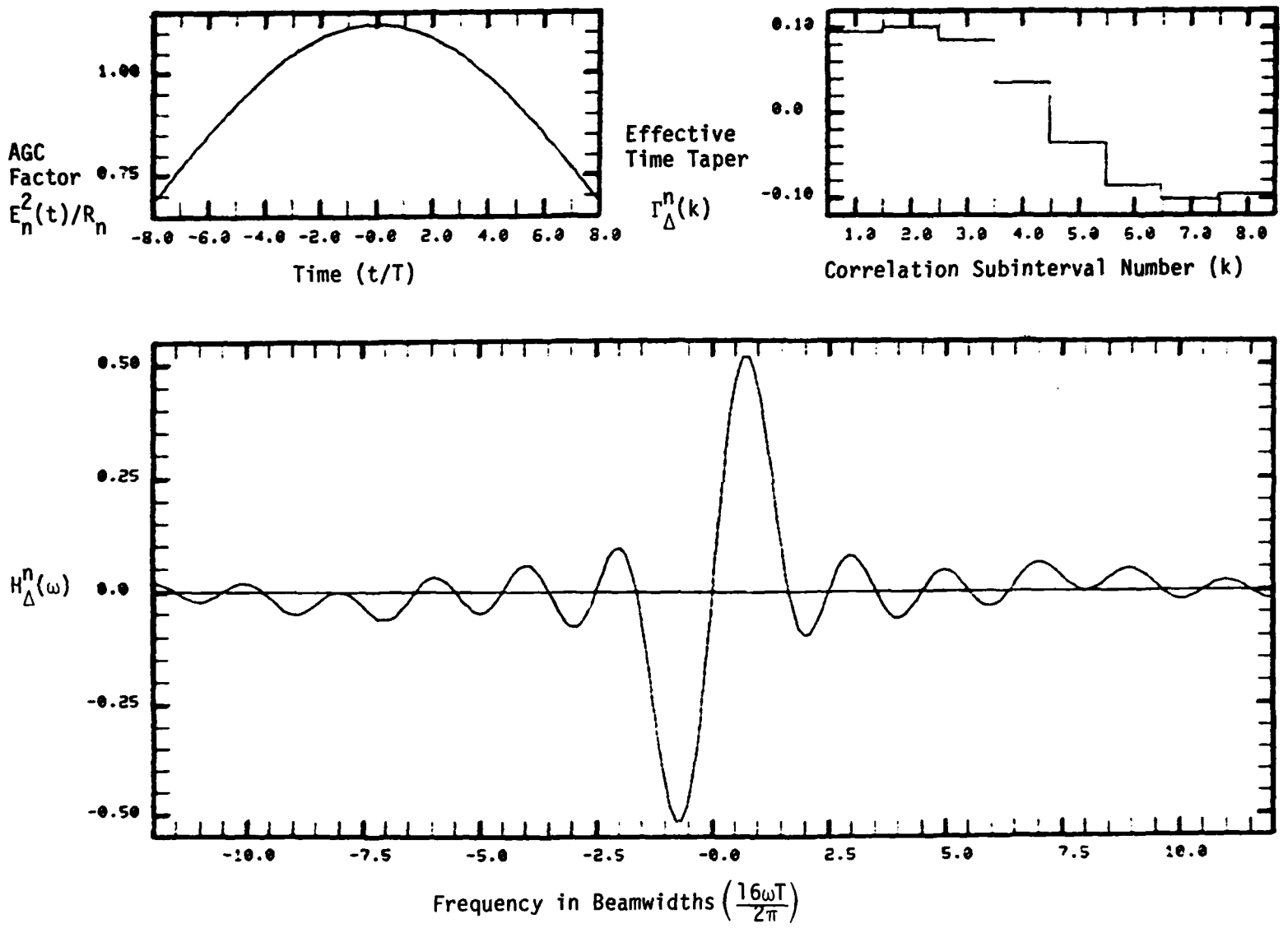

Fig. 6-4. Difference filter frequency response for scalloping frequency of $\frac{1}{2}\,\frac{2\pi}{16T}$ (210 Hz) and midscan phase of 0^0.

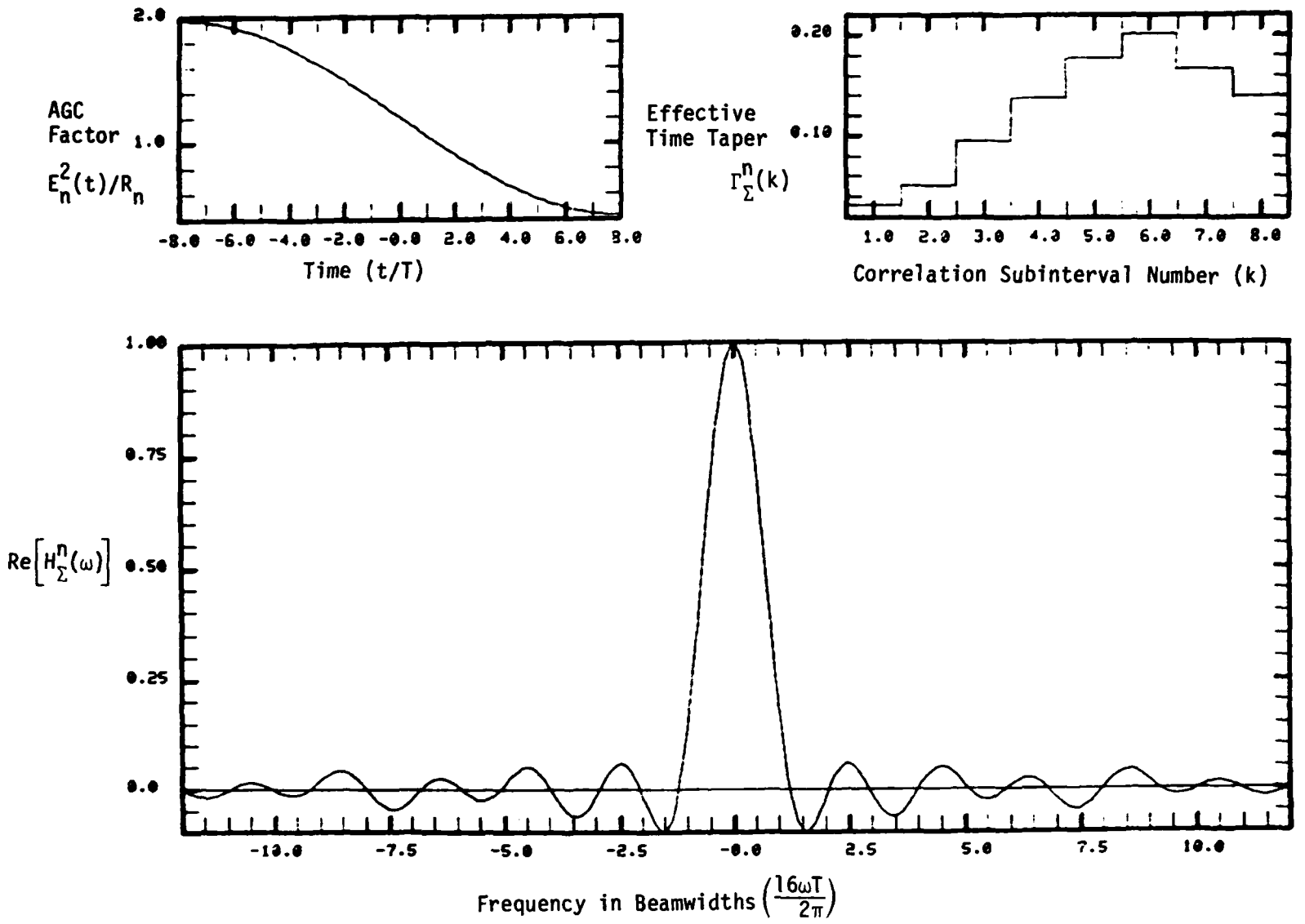

Fig. 6-5(a). Real part of sum filter frequency response for scalloping frequency of $\frac{1}{2}\frac{2\pi}{16T}$ (210 Hz) and midscan phase of 90^0.

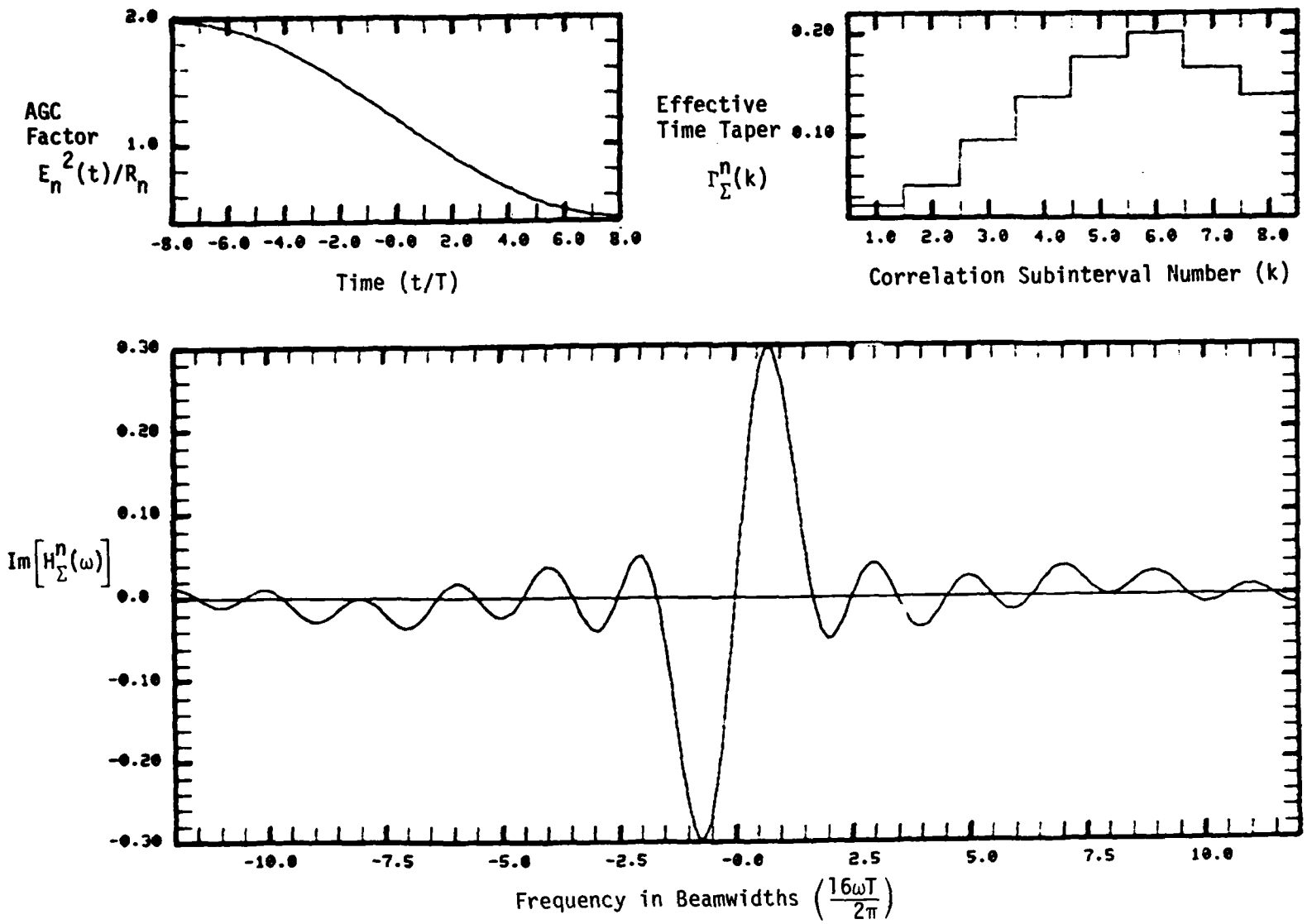

Fig. 6-5(b). Imaginary part of sum filter frequency response for scalloping frequency of $\frac{1}{2}\,\frac{2\pi}{16T}$ (210 Hz) and midscan phase of 90°.

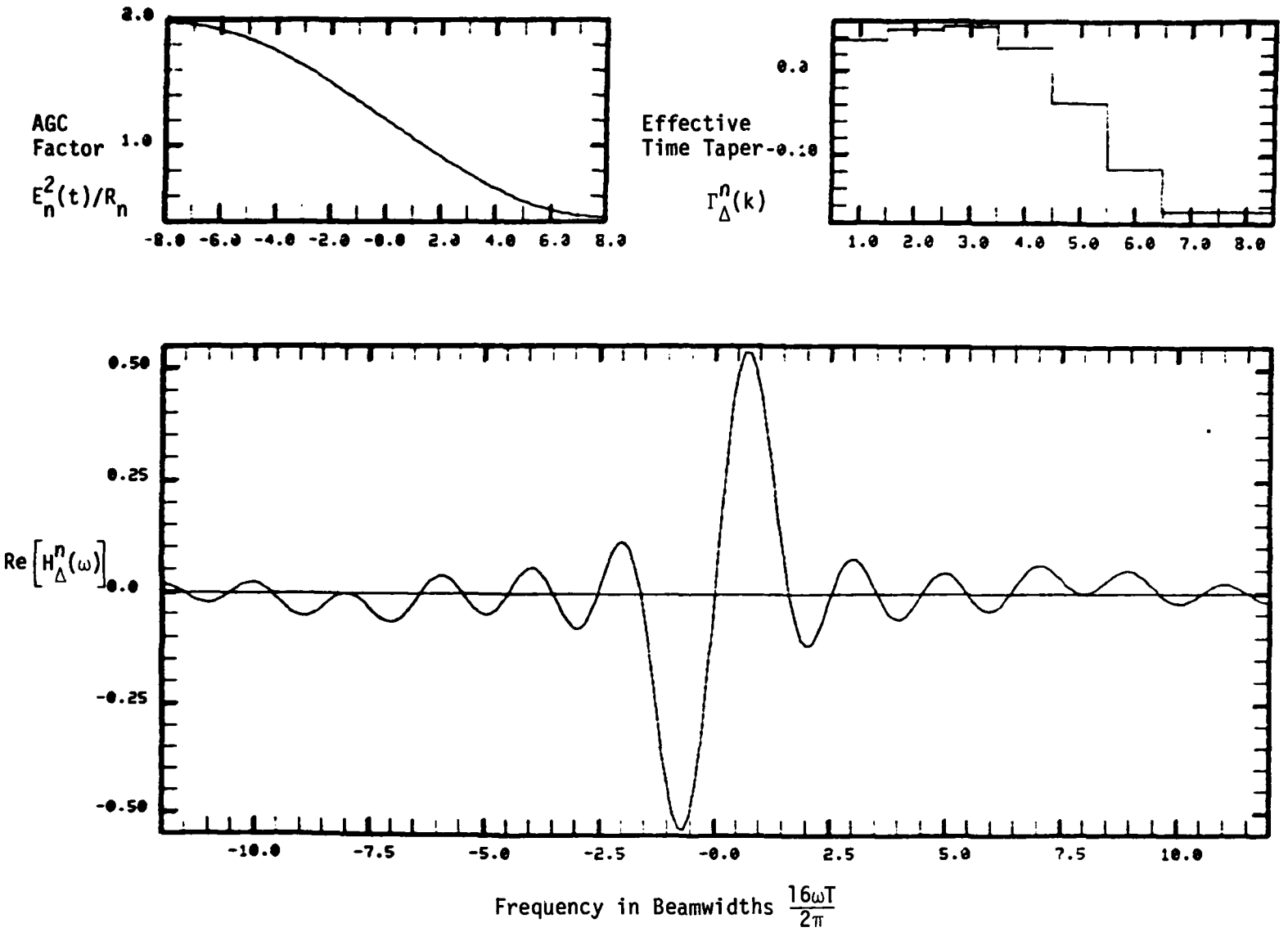

Fig. 6-6(a). Real part of difference filter frequency response for scalloping frequency of $\frac{1}{2}\,\frac{2\pi}{16T}$ (210 Hz) and midscan phase of 0°.

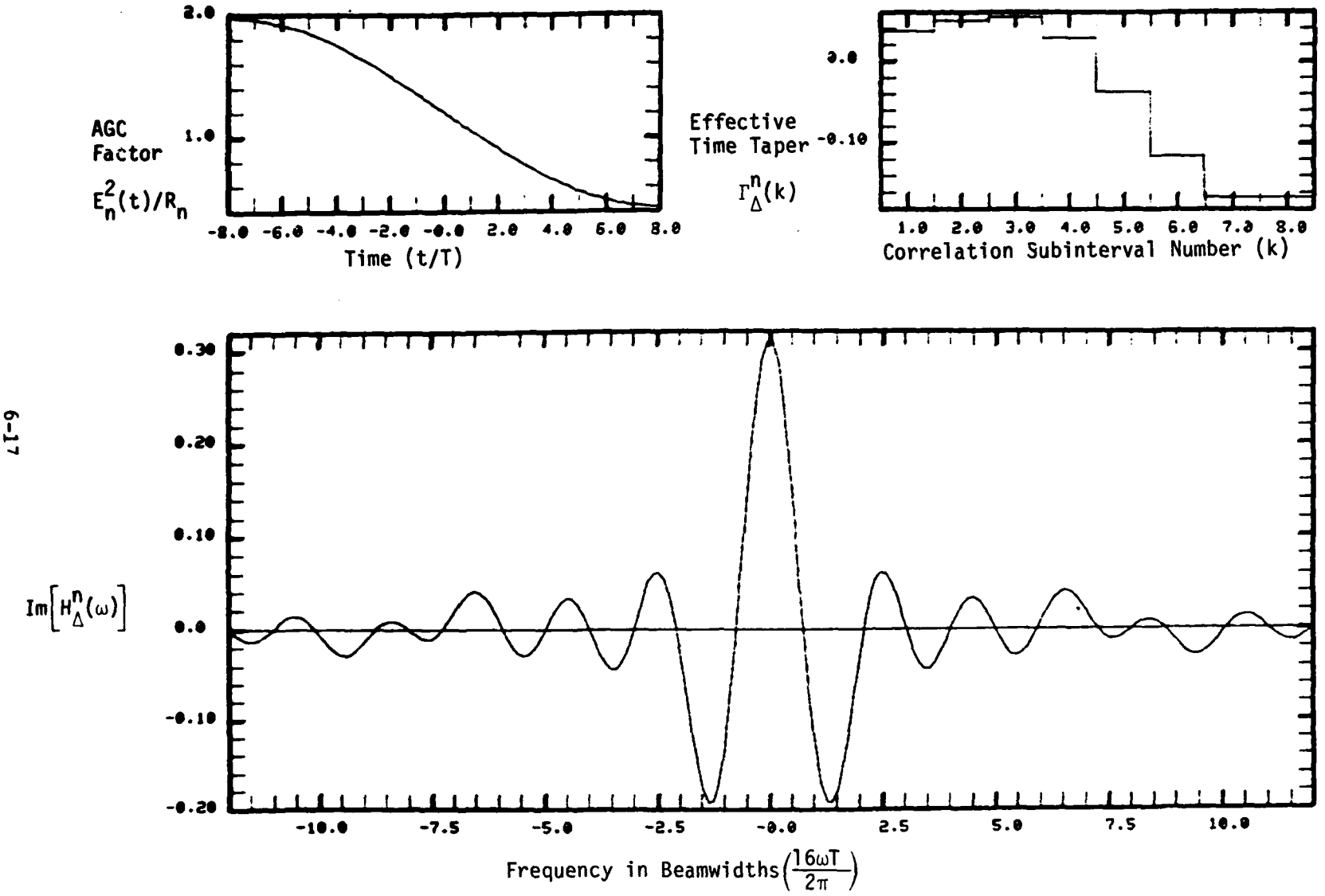

Fig. 6-6(b). Imaginary part of difference filter frequency response for scalloping frequency of $\frac{1}{2}\,\frac{2\pi}{16T}$ (210 Hz) and midscan phase of 90°.

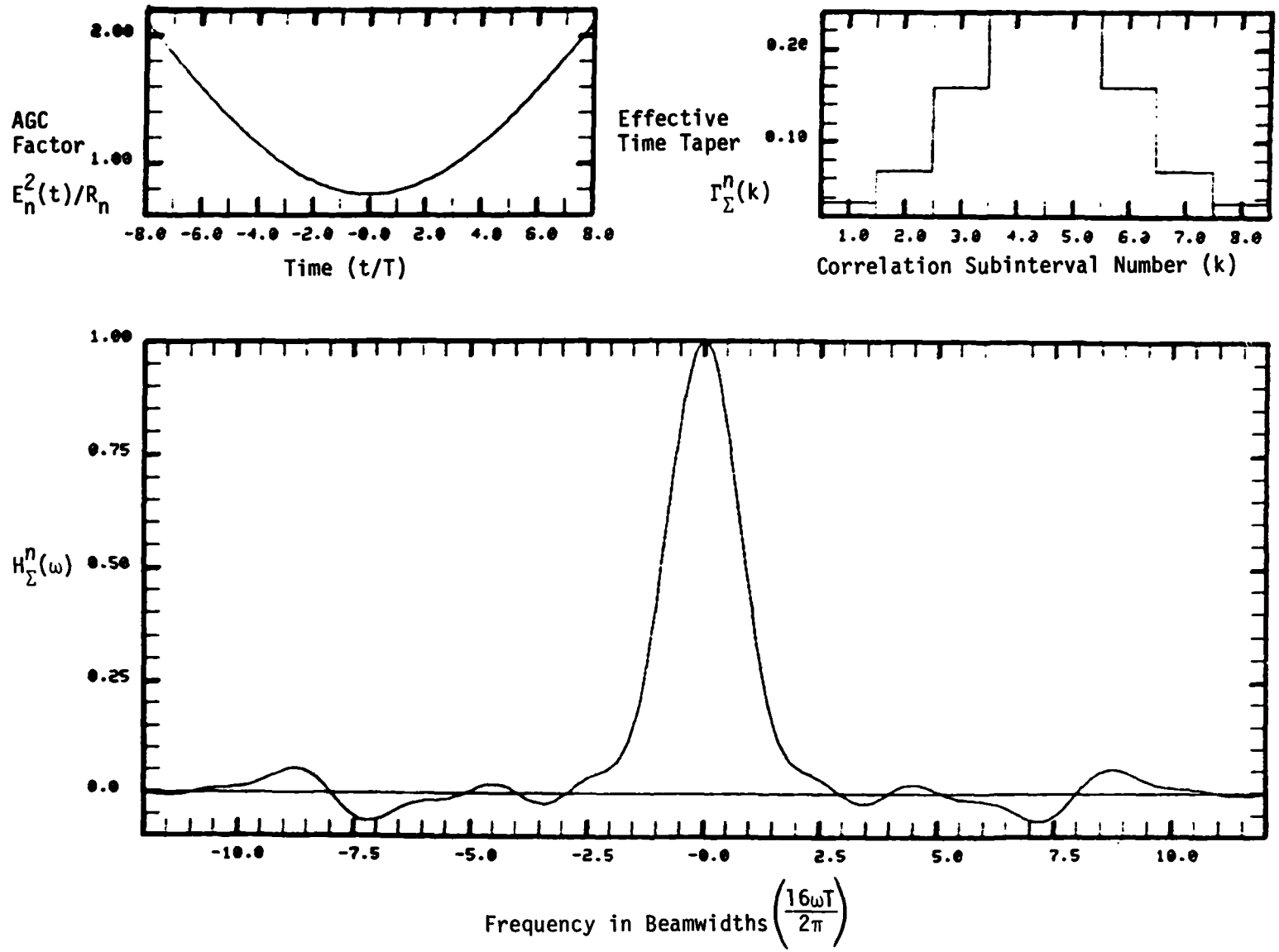

Fig. 6-7. Sum filter frequency response for scalloping frequency of $\frac{1}{2}\,\frac{2\pi}{16T}$ (210 Hz) and midscan phase of 180°.

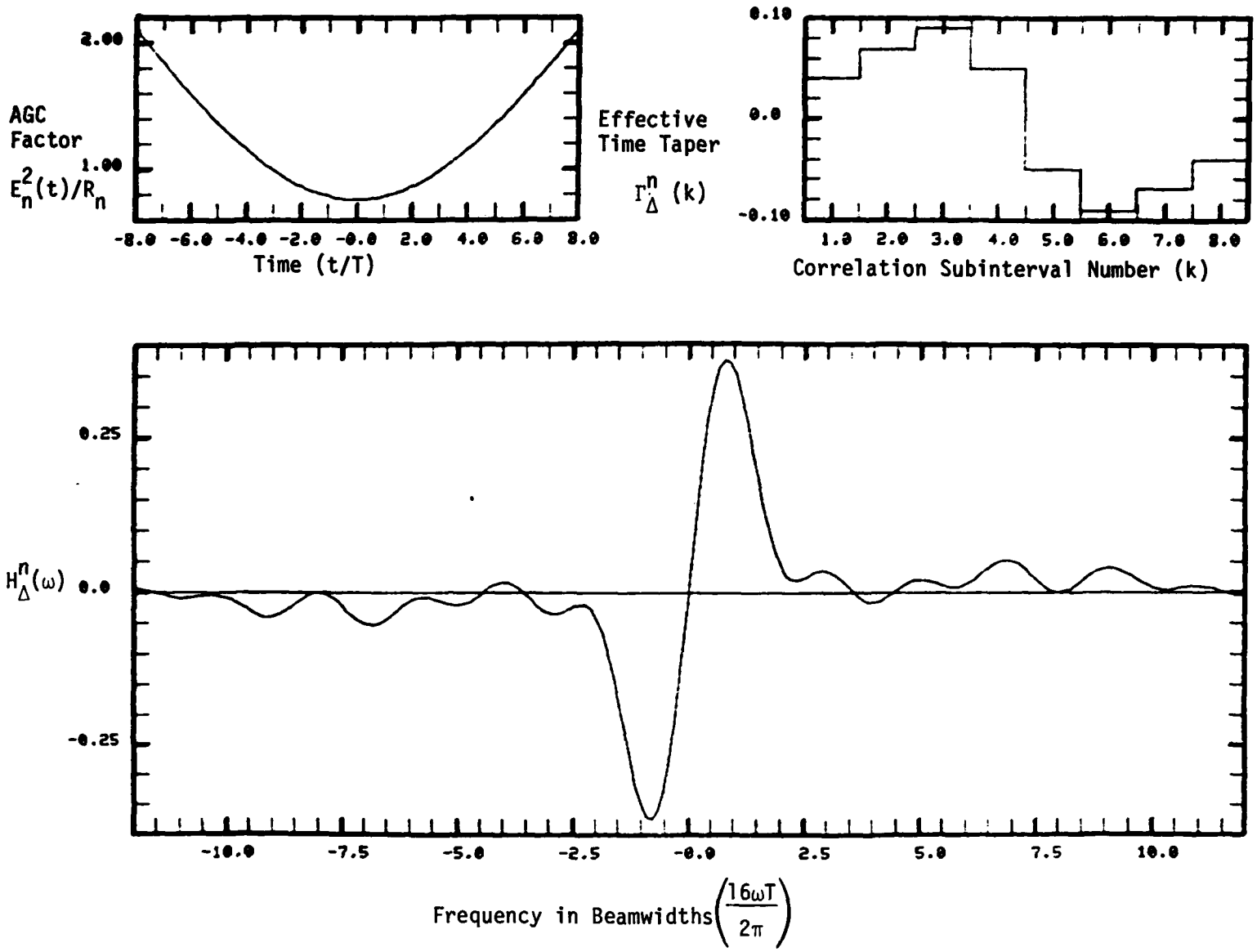

Fig. 6-8. Difference filter frequency response for scalloping frequency of $\frac{1}{2}\frac{2\pi}{16T}$ (210 Hz) and midscan phase of 180^0.

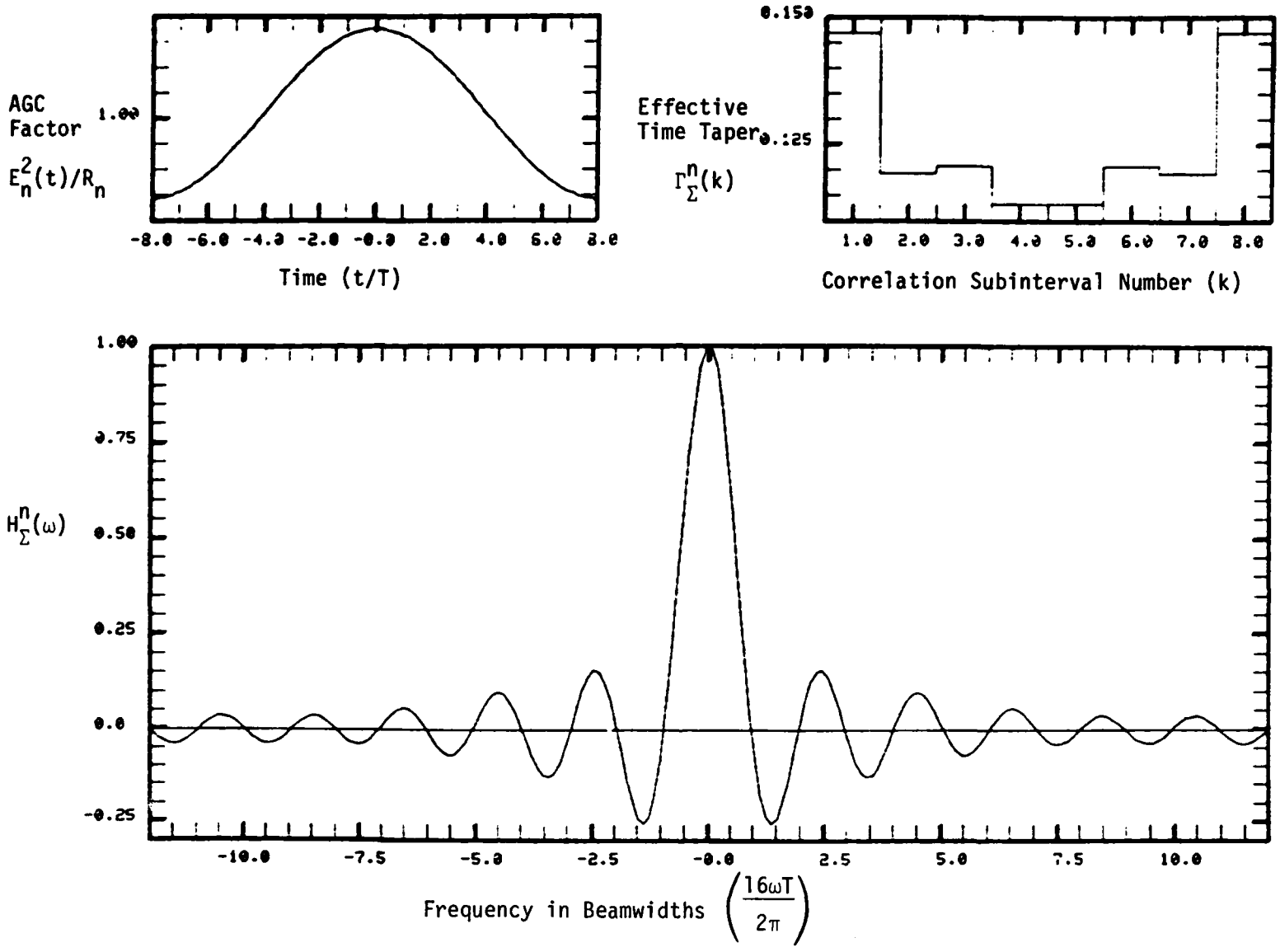

Fig. 6-9. Sum filter frequency response for scalloping frequency of $\frac{2\pi}{16T}$ (420 Hz) and midscan phase of 0°.

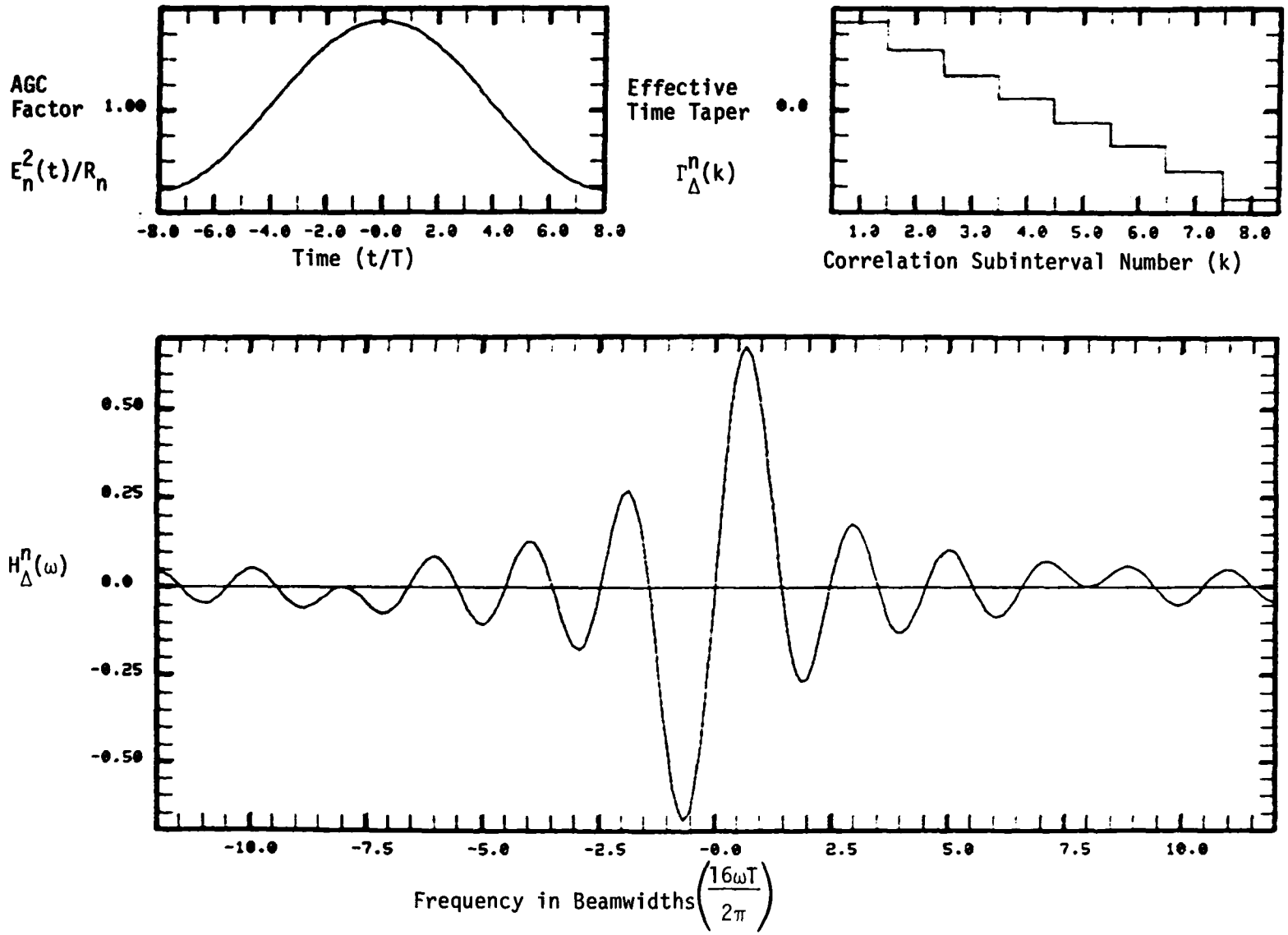

Fig. 6-10. Difference filter frequency response for scalloping frequency of $\frac{2\pi}{16T}$ (420 Hz) and midscan phase of 0°.

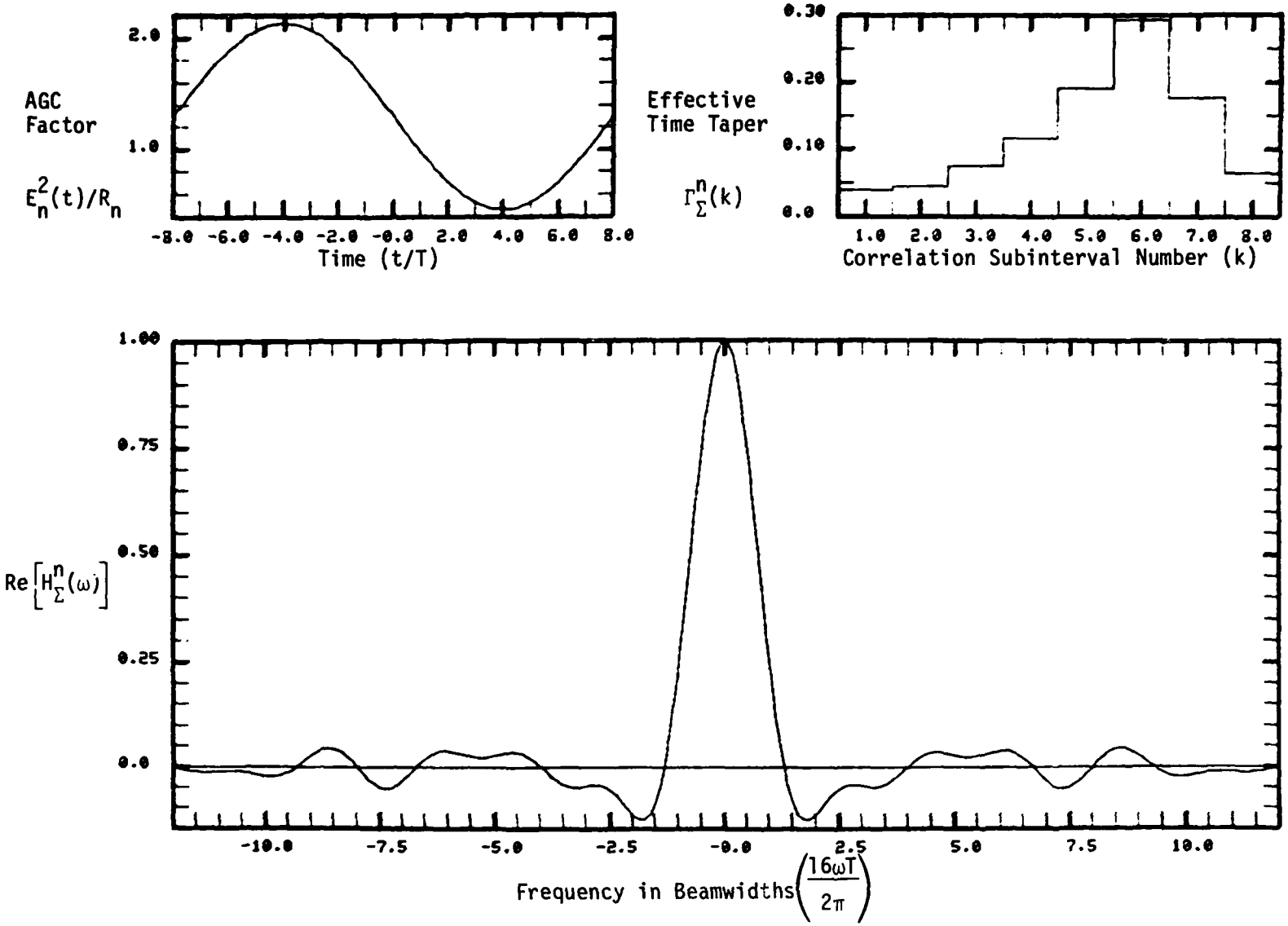

Fig. 6-11(a). Real part of sum filter frequency response for scalloping frequency of $\frac{2\pi}{16T}$ (420 Hz) and midscan phase of 90°.

Hz)

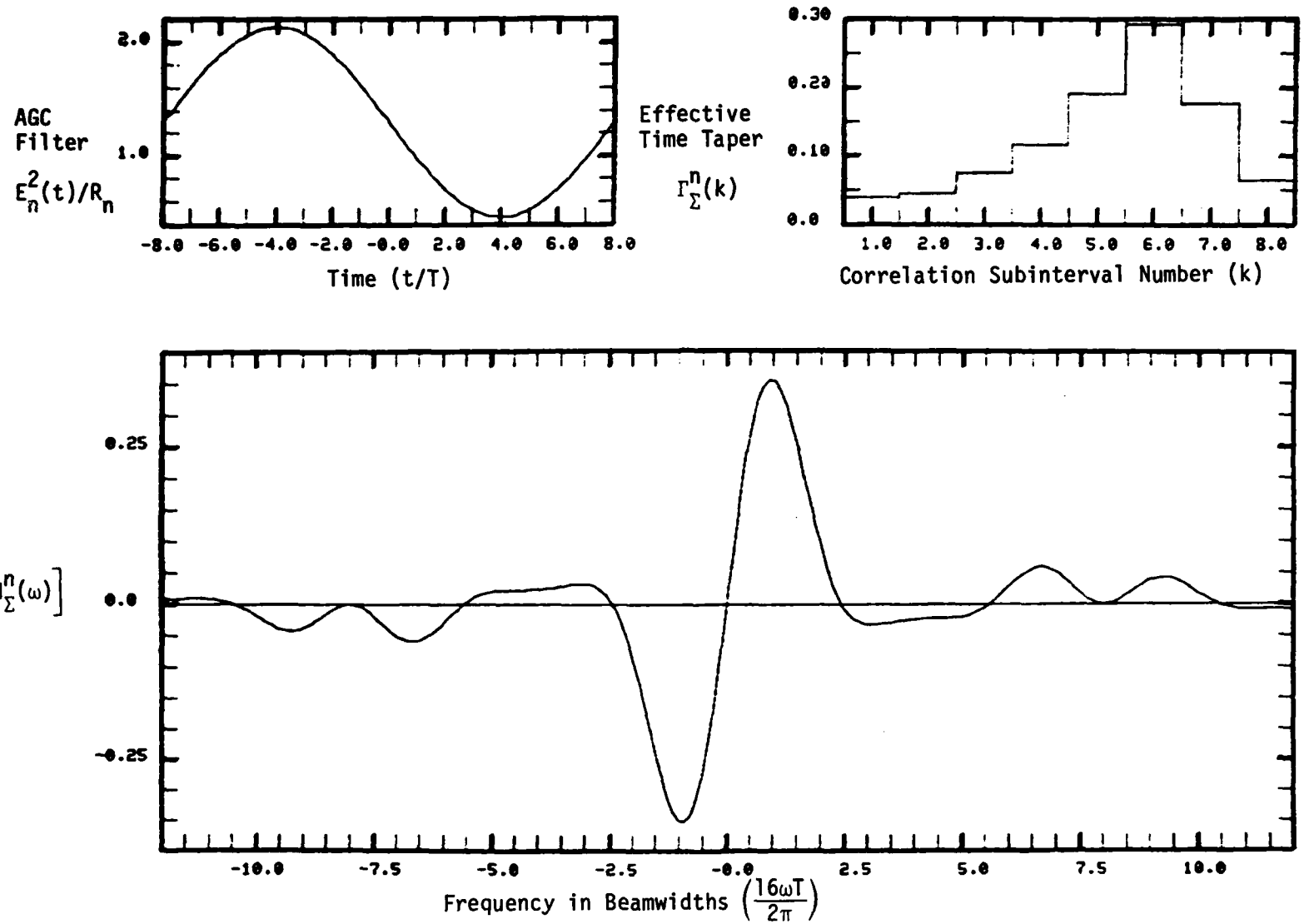

Fig. 6-11(b). Imaginary part of sum filter frequency response for scalloping frequency of $\frac{2\pi}{16T}$ (420 Hz) and midscan phase of 90°.

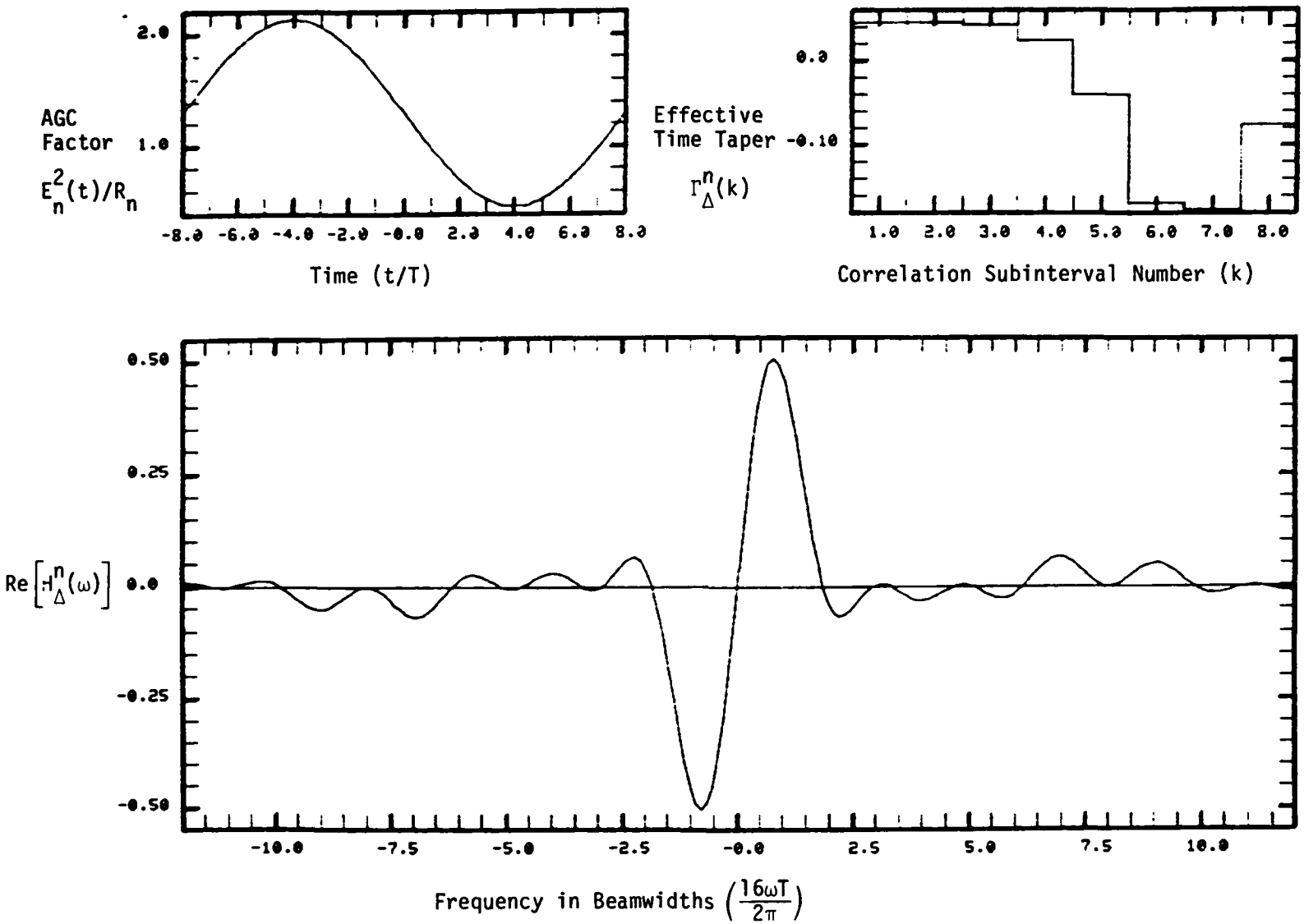

Fig. 6-12(a). Real part of difference filter frequency response for scalloping frequency of $\frac{2\pi}{16T}$ (420 Hz) and midscan phase of 90°.

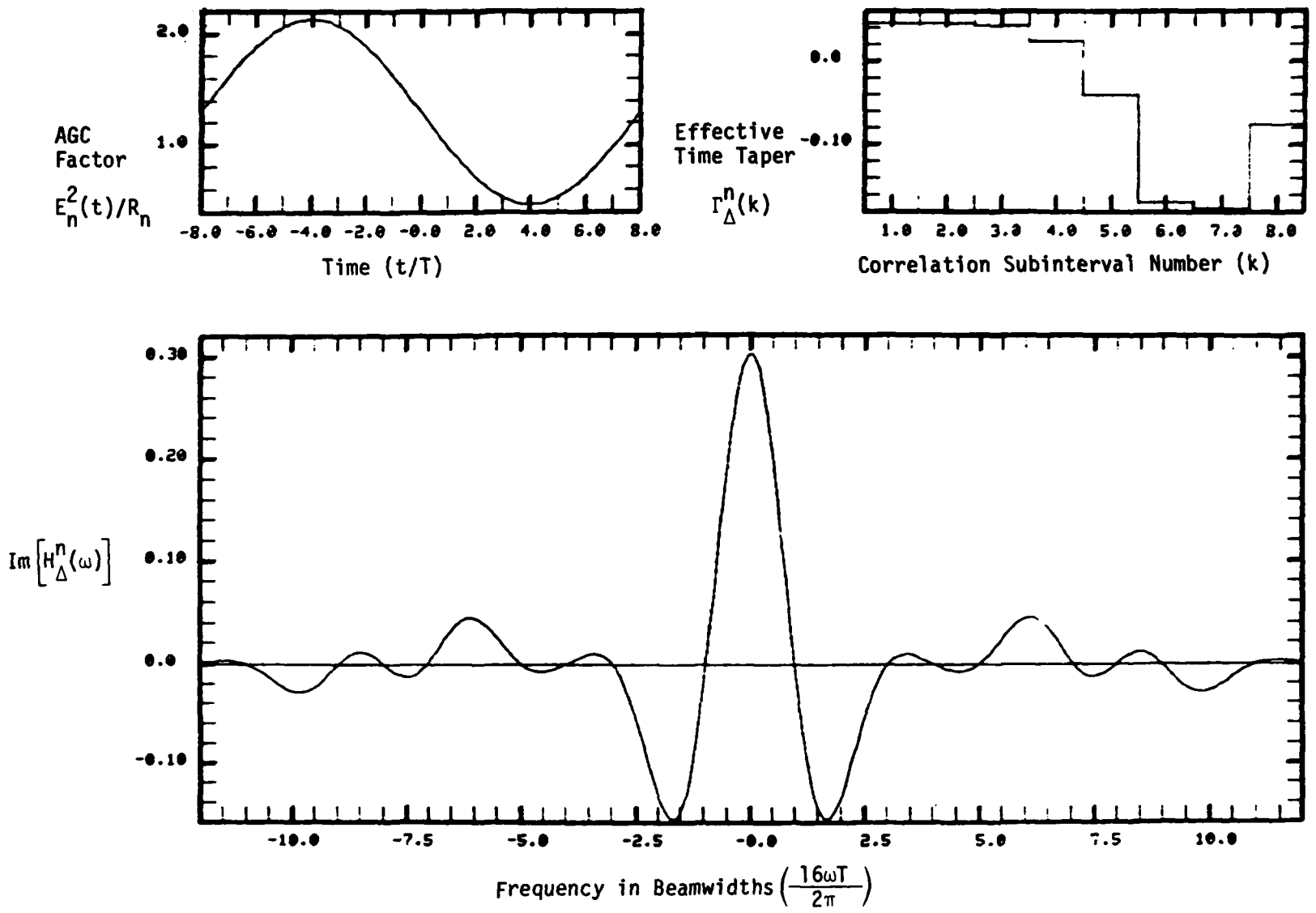

Fig. 6-12(b). Imaginary part of difference frequency response for scalloping frequency of $\frac{2\pi}{16T}$ (420 Hz) and midscan phase of 90°.

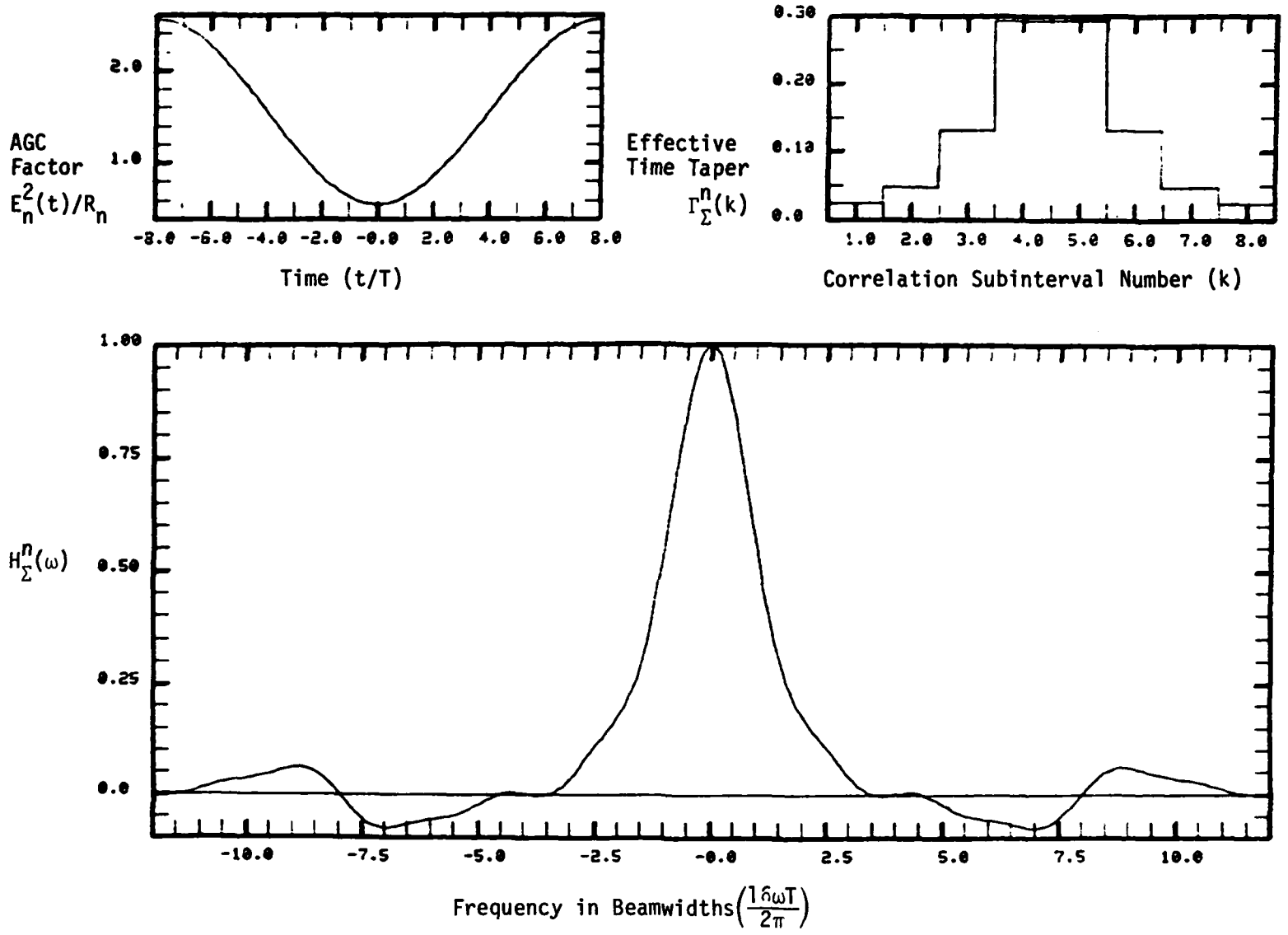

Fig. 6-13. Sum filter frequency response for scalloping frequency of $\frac{2\pi}{16T}$ (420 Hz) and midscan phase of 180^0.

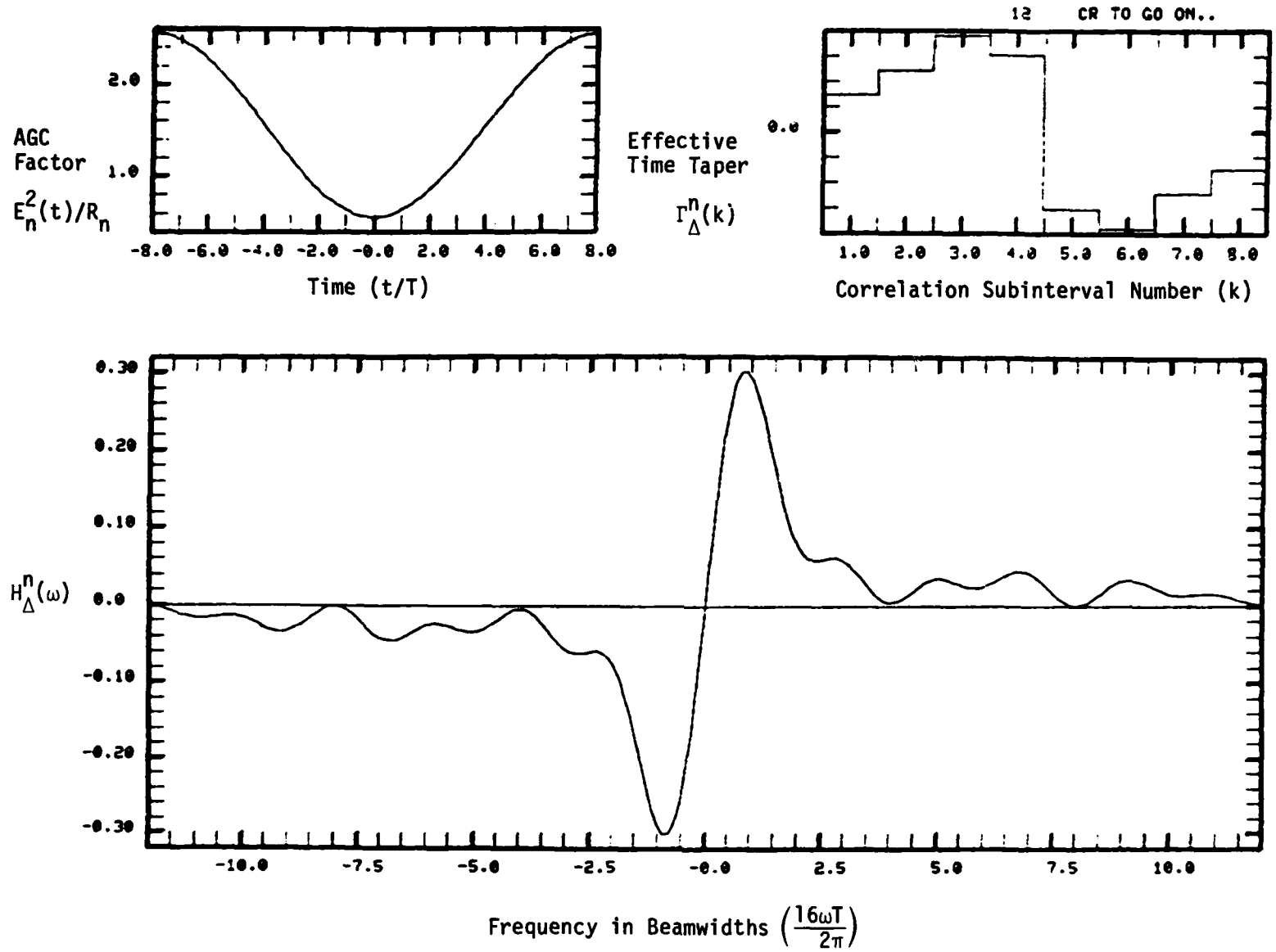

Fig. 6-14. Difference filter frequency response for scalloping frequency of $\frac{2\pi}{16T}$ (420 Hz) and midscan phase of 180^0.

TABLE 6-2a MAINLOBE/SIDELOBE CHARACTERISTICS OF $\mathrm{Re}\ H_{\Sigma}^{n}(\omega)$ UNDER DIFFERENT SCALLOPING CONDITIONS

Scalloping Frequency	Midscan Phase	Peak Sidelobe	Mainlobe Peak	Mainlobe Width
0 (Constant AGC)	any	0.54 (-25 dB)	1.0 (0 dB)	2.98
$\frac{1}{2}\ \frac{2\pi}{16T}$	0°	.067 (-23 dB)	1.0 (0 dB)	2.56
	90°	.098 (-20 dB)	1.0 (0 dB)	2.43
	180°	.065 (-24 dB)	1.0 (0 dB)	5.84
$\frac{2\pi}{16T}$	0°	.257 (-12 dB)	1.0 (0 dB)	1.89
	90°	.128 (-18 dB)	1.0 (0 dB)	2.62
	180°	.071 (-23 dB)	1.0 (0 dB)	6.95

TABLE 6-2b MAINLOBE/SIDELOBE CHARACTERISTICS OF $\mathrm{Im}\ H_{\Sigma}^{n}(\omega)$ UNDER DIFFERENT SCALLOPING CONDITIONS

Scalloping Frequency	Midscan Phase	Peak Sidelobe	Mainlobe Peak	Mainlobe Width
0 (Constant AGC)	any	0 (-∞ dB)	0 (-∞ dB)	0
$\frac{1}{2}\ \frac{2\pi}{16T}$	0°	0 (-∞ dB)		0 (-∞ dB)0
	90°	.049 (-26 dB)	.296 (11 dB)	3.34
	180°	0 (-∞ dB)	0 (-∞ dB)	4.87
$\frac{2\pi}{16T}$	0°	0 (-∞ dB)	0 (-∞ dB)	0
	90°	.059 (-25 dB)	.353 (-9 dB)	4.87
	180°	0 (-∞ dB)	0 (-∞ dB)	0

TABLE 6-3a MAINLOBE/SIDELOBE CHARACTERISTICS OF Re $H_{\Delta}^{n}(\omega)$ UNDER DIFFERENT SCALLOPING CONDITIONS

Scalloping Frequency	Midscan Phase	Peak Sidelobe	Mainlobe Peak	Mainlobe Width
0 (Constant AGC)	any	.059 (-25 dB)	.471 (-7 dB)	3.54
$\frac{1}{2}\frac{2\pi}{16T}$	0°	.097 (-20 dB)	.514 (-6 dB)	3.28
	90°	.116 (-19 dB)	.536 (-5 dB)	3.22
	180°	.053 (-26 dB)	.374 (-9 dB)	7.14
$\frac{2\pi}{16T}$	0°	.268 (-11 dB)	.670 (-3 dB)	2.85
	90°	.066 (-24 dB)	.504 (-6 dB)	3.70
	180°	.062 (-24 dB)	.301 (-10 dB)	-

TABLE 6-3b MAINLOBE/SIDELOBE CHARACTERISTICS OF Im $H_{\Delta}^{n}(\omega)$ UNDER DIFFERENT SCALLOPING CONDITIONS

Scalloping Frequency	Midscan Phase	Peak Sidelobe	Mainlobe Peak	Mainlobe Width
0 (Constant AGC)	any	0 (-∞ dB)	0 (-∞ dB)	0
$\frac{1}{2}\frac{2\pi}{16T}$	0°	0 (-∞ dB)	0 (-∞ dB)	0
	90°	.193 (-14 dB)	.309 (-10 dB)	.149
	180°	0 (-∞ dB)	0 (-∞ dB)	0
$\frac{2\pi}{16T}$	0°	0 (-∞ dB)	0 (-∞ dB)	0
	90°	.157 (-16 dB)	.300 (.10 dB)	1.93
	180°	0 (-∞ dB)	0 (-∞ dB)	0

1. Errors in Tracker Position due to Multipath Terms in (6-1) and (6-2)

In this case, one is primarily concerned with a large response in H_Δ at the frequency of the multipath signal. For relative multipath phases near 0° or 180°, $Re(H_\Delta)$ is of greatest concern, while for multipath phases near ±90°, $Im(H_\Delta)$ is of concern. The mainlobe shape of H_Δ in Figs. 6-4, 6-6, 6-8, 6-10, and 6-12 is substantially different from the nominal shape in Fig. 6-2; however, the mainlobe region extent is quite similar. Thus, the "in-beam/out-of-beam" criteria do not change significantly when AGC gain perturbations occur. The sidelobes are seen to increase significantly (e.g., over 6 dB) in some cases, which would primarily be of concern for the elevation system.

2. Errors in Tracker Position due to the Signal Terms in (6-1) and (6-2)

In this case, one is primarily concerned with the possibility that H_Δ/H_Σ evaluated at the direct signal frequency will not drive the tracker to the desired null position. In particular, one is concerned that $8\omega_t = Re(H_\Delta/H_\Sigma) = 0$ at the direct signal frequency. Making a first-order expansion of (II.3-59) for the term i=0, j=0, we find that

$$\delta\omega_t \approx Re(H_\Delta)/Re(H_\Sigma) + Im(H_\Delta)\ Im(H_\Sigma)/[Re(H_\Sigma)]^2 \qquad (6\text{-}26)$$

From properties 1) and 3) of the frequency response function, we conclude that the first term in (6-26) is odd, while properties 2) and 4) show that the section term in (6-26) is odd. Thus, $\delta\omega_t$ in (6-26) will have the desired property of being zero at the direct signal frequency. This suggests that time variations can affect the rate at which the tracker achieves its null position, but do not affect the null position.

B. Reference Scalloping

As noted in Chapter 4 of Volume II, there is a multipath error mechanism unique to DMLS based on reflections of the reference signal which can potentially cause large errors even when the reflecting object is well out of beam. In this section we shall review the origin of these errors, analyze their impact, and investigate their dependence on various system parameters.

1. Review of Single-Scan DMLS Errors

The DMLS digital correlator receiver computes its angle estimates from the outputs $\Sigma(n)$, $\Delta(n)$ of the sum and difference filters. Referring to Eqs. (6-1) and (6-2) of the previous section, we see that the cross-product multipath components contributing to (6-1) and (6-2) can be divided into two types: components with mainlobe frequencies $d(n)\omega_{ijn}$ falling near the tracked frequency $\omega_t(n)$, and components with sidelobe frequencies $d(n)\omega_{ijn}$ separated from $\omega_t(n)$ by more than about $1\frac{1}{2}$ to 2 beamwidths (the half-width of $H_\Delta^n(\omega)$ - see Table 6-3a). Mainlobe components may of course be produced by scatterers which are inbeam, but additional mainlobe components can arise from out-of-beam reflections of the reference signal. To see this, we evaluate the cross-product frequencies $d(n)\omega_{ijn}$ relative to the direct signal frequency $d(n)\omega_{00n}$, as in (II.4-17),*

$$d(n)\omega_{ikn} = d(n)\omega_{00n} + \omega_i^{\,a} + d(n)\,(\omega_i^{\,s} + \omega_k^{\,'s}) \qquad (6\text{-}27)$$

---

*The right side of (6-27) should also contain a term $0.5\,(\omega_{off}/\omega)\,(\omega_i^{\,s} + \omega_k^{\,'s})$, where ω_{off} is the reference-array offset frequency ($2\pi \times 83.2$ kHz). This term is retained in the simulation model for accuracy, but it may be safely ignored for analytical purposes because ω_{off}/ω_r is very small.

where the relative angle frequency ω_i^a of the ith component and the relative scalloping frequencies ω_i^s, $\omega_k'^s$ of the ith angle signal and kth reference signal components, with respect to the direct components, are defined by

$$\omega_i^a = \omega_r \frac{v_s(\cos\gamma_i - \cos\gamma_0)}{c} \tag{6-28}$$

$$\omega_i^s = \omega_r \frac{v_a(\cos\beta_i - \cos\beta_0)}{c} \tag{6-29}$$

$$\omega_k'^s = \omega_r \frac{v_a(\cos\beta_k' - \cos\beta_0')}{c} \tag{6-30}$$

In these equations, ω_r is the source carrier frequency (2π x 5.08 GHz), v_s is the source velocity, v_a is the aircraft velocity, c is the speed of light, γ_i is the angle between the source velocity vector (on positive-directed scans) and the vector from the source to the ith scatterer, and β_i, β_i' are the angles between the aircraft velocity vector and the vector from the aircraft to the ith scatterer for the angle and reference signals, respectively.

In a similar manner, the direct signal frequency is evaluated approximately from (II.3-34) and (II.3-35) as†

---

†Additional terms proportional to ω_{off}/ω_r, namely $\frac{1}{2}[\omega_r\, v_a/c\, (\cos\beta_0 + \cos\beta_0') + d(n)\omega_r\, v_s/c\, \cos\gamma_0]$, actually make the direct signal frequency $d(n)\omega_{00n}$ slightly scan-dependent, but these are very small and may be neglected.

$$d(n)\omega_{00n} = \omega_{off} + K \cos \gamma_0$$

$$= \omega_{off} + K \sin \theta_c \qquad (6\text{-}31)$$

where ω_{off} is the reference-array offset frequency (2π x 83.2 kHz), θ_c is the conical scan plane angle of the direct signal,

$$\theta_c = \frac{\pi}{2} - \gamma_0 \qquad (6\text{-}32)$$

and K is the angle-to-frequency coding factor,

$$K = \omega_r \frac{v_s}{c} \qquad (6\text{-}33)$$

a. Static Multipath

In a static situation the receiver is stationary and the scalloping frequencies are zero. For any given array component i, the cross-product frequencies $d(n)\omega_{ikn}$ are the same for all reference components j. Thus, the expressions (6-1), (6-2) for $\Sigma(n)$, $\Delta(n)$ reduce to single sums over the array components

$$\Sigma(n) = A_n \sum_{i=0}^{M} \rho_i H_\Sigma^n[d(n)\ \omega_{00n} + \omega_i^a - \omega_t(n)] \operatorname{expj}[-d(n)\phi_{in}]$$

$$\times H[\omega_{00n} + d(n)\omega_i^a] \operatorname{expj}\{-d(n)\ \psi[\omega_{00n} + d(n)\omega_i^a]\} \qquad (6\text{-}34)$$

$$\Delta(n) = A_n \sum_{i=0}^{M} \rho_i \, jH_\Delta^n \left(d(n)\omega_{00n} + \omega_i^a - \omega_t(n)\right) \exp j[-d(n)\phi_{in}]$$

$$\times H\left(\omega_{00n} + d(n)\ \omega_i^a\right) \exp j\left[-d(n)\psi\left(\omega_{00n} + d(n)\omega_i^a\right)\right] \qquad (6\text{-}35)$$

where

$$A_n = \frac{1}{4} \sum_{k=0}^{M} \rho_k' \exp j\left(d(n)\phi_{kn}'\right) \qquad (6\text{-}36)$$

To obtain this expression we used the definition (II.3-53) for the cross-product phases

$$\alpha_{ikn} = \phi_{in} - \phi_{kn}' + \psi(\omega_{ikn}) \qquad (6\text{-}37)$$

where $\psi(\cdot)$ is the phase of the complex sector filter transfer function and ϕ_{in}, ϕ_{kn}' are the nth scan phases for the ith angle signal component and kth reference signal component, respectively. From (II.3-36) and (II.3-37),*

$$\phi_{in} = \phi_{0n} + (\tilde{\phi}_i - \tilde{\phi}_0) + \omega_i{}^s(n-1)T_s - \frac{1}{2}\, d(n)\omega_{off}(\tau_i - \tau_0) \qquad (6\text{-}38)$$

---

*The right sides of (6-38) and (6-39) should contain the additional terms $0.5\ d(n)\ (\omega_{off}/\omega_r)\ \omega_i{}^s(n-1)T_s$ and $-0.5\ d(n)\ (\omega_{off}/\omega_r)\ \omega_i{}'^s(n-1)T_s$, respectively. As with the similar term missing from (6-27), these terms are retained in the simulation model but they are small enough to be ignored for analytical purposes. The last term in (6-38) or (6-39) is also proportional to the relatively small reference-array offset frequency ω_{off}, and so it is usually negligible too. However, in some cases the relative multipath time delay $(\tau_i - \tau_0)$ or $(\tau'_k - \tau'_0)$ is long enough that this term makes a difference (see Section 5 below).

$$\phi'_{kn} = \phi'_{0n} + (\tilde{\phi}'_k - \tilde{\phi}'_0) + \omega_k'^s(n-1)T_s + \frac{1}{2}\, d(n)\omega_{off}(\tau'_k - \tau'_0) \qquad (6\text{-}39)$$

In these expressions, T_s is the scan time, τ_i, τ'_k are the midscan time delays for the ith angle signal and kth reference signal components, and $\tilde{\phi}_i$, $\tilde{\phi}'_k$ are the effective midscan phases of the ith angle signal and kth reference signal components on the first scan:

$$\tilde{\phi}_i = \phi_i - \omega_r \tau_i \qquad (6\text{-}40)$$

$$\tilde{\phi}'_k = \phi'_k - \omega_r \tau'_k \qquad (6\text{-}41)$$

where ϕ_i and ϕ'_k are the phase changes due to reflection (or, diffraction).

b. Reference Scalloping Multipath

Reference scalloping errors are produced in a dynamic environment in which the scalloping frequencies ω_i^s, $\omega_k'^s$ are non-zero. They result from cross products of the direct component of the array signal with scattered components of the reference signal. In order to isolate the effects of reference scalloping errors from those of normal inbeam multipath errors, we shall assume that all scattered angle signal components are well out of beam, i.e., that ω_i^a is large enough to make $H_\Sigma^n(d(n)\omega_{ikn})$ and $H_\Delta^n(d(n)\omega_{ikn})$ negligibly small, for each $i \neq 0$. In this case only the $i=0$ terms contribute to $\Sigma(n)$ and $\Delta(n)$, and equations (6-1) and (6-2) reduce to single sums over the reference components k.

$$\Sigma(n) = \rho_0 \sum_{k=0}^{M} \rho'_k \, H_\Sigma^n[d(n)\omega_{00n} - d(n)\omega_k'^{s} - \omega_t(n)] \, \exp j(\phi'_{kn})$$

$$\times H(\omega_{00n} - \omega_k'^{s}) \, \exp j[-\psi(\omega_{00n} - \omega_k'^{s})] \qquad (6\text{-}42)$$

$$\Delta(n) = \rho_0 \sum_{j=0}^{M} \rho'_k \, jH_\Delta^n[d(n)\omega_{00n} - d(n)\omega_k'^{s} - \omega_t(n)]$$

$$\times H(\omega_{00n} - \omega_k'^{s}) \, \exp j[-\psi(\omega_{00n} - \omega_k'^{s})] \qquad (6\text{-}43)$$

We see that $\Sigma(n)$, $\Delta(n)$ are computed from expressions which are identical (except for a common scale factor) to the ones derived for a static situation, with the correspondences

$$-d(n)\,\omega_k'^{s} \longleftrightarrow \omega_k^{a} \qquad (6\text{-}44)$$

$$\rho'_k \longleftrightarrow \rho_k \qquad (6\text{-}45)$$

$$-\phi'_{kn} \longleftrightarrow \phi_{kn} \qquad (6\text{-}46)$$

Thus each reference scalloping component can be treated as an equivalent static component with angle code equal to (±) the scalloping frequency and opposite phase.

The theoretical and experimental static error traces given in Chapter 4 of Volume II are therefore equally applicable to the case of single-scan reference scalloping errors. However, because reference scalloping is intrin-

sically a dynamic effect, motion averaging effects must always be considered when evaluating the basic error mechanism. Reference scalloping errors are motion averaged in the same manner as inbeam multipath errors. But we note from (6-44) that the equivalent inbeam multipath angle for reference scalloping changes sign with each change of scan direction. The resulting motion averaging grating lobe structure is a function of the scan format. This dependence will be discussed in more detail below.

2. Motion Averaging of Reference Scalloping Errors

The nth scan estimate of the direct signal's angle frequency, $\omega_t(n) + \delta\omega_t(n)$, is obtained by adding to the tracked frequency $\omega_t(n)$ a frequency proportional to $\mathrm{Im}[\Delta(n)/\Sigma(n)]$, as in (II.3-59).

$$\omega_t(n) + \delta\omega_t(n) = \omega_t(n) - \mathrm{Im}\left[\frac{\Delta(n)}{\Sigma(n)}\right] \frac{2\pi}{16T} \tag{6-47}$$

where 16T is the total correlation time for the scan ($16T = 0.95T_s$). The motion-averaged angle frequency estimate ω_t for an entire data frame is obtained by averaging the single-scan estimates, as in (II.3-61),

$$\hat{\omega}_t = \frac{1}{N_v} \sum_{\substack{\text{valid} \\ \text{scans } n}} \left[\omega_t(n) + \delta\omega_t(n)\right] \tag{6-48}$$

where N_v is the number of valid scans.

In order to determine the amount by which motion averaging reduces the single-scan errors, it is thus necessary to effectively characterize the variation of $\Delta(n)/\Sigma(n)$ with scan number n. In general, this is very compli-

cated, because of the variety of ways in which scan dependence enters into the expressions (6-42) and (6-43) for $\Sigma(n)$ and $\Delta(n)$. Therefore, we shall make some simplifying assumptions which allow a useful theory to be generated focusing on the essential aspects of the reference scalloping effect.

(1) The tracker frequency $\omega_t(n)$ is assumed to be reset to the direct signal frequency $d(n)\omega_{00n}$ at the beginning of every scan. Thus, the analytical results will be independent of the initial tracker error, and they will also fail to include some second-order motion averaging perturbations which are produced as the actual tracker (even one which is initially error-free) is pulled off course during a data frame by the succession of error-laden single scan estimates.

(2) The validation tests are ignored, so that N_v is equal to the total number of scans in a data frame, 2N, and the summation in (6-48) is over all 2N scans.

(3) The sector filter transfer function is assumed to pass all frequencies in its passband without distortion; i.e., $H(\omega)\, e^{j\psi(\omega)} = 1$.

(4) The last term in the expression (6-39) for the reference signal component phases ϕ'_{kn} is assumed to be negligible, and ϕ'_{kn} is determined from

$$\phi'_{kn} = \phi'_{0n} + (\tilde{\phi}'_k - \tilde{\phi}'_0) + \omega'^{s}_k (n-1)T_s \qquad (6\text{-}49)$$

This assumption will later be dropped in Section 5, where the effects of very long multipath time delays $(\tau'_k - \tau_0)$ will be examined

(5) The AGC gain is assumed to be uniform, $E_n^2(t_k)/R_n = 1$, which means that the complicated scan-dependent distortions of the sum and difference filter frequency responses $H^n_\Sigma(\omega)$, $H^n_\Delta(\omega)$ considered in Section A are ignored here. These frequency

responses are therefore replaced by the functions $H_\Sigma(\omega)$, $H_\Delta(\omega)$ defined in (6-6), (6-7), which have the following properties: $H_\Sigma(\omega) = H_\Sigma(-\omega)$, $H_\Delta(\omega) = -H_\Delta(-\omega)$, $H_\Sigma(0) = 1$, $H_\Delta(0) = 0$, $\mathrm{Im}[H_\Sigma(\omega)] = \mathrm{Im}[H_\Delta(\omega)] = 0$.

(6) It is assumed that only a single multipath component is present; i.e., $\rho'_k = 0$ for $k > 2$.

The angle frequency estimate for a complete data frame is calculated from (6-48), (6-47), (6-31), and assumptions (1) and (2),

$$\hat{\omega}_t = \omega_{off} + K \sin\theta_c + \frac{1}{2N} \sum_{n=1}^{2N} \delta\omega_t(n)$$

$$= \omega_{off} + K \left\{\sin\theta_c - \frac{1}{2N} \sum_{n=1}^{2N} \frac{2\pi}{16KT} \mathrm{Im}\left[\frac{\Delta(n)}{\Sigma(n)}\right]\right\} \tag{6-50}$$

The conical angle estimate $\hat{\theta}_c$ is obtained from $\hat{\omega}_t$ according to (II.3-62),

$$\hat{\theta}_c = \sin^{-1}[(\hat{\omega}_t - \omega_{off})/K] \tag{6-51}$$

Letting $\hat{\varepsilon}$ denote the frame averaged angle error,

$$\hat{\varepsilon} = \hat{\theta}_c - \theta_c \tag{6-52}$$

and expanding $\sin^{-1}x$ to first-order around $x = \sin\theta_c$ on the assumption that the error is small, we approximate (6-51) as

$$\theta_c + \hat{\varepsilon} = \sin^{-1}[\sin\theta_c] + \frac{1}{2N} \sum_{n=1}^{2N} \varepsilon(n) \tag{6-53}$$

where

$$\varepsilon(n) = -\theta_B \, \mathrm{Im}\left[\frac{\Delta(n)}{\Sigma(n)}\right] \frac{1}{\cos\theta_c} \tag{6-54}$$

and θ_B is the effective beamwidth,

$$\theta_B = \frac{2\pi c}{\omega_r} \frac{1}{16 v_s T} = \frac{2\pi}{16KT} \tag{6-55}$$

Simplifying (6-53) we obtain

$$\hat{\varepsilon} = \frac{1}{2N} \sum_{n=1}^{2N} \varepsilon(n) \tag{6-56}$$

It is easily shown by the same first-order expansion that $\varepsilon(n)$ is the approximate angle error corresponding to the nth scan frequency estimate $\omega_t(n) + \delta\omega_t(n)$; i.e.,

$$\theta_c + \varepsilon(n) = \sin^{-1}\left[\left(\omega_t(n) + \delta\omega_t(n) - \omega_{off}\right)/K\right] \tag{6-57}$$

Under assumptions (1) to (6) above, the expressions (6-42), (6-43) for $\Sigma(n)$, $\Delta(n)$ reduce to

$$\Sigma(n) = \rho_0\rho_0' \, e^{-j\phi_{0n}'}\left[1 + \rho H_\Sigma(\omega_s') \, e^{-j\phi} \, e^{-j\omega_s(n-1)T_s}\right] \tag{6-58}$$

$$\Delta(n) = \rho_0\rho_0' e^{-j\phi_{0n}'} \, \rho \, d(n) \, jH_\Delta(\omega_s') \, e^{-j\phi} \, e^{-j\omega_s'(n-1)T_s} \tag{6-59}$$

where we have introduced a simplified notation for the relative multipath parameters of the single component.

$$\rho = \rho_1'/\rho_0' \tag{6-60}$$

$$\omega_s' = \omega_1'^{s} \tag{6-61}$$

$$\phi = \tilde{\phi}_1 - \tilde{\phi}_0 \tag{6-62}$$

Thus, the single scan error is calculated as

$$\varepsilon(n) = \frac{\theta_B}{\cos\theta_c} \operatorname{Re} \left\{ \rho H_\Delta(\omega_s') \, e^{-j\phi} \frac{d(n) \, e^{-j\omega_s'(n-1)T_s}}{1 + \rho H_\Sigma(\omega_s') \, e^{-j\phi} \, e^{-j\omega_s'(n-1)T_s}} \right\} \tag{6-63}$$

Assuming $\rho < 1$, the second term in the denominator in (6-63) has complex magnitude less than unity, and hence a power series expansion of (6-63) is valid:

$$\varepsilon(n) = \frac{\rho\theta_B}{\cos\theta_c} \operatorname{Re} \left\{ H_\Delta(\omega_s') \, e^{-j\phi} \sum_{m=0}^{\infty} (-1)^m \left[\rho H_\Sigma(\omega_s')\right]^m e^{-jm\phi} \right.$$
$$\left. \times \, d(n) \, e^{-j(m+1)\omega_s'(n-1)T_s} \right\} \tag{6-64}$$

The motion averaged angle error for a complete data frame is then calculated from (6-56) as

$$\hat{\varepsilon} = \frac{\rho\theta_B}{\cos\theta_c} \operatorname{Re} \left\{ H_\Delta(\omega_s') \, e^{-j\phi} \sum_{m=0}^{\infty} (-1)^m \, [\rho H_\Sigma(\omega_s')]^m \, e^{-jm\phi} \, D[(m+1)\omega_s' T_s] \right\} \tag{6-65}$$

where $D(\cdot)$ is the Fourier transform of the sequence $d(n+1)$,

$$D(\alpha) = \frac{1}{2N} \sum_{n=0}^{2N-1} d(n+1) \, e^{-jn\alpha}$$

$$= \frac{1}{2N} \sum_{n=1}^{2N} d(n) \, e^{-j(n-1)\alpha} \tag{6-66}$$

Both error expressions (6-64) and (6-65) are given as power series in ρ; the difference between them is in the expansion coefficients. Whereas the coefficient of ρ^m in the expansion for the single scan error $\varepsilon(n)$ has a factor, $d(n)\, e^{-j(m+1)\omega_s'(n-1)T_s}$, with unit complex magnitude, the corresponding factor in the expression for the frame averaged error $\hat{\varepsilon}$ is an average of the single scan factors, $D[(m+1)\omega_s' T_s]$. Thus, the function $D(\cdot)$ may be termed the <u>motion averaging function</u> corresponding to the scan format function $d(n)$. The total motion averaging factor is obtained as a weighted average of $D(\cdot)$ evaluated at the harmonics of the scalloping frequency ω_s'.

3. Behavior of the Motion Averaging Function

The following properties of $D(\alpha)$ are easily derived from the definition (6-56), using only the assumptions that $d(n) = \pm 1$ and $\sum_{n=1}^{2N} d(n) = 0$.

$$|D(\alpha)| \leq 1 \text{ for all } \alpha \tag{6-67}$$

$$D(\alpha + 2\pi) = D(\alpha) \text{ for all } \alpha \tag{6-68}$$

(i.e., $D(\alpha)$ is periodic with period 2π)

$$\frac{1}{2\pi} \int_0^{2\pi} D(\alpha)\, d\alpha = 0 \tag{6-69}$$

$$\frac{1}{2\pi} \int_0^{2\pi} |D(\alpha)|^2\, d\alpha = \left(\frac{1}{2N}\right)^2 \sum_{n=1}^{2N} [d(n)]^2 = \frac{1}{2N} \tag{6-70}$$

According to (6-70) the mean square value of the motion averaging function is independent of the scan format function $d(n)$. However, the structure of the peaks and valleys in the spectrum of $D(\alpha)$ is very much dependent on $d(n)$.

a. Results for Commonly Cited Scan Sequences

Analytic expressions are obtainable for the two cases most often considered:*

(i) <u>the scan sequence finally proposed</u>

$$d(n) = d_P(n) = \begin{cases} +1, & 1 \leq n \leq N \\ -1, & N+1 \leq n \leq 2N \end{cases} \tag{6-71}$$

---

*At points α where the denominator in (6-72) or (6-74) vanishes:

$D_P(\alpha) = 0$ for $\alpha = 0, \pm 2\pi, \pm 4\pi, \pm 6\pi, \ldots$

$D_A(\alpha) = 1$ for $\alpha = \pm\pi, \pm 3\pi, \pm 5\pi, \ldots$

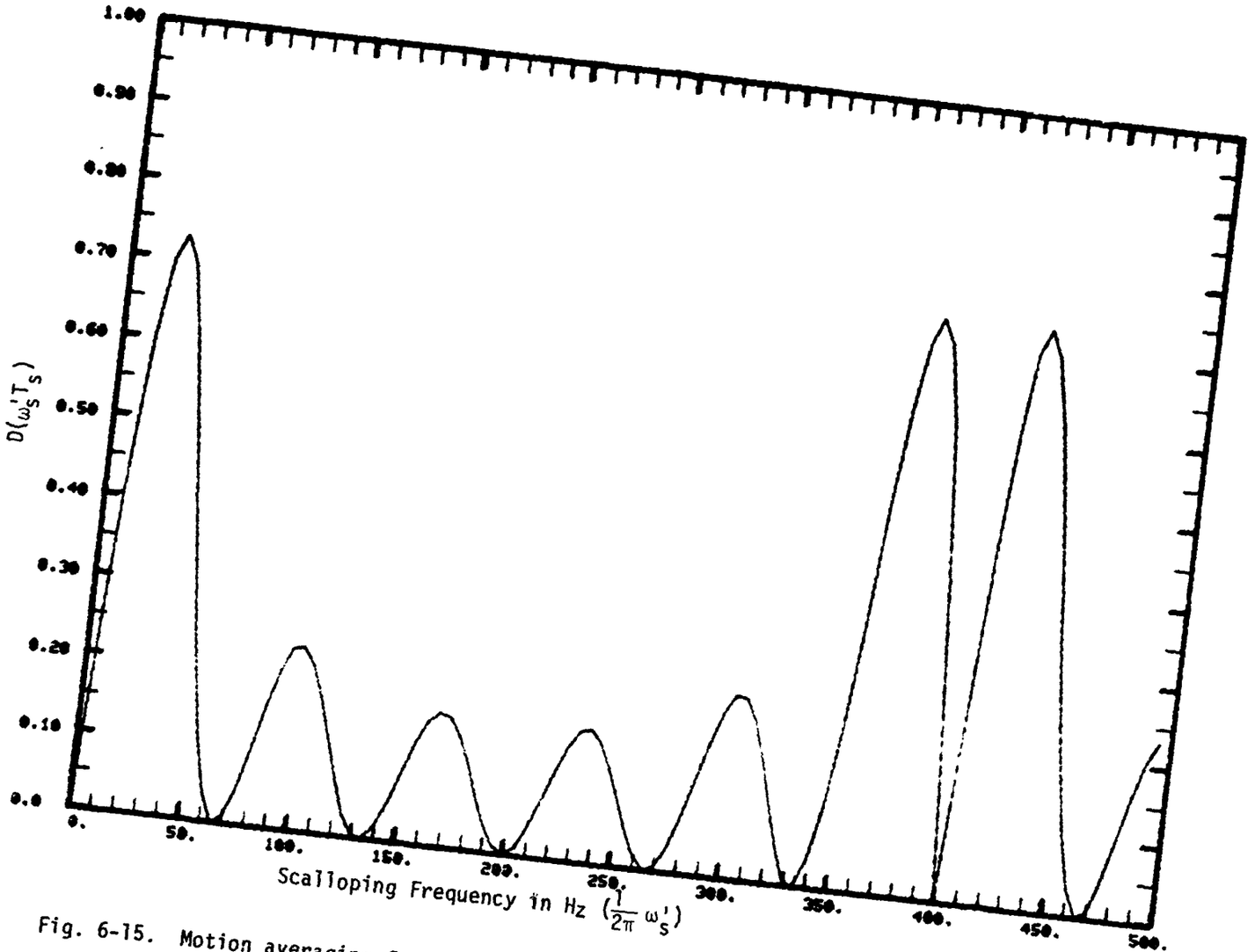

Fig. 6-15. Motion averaging factor for proposed scan sequence $d_p(n)$ (++++++------).

$$D(\alpha) = D_p(\alpha) = je^{-j(N-\frac{1}{2})} \frac{\sin^2\left(\frac{N\alpha}{2}\right)}{N \sin\frac{\alpha}{2}}$$

$$\text{or} \quad |D_p(\alpha)| = \frac{\sin^2 \frac{N\alpha}{2}}{N\left|\sin\frac{\alpha}{2}\right|} \tag{6-72}$$

(ii) <u>the alternating scan sequence initially proposed</u>

$$d(n) = d_A(n) = (-1)^{n-1}, \quad 1 < n < 2N \tag{6-73}$$

$$D(\alpha) = D_A(\alpha) = je^{-j(N-\frac{1}{2})^2} \frac{\sin N\alpha}{2N \cos\frac{\alpha}{2}}$$

$$\text{or} \quad |D_A(\alpha)| = \frac{|\sin N\alpha|}{2N\left|\cos\frac{\alpha}{2}\right|} \tag{6-74}$$

These two motion averaging functions are plotted in Figs. 6-15 and 6-16 over 1 1/4 periods ($0 < \alpha < \frac{5\pi}{2}$) for the 1° azimuth system ($2N = 12$). Since $T_s = 2.$ msec, this corresponds to a scalloping frequency range $0 < \omega_s' < 2\pi \times 500$ Hz. We ·e that the motion averaging function $D_A(\alpha)$ for the alternating scan sequence has a large peak at $\alpha = \pi$, while the motion averaging function $D_P(\alpha)$ for the proposed sequence has peaks at $\alpha = \delta$, $2\pi \pm \delta$ for $\delta \approx 0.124\pi$. These peaks correspond to scalloping frequencies $\frac{1}{2}\omega_s'$ of 200 Hz for the alternating scan sequence and 25 Hz, 375 Hz, 425 Hz for the proposed sequence.

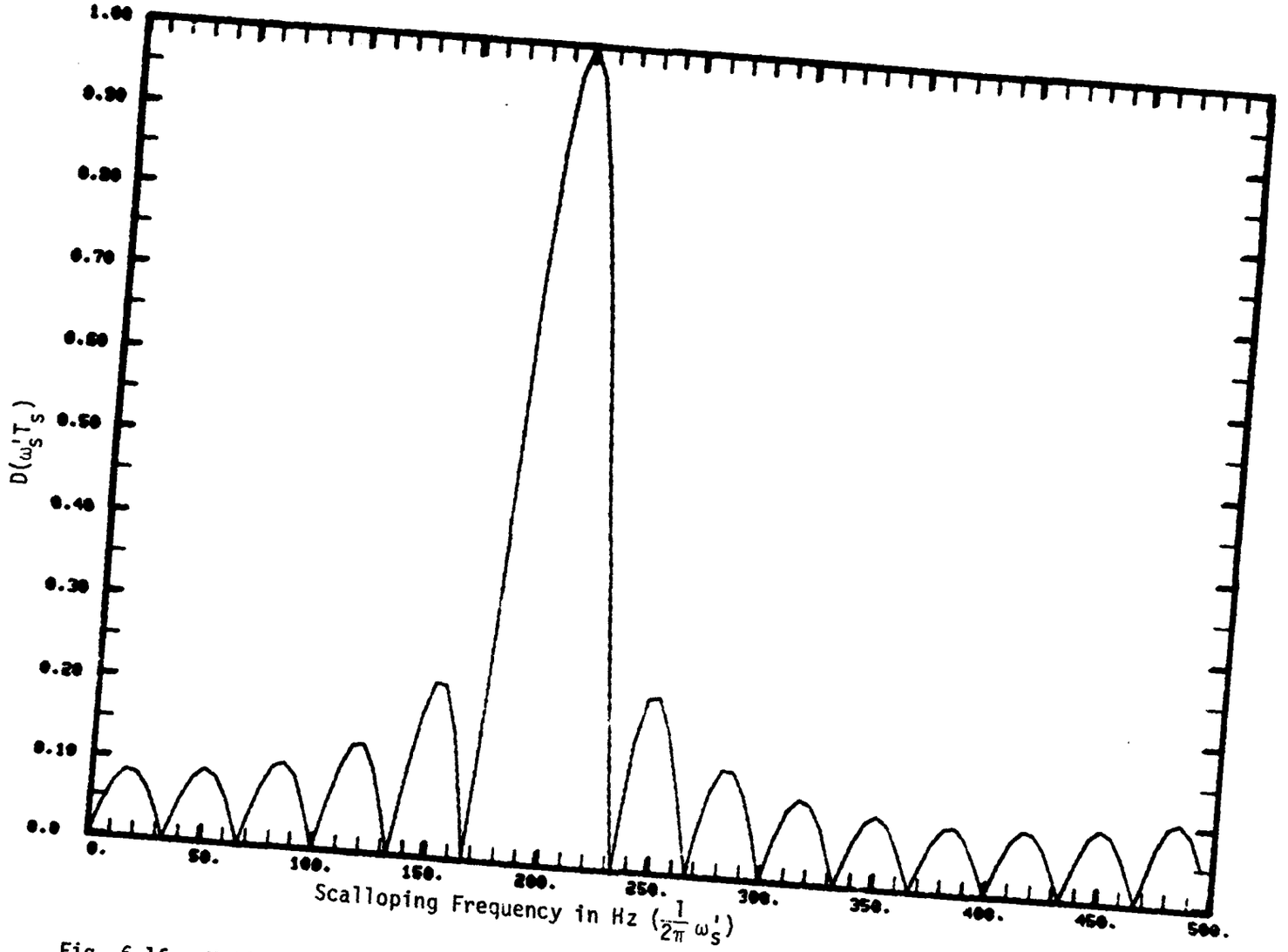

Fig. 6-16. Motion averaging factor for alternating scan sequence $d_A(n)$ (+-+-+-+-+-+-).

b. Measures for Ranking the Motion Averaging Functions

An exhaustive study has been undertaken to determine the amount of motion averaging for every possible scan format function d(n), for the 1° azimuth case 2N = 12. In general there are $\binom{2N}{N}$ † distinct scan format functions with the property $\sum_{n=1}^{2N} d(n) = 0$. The functions d(n) have been sorted according to various measures on the corresponding motion averaging factors $D(\alpha)$, given by

$$m_k(d) = \frac{1}{2\pi} \int_0^{2\pi} |D(\alpha)|^k \, d\alpha \qquad k = 1, 2 \tag{6-75}$$

$$\sigma_k^2(d) = \frac{1}{2\pi} \int_0^{2\pi} |D(\alpha)|^{2k} \, d\alpha - [m_k(d)]^2 \qquad k = 1, 2 \tag{6-76}$$

$$\mu(d) = \max_{0<\alpha<2\pi} |D(\alpha)| \tag{6-77}$$

The functional $m_1(d)$ is the average value over all scalloping frequencies of the complex magnitude of the motion averaging function $D(\cdot)$. The functional $m_2(d)$, the mean square value of $|D(\cdot)|$ is useless as a discriminant because of the property (6-70). The functionals $m_1(d) + \sigma_1(d)$ and $m_2(d) + \sigma_2(d)$ measure the 1σ upper limits of $|D(\cdot)|$ and $|D(\cdot)|^2$, respectively. The functional $\mu(d)$ measures the motion averaging effect for the worst possible scalloping frequency.

---

†For any integers m,n with $0 < n < m$, the notation $\binom{m}{n}$ refers to the number of possible combinations that can result from choosing n items from a group of m items; i.e., $\binom{m}{n} = m!/[n!(m-n)!]$.

c. Average Measures for Random Scan Sequences

In addition to having a rank ordering of scan sequences according to a given measure, it is also useful to know the amount by which the measure of any particular scan sequence differs from that of a "representative" sequence. Thus, for each of the four measures $m_1(d)$, $\sigma_1^2(d)$, $\sigma_2^2(d)$, $\mu(d)$, we shall compute an expected value, denoted $E_0 m_1(d)$, $E_0\sigma_1^2(d)$, $E_0\sigma_2^2(d)$, $E_0\mu(d)$. The operator E_0 represents expectation over randomly chosen sequences with the property $\sum_{n=1}^{2N} d(n) = 0$, with each possible sequence equiprobable.

Analytic results can be obtained for the measure $\sigma_2^2(d)$. In this case we use (6-70) and properties of Fourier transforms to write

$$\left(\frac{1}{2N}\right)^2 + \sigma_2^2(d) = \frac{1}{2\pi} \int_0^{2\pi} |D(\alpha)|^4 \, d\alpha = \left(\frac{1}{2N}\right)^2 \sum_{n-(2N-1)}^{2N-1} [K_d(n)]^2 \qquad (6\text{-}78)$$

where $K_d(n)$ is the autocorrelation function of $d(n)$,

$$K_\alpha(n) = \sum_{m=0}^{2N-|n|} d(m)\, d(m+n) \qquad (6\text{-}79)$$

the expected value of $[K_d(n)]^2$ is written as

$$E_0[K(n)]^2 = \sum_{m=0}^{2N-|n|} \sum_{m'=0}^{2N-|n|} E_0 d(m)\, d(m')\, d(m+n)\, d(m'+n) \qquad (6\text{-}79a)$$

Thus, the calculation of $E_0\sigma_2^2(d)$ reduces to the evaluation of a sum of terms of the form $E_0 d(n_1)\, d(n_2)\, d(n_3)\, d(n_4)$. These expectations are given by

$$E_0 d(n_1)d(n_2)d(n_3)d(n_4) = \begin{cases} 1, & \text{all } n_i\text{'s equal or two pairs equal} \\ \frac{3}{(2N-1)(2N-3)}, & \text{all } n_i\text{'s unequal} \\ \frac{-1}{2N-1}, & \text{otherwise} \end{cases} \tag{6-80}$$

For $n \neq 0$, the double summation in (6-79a) contains: $2N-|n|$ terms of the first type; max $[0, 4(N-|n|)]$ terms of the third type; and $(2N-|n|)(2N-|n|-1) - \max[0, 4(N-|n|)]$ terms of the second type. Summing these in (6-78) yields

$$E_0 \sigma_2^2(d) = \left(\frac{1}{2N}\right)^2 \left[1 + \frac{1}{2N(2N-1)(2N-3)}\right] \tag{6-81}$$

In a similar manner we can evaluate an unconditional expectation, denoted by E, over all equiprobable random ± 1 - valued sequences, not necessarily satisfying $\sum_{n=1}^{2N} d(n) = 0$. In this case the expression corresponding to (6-80) is simpler,

$$E\, d(n_1)d(n_2)d(n_3)d(n_4) = \begin{cases} 1, & \text{all } n_i\text{'s equal or two pairs equal} \\ 0, & \text{otherwise} \end{cases} \tag{6-82}$$

and $E\sigma_2^2(d)$ is evaluated from (6-78) as

$$E\sigma_2^2(d) = \left(\frac{1}{2N}\right)^2 \left(1 - \frac{1}{2N}\right) \tag{6-83}$$

d. Ranking of Scan Sequences by Motion Averaging Effectiveness for 1° Azimuth Case (2N = 12)

In this section we tabulate the results of numerically evaluating the motion averaging measures for all possible scan format sequences d(n) of length 2N = 12 (1° azimuth) with property $\sum_{n=1}^{12} d(n) = 0$. Although there are $\binom{12}{6} = 924$ such sequences, several symmetry properties of $|D(\alpha)|$ make some sequences equivalent with respect to the given measures. In all of the following, let $\tilde{D}(\alpha)$ denote the motion averaging function for the sequence $\tilde{d}(n)$, i.e.,

$$\tilde{D}(\alpha) = \frac{1}{2N} \sum_{n=1}^{2N} \tilde{d}(n)\, e^{-j(n-1)\alpha} \tag{6-83a}$$

(1) $\tilde{d}(n) = -d(n)$, $n = 1, \ldots, 2N$, (sign reversal)

then $$|\tilde{D}(\alpha)| = |D(\alpha)| \tag{6-84}$$

(2) If $\tilde{d}(n) = d(2N+1-n)$, $n = 1, \ldots, 2N$ (sequence reversal)

then $$|\tilde{D}(\alpha)| = |D(\alpha)| \tag{6-85}$$

(3) If $\tilde{d}(n) = d(n)\,(-1)^{n-1}$ $n = 1, \ldots, 2N$ (alternate scan sign reversal)

then $$|\tilde{D}(\alpha)| = |D(\pi-\alpha)| \tag{6-86}$$

All of the chosen measures depend only on the complex magnitude of $D(\alpha)$ and they are all obtained by averaging or maximizing $|D(\alpha)|$ over a complete period. Thus, it is apparent that any group of sequences related by the operations of sign reversal, sequence reversal, or alternate scan sign reversal (or combinations of these) will have equal measures. It can be shown in

AD-A148 524 MLS MULTIPATH STUDIES PHASE 3 VOLUME 3 APPLICATION OF 2/4
MODELS TO MLS ASSES..(U) MASSACHUSETTS INST OF TECH
LEXINGTON LINCOLN LAB J E EVANS ET AL. 08 JUN 81
UNCLASSIFIED ATC-88-VOL-3-PT-2 FAA-RD-79-21-VOL-3-PT2 F/G 17/7 NL

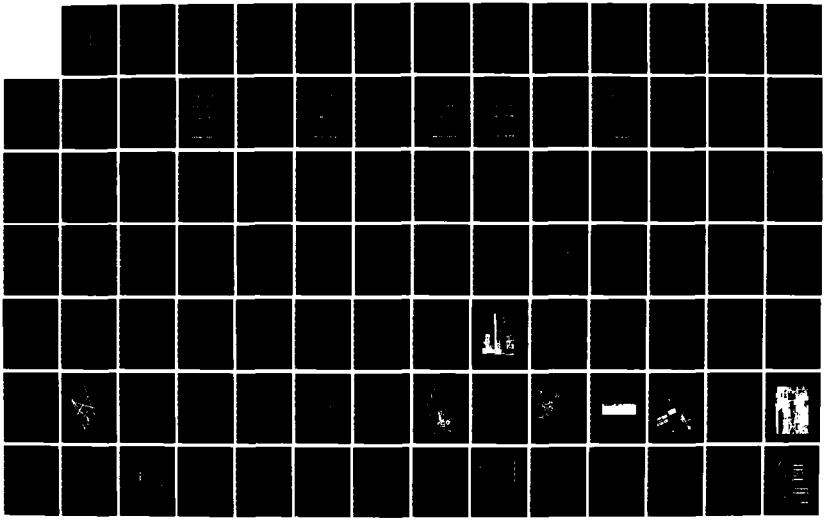

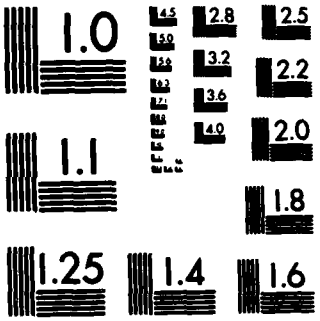

MICROCOPY RESOLUTION TEST CHART
NATIONAL BUREAU OF STANDARDS-1963-A

general that there are $\frac{1}{4}\left[\binom{2N}{N} + 2^N - \frac{1}{2}\binom{N}{N/2}\right]$ * distinct equivalence classes. So, for the case 2N = 12 the various motion averaging measures have to be evaluated for just 197 sequences instead of 924.

The ten best and ten worst scan sequences were determined with respect to each of the four measures $m_1(d)$, $m_1(d) + \sigma_1(d)$, $m_2(d) + \sigma_2(d)$, $\mu(d)$. Only one representative sequence was considered from each equivalence class. There was considerable overlap among the four lists and as a result the total number of sequences ranking in the top ten or bottom ten for at least one of the four measures was just 29. These 29 sequences are listed in Table 6-4 along with their corresponding motion averaging measures. The sequences are numbered for ease of reference and an obvious shorthand notation is used to specify each particular d(n); e.g., the proposed sequence $d_P(n)$ is designated as ++++++------ (#63 in the table) and the alternating scan sequence d_A as +-+-+-+-+-+- (#1365 in the table). The numbering scheme represents each sequence by the decimal equivalent of its binary representation obtained by converting +'s to 0's and -'s to 1's.

It is seen that the 29 listed sequences can be divided into two groups. The first 12 sequences have the smallest average $|D(\cdot)|$ but also have the largest peak $|D(\cdot)|$. The sequences in this group all possess considerable symmetry and their motion averaging spectra contain at least one high peak (e.g., see Figs. 6-15 and 6-16). The last 17 sequences are more randomly asymmetric and their motion averaging spectra are flatter. This results in good "worst case" performance, but these sequences also have the poorest

---

*The last term in brackets, $-0.5\binom{N}{N/2}$, is absent if N/2 is not an integer (i.e., if the number of scans, 2N, is not divisible by 4).

TABLE 6-4

COMPARISON OF MOTION AVERAGING MEASURES FOR VARIOUS SCAN SEQUENCES OF LENGTH 12

Scan Sequence d(n)	Motion Averaging Measures			
	$m_1(d)$	$m_1(d)+\sigma_1(d)$	$\sqrt{m_2(d)+\sigma_2(d)}$	$\mu(d)$
(1365) +-+-+-+-+-+-	.1665	.4023	.5516	1.0000
(819) ++--++--++--	.1936	.4077	.4806	.7082
(63) ++++++------	.1987	.4081	.4806	.7292
(455) +++---+++---	.2008	.4082	.4661	.6812
(1445) +-+---+++-+-	.2015	.4082	.4661	.6901
(963) ++----+++--	.2112	.4080	.4564	.6681
(504) +++------+++	.2137	.4078	.4564	.6715
(1625) +--++-+--++-	.2141	.4077	.4380	.6181
(924) ++---+++--++	.2157	.4075	.4630	.6832
(910) ++---+++---+	.2164	.4075	.4598	.6707
(1370) +-+-+-+--+-+	.2188	.4071	.4598	.6754
(1366) +-+-+-+-+--+	.2248	.4059	.4630	.6682
(700) ++-+-+----++	.2612	.3842	.3750	.4105
(937) ++---+-+-++-	.2623	.3829	.3750	.4349
(874) ++--+--+-+-+	.2643	.3804	.3750	.4080
(732) ++-+--+---++	.2665	.3775	.3653	.4050
(442) +++--+---+-+	.2672	.3764	.3652	.4032
(470) +++---+-+--+	.2697	.3726	.3652	.4562
(366) +++-+--+---+	.2703	.3716	.3652	.4074
(347) +++-+-+--+--	.2708	.3707	.3653	.3992
(377) +++-+----++-	.2709	.3707	.3653	.4233
(629) ++-++---+-+-	.2715	.3697	.3652	.4354
(1118) +-+++-+----+	.2715	.3696	.3653	.4264
(1889) +---+--++++-	.2725	.3679	.3652	.4383
(221) ++++--+---+-	.2727	.3674	.3653	.4425
(359) +++-+--++---	.2729	.3670	.3653	.4576
(634) ++-++----+-+	.2733	.3662	.3653	.4447
(237) +++---+--+-	.2746	.3636	.3536	.3994
(437) +++--+--+-+-	.2747	.3634	.3652	.4635
"Average" Sequence*	.2511	.3928	.4083	.5388

*These figures were obtained by making the substitutions $m_1(d) \rightarrow E_0 m_1(d)$, $\sigma_1^2(d) \rightarrow E_0 \sigma_1^2(d)$, $\sigma_2^2(d) \rightarrow E_0 \sigma_2^2(d)$, $\mu(d) \rightarrow E_0 \mu(d)$.

average performance. The ranking according to the two remaining measures $m_1(d) + \sigma_1(d)$ and $m_2(d) + \sigma_2(d)$, are highly correlated with the rankings relative to the "worst case" measure $\mu(d)$. Some representative motion averaging functions corresponding to scan sequences listed in Table 6-4 are plotted in Figs. 6-17 to 6-20.

4. The Motion Averaged Errors

In the previous section the various possible scan sequences were rated solely on the basis of their motion averaging effectiveness with no consideration given to the magnitude of the errors being averaged. In this section we will show in more detail the effects on the actual errors of varying the scan format and we will see that the two rankings are highly correlated.

a. Dependence of the Error Amplitudes on the Motion Averaging Function

The study of the motion averaging function alone is a useful concept because it is largely independent of the exact nature of the receiver processing. The only critical assumptions needed to derive an expression for the frame averaged error of the general form of (6-65) are that it change sign with d(n) and that it can be obtained as a convergent series of sinusoidal terms whose phases change linearly from scan to scan; i.e., the single scan errors are of the form

$$\varepsilon(n) = \sum_{m=0}^{\infty} \varepsilon_m(n) \tag{6-87}$$

where

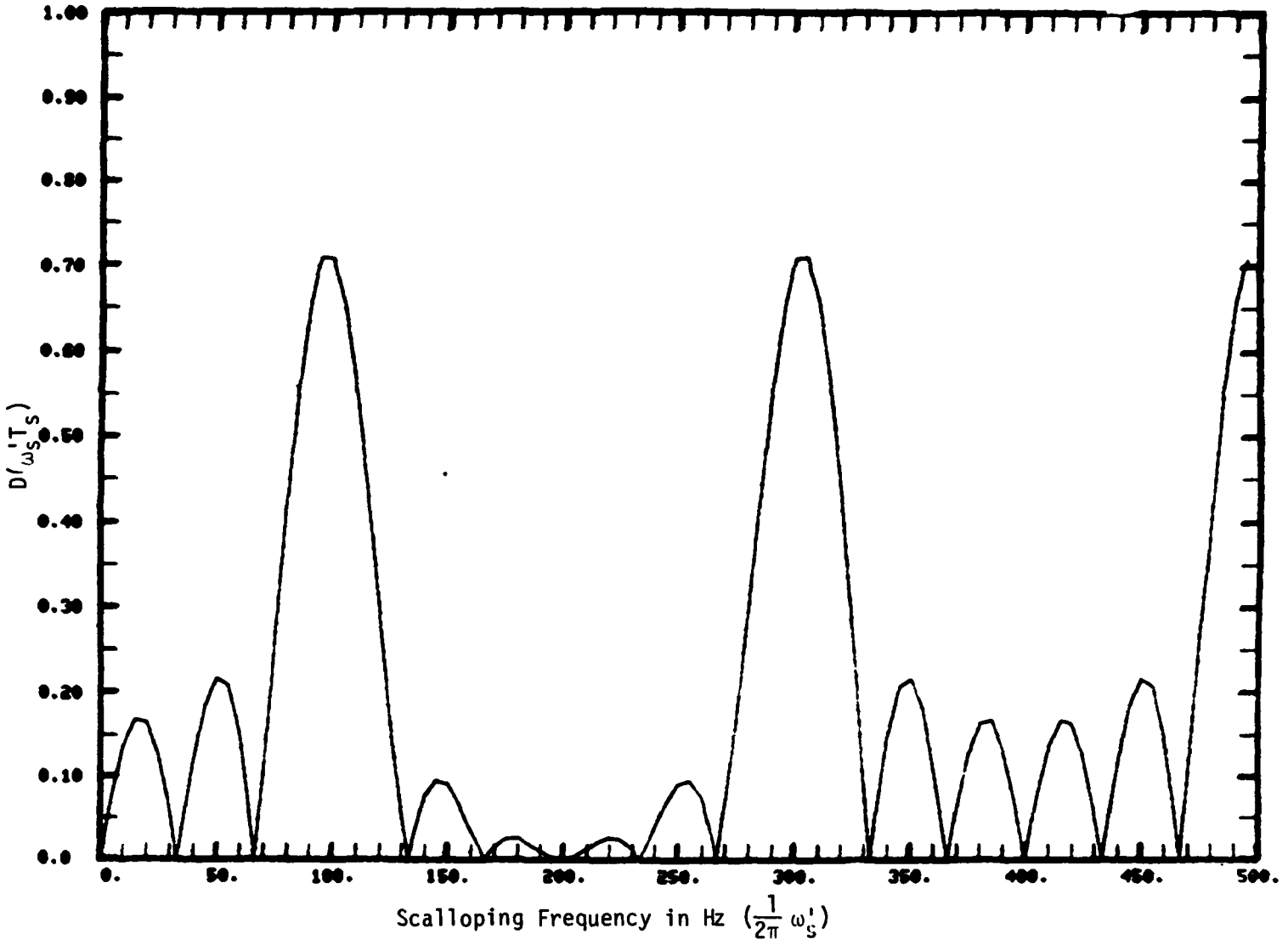

Fig. 6-17. Motion averaging factor for scan sequence #819 (++--++--++--).

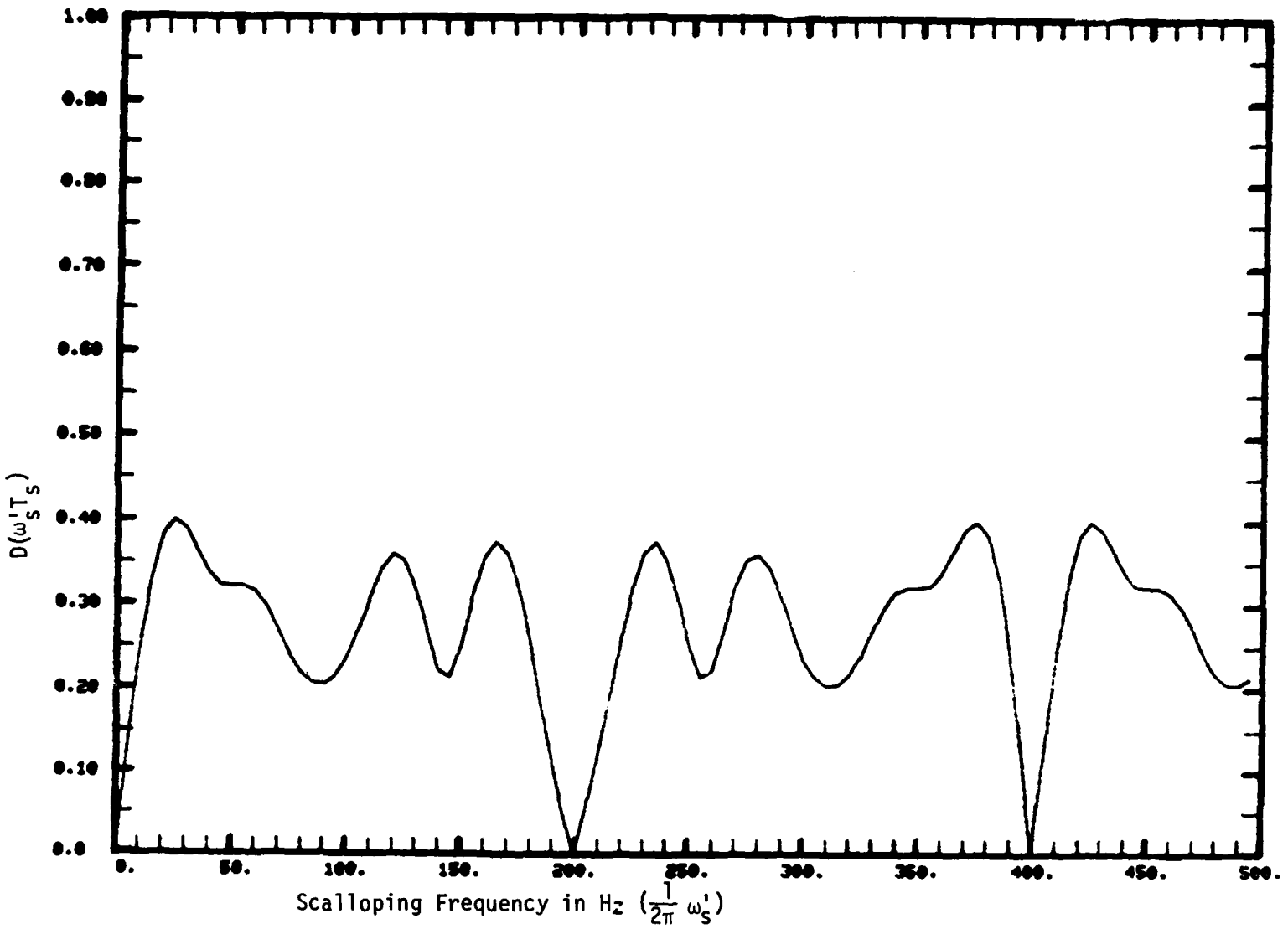

Fig. 6-18. Motion averaging factor for scan sequence #237 (++++---+--+-).

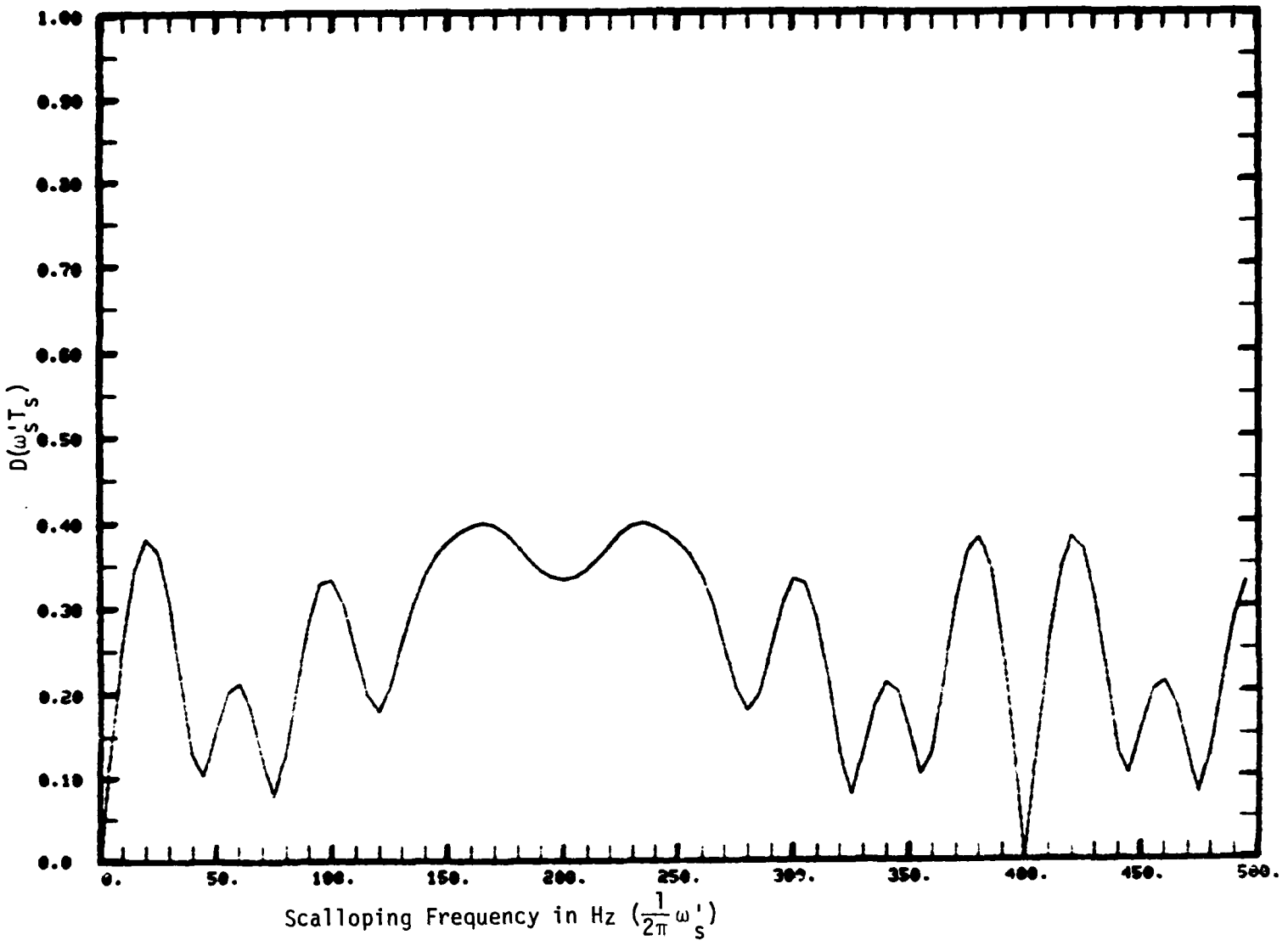

Fig. 6-19. Motion averaging factor for scan sequence #347 (+++-+-+--+--).

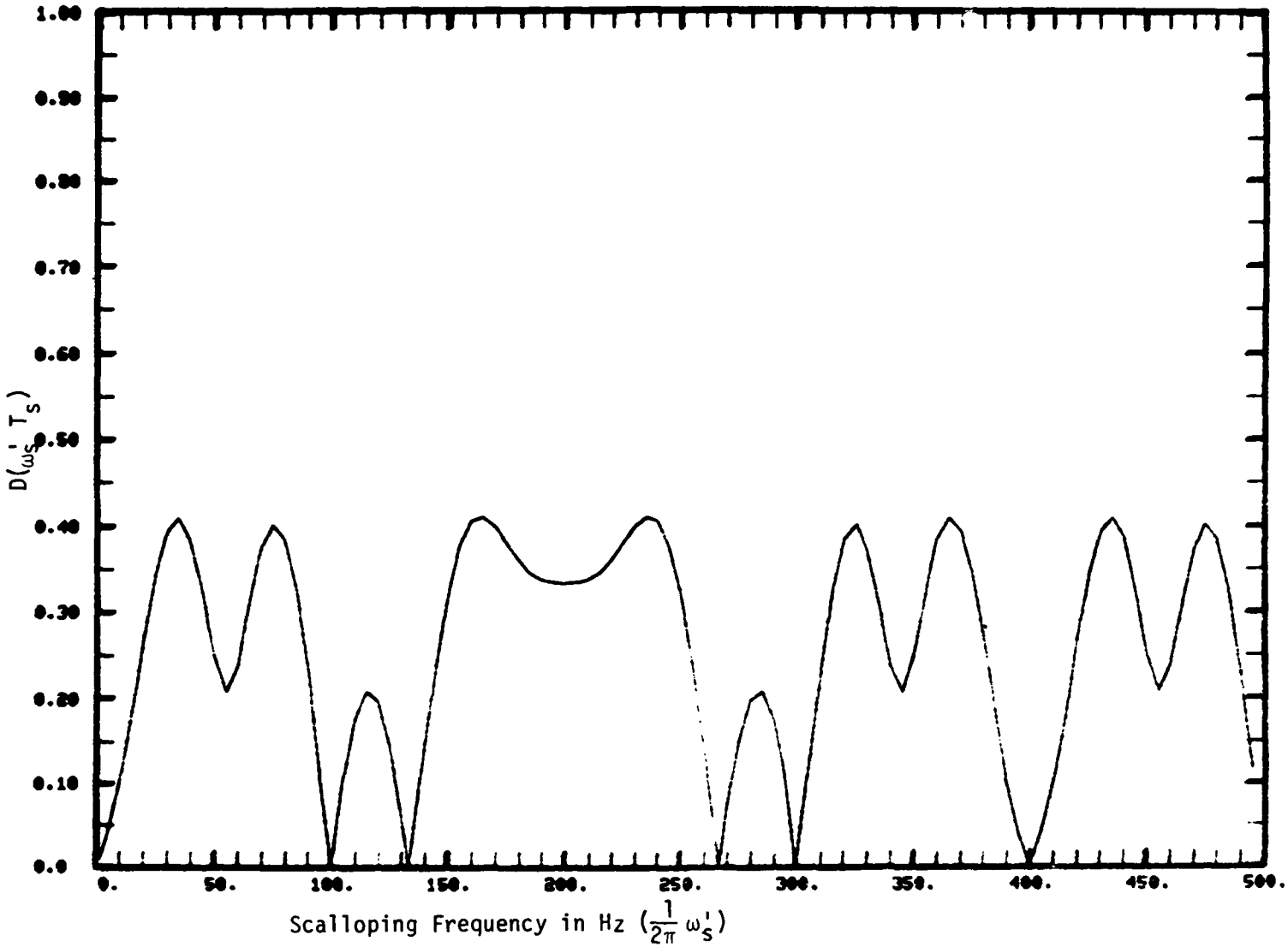

Fig. 6-20. Motion averaging factor for scan sequence #700 (++-+-+----++).

$$\varepsilon_m(n) = \varepsilon_m^{pk} d(n) \, \mathrm{Re}\left[e^{-j(\Phi_m + \Phi_m' n)}\right], \qquad m = 0, 1, 2, \ldots \tag{6-88}$$

and ε_m^{pk}, Φ_m, Φ_m' are independent of the scan number n. The amplitude factor ε_m^{pk} is interpreted as the mth order error component that results from the worst-case initial phase Φ_m; i.e.,

$$\varepsilon_m^{pk} = \max_{\Phi_m} |\varepsilon_m(n)| \tag{6-89}$$

These assumptions lead directly to an expression for the frame averaged error which is analogous to (6-65).

$$\hat{\varepsilon} = \sum_{m=0}^{\infty} \hat{\varepsilon}_m \tag{6-90}$$

where

$$\hat{\varepsilon} = \pm \varepsilon_m^{pk} \; \mathrm{Re}\left[e^{-j\Phi_m} D(\Phi_m')\right] \tag{6-91}$$

The peak value of this mth order component of the frame error is evaluated as

$$\hat{\varepsilon}_m^{pk} \equiv \max_{\Phi_m} |\hat{\varepsilon}_m| = \varepsilon_m^{pk} \; |D(\Phi_m')| \tag{6-92}$$

i.e., the peak value of the mth order component of the frame error is scaled down from the peak value of the mth order component of the single scan error by the complex magnitude of the motion averaging function evaluated at the

scan-to-scan phase change Φ'_m.

The peak values of the total single scan and frame errors ε^{pk}, $\hat{\varepsilon}^{pk}$ cannot be obtained by simply adding the peak values of the mth order components, because the initial phases $\{\Phi_m\}$ are generally not independent of each other. However, the following bounds are apparent.

$$\varepsilon_0^{pk} - \sum_{m=1}^{\infty} \varepsilon_m^{pk} < \varepsilon^{pk} < \sum_{m=0}^{\infty} \varepsilon_m^{pk} \tag{6-93}$$

$$\hat{\varepsilon}_0^{pk} - \sum_{m=1}^{\infty} \hat{\varepsilon}_m^{pk} < \hat{\varepsilon}^{pk} < \sum_{m=0}^{\infty} \hat{\varepsilon}_m^{pk} \tag{6-94}$$

where

$$\varepsilon^{pk} \equiv \max_{\{\Phi_m\}} \varepsilon(n) \tag{6-95}$$

$$\hat{\varepsilon}^{pk} \equiv \max_{\{\Phi_m\}} \hat{\varepsilon} \tag{6-96}$$

For the proposed DMLS processor the peak mth order single scan error component is evaluated from the expansion (6-64) as

$$\varepsilon_m^{pk} = \frac{\theta_c}{|\cos\theta_c|} \quad |H_\Delta(\omega'_s)| \; |H_\Sigma(\omega'_s)|^m \quad \rho^{m+1} \tag{6-97}$$

The initial phase Φ_m and scan-to-scan phase increment Φ'_m are identified as

$$\Phi_m = (m+1)\,\phi \pm m\pi \tag{6-98}$$

$$\phi_m' = (m+1)\ \omega_s' T_s \tag{6-99}$$

Therefore the peak value of the mth order component of the frame averaged error is evaluated from (6-92) as

$$\hat{\varepsilon}_m^{pk} = \frac{\theta_c}{|\cos\theta_c|}\ |H_\Delta(\omega_s')|\ |H_\Sigma(\omega_s')|^m\ \rho^{m+1}\ D[(m+1)\omega_s' T_s] \tag{6-100}$$

The bounds (6-93) and (6-94) on the peak total errors then take the form

$$\frac{\rho\theta_B}{|\cos\theta_c|}\ |H_\Delta(\omega_s')|\ \frac{1 - 2\rho|H_\Sigma(\omega_s')|}{1 - \rho|H_\Sigma(\omega_s')|} < \varepsilon^{pk} < \frac{\rho\theta_B}{|\cos\theta_c|}\ |H_\Delta(\omega_s')|\ \frac{1}{1 - \rho|H_\Sigma(\omega_s')|} \tag{6-101}$$

$$\frac{\rho\theta_B}{|\cos\theta_c|}\ |H_\Delta(\omega_s')|\ [|D(\omega_s' T_s)| - C(\rho,\ \omega_s',\ d)] < \hat{\varepsilon}^{pk}$$

$$< \frac{\rho\theta_B}{|\cos\theta_c|}\ |H_\Delta(\omega_s')|\ [|D(\omega_s' T_s)| + C(\rho,\ \omega_s',\ d)] \tag{6-102}$$

where

$$C(\rho,\ \omega_s',\ d) = \sum_{m=1}^{\infty} |H_\Sigma(\omega_s')|^m\ \rho^m\ D[(m+1)\omega_s' T_s] \tag{6-103}$$

We observe that if ρ becomes small the upper and lower bounds approach each other. The peak single scan error becomes proportional to the magnitude of the difference filter frequency response $|H_\Delta(\omega_s')|$, whereas the peak frame

error is scaled down from the peak single scan error by the motion averaging factor $|D(\omega_s' T_s)|$. Figure 6-21 shows the first order static error characteristic.

b. Error Rankings for Scan Sequences of Length 12 in the Presence of -3 dB Multipath

This section assesses the various scan sequences for the 1° azimuth case 2N = 12 according to the peak frame averaged errors $\hat{\varepsilon}^{pk}$ defined in (6-96), i.e., the amplitude of the frame error ($\hat{\varepsilon}$) vs. multipath phase (ϕ) curve. In this study the multipath amplitude was fixed at -3 dB ($\rho = 0.707$) and we were concerned with the variation of $\hat{\varepsilon}^{pk}$ with scalloping frequency ω_s' and scan format function d(n); we indicate this dependence explicitly by writing

$$\hat{\varepsilon}^{pk} = \hat{\varepsilon}^{pk}(\omega_s', d) \tag{6-104}$$

Our attention will be confined to two measures for ranking the scan sequences d(n) according to their error amplitudes: the average (over scalloping frequency) peak error $m_1''(d)$ and the peak error $\mu''(d)$ for the worst-case scalloping frequency, both measured in units of θ_B. In addition, we will consider two corresponding measures $m_1'(d)$, $\mu'(d)$ based on the first-order approximation to $\hat{\varepsilon}^{pk}$ given by the first term in the bound (6-102). The definitions of these four measures are:

$$\theta_B \, m_1''(d) = \frac{1}{2W} \int_{-W}^{W} \hat{\varepsilon}^{pk}(\omega_s', d) \, d\omega_s' \tag{6-105a}$$

$$\theta_B \, \mu''(d) = \max_{-W \le \omega_s' \le W} \hat{\varepsilon}^{pk}(\omega_s', d) \tag{6-105b}$$

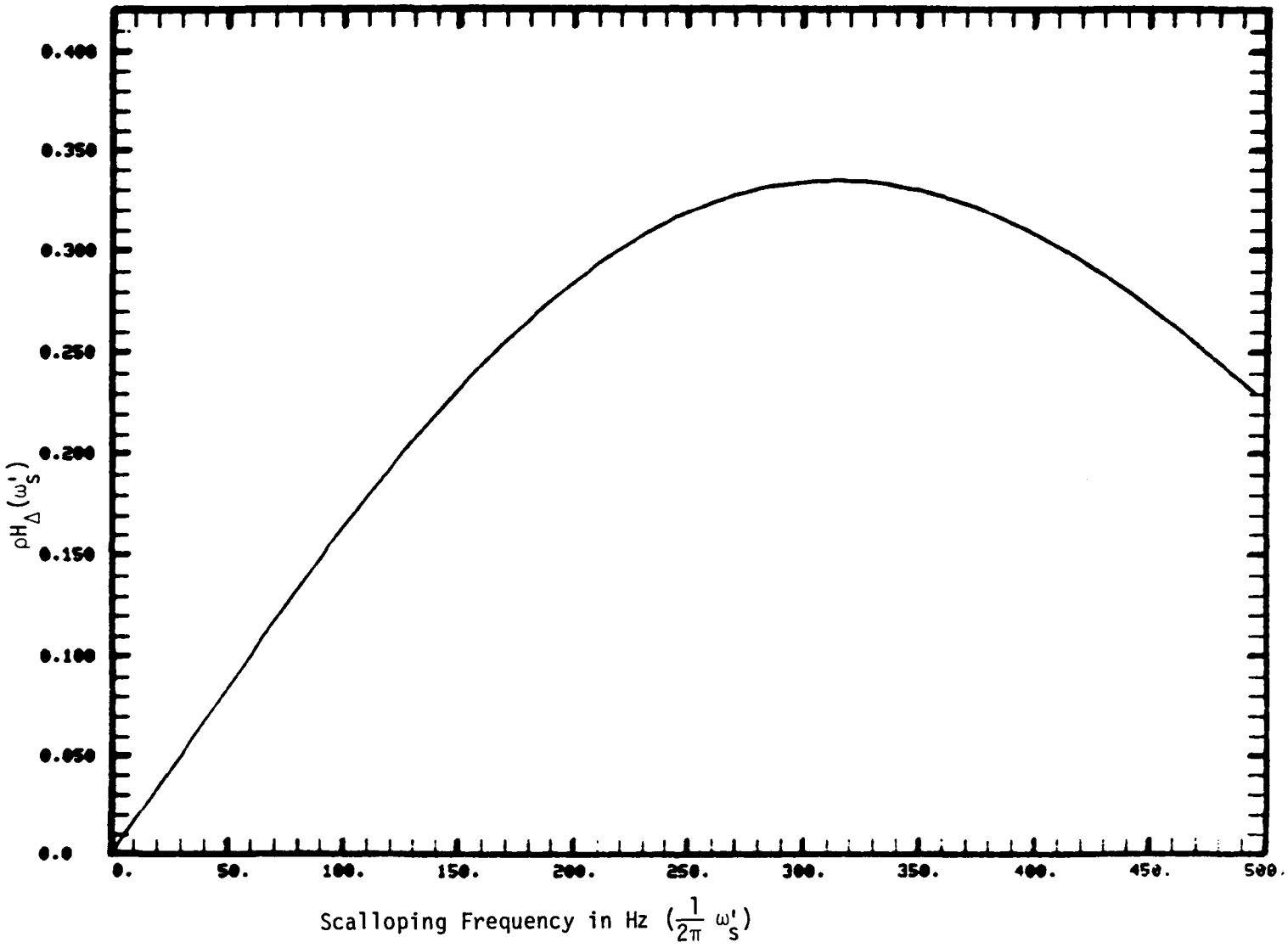

Fig. 6-21. First-order static error characteristic, $\rho H_\Delta(\omega_s')$.

$$\theta_B m_1'(d) = \frac{1}{2W} \int_{-W}^{W} \frac{\rho\theta_B}{|\cos\theta_c|} |H_\Delta(\omega_s')| \; |D(\omega_s' T_s)| d\omega_s' \tag{6-106a}$$

$$\theta_B \mu'(d) = \max_{-W \le \omega_s' \le W} \frac{\rho\theta_B}{|\cos\theta_c|} |H_\Delta(\omega_s')| \; |D(\omega_s' T_s)| \tag{6-106b}$$

The scalloping frequency upper limit W has been chosen arbitrarily to be $2\pi \times$ 500 Hz. There is no "natural" upper limit as in the case of the previous motion averaging measures $m_1(d)$, $\mu(d)$ based solely on motion averaging function $D(\cdot)$, because $\hat{\varepsilon}^{pk}(\omega_s', d)$ is weighted by the static error characteristic and hence is not periodic. In principle another weighting function could be introduced to reflect the relative importance of errors at different scalloping frequencies; in our tests all scalloping frequencies up to 500 Hz were given equal weight.

The peak error function possesses several symmetries akin to the ones already observed for the motion averaging function. It follows from the expression (6-65) for $\hat{\varepsilon}$ that

$$\hat{\varepsilon}^{pk}(-\omega_s', \tilde{d}) = \hat{\varepsilon}^{pk}(\omega_s', d), \qquad \text{for } \tilde{d}(n) = \begin{matrix} d(n) \\ -d(n) \\ d(2N+1-n) \end{matrix} \tag{6-107}$$

Thus, the errors only need to be evaluated for positive scalloping frequencies, and scan sequences which are related by the operations of sign reversal or sequence reversal are equivalent [there is no additional equivalence be-

tween sequences related by alternate scan sign reversal as in (6-86)]. The number of distinct equivalence classes that have to be examined are $\frac{1}{4}[\binom{2N}{N} + 2^N + \binom{N}{N/2}]$,* or 252 for 2N = 12.

Tables 6-5 to 6-10 list the ten best and the ten worst sequences, as ranked according to each of the "average" performance measures $m_1(d)$, $m_1'(d)$, $m_1''(d)$, and the "worst case" performance measures $\mu(d)$, $\mu'(d)$, $\mu''(d)$. As in Table 6-3 each sequence is numbered by the decimal equivalent of its binary representation (+ ---> 0, - ---> 1). From Tables 6-5b, 6-6b, 6-7b, 6-8a, 6-9a, and 6-10, we again note the inverse correlation between average performance and worst case performance. Not one sequence listed in the table as ranking high (low) with respect to the average measures $m_1(d)$, $m_1'(d)$, or $m_1''(d)$ ranks in the top (bottom) half with respect to the worst case measures $\mu(d)$, $\mu'(d)$, and $\mu''(d)$, and conversely only two sequences listed as ranking high (low) with respect to $\mu(d)$, $\mu'(d)$, or $\mu''(d)$ rank in the top (bottom) half with respect to $m_1(d)$, $m_1'(d)$, or $m_1''(d)$. Thus the choice of scan function always requires a compromise between good performance on the average and good performance under the most adverse circumstances.

This trade-off is best illustrated by the performance of the one truly outstanding sequence listed in the tables, the alternating scan sequence $d_A(n)$ (#1365). This scan format achieves best average performance by a wide margin according to all three measures, but conversely it ranks dead last among all sequences according to any of the worst case measures.

---

*The last term in brackets is absent if N/2 is not an integer (i.e., if the number of scans, 2N, is not divisible by 4).

TABLE 6-5a

TOP TEN AND BOTTOM TEN SCAN SEQUENCES RANKED ACCORDING TO $m_1(d)$ = AVERAGE OF $|D(\omega_s' T_s)|$

Scan Sequence d(n)	$m_1(d)$		$m_1'(d)$		$m_1''(d)$	
	Rank*	Value	Rank*	Value	Rank*	Value
(1365) +-+-+-+-+-+-	1	.1665	1	.0386	1	.0597
(819) ++--++--++--	2~	.1936	5	.0478	6	.0707
(1638) +--++--++--+	2~	.1936	2	.0456	4	.0700
(63) ++++++------	4~	.1988	9	.0502	8	.0717
(1386) +-+-+--+-+-+	4~	.1988	3	.0462	2	.0679
(455) +++---++---	6	.2008	13	.0531	15	.0774
(1445) +-+--+-++-+-	7	.2017	4	.0473	7	.0716
(963) ++----+++--	8~	.2115	17	.0538	13	.0770
(1686) +--+-++-+--+	8~	.2115	8	.0498	14	.0771
(1197) +-++-+-+--+-	10~	.2140	6	.0488	3	.0696
(504) +++-------+++	10~	.2140	25	.0554	68	.0853
(377) +++-+----++-	-10	.2709	-4	.0669	-8	.0966
(629) ++-++---+-+-	-9	.2715	-21	.0652	-36	.0937
(1118) +-+++-+----+	-8	.2715	-18	.0654	-9	.0965
(1889) +---+--+++-	-7	.2725	-2	.0670	-1	.1001
(221) +++--+---+-	-6	.2727	-9	.0661	-2	.0987
(359) +++-+--+---	-5	.2729	-6	.0665	-13	.0961
(634) ++-++----+-+	-4	.2733	-10	.0659	-10	.0965
(474) +++---+--+-+	-2~	.2746	-1	.0672	-25	.0944
(237) +++--+--+-+-	-2~	.2746	-5	.0669	-59	.0927
(437) +++--+--+-+-	-1	.2747	-12	.0658	-3	.0973
"Average" Sequence**		.2511		.0610		.0889

*Positive (negative) numbers denote position with respect to smallest (largest) $m_1(d)$, $m_1'(d)$, or $m_1''(d)$. Tied positions are indicated by ~.

**The values listed are $E_0 m_1(d)$, $E_0 m_1'(d)$, $E_0 m_1''(d)$.

TABLE 6-5b

TOP TEN AND BOTTOM TEN SCAN SEQUENCES RANKED ACCORDING TO $m_1(d)$ = AVERAGE OF $|D(\omega_s' T_s)|$

Scan Sequence		$\mu(d)$		$\mu'(d)$		$\mu''(d)$	
$\underline{d}(n)$		Rank*	Value	Rank*	Value	Rank*	Value
(1365)	♦-♦-♦-♦-♦-♦-	-1	1.0000	-1	.2838	-1	.4048
(819)	♦♦--♦♦--♦♦--	-4~	.7082	-2	.2362	-81	.2174
(1638)	♦--♦♦--♦♦--♦	-4~	.7082	-3	.2356	-62	.2376
(63)	♦♦♦♦♦♦------	-2~	.7292	-4	.2333	-63	.2347
(1386)	♦-♦-♦--♦-♦-♦	-2~	.7292	-9	.2212	-64	.2327
(455)	♦♦♦---♦♦♦---	-9	.6812	-6	.2256	-76	.2282
(1445)	♦-♦--♦-♦♦-♦-	-6	.6981	-15	.2178	-72~	.2228
(963)	♦♦---♦♦♦♦--	-15~	.6680	-11	.2205	-77	.2193
(1686)	♦--♦-♦♦-♦--♦	-15~	.6680	-18	.2142	-28	.2544
(1197)	♦-♦♦-♦-♦--♦-	-11~	.6715	-22	.2181	-72~	.2228
(584)	♦♦♦--------♦♦♦	-11~	.6715	-13	.2188	-60	.2454
(377)	♦♦♦-♦-----♦♦-	11	.4233	13	.1383	3~	.1738
(629)	♦♦-♦♦---♦-♦-	14	.4354	8	.1321	43	.1798
(1118)	♦-♦♦♦-♦-----♦	12	.4264	6	.1291	31	.1784
(1809)	♦---♦--♦♦♦♦-	15	.4383	25	.1463	27~	.1779
(221)	♦♦♦♦--♦---♦-	17	.4425	16	.1416	14	.1757
(359)	♦♦♦-♦--♦♦---	27	.4576	41	.1516	47	.1804
(634)	♦♦-♦♦-----♦♦	21~	.4448	15	.1415	50	.1805
(474)	♦♦♦--♦--♦-♦	2~	.3994	1	.1212	66	.1845
(237)	♦♦♦-♦--♦-♦-	2~	.3994	3	.1278	22	.1767
(437)	♦♦♦--♦-♦-♦-	34	.4634	24	.1463	110~	.1973
"Average" Sequence**			.5388		.1727		.2090

*Positive (negative) numbers denote position with respect to smallest (largest) $\mu(d)$, $\mu'(d)$, or $\mu''(d)$. Tied positions are indicated by ~.

**The values listed are $E_0\mu(d)$, $E_0\mu'(d)$, $E_0\mu''(d)$.

TABLE 6-6a

TOP TEN AND BOTTOM TEN SCAN SEQUENCES RANKED ACCORDING TO $m_l'(d)$ = AVERAGE OF $\rho|D(\omega_s'T_s)H_\Delta(\omega_s')|$

Scan Sequence d(n)	$m_l(d)$		$m_l'(d)$		$m_l''(d)$	
	Rank*	Value	Rank*	Value	Rank*	Value
(1365) +-+-+-+-+-+-	1	.1665	1	.0386	1	.0597
(1638) +--++--++--+	2~	.1936	2	.0456	4	.0700
(1386) +-+-+--+-+-+	4~	.1988	3	.0462	2	.0679
(1445) +-+--+++-+-	7	.2017	4	.0473	7	.0716
(819) ++--++--++--	2~	.1936	5	.0478	6	.0707
(1197) +-++-+-+--+-	10~	.2140	6	.0488	3	.0696
(1737) +--+--++-++-	13~	.2158	7	.0493	5	.0701
(1686) +--+-++-+--+	8~	.2115	8	.0498	14	.0771
(63) ++++++------	4~	.1988	9	.0502	8	.0717
(1625) +--++-+--++-	12	.2143	10	.0510	12	.0768
(634) ++-+++---+-+	-4	.2733	-10	.0659	-10	.0965
(221) ++++--+---+-	-6	.2727	-9	.0661	-2	.0987
(470) +++---+-+--+	-14	.2697	-8	.0665	-12	.0962
(461) +++---++--+-	-16	.2681	-7	.0665	-18	.0952
(359) +++-+--++---	-5	.2729	-6	.0665	-13	.0961
(237) +++++--+--+-	-2~	.2746	-5	.0669	-59	.0927
(377) +++-+---++-	-10	.2709	-4	.0669	-8	.0966
(573) ++-+++---+-	-12~	.2704	-3	.0670	-51	.0931
(1889) +---+--++++-	-7	.2725	-2	.0670	-1	.1001
(474) +++---+--+-+	-2~	.2746	-1	.0672	-25	.0944
"Average" Sequence**		.2511		.0610		.0889

*Positive (negative) numbers denote position with respect to smallest (largest) $m_l(d)$, $m_l'(d)$, or $m_l''(d)$. Tied positions are indicated by ~.

**The values listed are $E_0 m_l(d)$, $E_0 m_l'(d)$, $E_0 m_l''(d)$.

TABLE 6-63

TOP TEN AND BOTTOM TEN SCAN SEQUENCES RANKED ACCORDING TO $m_1'(d)$ = AVERAGE OF $\rho|D(\omega_s'T_s)H_\Delta(\omega_s')|$

Scan Sequence d(n)		μ(d)		μ'(d)		μ"(d)	
		Rank*	Value	Rank*	Value	Rank*	Value
(1365)	♦-♦-♦-♦-♦-♦-	-1	1.0000	-1	.2838	-1	.4048
(1638)	♦--♦♦--♦♦--♦	-4~	.7082	-3	.2356	-62	.2376
(1386)	♦-♦-♦--♦-♦-♦	-2~	.7292	-9	.2212	-64	.2327
(1445)	♦-♦--♦-♦♦-♦-	-6	.6901	-15	.2178	-72~	.2228
(819)	♦♦--♦♦--♦♦--	-4~	.7082	-2	.2362	-81	.2174
(1197)	♦-♦♦-♦-♦--♦-	-11~	.6715	-22	.2101	-72~	.2228
(1737)	♦--♦--♦♦-♦♦-	-7~	.6832	-7	.2242	-46	.2513
(1686)	♦--♦-♦♦-♦--♦	-15~	.6680	-18	.2142	-28	.2544
(63)	♦♦♦♦♦♦------	-2~	.7292	-4	.2333	-63	.2347
(1625)	♦--♦♦-♦--♦♦-	-54	.6182	-31	.2029	-48	.2512
(634)	♦♦-♦♦----♦-♦	21~	.4448	15	.1415	50	.1805
(221)	♦♦♦♦--♦---♦-	17	.4425	16	.1416	14	.1757
(478)	♦♦---♦-♦--♦	26	.4561	43	.1518	27~	.1779
(461)	♦♦---♦♦--♦-	28	.4444	32	.1479	5~	.1745
(389)	♦♦♦-♦--♦---	27	.4576	41	.1516	47	.1804
(237)	♦♦♦---♦--♦-	2~	.3994	3	.1278	22	.1767
(377)	♦♦♦-♦---♦♦-	11	.4233	13	.1383	3~	.1738
(573)	♦♦-♦♦----♦-	7~	.4075	11	.1347	7	.1748
(1809)	♦---♦--♦♦♦-	15	.4383	25	.1463	27~	.1779
(474)	♦♦---♦--♦-♦	2~	.3994	1	.1212	66	.1845
"Average" Sequence**			.5388		.1727		.2090

*Positive (negative) numbers denote position with respect to smallest (largest) μ(d), μ'(d), or μ"(d). Tied positions are indicated by ~.

**The values listed are $E_0\mu(d)$, $E_0\mu'(d)$, $E_0\mu''(d)$.

TABLE 6-7a

TOP TEN AND BOTTON TEN SCAN SEQUENCES RANKED ACCORDING TO $m_1''(d)$ = AVERAGE OF $\dfrac{\hat{\varepsilon}^{pk}(\omega_s',d)}{\theta_B}$

Scan Sequence d(n)	$m_1(d)$		$m_1'(d)$		$m_1''(d)$	
	Rank*	Value	Rank*	Value	Rank*	Value
(1365) +-+-+-+-+-+-	1	.1665	1	.0386	1	.0597
(1386) +-+-+--+-+-+	4~	.1988	3	.0462	2	.0679
(1197) +-++-+-+--+-	10	.2140	6	.0488	3	.0696
(1638) +--++--+-+--+	2~	.1936	2	.0456	4	.0700
(1737) +--+--++-++-	13~	.2158	7	.0493	5	.0701
(819) ++--++--+-+--	2~	.1936	5	.0478	6	.0707
(1445) +-+--+-++-+-	7	.2017	4	.0473	7	.0716
(63) +++++++------	4~	.1988	9	.0502	8	.0717
(603) ++-++-+--+--	19~	.2268	16	.0537	9	.0763
(1370) +-+-+-+--+-+	16	.2189	11	.0511	10	.0763
(634) ++-++-----+-+	-4	.2733	-10	.0659	-10	.0965
(1118) +-+++-+----+	-8	.2715	-18	.0654	-9	.0965
(377) +++-+----++-	-10	.2709	-4	.0669	-8	.0966
(1145) +-+++----++-	-28	.2655	-11	.0659	-7	.0967
(238) +++--+---+-+	-85	.2572	-32	.0646	-6	.0967
(970) ++----++-+-+	-60	.2608	-41	.0645	-5	.0967
(442) +++--+---+-+	-19	.2672	-37	.0646	-4	.0969
(437) +++--+--+-+-	-1	.2747	-12	.0658	-3	.0973
(221) ++++--+---+-	-6	.2727	-9	.0661	-2	.0987
(1889) +---+--++++-	-7	.2725	-2	.0670	-1	.1001
"Average" Sequence**		.2511		.0610		.0889

*Positive (negative) numbers denote position with respect to smallest (largest) $m_1(d)$, $m_1'(d)$, or $m_1''(d)$. Tied positions are indicated by ~.

**The values listed are $E_0 m_1(d)$, $E_0 m_1'(d)$, $E_0 m_1''(d)$.

TABLE 6-76

TOP TEN AND BOTTOM TEN SCAN SEQUENCES RANKED ACCORDING TO $m_j''(d)$ = AVERAGE OF $\frac{\hat{C}^{Rk}(\omega_s', d)}{\theta_B}$

Scan Sequence d(n)	μ(d) Rank*	μ(d) Value	μ'(d) Rank*	μ'(d) Value	μ"(d) Rank*	μ"(d) Value
(1365) +-+-+-+-+-+-	-1	1.0100	-1	.2838	-1	.4048
(1386) +-+-+--+-+-+	-2~	.7292	-9	.2212	-64	.2327
(1197) +-+-+-+--+-	-11~	.6715	-22	.2181	-72~	.2228
(1638) +--+-+--+-+-	-4~	.7082	-3	.2356	-62	.2376
(1737) +--+--+-+-+-	-7~	.6832	-7	.2242	-46	.2513
(819) ++--+-+--+--	-4~	.7082	-2	.2362	-81	.2174
(1446) +-+--+-+-+-	-6	.6901	-15	.2178	-72~	.2228
(63) ++++++------	-2~	.7292	-4	.2333	-63	.2347
(683) ++-++-+--+--	-60~	.6084	-41	.1964	-26	.2546
(1370) +-+-+-+--+-+	-10	.6754	-29	.2049	-75	.2204
(634) ++-++----+-+	21~	.4448	15	.1415	50	.1805
(1118) +-+++-+----+	12	.4264	6	.1291	31	.1784
(377) +++-+---++-	11	.4233	13	.1383	3~	.1738
(1146) +-+++---+-+-	19	.4438	30	.1477	27~	.1779
(238) +++--+---+	36	.4667	36	.1503	9	.1752
(970) ++---++-+-+	16	.4406	26	.1467	33	.1786
(442) +++-+---+-+	4	.4032	5	.1288	67	.1847
(437) +++-+--+-+-	34	.4634	24	.1463	110~	.1973
(221) ++++-+---+-	17	.4425	16	.1416	14	.1757
(1009) +---+-++++-	15	.4383	25	.1463	27~	.1779
"Average" Sequence**		.5388		.1727		.2090

*Positive (negative) numbers denote position with respect to smallest (largest) μ(d), μ'(d), or μ"(d). Tied positions are indicated by ~.

**The values listed are $E_0\mu(d)$, $E_0\mu'(d)$, $E_0\mu''(d)$.

TABLE 6-8a

TOP TEN AND BOTTOM TEN SCAN SEQUENCES RANKED ACCORDING TO $\mu(d)$ = MAXIMUM VALUE OF $|D(\omega_s' T_s)|$

Scan Sequence d(n)	$m_1(d)$		$m_1'(d)$		$m_1''(d)$	
	Rank*	Value	Rank*	Value	Rank*	Value
(347) ++++-+-+----	-11	.2708	-38	.0645	-49	.0933
(474) +++-----+-+	-2~	.2746	-1	.0672	-25	.0944
(237) ++++---+--+-	-2~	.2746	-5	.0669	-59	.0927
(442) +++--+---+-+	-19	.2672	-37	.0646	-4	.0969
(1761) +---+---++++-	-22~	.2665	-14	.0657	-40	.0936
(732) ++-+---+---++	-22~	.2665	-40	.0645	-57	.0930
(366) +++-+--+---+	-12~	.2704	-31	.0649	-83	.0916
(573) ++-+++----+-	-12~	.2704	-3	.0670	-51	.0931
(874) ++---+--+-+-	-39	.2643	-114	.0618	-84	.0915
(708) ++-+-+----++	-57	.2612	-34	.0646	-54	.0930
(1370) +-+-+-+--+-+	16	.2189	11	.0511	10	.0763
(468) +++---++---	6	.2008	13	.0531	15	.0774
(924) ++---+---++	13~	.2158	35	.0562	24	.0799
(1737) +---+--++-+-	13~	.2158	7	.0493	5	.0701
(1445) +-+---+++--	7	.2017	4	.0473	7	.0716
(1638) +--++--+--+	2~	.1936	2	.0456	4	.0700
(819) ++--++--+--	2~	.1936	5	.0470	6	.0707
(63) +++++------	4~	.1908	9	.0502	8	.0717
(1386) +-+-+--+-+	4~	.1908	3	.0462	2	.0679
(1365) +-+-+-+-+-	1	.1665	1	.0386	1	.0597
"Average" Sequence**		.2511		.0610		.0889

*Positive (negative) numbers denote position with respect to smallest (largest) $m_1(d)$, $m_1'(d)$, or $m_1''(d)$. Tied positions are indicated by ~.

**The values listed are $E_0 m_1(d)$, $E_0 m_1'(d)$, $E_0 m_1''(d)$.

TABLE 6-86

TOP TEN AND BOTTOM TEN SCAN SEQUENCES RANKED ACCORDING TO $\mu(d)$ = MAXIMUM VALUE OF $|D(\omega'_s T_s)|$ (Cont.)

Scan Sequence d(n)	$\mu(d)$ Rank*	$\mu(d)$ Value	$\mu'(d)$ Rank*	$\mu'(d)$ Value	$\mu''(d)$ Rank*	$\mu''(d)$ Value
(347) +++-+-+--+--	1	.3992	2	.1239	19	.1762
(474) +++--+-+-+	2~	.3994	1	.1212	66	.1845
(237) ++++--+--+-	2~	.3994	3	.1278	22	.1767
(442) +++--+--+-+	4	.4032	5	.1288	67	.1847
(1761) +--+--++++-	5~	.4050	7	.1320	25~	.1778
(732) ++-+-+--++	5~	.4050	4	.1286	35	.1789
(366) +++-+-+---+	7~	.4075	9	.1335	48	.1804
(573) ++-+++---+-	7~	.4075	11	.1347	7	.1748
(874) ++--+-+-+-+	9	.4080	12	.1354	52	.1809
(700) ++-+-+---++	10	.4105	10	.1337	15	.1757
(1370) +-+-+-+--+-+	-10	.6754	-29	.2049	-75	.2204
(455) +++--++++--	-9	.6812	-6	.2256	-76	.2202
(924) ++---+++--++	-7~	.6832	-5	.2277	-61	.2436
(1737) +--+-++-++-	-7~	.6832	-7	.2242	-46	.2513
(1445) +-+--+++-+-	-6	.6901	-15	.2178	-72~	.2228
(1638) +--++-++--+	-4~	.7082	-3	.2356	-62	.2376
(819) ++-+++--++--	-4~	.7082	-2	.2362	-81	.2174
(63) ++++++------	-2~	.7292	-4	.2333	-63	.2347
(1386) +-+-+--+-+-+	-2~	.7292	-9	.2212	-64	.2327
(1365) +-+-+-+-+-+-	-1	1.0000	-1	.2838	-1	.4048
"Average" Sequence**		.5388		.1727		.2090

*Positive (negative) numbers denote position with respect to smallest (largest) $\mu(d)$, $\mu'(d)$, or $\mu''(d)$. Tied positions are indicated by ~.

**The values listed are $E_0\mu(d)$, $E_0\mu'(d)$, $E_0\mu''(d)$.

TABLE 6-9a

TOP TEN AND BOTTOM TEN SCAN SEQUENCES RANKED ACCORDING TO $\mu'(d)$ = MAXIMUM VALUE OF $\rho|D(\omega_s' T_s) H_\Delta(\omega_s')|$

Scan Sequence d(n)	$m_1(d)$		$m_1'(d)$		$m_1''(d)$	
	Rank*	Value	Rank*	Value	Rank*	Value
(474) ++++---+--+-+	-2~	.2746	-1	.0672	-25	.0944
(347) +++-+-+--+--	-11	.2708	-30	.0645	-49	.0933
(237) ++++---+--+-	-2~	.2746	-5	.0669	-59	.0927
(732) ++-+--+---++	-22~	.2665	-40	.0645	-57	.0930
(442) +++--+---+-+	-19	.2672	-37	.0646	-4	.0969
(1110) +-+++-+----+	-8	.2715	-18	.0654	-9	.0965
(1761) +--+---+++-	-22~	.2665	-14	.0657	-40	.0936
(629) ++-++--+-+-	-9	.2715	-21	.0652	-36	.0937
(366) +++-+--+---+	-12~	.2704	-31	.0649	-83	.0916
(708) ++-+-+----++	-57	.2612	-34	.0646	-54	.0930
(825) ++--++---+--	26~	.2293	47	.0573	39	.0826
(1386) +-+-+--+-+-+	4~	.1988	3	.0462	2	.0679
(910) ++---++---+	15	.2163	33	.0558	41	.0829
(1737) +--+--+-+-+-	13~	.2158	7	.0493	5	.0701
(455) +++---++---	6	.2008	13	.0531	15	.0774
(924) ++---+---++	13~	.2158	35	.0562	24	.0799
(63) +++++------	4~	.1988	9	.0502	8	.0717
(1638) +--++--++--+	2~	.1936	2	.0456	4	.0708
(819) ++--++--++--	2~	.1936	5	.0478	6	.0707
(1365) +-+-+-+-+-+-	1	.1665	1	.0306	1	.0597
"Average" Sequence**		.2511		.0610		.0889

*Positive (negative) numbers denote position with respect to smallest (largest) $m_1(d)$, $m_1'(d)$, or $m_1''(d)$. Tied positions are indicated by ~ .

**The values listed are $E_0 m_1(d)$, $E_0 m_1'(d)$, $E_0 m_1''(d)$.

TABLE 6-9b

TOP TEN AND BOTTOM TEN SCAN SEQUENCES RANKED ACCORDING TO $\mu'(d)$ = MAXIMUM VALUE OF $\rho|D(\omega_s' T_s) H_\Delta(\omega_s')|$

Scan Sequence d(n)	$\mu(d)$		$\mu'(d)$		$\mu''(d)$	
	Rank*	Value	Rank*	Value	Rank*	Value
(474) +++---+--+-+	2~	.3994	1	.1212	66	.1845
(347) +++-+-+--+--	1	.3992	2	.1239	19	.1762
(237) +++++--+--+-	2~	.3994	3	.1278	22	.1767
(732) ++-+--+---++	6	.4050	4	.1286	35	.1789
(442) +++--+---+-+	4	.4032	5	.1288	67	.1847
(1118) +-+++-+----+	12	.4264	6	.1291	31	.1784
(1761) +--+--++++-	5~	.4050	7	.1320	25~	.1778
(629) ++-++---+-+-	14	.4354	8	.1321	43	.1798
(366) +++-+--+---+	7~	.4075	9	.1335	48	.1804
(700) ++-+-+----++	10	.4105	10	.1337	15	.1757
(825) ++--++--++--	-38~	.6612	-10	.2207	-71	.2251
(1386) +-+-+--+-+-+	-2~	.7292	-9	.2212	-64	.2327
(910) ++---++---+	-13	.6707	-8	.2232	-70	.2252
(1737) +--+--++-++-	-7~	.6832	-7	.2242	-46	.2513
(455) +++---++----	-9	.6812	-6	.2256	-76	.2202
(924) ++---+---++	-7~	.6832	-5	.2277	-61	.2436
(63) +++++------	-2~	.7292	-4	.2333	-63	.2347
(1638) +--++--+--+	-4~	.7082	-3	.2356	-62	.2376
(819) ++--++--+--	-4~	.7082	-2	.2362	-81	.2174
(1365) +-+-+-+-+-+-	-1	1.0000	-1	.2838	-1	.4048
"Average" Sequence**		.5388		.1727		.2090

*Positive (negative) numbers denote position with respect to smallest (largest) $\mu(d)$, $\mu'(d)$, or $\mu''(d)$. Tied positions are indicated by ~.

**The values listed are $E_0\mu(d)$, $E_0\mu'(d)$, $E_0\mu''(d)$.

TABLE 6-10a

TOP TEN AND BOTTOM TEN SCAN SEQUENCES RANKED ACCORDING TO $\mu''(d)$ = MAXIMUM VALUE OF $\dfrac{\hat{\epsilon}^{pk}(\omega_s', d)}{\theta_B}$

Scan Sequence d(n)	$m_1(d)$		$m_1'(d)$		$m_1''(d)$	
	Rank*	Value	Rank*	Value	Rank*	Value
(1086) +-++++------+	-61~	.2605	-44	.0644	-97	.0907
(287) ++++--++----	73~	.2437	-125	.0615	81	.0861
(377) +++-+----++-	-10	.2709	-4	.0669	-8	.0966
(1478) +-+---+++--+	-99	.2556	-69	.0634	-47	.0934
(461) +++---++--+-	-16	.2681	-7	.0665	-18	.0952
(574) ++-+++------+	-26	.2663	-15	.0657	-15	.0956
(573) ++-+++----+-	-12~	.2704	-3	.0678	-51	.0931
(183) ++++-+--+---	-34~	.2647	-57	.0639	-104	.0904
(238) +++---+---+	-85	.2572	-32	.0646	-6	.0967
(317) +++-++----+-	-27	.2655	-23	.0652	-17	.0952
†(1369) +-+-+-+--++-	76	.2441	43	.0572	76	.0859
†(1381) +-+-+--++-+-	77	.2443	44	.0572	82	.0861
†(1393) +-+-+---+++-	71	.2434	110	.0607	-107	.0903
†(1477) +-+---+++-+-	92	.2478	102	.0603	46	.0835
†(1489) +-+---+-+++-	97	.2489	81	.0595	113	.0884
†(1873) +---+-+-+++-	67	.2427	88	.0598	67	.0852
†(938) ++---+-+-+-+	54	.2408	67	.0586	89	.0866
†(683) ++-+-+-+---	33	.2332	29	.0556	29	.0882
†(1366) +-++-+-+--+	17	.2247	12	.0524	22	.0795
(1365) +-+-+-+-+-+-	1	.1665	1	.0386	1	.0597
"Average" Sequence**		.2511		.0610		.0889

*Positive (negative) numbers denote position with respect to smallest (largest) $m_1(d)$, $m_1'(d)$, or $m_1''(d)$. Tied positions are indicated by ~.

**The values listed are $E_0 m_1(d)$, $E_0 m_1'(d)$, $E_0 m_1''(d)$.

†Twelve additional sequences (#'s 343,349,373,469,686,698,746,853,1117,1141,1237,1333) are tied with these sequences in rank according to $\mu''(d)$.

TABLE 6-10b

TOP TEN AND BOTTOM TEN SCAN SEQUENCES RANKED ACCORDING TO $\mu''(d)$ = MAXIMUM VALUE OF $\dfrac{\hat{\varepsilon}^{pk}(\omega'_s, d)}{\theta_B}$

Scan Sequence d(n)	$\mu(d)$ Rank*	$\mu(d)$ Value	$\mu'(d)$ Rank*	$\mu'(d)$ Value	$\mu''(d)$ Rank*	$\mu''(d)$ Value
(1086) +-++++------+	64~	.4887	66~	.1590	1	.1724
(207) ++++--++----	82~	.4987	104	.1660	2	.1732
(377) +++-+----++-	11	.4233	13	.1383	3~	.1738
(1478) +-+---+++--+	18	.4427	28	.1473	3~	.1738
(461) +++---++--+-	20	.4444	32	.1479	5~	.1745
(574) ++-+++------+	32	.4616	33	.1487	5~	.1745
(573) ++-+++----+-	7~	.4075	11	.1347	7	.1748
(183) +++-+--+---	100~	.5047	74	.1604	8	.1748
(238) +++---++---+	36	.4667	36	.1503	9	.1752
(317) +++-++----+-	23	.4451	18	.1424	10	.1752
†(1369) +-+-+-+--++-	-17~	.6667	-58~	.1892	-2~	.2698
†(1381) +-+-+--++-+-	-17~	.6667	-58~	.1892	-2~	.2698
†(1393) +-+-+---+++-	-17~	.6667	-58~	.1892	-2~	.2698
†(1477) +-+---+++-+-	-17~	.6667	-58~	.1892	-2~	.2698
†(1489) +-+---+-+++-	-17~	.6667	-58~	.1892	-2~	.2698
†(1873) +---+-+-+++-	-17~	.6667	-58~	.1892	-2~	.2698
(938) ++---+-+-+-+	-17~	.6667	-57	.1892	-2~	.2698
(683) ++-+-+-+-+--	-17~	.6667	-54	.1904	-2~	.2698
(1366) +-+-+-+-+--+	-14	.6682	-43	.1949	-2~	.2698
(1365) +-+-+-+-+-+-	-1	1.0000	-1	.2838	-1	.4048
"Average" Sequence**		.5388		.1727		.2090

*Positive (negative) numbers denote position with respect to smallest (largest) $\mu(d)$, $\mu'(d)$, or $\mu''(d)$. Tied positions are indicated by ~.

**The values listed are $E_0\mu(d)$, $E_0\mu'(d)$, $E_0\mu''(d)$.

†There are 12 additional sequences (#'s 343, 349, 373, 469, 686, 698, 746, 853, 1117, 1141, 1237, 1333) which are tied with these sequences in all 3 categories.

From Tables 6-5a, 6-6a, 6-7b, and 6-8b, we observe the nearly total correlation between the rankings according to the two measures $m_1(d)$, $m_1'(d)$ [and also between $\mu(d)$, $\mu'(d)$]. Only four of the sequences listed in those four tables have ranks under the pairs of corresponding measures which differ by more than ten places. This results from the fact that the motion averaging factor $|D(\omega_s' T_s)|$ is symmetric around $\omega_s' = \frac{\pi}{T_s}$ and the first-order error characteristic $|H_\Delta(\omega_s')|$ is very flat in the region $\frac{\pi}{T_s} < \omega_s' < \frac{2\pi}{T_s}$ and it serves to justify the attention we gave to studying the motion averaging factor by itself.

The correlation between these simpler performance measures and the measures based on the actual error amplitudes is also good though not astounding. The differences arise from the non-negligible contribution of the higher order terms in the error expansion (6-65) for the chosen multipath amplitude (-3 dB).

A most striking example of this effect can be seen in the case of the 21 scan sequences which are tied for second worst "worst case" error performance while ranking outside the bottom ten under both of the simpler "worst case" averaging measures (see Tables 6-10a, b). Each of these scan sequences is characterized by a motion averaging function $|D(\omega_s' T_s)|$ with a global maximum or near-maximum at half the scan rate ($\omega_s' = \frac{\pi}{T_s}$). At this particular value of the scalloping frequency the error series (6-65) may be summed to yield a closed form expression because $D[(m+1)\omega_s' T_s]$ is either zero or $D(\pi)$ depending on whether m is odd or even. The result is

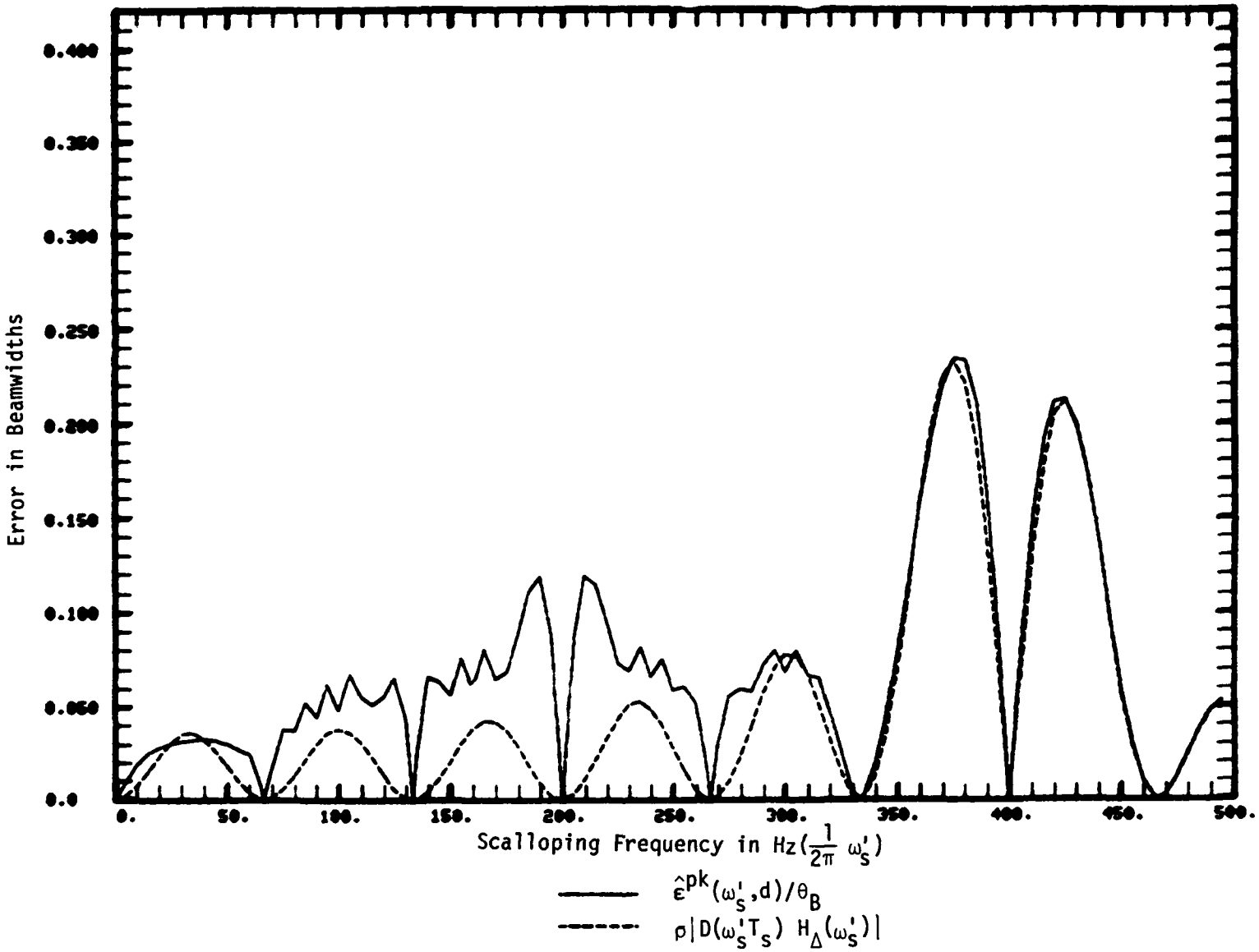

Fig. 6-22. Motion averaged errors for proposed scan sequence $d_p(n)$ (++++++------).

$$\hat{\varepsilon} = \frac{\rho\theta_B}{|\cos\theta_c|} \; \mathrm{Re} \; \frac{\rho H_\Delta(\frac{\pi}{T_s})e^{-j\phi}D(\pi)}{1-[\rho H_\Sigma(\frac{\pi}{T_s})e^{-j\phi}]^2}$$

The error amplitude $\hat{\varepsilon}^{pk}(\frac{\pi}{T_s}, d)$ is obtained by maximizing $|\hat{\varepsilon}|$ over ϕ, yielding

$$\hat{\varepsilon}^{pk}(\frac{\pi}{T_s}, d) = \frac{\theta_B}{|\cos\theta_c|} \; \frac{\rho|H_\Delta(\frac{\pi}{T_s})\, e^{-j\phi}D(\pi)}{1-[\rho H_\Sigma(\frac{\pi}{T_s})e^{-j\phi}]^2}$$

Thus, the effect of the constructive superposition of all the even-numbered terms in the error series (6-65) is to increase the error amplitude by a factor of $\{1-[\rho H_\Sigma(\frac{\pi}{T_s})]^2\}^{-1} = 1.426$ over the first-order approximation. From the definition (6-66) of $D(\alpha)$ we see that the value of $|D(\pi)|$ must be drawn from the finite set $\{1 - \frac{4K}{2N}, 0 < k < \frac{N}{2}\}$. The alternating scan sequence $d_A(n)$ and its sign reversed counterpart $-d_A(n)$ are the only sequences with $|D(\pi)| = 1$. There are $2N^2$ sequences (in $\frac{2N(N+1)}{4}$ distinct equivalence classes) with the next highest value, $|D(\pi)| = 1 - \frac{4}{2N}$. The sequences listed in Tables 6-10a, b as tied for second worst "worst case" error performance among sequences of length $2N = 12$ are a selection of $\frac{2N(N+1)}{4}$ sequences from different equivalence classes whose motion averaging functions satisfy $|D(\pi)| = \frac{2}{3}$.

Figures 6-22 and 6-23 show the peak and first order motion averaged errors for the final and initial scan sequences. We see that the principal effect of the higher order terms is to increase the errors at subharmonics of the frequency which yields the peak errors. Figures 6-24 to 6-27 show the peak and first order motion averaged errors for several other scan sequences

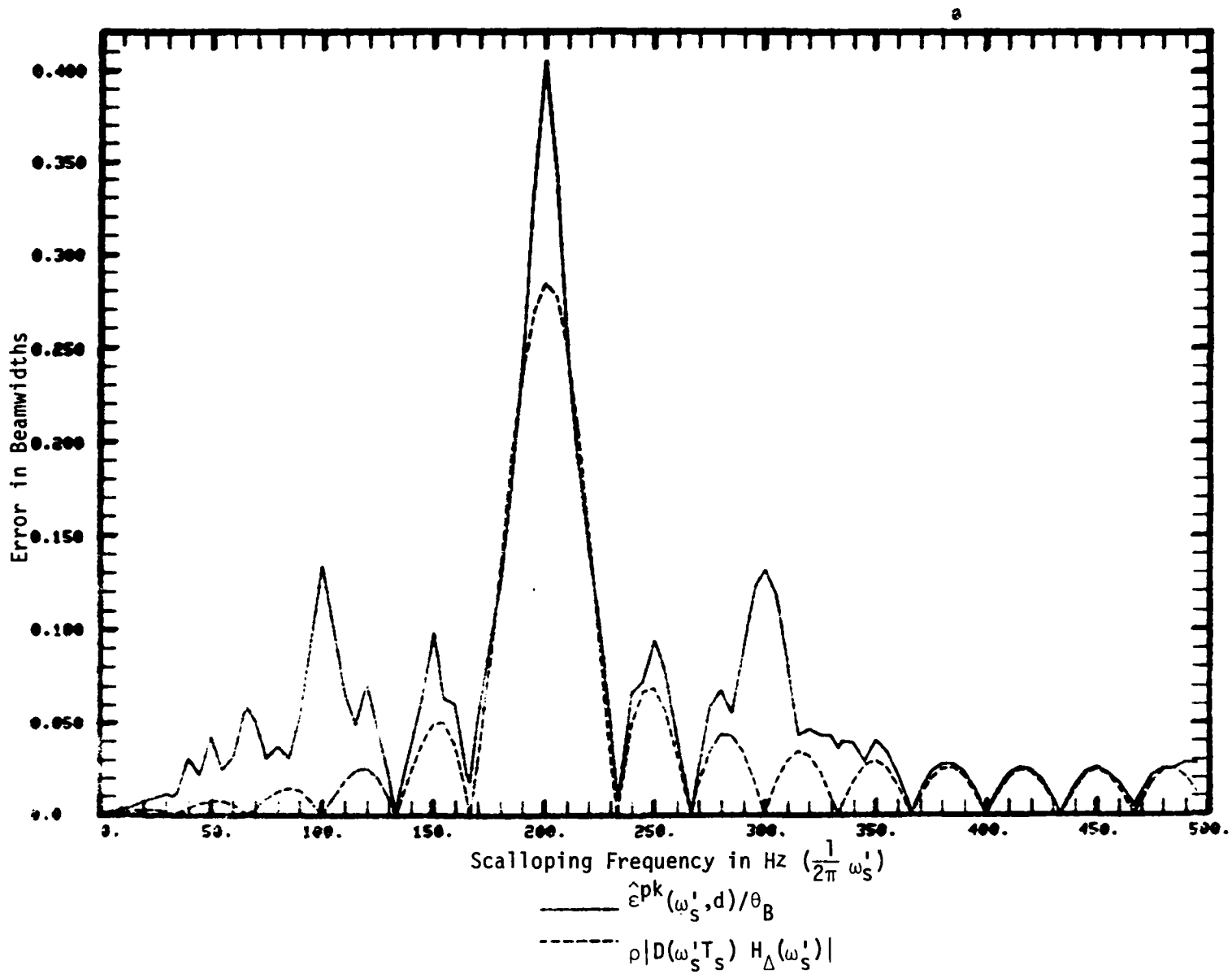

Fig. 6-23. Motion averaged errors for alternating scan sequence $d_A(n)$ (+-+-+-+-+-+-).

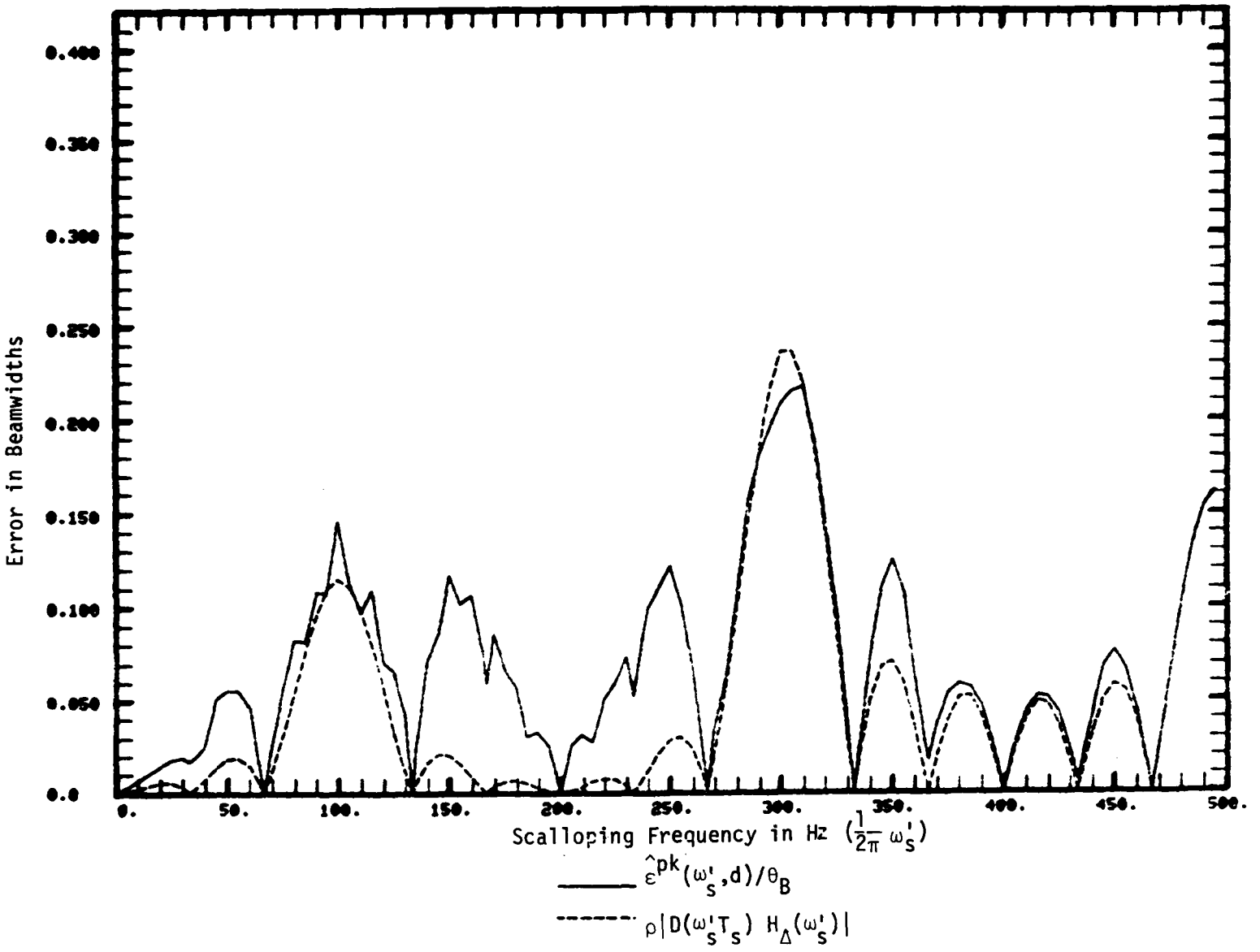

Fig. 6-24. Motion averaged errors for scan sequence #819 (++--++--++--).

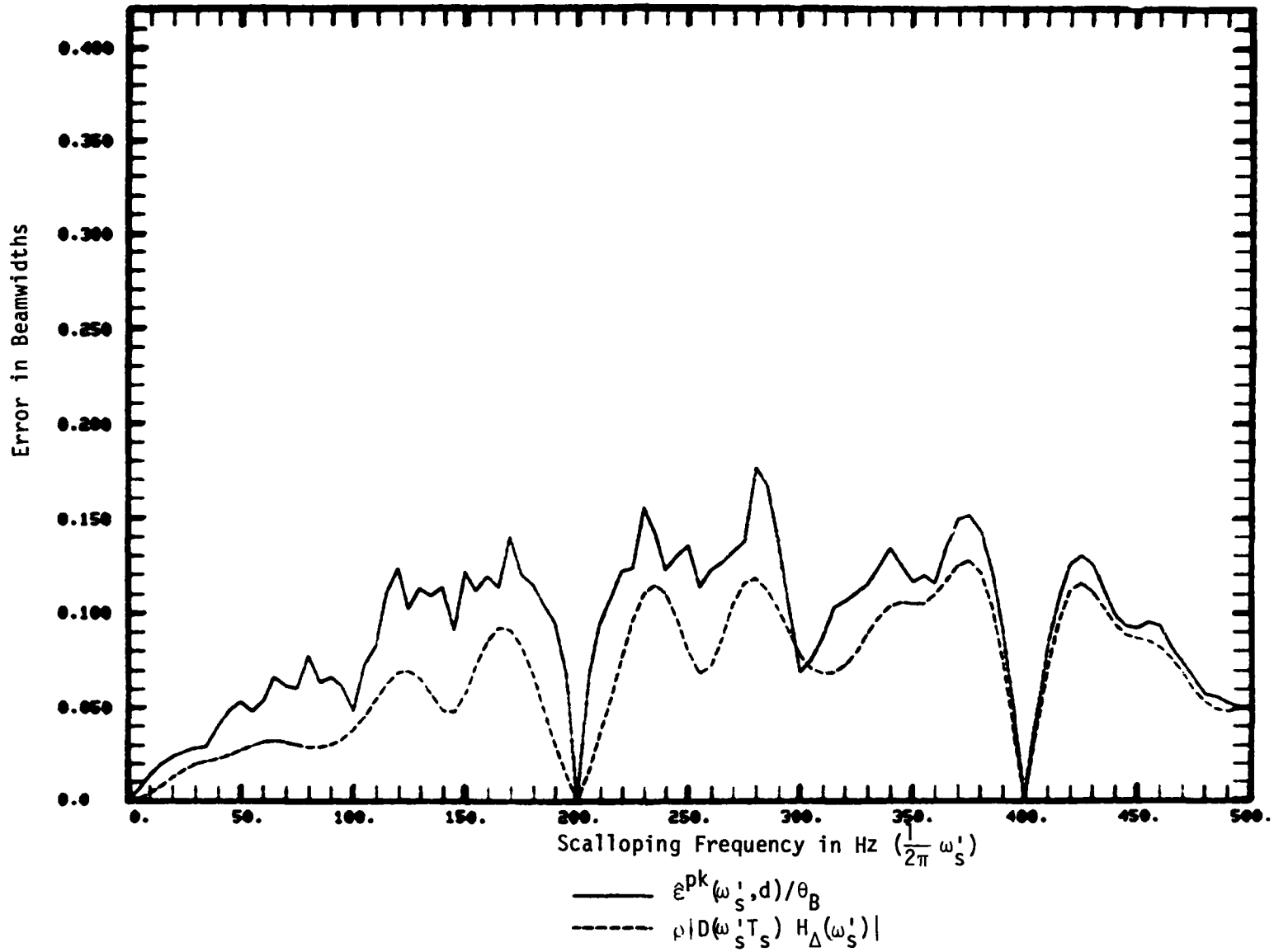

Fig. 6-25. Motion averaged errors for scan sequence #237 (++++---+--+-).

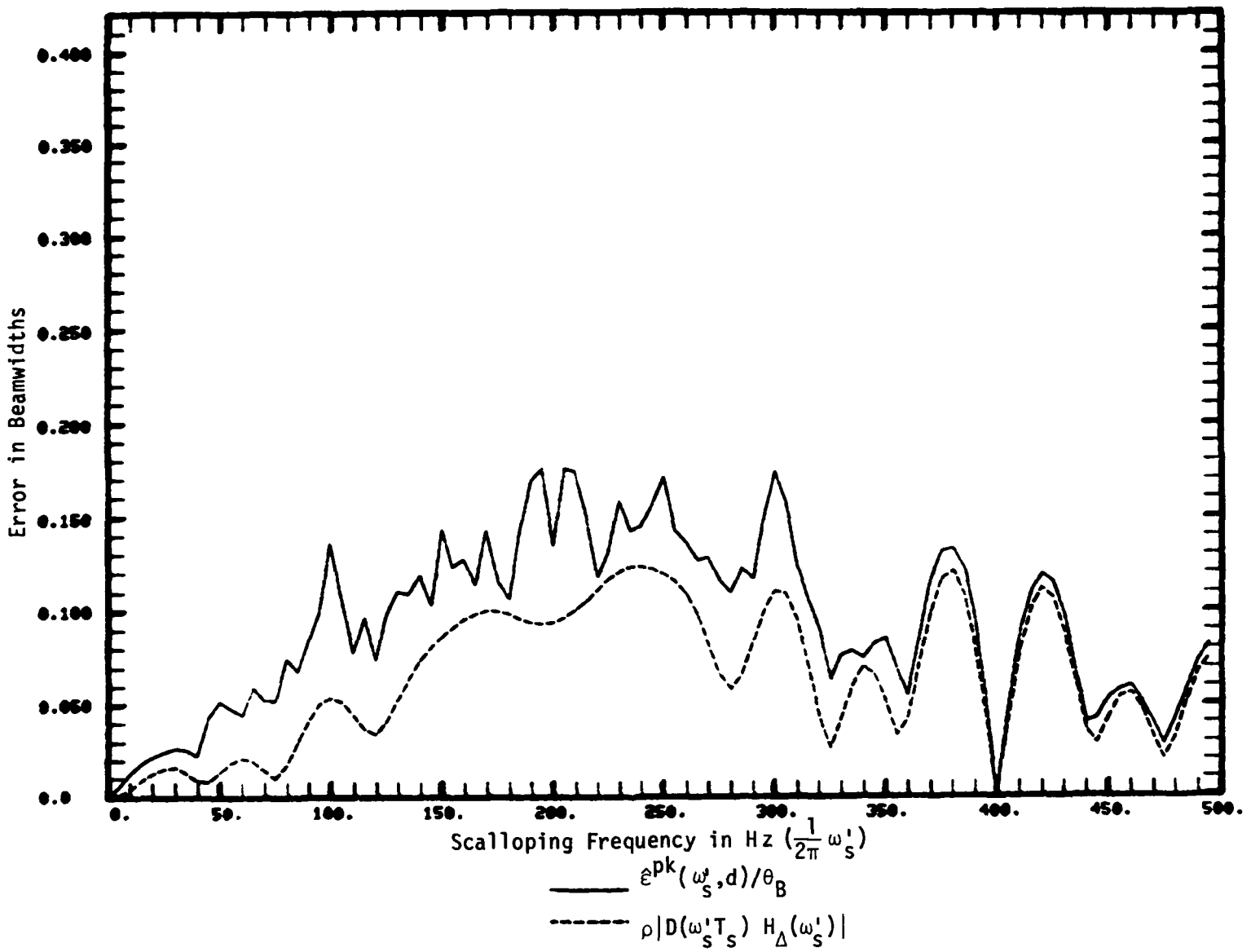

Fig. 6-26. Motion averaged errors for scan sequence #347 (+++-+-+--+--).

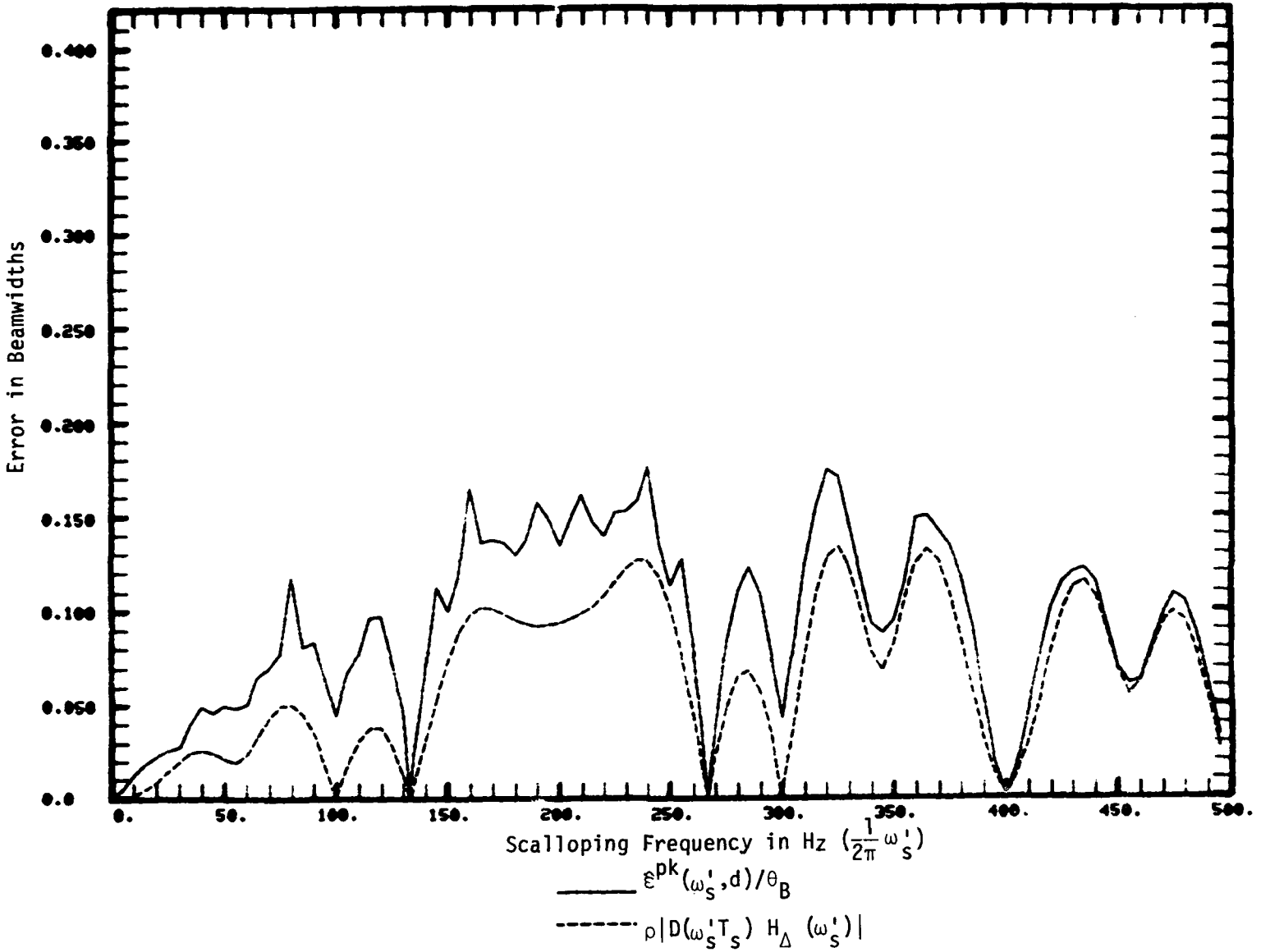

Fig. 6-27. Motion averaged errors for scan sequence #700 (++-+-+----++).

from Tables 6-5 to 6-10 which have more of the nature of a pseudorandom sequence. For these sequences, the shape of the peak error curve more closely follows that of the first order error.

5. The Effect of Non-Negligible Multipath Time Delays

In all of the previous sections we have assumed that the last term in equations (6-39) for the reference phase ϕ'_{jn} is negligible because the reference array offset frequency ω_{off} is very small relative to the usual relative multipath time delays. Occasionally we have modeled scenarios for which the relative multipath time delay is long enough (on the order of several microseconds) to cause a sizable phase correction. In these cases we have noticed that the error vs. scalloping frequency curve is somewhat modified from the predicted curve based on zero time delay.

In general the effect of nonzero time delays cannot be summarized neatly. However, we shall discuss a partial characterization of the effect for a certain class of symmetric scan sequences which includes both the proposed sequence $d_P(n)$ and the alternating scan sequence $d_A(n)$ defined earlier.

If the last term in (6-39) is retained throughout all the analysis of Section 3, we see that the effect is to replace the motion averaging function $D[(m+1)\omega'_s T_s]$ in (6-65) with a function $D'[(m+1)\omega'_s T_s;\ \omega_{off}\tau]$, where

$$\tau \equiv \tau'_l - \tau'_U = \text{relative multipath delay} \tag{6-108}$$

and $D'(\alpha;\beta)$ is defined by

$$D'(\alpha;\beta) = \frac{1}{2}\,[D^{+}(\alpha)\,e^{j\beta/2} - D^{-}(\alpha)\,e^{-j\beta/2}] \tag{6-109}$$

$$D^{+}(\alpha) \equiv \frac{1}{N} \sum_{\substack{n: \\ d(n) = +1}} e^{-j(n-1)\alpha} \tag{6-110}$$

$$D^{-}(\alpha) \equiv \frac{1}{N} \sum_{\substack{n: \\ d(n) = -1}} e^{-j(n-1)\alpha} \tag{6-111}$$

In terms of $D^{+}(\alpha)$, $D^{-}(\alpha)$, the motion averaging function for zero time delay is expressed as

$$D(\alpha) = \frac{1}{2}\,[D^{+}(\alpha) - D^{-}(\alpha)] \tag{6-112}$$

We shall consider only symmetric scan sequences with the property that $D^{+}(\alpha)$, $D^{-}(\alpha)$ are phase-shifted versions of each other, i.e.,

$$D^{-}(\alpha) = e^{-j\gamma(\alpha)}D^{+}(\alpha) \tag{6-113}$$

for some real function $\gamma(\alpha)$. It is easy to show that this relation is true for any of the 2^N sequences (in 2^{N-1} distinct equivalence classes) which reproduce themselves under the successive operations of sequence reversal followed by sign reversal, i.e., sequences satisfying $d(n) = -d(2N+1)$, $n = 1, \ldots, 2N$.

Under the assumption (6-113) the modified motion averaging function $D'(\alpha;\beta)$ factors as follows:

$$D'(\alpha;\beta) = \frac{1}{2} D^{+}(\alpha) \left[e^{j\beta/2} - e^{-j\left(\gamma(\alpha) + \beta/2\right)}\right] \tag{6-114}$$

or

$$|D'(\alpha;\beta)| = |D^{+}(\alpha)| \sqrt{[1 - \cos(\gamma(\alpha) + \beta)]/2} \tag{6-115}$$

Similarly

$$|D(\alpha)| = |D^{+}(\alpha)| \sqrt{[1 - \cos \gamma(\alpha)]/2} \tag{6-116}$$

Thus, both motion averaging functions can be expressed as a product of two spectra: the first one is unaffected by the time delay and the second one is simply shifted with respect to the variable $\gamma(\alpha)$ by an amount $-\beta = -\omega_{off}\tau$. If the phase difference $\gamma(\alpha)$ is linear, $\gamma(\alpha) = \gamma\alpha$ where γ is a constant, the shift of the second factor translates directly into an undistorted shift of $-\beta/\gamma = -\omega_{off}\tau/\gamma$ with respect to α. The shifted factor is generally not symmetric around $\alpha = 0$ and hence the reference scalloping error curves are no longer identical for positive and negative scalloping frequencies.

The motion averaging functions for the proposed sequence $d_P(n)$ and the alternating scan sequence $d_A(n)$ both satisfy (6-113) with linear phase shifts $\gamma(\alpha) = \gamma_P\alpha \equiv$ and $\gamma(\alpha) = \gamma_A\alpha \equiv \alpha$ respectively. The spectra $|D_P^{+}(\alpha)|, |D_P^{+}(\alpha)|$ of the positive parts of $d_P(n)$, $d_A(n)$ are calculated as*

$$|D_P^{+}(\alpha)| = \left|\frac{\sin \frac{N\alpha}{2}}{N \sin \frac{\alpha}{2}}\right| \tag{6-117}$$

---

*$|D^{+}P(\alpha)| = 1$ for $\alpha = 0, \pm 2\pi, \pm 4\pi, \ldots$

$|D^{+}A(\alpha)| = 1$ for $\alpha = 0, \pm \pi, \pm 2\pi, \ldots$

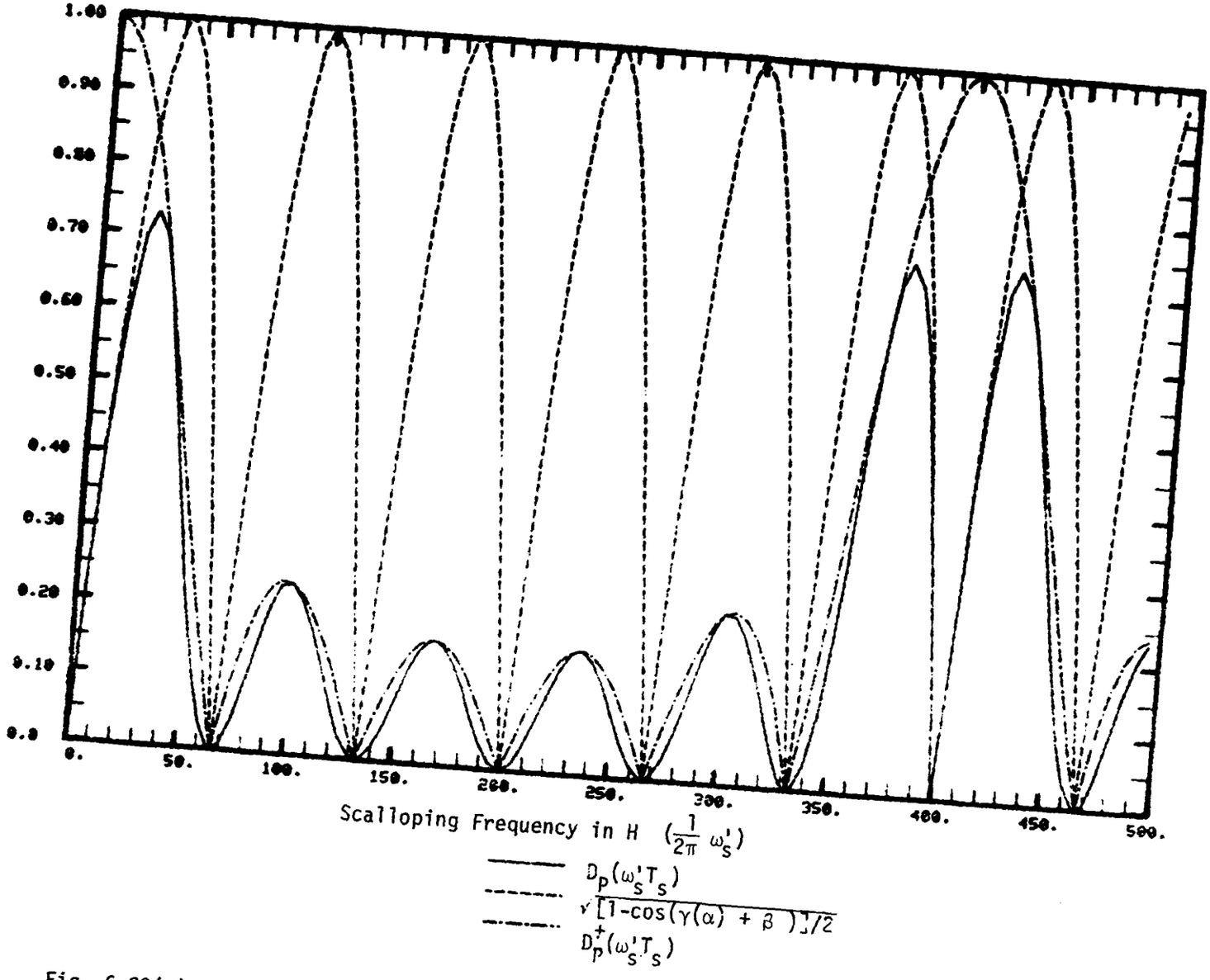

Fig. 6-28(a). Motion averaging factor for proposed scan sequence $d_p(n)$ (++++++------) with zero multipath time delay.

$$|D_p^+(\alpha)| = \left|\frac{\sin N\alpha}{N \sin \alpha}\right| \tag{6-118}$$

In Figs. 6-28a and 6-29a we plot the two factors $\sqrt{[1 - \cos(\delta(\alpha) + \beta)]/2}$ and $\sqrt{[1 - \cos \gamma(\alpha)]/2}$ together with the resulting zero delay averaging function $|D(\alpha)|$, for the proposed and alternating scan sequences of length 2N = 12. In Figs. 6-28b and 6-29b we plot the corresponding spectra when the time delay is $\tau = \pi/\omega_{off} = 6$ μsec (equivalent to a path length difference of about one nautical mile). We note that, at this particular value of the multipath time delay, the motion averaging function for the alternating scan sequence is exactly shifted by half a period; the large grating lobe at 200 Hz (half scan rate) is replaced by identical ones at 0 Hz and 400 Hz. The effect of the 6 μsec time delay on the motion averaging function for the proposed scan sequence is more complicated to describe. Each of the minor lobes in the original spectrum is divided into two smaller lobes as a result of the time delay; however, the double major lobe around 400 Hz (scan rate) in the original spectrum is merged to form a larger single major lobe at 400 Hz. In fact, we observe that the motion averaging function for the alternating scan sequence if the multipath delay is 6 μsec. Thus, we conclude that the reference scalloping error curves may be dramatically affected by very large relative multipath time delays.

C. Array Scalloping

In this section, we consider the case where all reflected signals components are angularly well out of beam, but that the multipath frequencies $d(n)\,\omega_{ikn}$ are within the main lobe of H_Σ or H_Δ for some n by virtue of a large

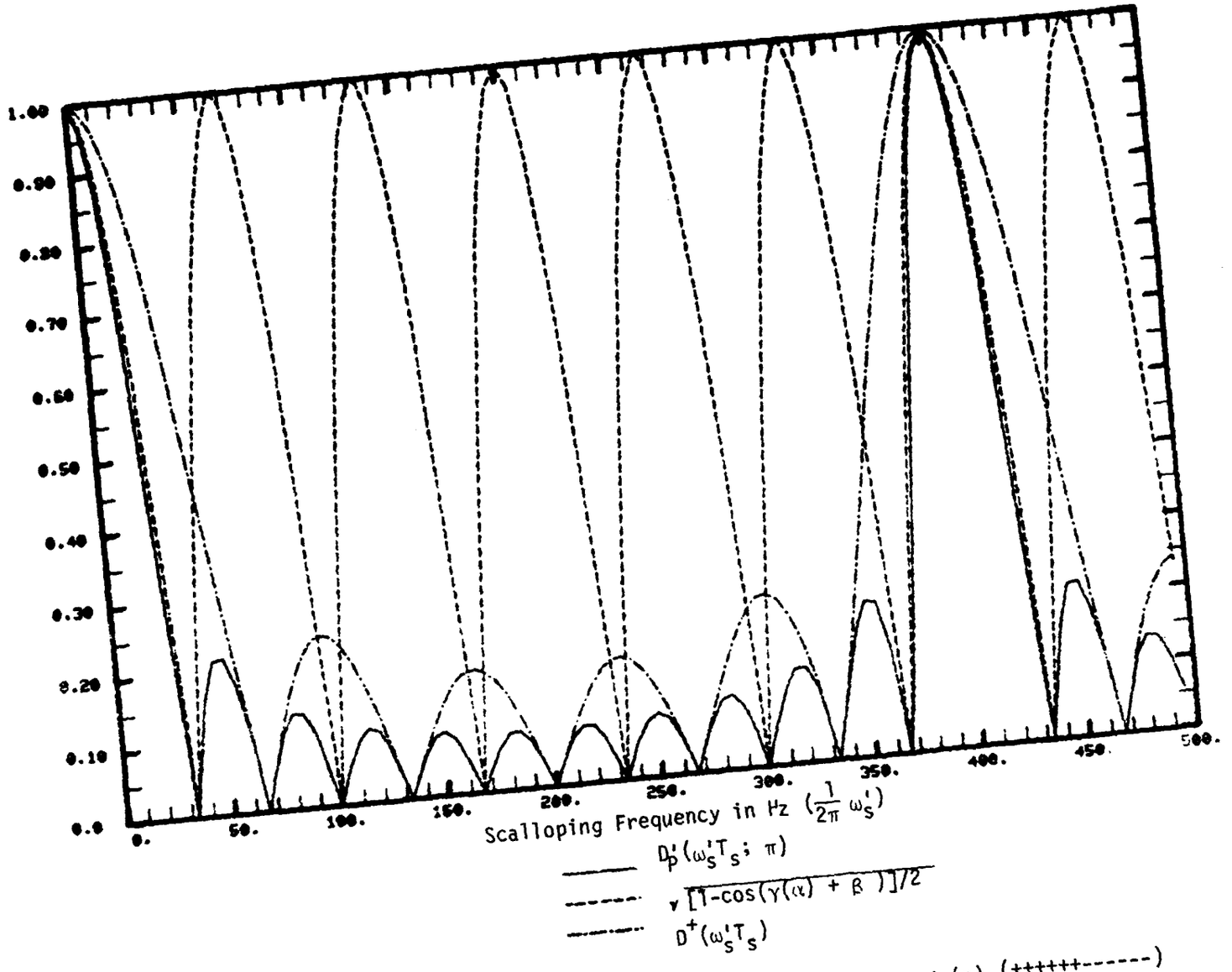

Fig. 6-28(b). Motion averaging factor for proposed scan sequence $d_p(n)$ (++++++------) with multipath time delay of 6 μsec.

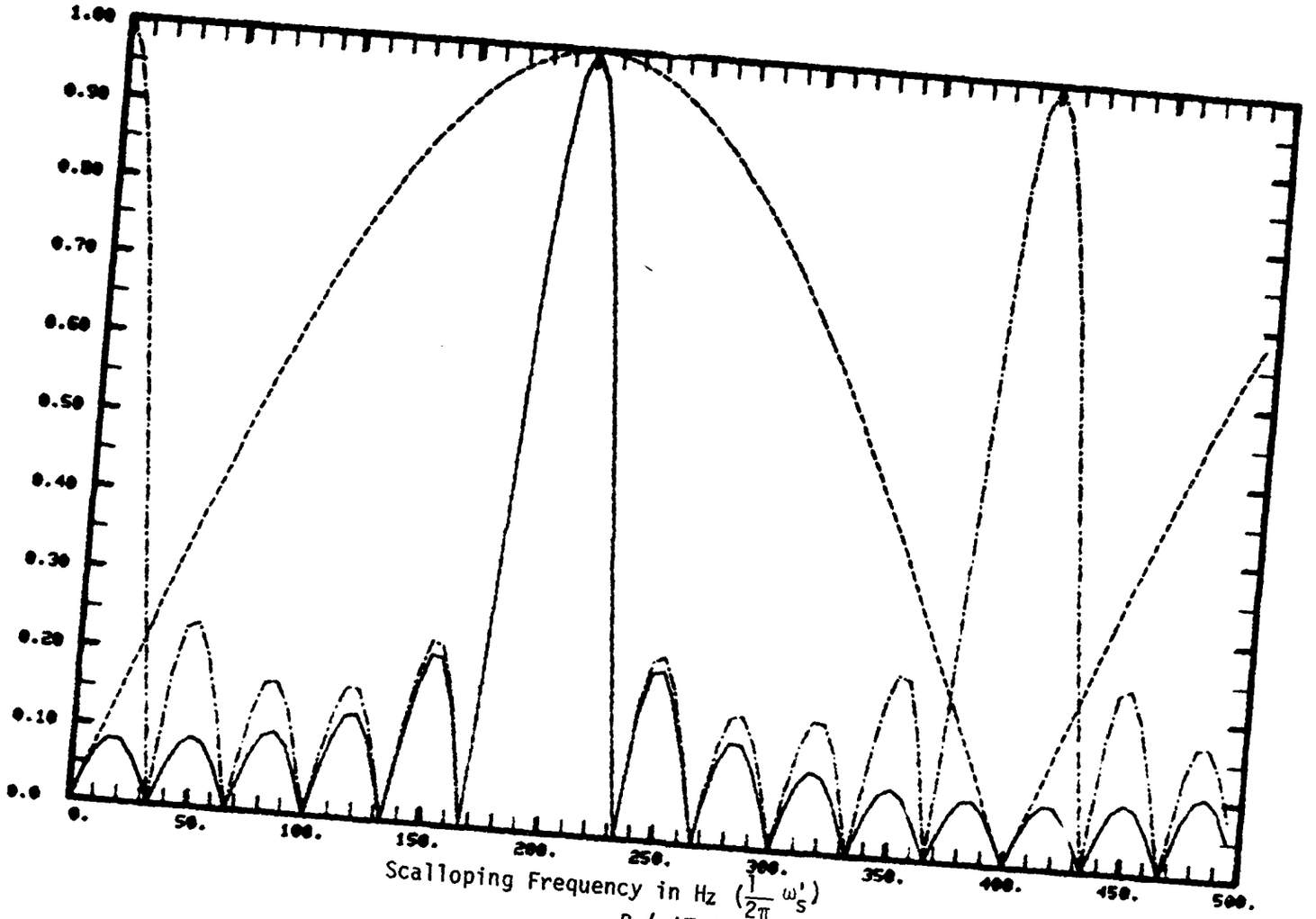

$D_A(\omega_s' T_s)$

$\sqrt{[1-\cos(\gamma(\alpha)+\beta)]/2}$

$D_A^+(\omega_s' T_s)$

Fig. 6-29(a). Motion averaging factor for alternating scan sequence $d_A(n)$ (+-+-+-+-+-+-) with zero multipath time delay.

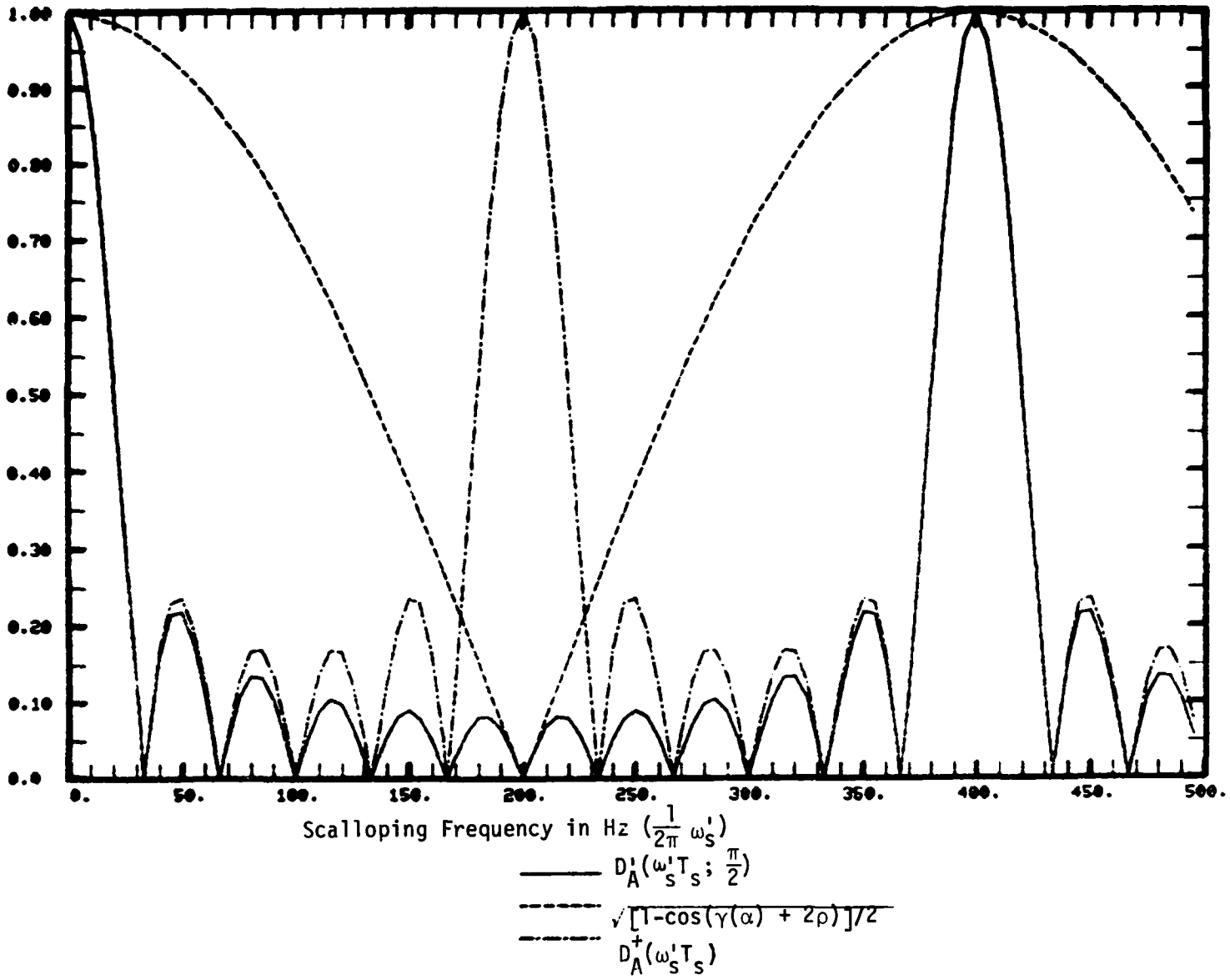

Fig. 6-29(b). Motion averaging factor for alternating scan sequence $d_A(n)$ (+-+-+-+-+-+-) with multipath time delay of 6 μsec.

scalloping frequency. A first order expansion of the equations (6-1) and (6-2) analogous to that used above then yields for the array multipath error

$$\varepsilon_1^a(n) = \frac{\theta_B}{\cos\theta_c} \sum \tilde{\rho}_i H_\Delta [\omega_i^a + d(n)\omega_i^s] \cos [\tilde{\phi}_i + \omega_i^s(n-1)T_s] \qquad (6\text{-}119)$$

Equation (6-119) is analogous to the first-order static error expression (II. 4-34). The multipath angle frequencies ω_i^a are shifted from their static values by the array scalloping frequencies ω_i^s, the direction of the shift depending on the scan direction. The sign alternation in (6-119) arises from the fact that the coding factor changes sign when the commutation direction changes while ω_s is unchanged.

The effect of the scalloping frequency is thus to yield the effective DMLS separation angles of

$$\tilde{\theta}_{sep}(i) \approx \theta_m(i) - \theta_c \pm \omega_s/K$$

$$\triangleq \theta_{sep}(i) \pm \omega_s/K \qquad (6\text{-}120)$$

The question then is whether values of ω_s may be expected in representative airport environments are large enough to cause $\tilde{\theta}_{sep}(i)$ to be inbeam.

This question was examined in some detail in a study on Doppler reference scalloping [41]. In Fig. 6-30, we summarize the geometry for scalloping frequency computations. For a fixed β_d, the two rays

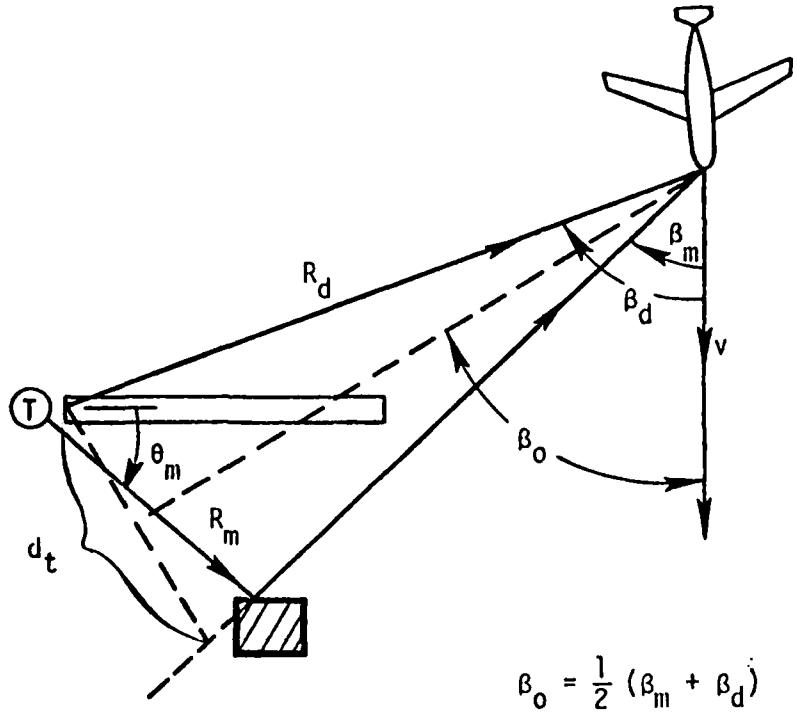

$$\beta_o = \frac{1}{2}(\beta_m + \beta_d)$$

$$\Delta\beta = \beta_m - \beta_d$$

$$f_s = \frac{v}{\lambda}(\cos\beta_d - \cos\beta_m)$$

$$= \frac{v}{\lambda}[\cos(\beta_o - 0.5\Delta\beta) - \cos(\beta_o + 0.5\Delta\beta)] \approx \frac{v}{\lambda}\Delta\beta \sin\beta_o$$

where $\Delta\beta$ is in radians

$$\Delta\beta \approx d_t/R_d$$

Fig. 6-30. Scalloping frequency geometry.

$\beta_m = \pm \cos^{-1}(\cos \beta_d - v_a \delta\theta_{sep}/v_s \cos \theta_d)$ define scatterer locations with a separation angle shift of $\delta\theta_{sep}$.

To determine the "dynamic inbeam" region, one must find appropriate intersections of the β_m rays with θ_m rays such that

$$|\theta_m \pm \delta\ \theta_{sep}| \approx 1.5 \text{ beamwidths}$$

This process is illustrated in Fig. 6-31. We see that the dynamic inbeam region extends well outside the static boundary for scatterers near or beyond the threshold, and in fact, includes building areas as well as taxiways. Consequently, in DMLS siting or critical areas determination, one might need to consider a much larger area of the airport surface than was the case with the other systems.

In the next sections, we consider in greater depth what the nature of the error would be for a single multipath signal in a dynamic situation, including motion averaging effects.

1. Analytical Formulation

We consider the case of a single multipath signal with the simplified notation of eqs. (2-60) to (2-62). Moreover, we assume that:

(a) the multipath is angularly out of beam, i.e., $H_\Delta(\omega_i^a)$ and $H_\Sigma(\omega_i^a)$ are negligible

and

(b) the scalloping frequencies ω_s and ω_s' are large enough so that the reference scalloping contributions are out of beam, i.e., $H_\Delta(\omega_s)$ and $H_\Sigma(\omega_s)$ are negligible.

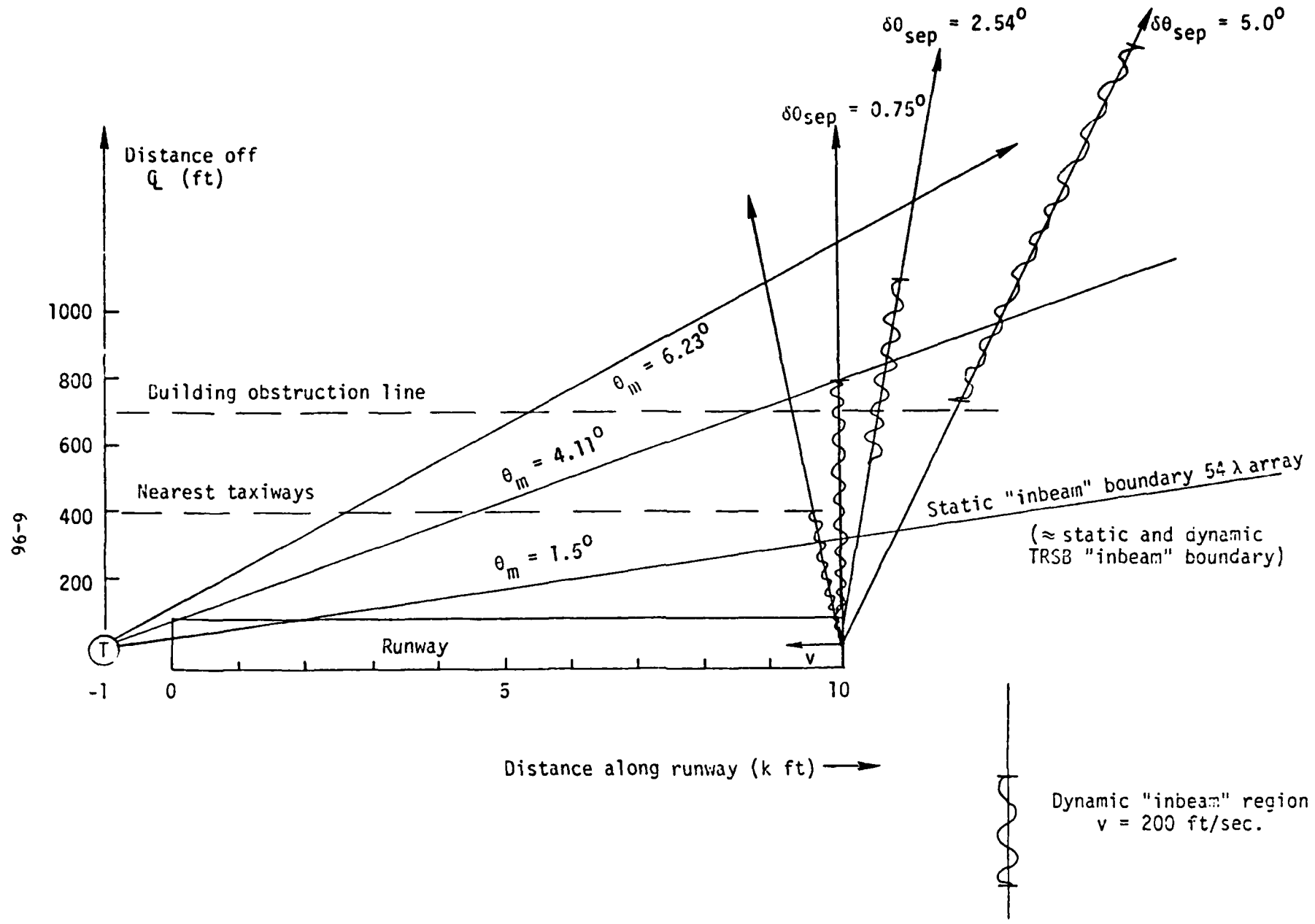

Fig. 6-31. Dynamic DMLS "inbeam" multipath region for reflected array x direct reference component.

Given these two assumptions plus those used in the preceding section, it is straightforward to show that the single scan error is given by

$$\varepsilon(n) = \frac{\theta_B}{\cos\theta_c} \quad \mathrm{Re}\ \{\rho H_\Delta[\omega_{sep} + d(n)\ \omega_s] \frac{e^{-j\phi_n}}{1+\rho e^{-j\phi_n} H_\Sigma\ [\omega_{sep} + d(n)\ \omega_s]} \tag{6-121}$$

where

$$\phi_n = \phi - \omega_s\ (n-1)\ T_s \tag{6-122}$$

Given assumptions (a) and (b), it follows that H_Δ and H_Σ in (6-121) can be non-negligible only for one value of d(n). Consequently, the motion averaged error is then

$$\hat{\varepsilon} = \frac{\rho\ \theta_B}{\cos\theta_c} \mathrm{Re}\ \{H_\Delta\ (\tilde{\omega}_{sep})\ \sum\ [-\rho H_\Sigma(\tilde{\omega}_{sep})]^m e^{-jm\phi}\ D^{\pm}\ [(m+1)\omega_s T] \tag{6-123}$$

where $\tilde{\omega}_{sep} = \omega_{sep} \pm \omega_s$ and $D^+(\alpha)$, $D^-(\alpha)$ are defined in (6-110) and (6-111) with the choice of sign corresponding to the $\tilde{\omega}_{sep}$ which is closest to the direct signal frequency. $D^{\pm}(\alpha)$ always has a peak at $\alpha = 2\pi$, but may have

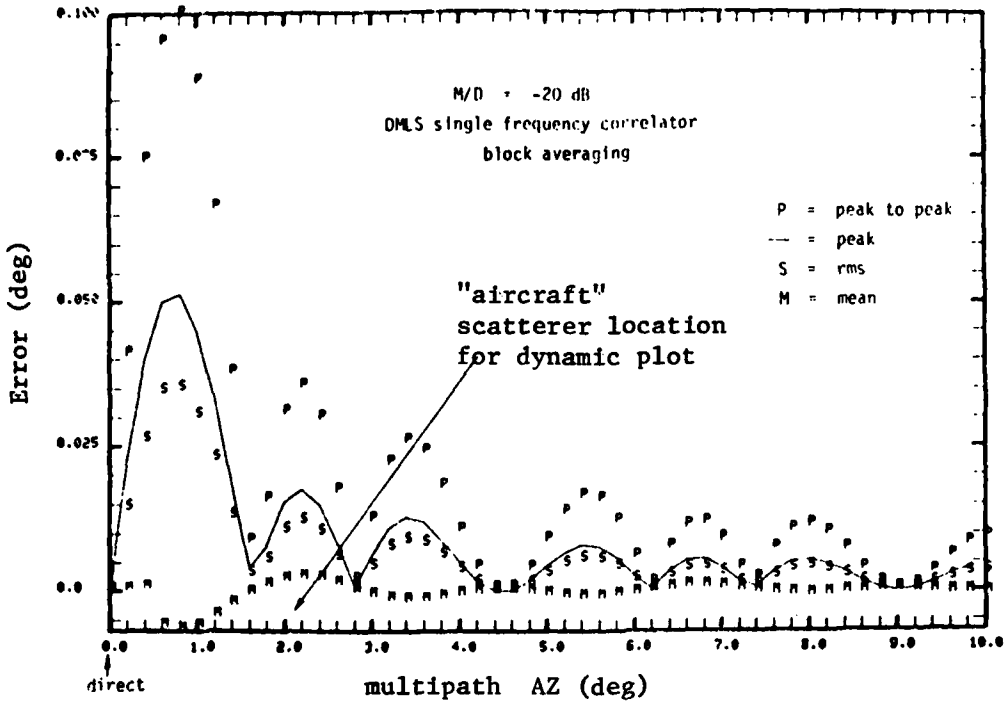

(a)

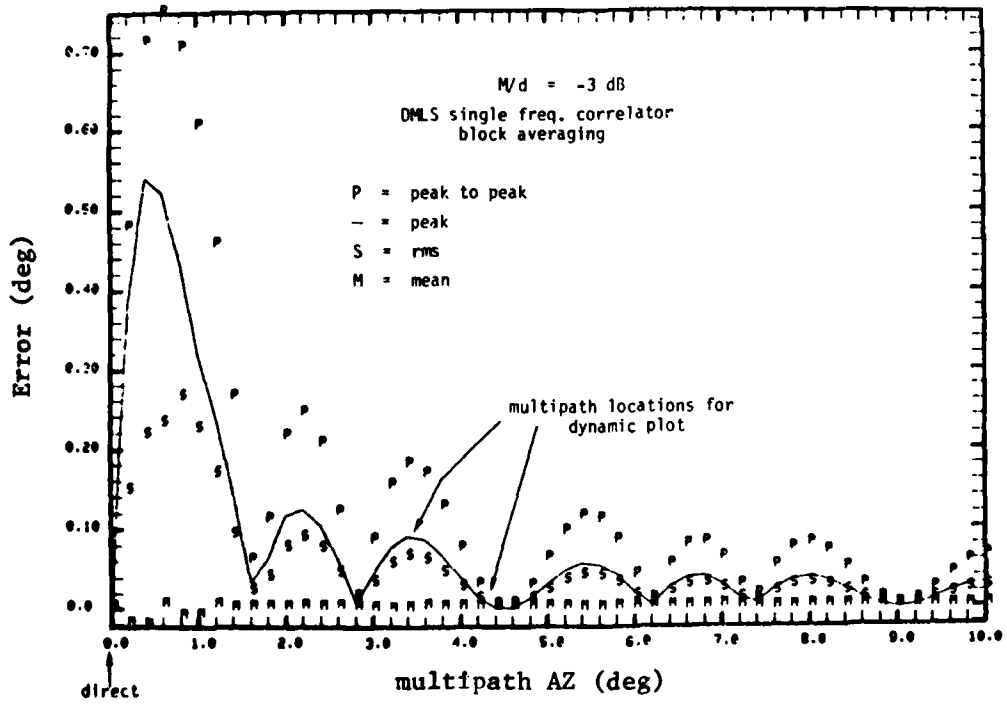

(b)

Fig. 6-32. DMLS single frequency static error vs. separation angle.

peaks at other frequencies as well [e.g., π for $d_A(n)$ of eq. (6-73)]. Thus, the error function has peaks at frequencies which are multiples of the subharmonics of the scan rate, i.e.,

$$f_s(k,n) = k/nT_s \tag{6-124}$$

Since N is a small number for azimuth (e.g., 6 for a 54λ array and 3 for a 108λ array), there is considerable overlap of the various contributions. Thus, the most attractive approach to quantitatively assessing the phenomena was by direct numerical evaluation of eq. (6-121).

2. Single Component Simulation Results

In this section, we present results of computer simulations of Doppler array scalloping error as a function of the characteristics for a single multipath component. The DMLS results here used the $d_A(n)$ scan format proposed for 54λ azimuth arrays, centerline emphasis on the reference array and a single frequency correlation algorithm.

A common way of characterizing the dynamic multipath performance for a given system is to plot the error as a function of scalloping rate for fixed multipath level and separation angle. The resulting error needs to be averaged over the rf phase between direct and multipath signals since at C-band this phase is generally not at the control of the system designer. To provide some perspective on the dynamic results, we show in Fig. 6-32 plots of static error vs. separation angle.

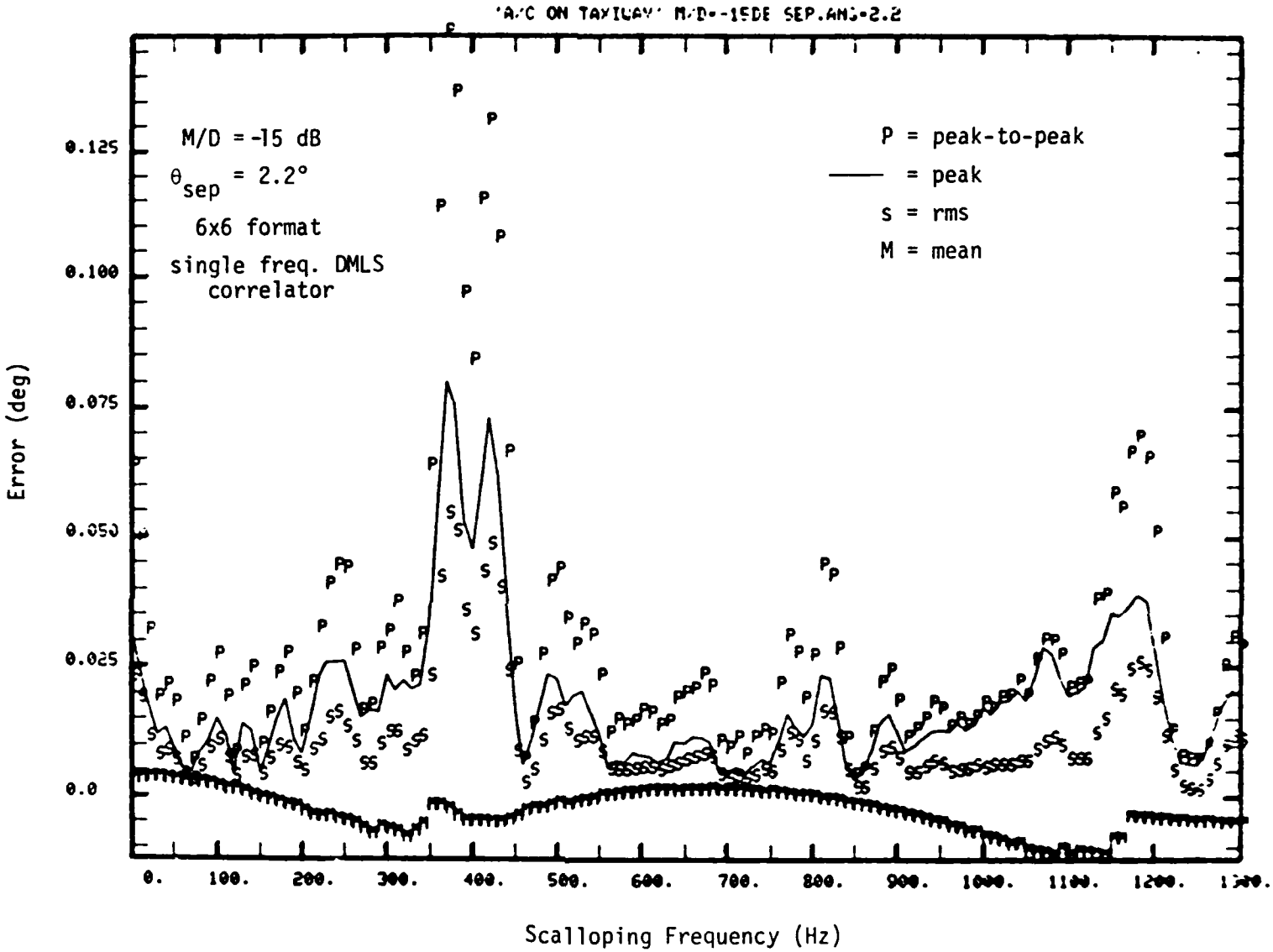

Fig. 6-33. DMLS dynamic error for out-of-beam azimuth multipath.

In Fig. 6-33, we plot the error as a function of scalloping frequency for multipath characteristics that might arise from a large aircraft on a taxiway, near the threshold, namely a separation angle of 2.2° (= arc tangent of 450/12000) and a multipath level of -15 dB. We see that peak errors over 0.05° occur near 400 Hz.

In Figs. 6-34 and 6-35, the error is plotted as a function of scalloping frequency for separation angles corresponding to hangar geometries at JFK and at Heathrow Airport. In both cases, we observe large peaks near multiples of the scan rate (400 Hz). However, the peak error still exceeds 0.05° at frequencies between these peaks.

It should be noted that high frequency scalloping rates typically change rather rapidly along the flight path so that one would not expect to remain at an unfavorable frequency for a long time period. Thus, scenario simulations are also necessary to assess the impact of array scalloping on a potential DMLS deployment. One such scenario is presented in Section F.

D. Lateral Diversity

"Conventional" DMLS elevation arrays utilize sequential commutation up (or down) on an array of vertical equispaced elements. As shown in Chapter IV, such a system has an inbeam static multipath rejection characteristic similar to that of TRSB. C. Earp suggested in 1974 [134] that the two source

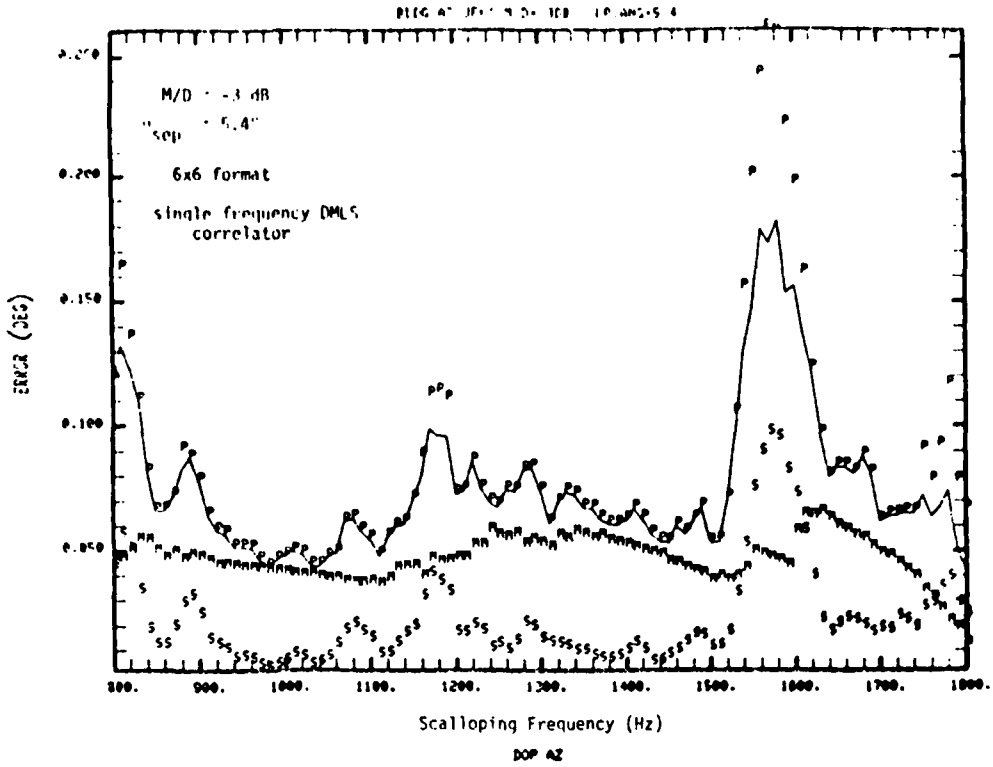

Fig. 6-34.

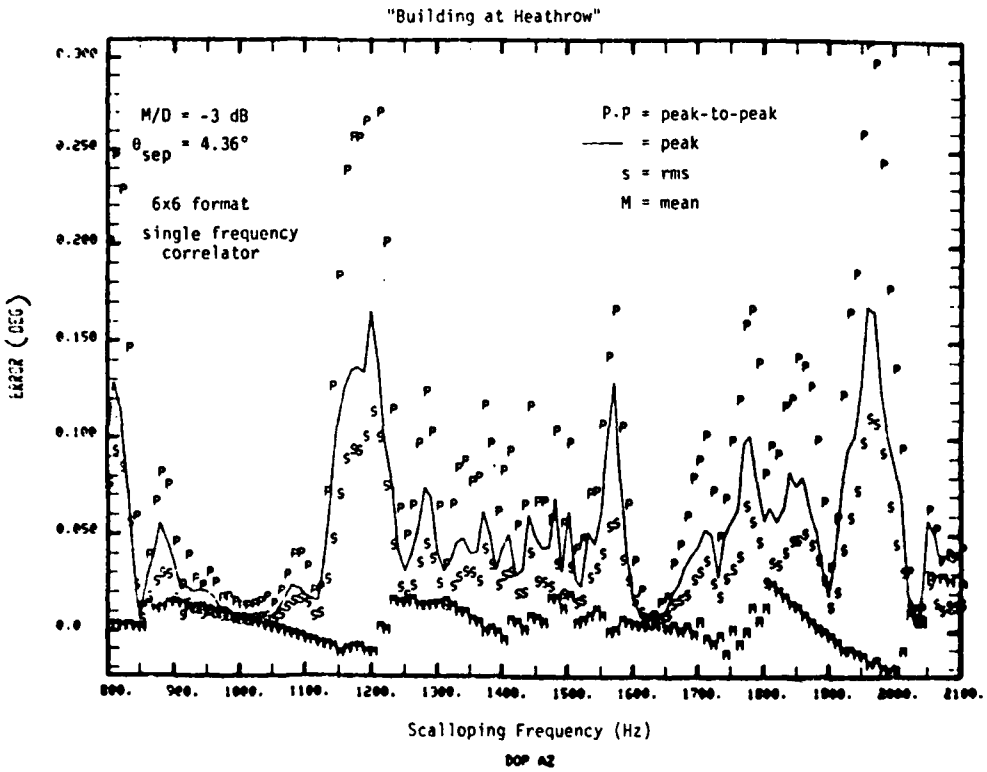

Fig. 6-35.

Figs. 6-34 and 6-35. Dynamic DMLS error vs. scalloping frequency for out-of-beam azimuth multipath.

nature of the DMLS system could be utilized to provide additional protection against inbeam elevation multipath from vertical walls.* The proposed lateral diversity implementation consisted of:

a) a sideband array with elements which are equispaced in height, but have differing lateral displacements;

b) a reference array with lateral displacements corresponding to the sideband displacements; and

c) an element excitation sequence such that, as successively higher (or lower) sideband elements are excited, the radiating reference element has the same lateral displacement as the currently radiating sideband element.

Figure 6-36 shows a simple example of the element excitation sequence that might be utilized on successive scans. We see tnat the sideband and reference elements move sideways in synchronism, during a given scan with the possibility of translating the reference array starting location laterally between scans.

The basic idea behind the array operation in the absence of multipath is identical to that which was utilized in the DMLS commutated reference azimuth array [28, Volume II of this report], namely that the vertical displacement between the radiating elements increases linearly with time. When multipath is present, one must consider the various detector cross products illustrated in Figure 6-37 to determine the net result.

---

*Additionally, it was claimed by C. Earp [134, 141] that simultaneous commutation of the reference and sideband signals could double the effective DMLS aperture. However, this was shown to be incorrect analytically (see Appendix C).

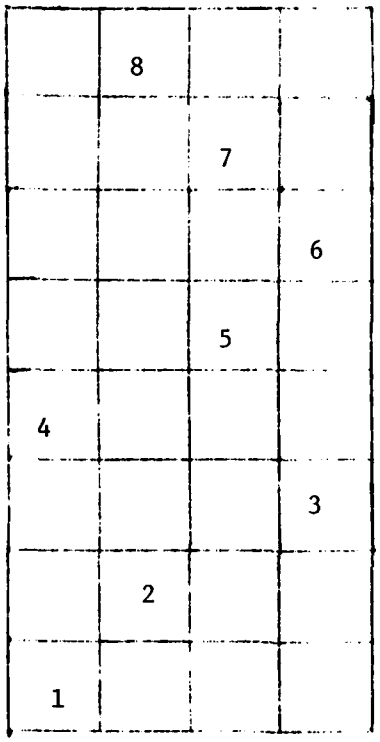

Sideband Array

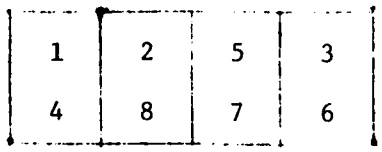

Reference Array

Fig. 6-36. Simple lateral diversity sequence.

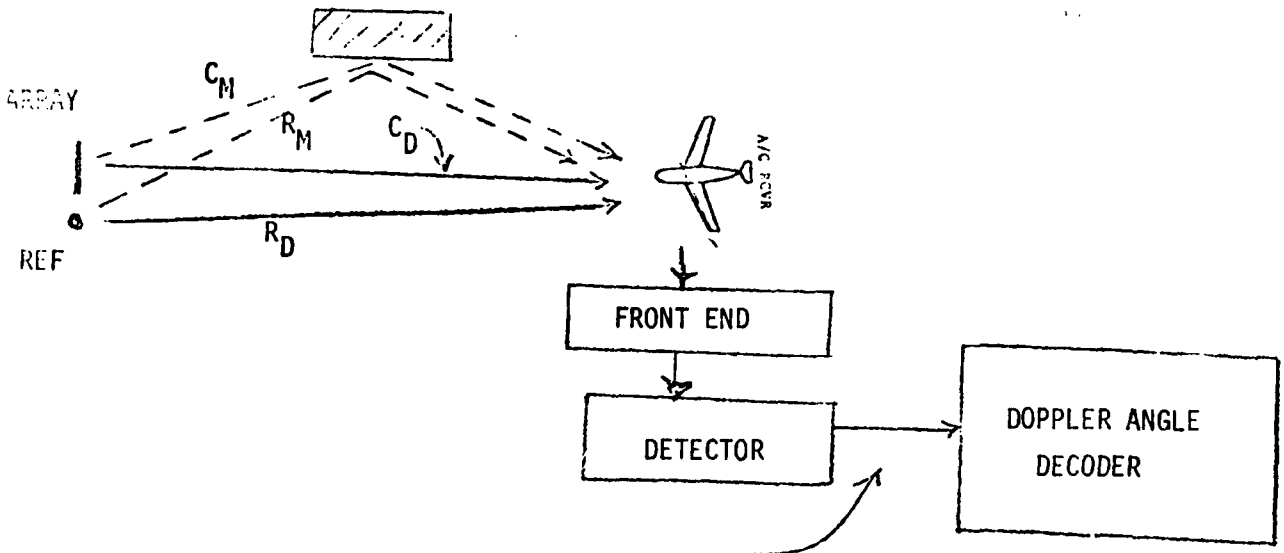

TERMS AT DETECTOR OUTPUT

Desired $C_D R_d$ = Ref. Dir x Arr Dir

Error Sources

$C_M R_D$ = Ref. Dir x Arr M/P

$C_M R_M$ = Ref M/P x Arr M/P

$C_D R_M$ = Ref M/P x Arr Dir

Fig. 6-37. Error components at Doppler angle encoder input for single multipath reflection.

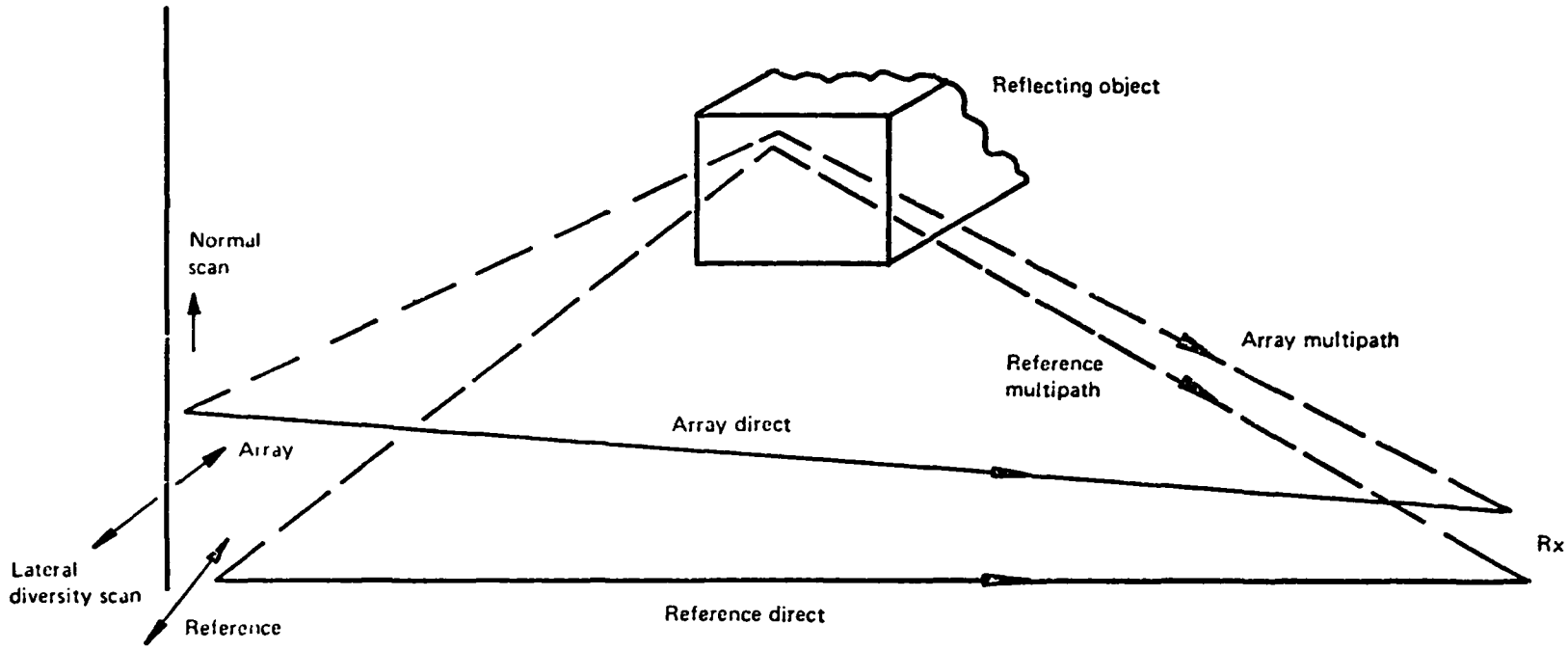

Fig. 6-38. Lateral diversity elevation with reflective object (from [7]).

Let us consider the case of a single vertical reflector such as illustrated in Figure 6-38. The various received signals when the nth element pair is radiating are then:

$$C_D = \exp j[\omega_o t + nk_{dz}\delta_v + k_{dy}\, y(n)\ ] \tag{6-125a}$$

$$C_M = \rho \exp j[(\omega_o + \omega_s)t + nk_{dm}\delta + k_{my}\, y(n)\ \phi_m) \tag{6-125b}$$

$$R_D = \exp j[(\omega_o + \omega_{off})t + k_{dy}\, y'(n) + \tilde{\phi}_d] \tag{6-125c}$$

$$R_M = \rho \exp j[(\omega_o + \omega_s - \omega_{off})t + k_{dy}\, y'(n) + \tilde{\phi}_m] \tag{6-125d}$$

where the wavenumbers are:

$$k_{dz} = 2\pi \sin E_d/\lambda$$

$$k_{dy} = 2\pi \sin \theta_d\ /\lambda$$

$$k_{mz} = 2\pi \sin E_m\ /\lambda$$

$$k_{my} = 2\pi \sin \theta_m\ /\lambda$$

E_d, θ_d = direct signal conical elevation and azimuth

E_m, θ_m = multipath signal conical elevation and azimuth

δ_v = sideband element spacing in elevation plane

$y(n)$ = lateral location of sideband array n^{th} element

$y'(n)$ = lateral location of reference array n^{th} element

= $y(n) + y_o$

ρ = relative multipath level

ϕ_m = sideband array relative phase

ω_s = scalloping frequency

Taking the cross products as indicated in Fig. 6-37, and making the usual approximation that the linear phase increments associated with k_z are equivalent to a sinusoid at the average angular rate, we obtain

$$C_D R_D^* = \exp j\left[(\omega_d + \omega_{off})t + \tilde{\theta} + k_{dy}\, y_o\right] \quad (6\text{-}126a)$$

$$C_D R_M^* = \rho \exp j\left[(\omega_d - \omega_s + \omega_{off})t + \phi(t) - \tilde{\phi}_m + \Delta k\, y_o\right] \quad (6\text{-}126b)$$

$$C_M R_D^* = \rho \exp j\left[(\omega_m + \omega_s + \omega_{off})t - \phi(t) + \phi_m - \Delta k\, y_o\right] \quad (6\text{-}126c)$$

$$C_M R_M^* = \rho^2 \exp j[(\omega_m + \omega_{off})t + \phi_m - \tilde{\phi}_m + k_{my} y_o] \quad (6\text{-}126d)$$

where

$$\phi(t) = \Delta k\ y(n) \text{ for } (n-1)T < t < nT \quad (6\text{-}127)$$

$$\Delta k = k_{dy} - k_{my} \quad (6\text{-}128)$$

Comparing equations (6-126) to (6-128) with the corresponding stationary reference equations (Vol. II, eqs. 3-34, 3-34, 3-52) we observe that the effect of the lateral displacements is to 1) phase modulate the $C_D R_M^*$ and $C_M R_D^*$ cross products and 2) to introduce a scan dependent phase variation ($\Delta k\ y_o$) between the $C_D R_D^*$ and $C_M R_M^*$ cross products. The effects of the phase modulations depend on the horizontal displacement sequence $\{y(n)\}$. Two cases are of particular interest:

1. Pseudorandom Sequence

The initial proposals for lateral diversity [7,134] suggested that the y(n) be a pseudorandom sequence uniformly distributed over the interval (-Ly/2, Ly/2) where Ly is the horizontal aperture width. In this case, the $C_D R_M^*$ and $C_M R_D^*$ terms can be viewed as multilevel digital phase-modulated signals with equidistant, equiprobable phase levels. Glance [135] has shown that the power spectrum of such a signal is given by:

$$G(\omega) \approx \frac{T}{4}\left[\frac{\sin(\omega-\omega_c)T/2}{(\omega-\omega_c)T/2}\right]^2 \left[1-\left(\frac{\sin\frac{\alpha}{2}}{n_h \sin \alpha/2n_h}\right)^2\right] \tag{6-129}$$

$$+ \quad \frac{T}{4}\left(\frac{\sin \alpha/2}{n_h \sin \alpha/2n_h}\right)^2 \left[\frac{\sin(\omega-\omega_c)\, n_v T}{(\omega-\omega_c)\, n_v T/2}\right]^2$$

where $\omega_c = 2\pi f_c$ = nominal frequency

$$\alpha = (k_{dy} - k_{my})\, Ly\, (1-1/n_h) \tag{6-130}$$

n_h = number of lateral positions

n_v = number of vertical positions

The last term in (6-129) represents the spectrum of the signal without lateral diversity while the first term represents the spread spectrum arising from the lateral diversity. The power at the nominal component frequency is thus reduced by approximately 4 dB at $\alpha/2 = \pi/2$, i.e., when

$$|\sin \theta_d - \sin \theta_m| = \lambda/2\, Ly \tag{6-131}$$

For $Ly = 7\lambda$, this corresponds to an angular separation of approximately 4°.

At greater angular separations, the first term in (6-129) dominates. For reasonably large n_v the spread spectrum is approximately flat over the inbeam region, in which case the rms in beam power approximately

$$P_\infty = \rho^2/n_v$$

Thus, n = 32 would yield a 15 dB reduction in multipath level for the given component. The spectrum splatter is increased somewhat since the spread spectrum spectral width is approximately n_v equivalent beamwidths with corresponding sidelobes. However, this increased width is still small relative to the range of received frequencies which must be coped with in any case and hence should not produce significant channelization constraints.

2. Piecewise Linear Lateral Displacement

Studies in the UK showed that certain alternative lateral position sequences could provide improved error reduction capability in the angular sector near the line of sight over that given by a "random" position sequence. In particular, it was proposed that a piecewise linear lateral displacement sequence such as illustrated in fig. 6-39 be utilized and an experimental array with this sequence was constructed (fig. 6-40).

The spectrum of the terms $C_D R_M^*$ and $C_M R_D^*$ and $C_M R^*_D$ corresponding to such a sequence can be conveniently obtained by noting that the phase sequence corresponding to

$$y(n) = n\delta_h$$

is equivalent to a sinusoid at the average angular rate

$$w_h = \delta_h \Delta k/T$$

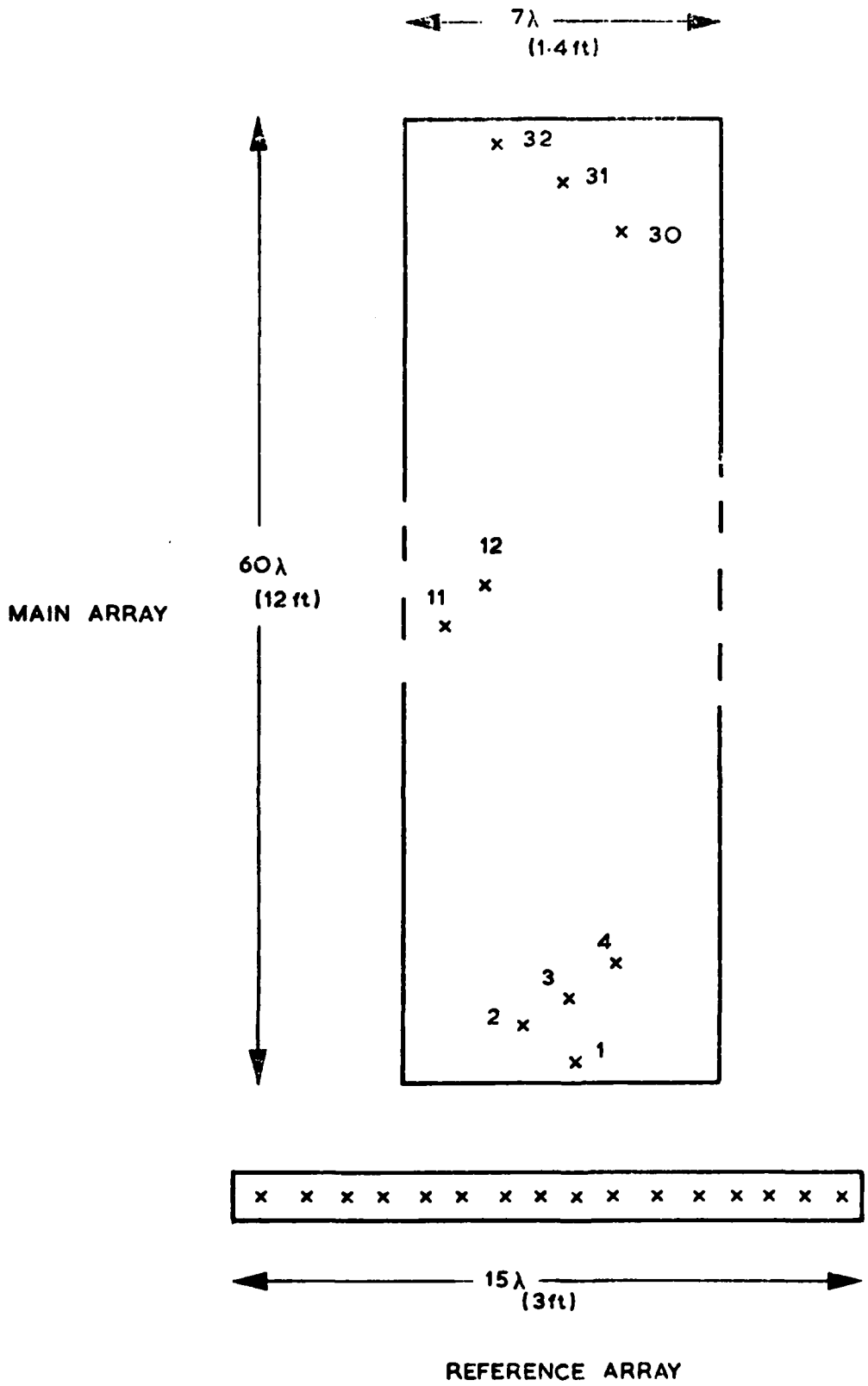

Fig. 6-39. Final UK lateral diversity array concept proposal.

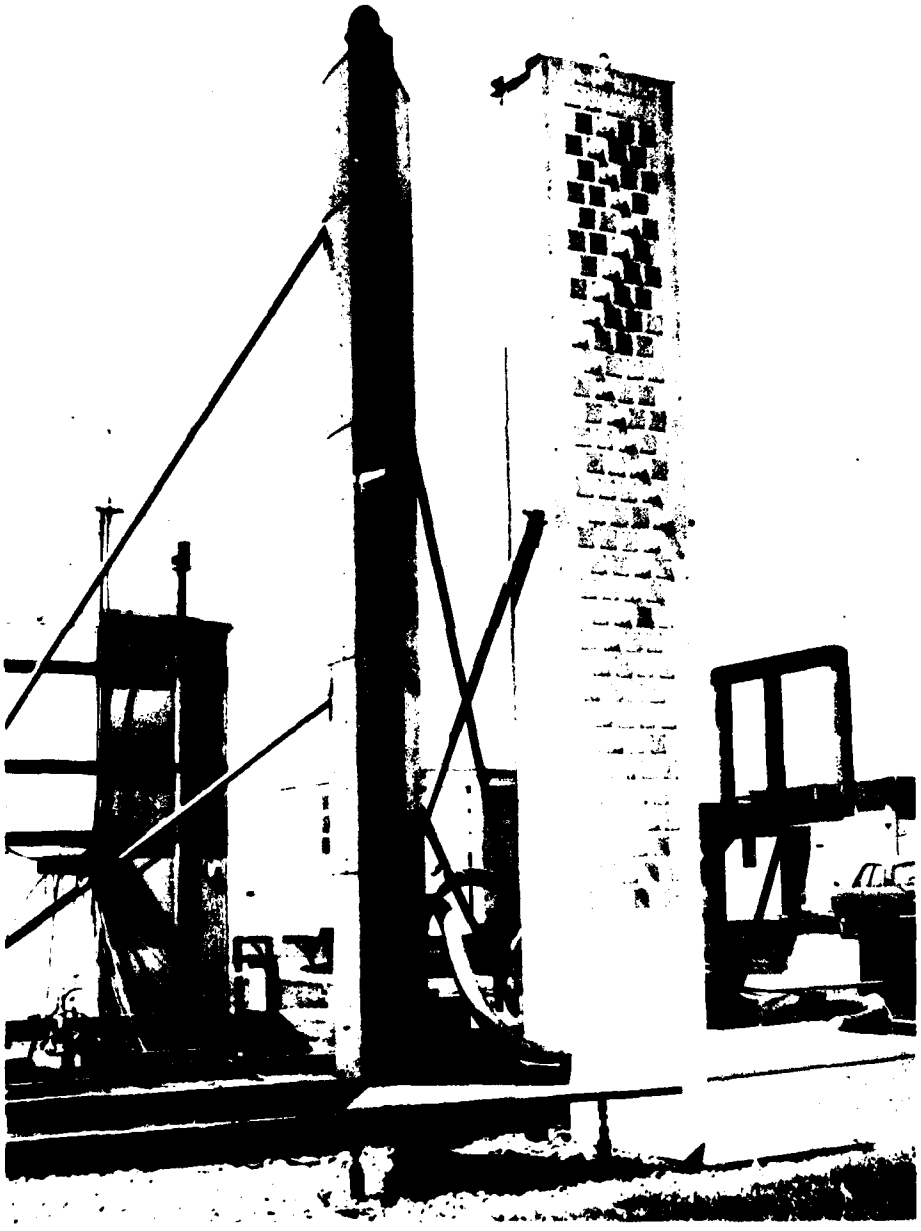

Fig. 6-40. Lateral diversity antenna used in initial trials alongside phase 1 antenna.

where δ_h is the horizontal element spacing in horizontal plane. Thus, the spectra of the cross terms are given by an expression of the form

$$G(w) = \frac{\sin(\omega-\omega_+)\, n_h T/2}{n_h \sin(\omega-\omega_+)\, T/2} \; \frac{\sin(\omega-\omega_o)\, n_+ n_h T}{n_+ \sin(\omega-\omega_o)\, n_h T} \tag{6-133}$$

$$+e^{j(\omega-\omega_o)n_+T} \; \frac{\sin(\omega-\omega_-)\, n_h\, T/2}{n_h \sin(\omega-\omega_-)\, T/2} \; \frac{\sin(\omega-\omega_o)\, n_-\, n_h T}{n_- \sin(\omega-\omega_o)\, n_- n_h T}$$

where $\omega_+ = \omega_o + \omega_h$

$\omega_- = \omega_o - \omega_h$

n_+ = number of lateral excursions in +y direction

n_- = " " " " " -y "

ω_o = angular frequency of component in absence of lateral diversity

For the proposed lateral diversity arrangement $\delta h = \lambda$, $n_h = 8$ and $n_+ = n/2$ in which case we see that the effect of lateral diversity is to translate the component frequency some

$$\frac{\delta h\ \Delta k/T}{2\pi/(n_v T)} = 32 \sin(\theta_d - \sin\theta_m) = 32\Delta\eta \tag{6-134}$$

beamwidths. However, the spectral width of the displaced component is approximately 4 beamwidths between -4 dB points and 8 beamwidths between the first nulls. Thus, if the cross product were at the direct signal frequency to

start with, it would become out of beam when the first null of the displaced component is 1.5 beamwidths away from the direct signal, i.e., $32\ \Delta\eta = 1.5 + 4.0$ or

$$\Delta\eta = 0.17 \tag{6-135}$$

which corresponds to an azimuth displacement of approximately 10°. By the same argument, we would expect a 3 dB error reduction when the −3 dB point on the spectra is 1.0 beamwidths away from the direct signal, i.e.,

$$\begin{aligned} 32\ \Delta\eta &\approx 1.0 + 2.0 = 3.0 \\ \Delta\eta &= 0.09 \quad \Rightarrow 5^{\circ} \end{aligned} \tag{6-136}$$

If the component frequency is displaced from the direct signal frequency, one of the two terms in (6-135) becomes out of beam faster than is indicated by (6-135) while the other team requires a greater $\Delta\eta$. Nevertheless, the crude estimates given by (6-135) and (6-136) agree fairly well with the UK experimental and simulation data in Figure 6-41. The region in which a sizable error reduction is <u>not</u> obtained is quite similar to that offered by a pseudorandom sequence.

Note also that if a signal component may have been out of beam originally, the use of this particular lateral diversity sequence may result in the component becoming inbeam if the scatterer azimuth yields the required value of ω_h. By contrast, with the pseudo random sequence, the multipath power is spread over a wide range of frequencies rather than being translated to two new frequencies $\pm\ \omega_h$ about the nominal frequency. This effect might be of

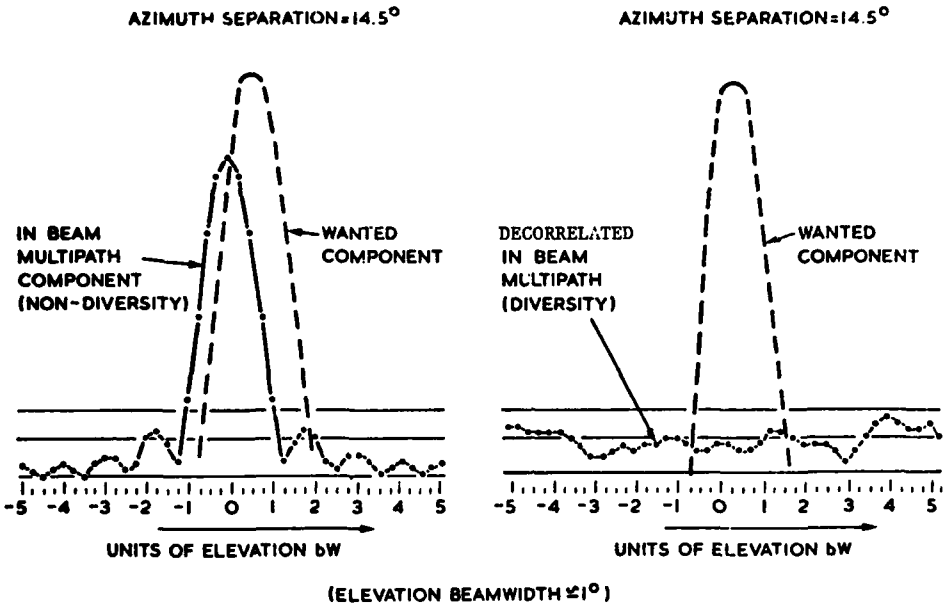

Simulation Results

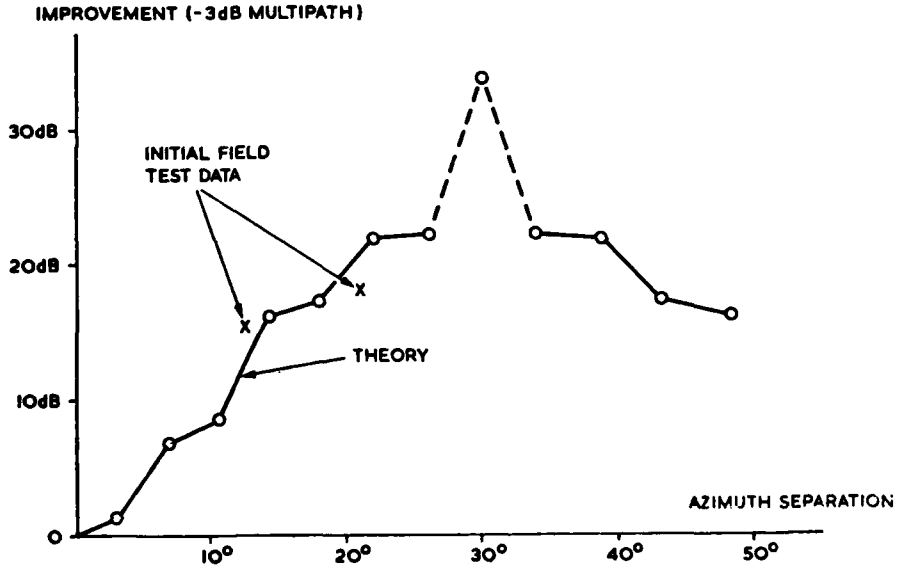

Fig. 6-41. Experimental and simulation results for performance improvement with lateral diversity.

principal concern at a site with irregular terrain having large cross tilts such that the ground reflection multipath appeared at a different azimuth than the direct signal.

Lateral displacements of y_o, the starting point in the reference array change the $C_M R_M^*$ phase relative to the $C_D R_D^*$ term. If ρ^2 is small so that the $C_M R_M^*$ term causes an error proportional to cos (relative phase), then variation of y_o between scans will yield an error reduction in static conditions of

$$F_{MM^*} = \frac{\sin \alpha'/2}{N_h \sin (\alpha'/2N_h)}$$

where $\alpha' = \Delta k \, Ly'$

Ly' = aperture available for y_o excursions

N_h = corresponding number of diversity positions for y_o.

For the UK experimental array $Ly' = 8$ and $N_h = 8$ so that there is a 4 dB reduction at $\pm$ 3.6°.

Additionally, the y_o displacements will vary the phase of the residual $C_D R_M^*$ and $C_M R_D^*$ components. However, these phase variations will be added on to those which correspond to classical motion averaging so that it is difficult to draw any clearcut conclusion as to the end result. If the normal motion averaging were quite good at the scalloping frequency of concern, it is likely that lateral diversity would degrade the overall performance against the $C_D R_M^*$ and $C_M R_D^*$ components, but improve performance against the $C_M R_M$ component.

E. Comparative Simulations of Scenarios Related to DMLS Multipath Mechanisms

In this section, we present several comparative scenarios related to the DMLS multipath performance issues discussed in the preceding sections. The first three scenarios examine the reference scalloping error mechanism in the context of the DMLS proposal changes made in November 1976 to reduce the magnitude of the effects which appeared in AWOP scenario 2. These changes consisted of a directional reference antenna pattern (to reduce the reference multipath level when on final approach) and a different scan format (so that multipath with scalloping frequencies near 200 Hz would no longer create sizable errors). These changes were quite effective in reducing the DMLS reference scalloping errors for AWOP scenario 2; however, it was contended that the basic error mechanism could be significant in other airport geometries, such as are considered in the first three scenarios.

Scenarios 1 and 2 are concerned with the building geometry at Brussels National Airport runway 07-25-L. The first scenario was developed by using building locations shown on an ICAO landing chart and applying terrain profile and building material simplifications similar to those used in the AWOP "standard" scenarios of Chapter II. The second scenario refines the scenario 1 to take into account additional features of the June 1977 Brussels airport environment (e.g., terrain profile, shadowing by intervening objects, inhomogeneity in building wall materials) to yield a comparative scenario which more nearly approximates the airport environment at the time of the DMLS and TRSB field tests.

Studies within the UK [136] suggested that irregular surfaces such as staggered hangar doors could yield such rapid variation in the multipath

characteristics that the DMLS reference scalloping error characteristic would be quite different from that suggested in part B of the present chapter. To examine this issue, a comparative scenario was developed based on a series of buildings with staggered doors which border runway 07-25L at Sydney International Airport. Results are reported both for the nominal DMLS model and an alternative model in which the multipath characteristics are recomputed for the last half of an azimuth frame.

The scalloping rates associated with the DMLS array scalloping phenomena typically were high enough so that the rate of change of Doppler frequency is high (i.e., low "persistence"). Thus, there was some question as to the duration of such errors in practical geometries. The final scenario compares the DMLS and TRSB azimuth subsystems in a geometry [based on building locations at Heathrow (UK)] which might be expected to give rise to array scalloping effects.

1. Comparative Scenario Based on ICAO 1977 Landing Chart of Brussels National Airport

Figure 6-42 shows the map of Brussels National Airport which was used to develop a comparative azimuth multipath scenario. Figures 6-43 and 6-44 show the simulation airport map for the scenario as well as the computed multipath levels where each of the four buildings highlighted in Fig. 6-42 was modeled as a flat rectangular plate as follows:

B1:	masonry ($\varepsilon/\varepsilon_0$ = 15)	8 meters high
B2:	metal	15 " "
B3:	"	15 " "
B4:	"	20 " "

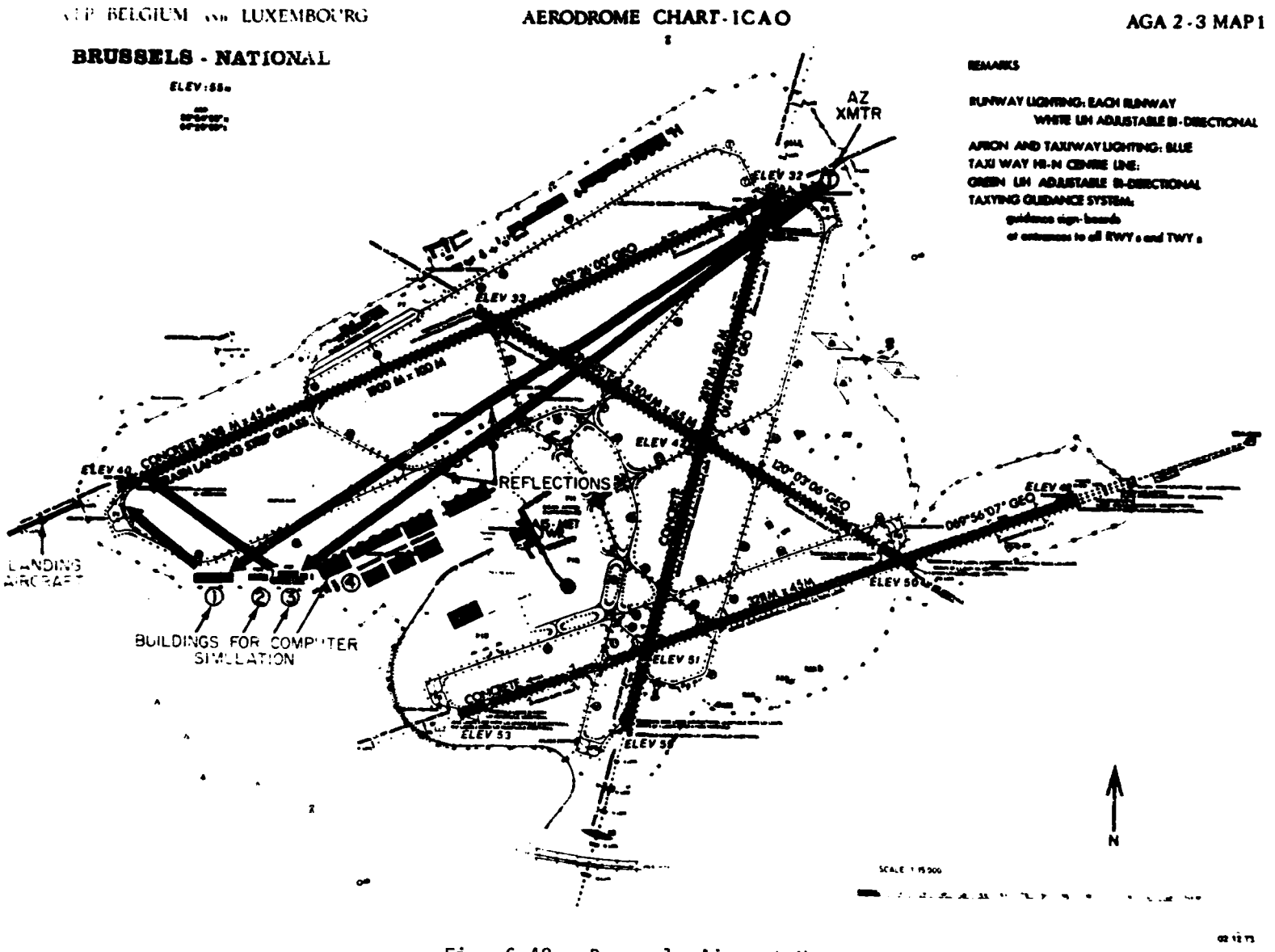

Fig. 6-42. Brussels Airport Map.

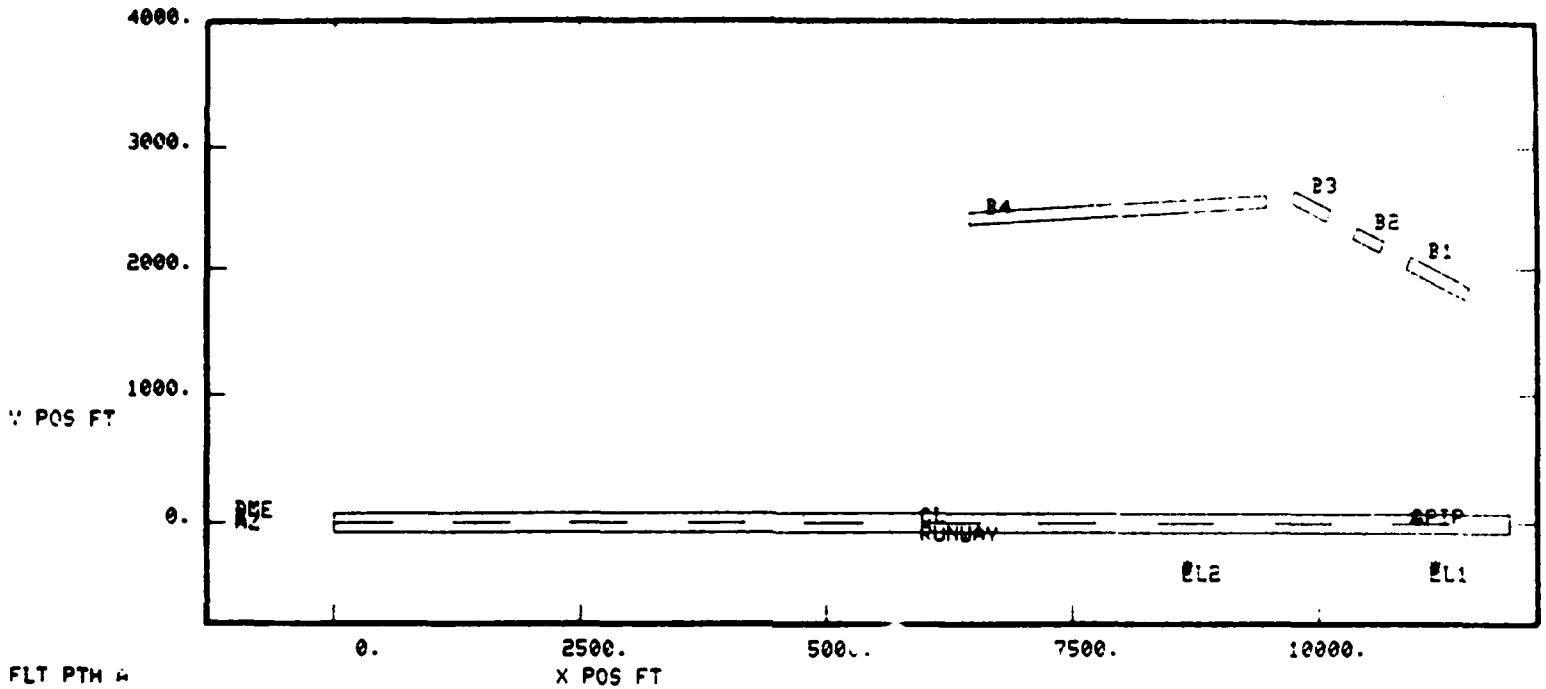

FLT PTH #

AZ SYSTEM

OBST	RANK	AMP	DIST	RDOP
G	2	0	3844.8	0.
B1	4	25	2457.7	-368.
B2	3	16	3054.6	-398.
B3	1	-1	3616.3	-422.
B4	5	34	280.9	-34.
D	0	80	0.0	0.

EL SYSTEM

OBST	RANK	AMP	DIST	RDOP
G	1	0	3844.8	1.
B1	2	13	3440.8	-798.
B2	5	56	3791.9	-672.
B3	4	52	3756.8	-510.
B4	3	46	3827.0	-392.
D	0	80	0.0	0.

AMP = peak M/D ratio (dB)
DIST = distance (ft) along flight path at which peak M/D ratio occured
RDOP = scalloping frequency in Hz at point of peak M/D ratio

Fig. 6-43. Airport map for "system sensitivity" scenario derived from Fig. 6-42.

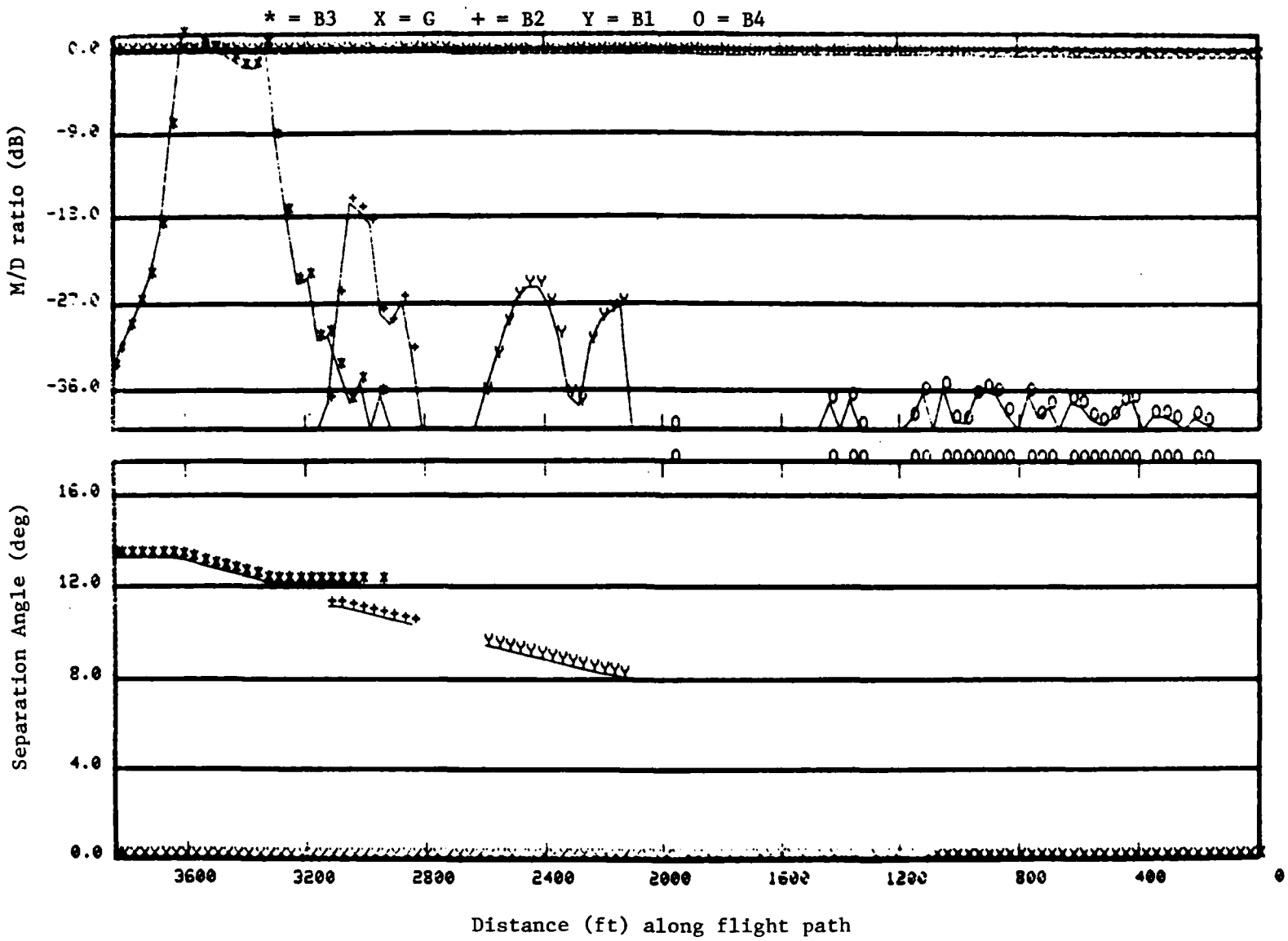

Fig. 6-44. Azimuth multipath characteristics for scenario of Fig. 6-43.

The simplifying assumptions used for the AWOP scenarios were utilized here, in particular:

a) airport surface contours on and off the runway are ignored, i.e., the terrain is flat and homogeneous

b) blockage of the building reflection paths by intervening objects or vegetation is ignored

c) the building wall surface is homogeneous (e.g., windows and door staggering are not considered)

and

d) the aircraft antenna pattern is omnidirectional

Figure 6-45 shows the computed TRSB and DMLS azimuth errors for a scenario in which the aircraft approach speed is 108 knots before threshold and 103 knots thereafter with a 50 foot threshold crossing height on a 20:1 glideslope. The sizable DMLS errors arise because the multipath from building B3 is near one of the large peaks in the motion averaging function $D_p(\alpha)$ (recall Fig. 6-16). However, since the building is angularly out of beam, the TRSB errors (due to azimuth sidelobes) were low. Several variants on this scenario were run with various approach velocities and threshold crossing heights. The region and duration of noticeable errors (e.g., errors >0.02°) were roughly the same in each case, but the peak levels varied as indicated in Table 6-11.

2. Comparative Scenario Based on Brussels Airport Environment of June 1977

Several features of the Brussels airport environment not considered in the preceding scenario were included in this scenario. Specifically, we consider

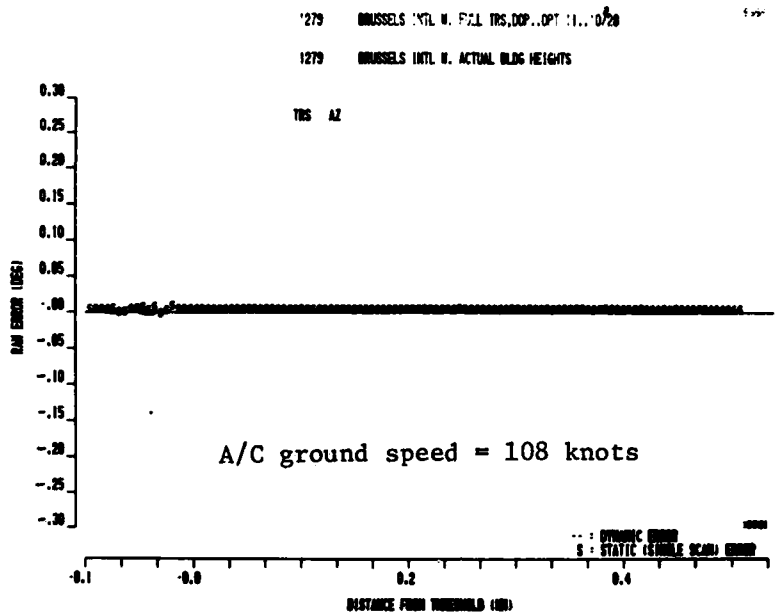

Brussels scenario threshold crossing height of 50 ft. (TRSB)

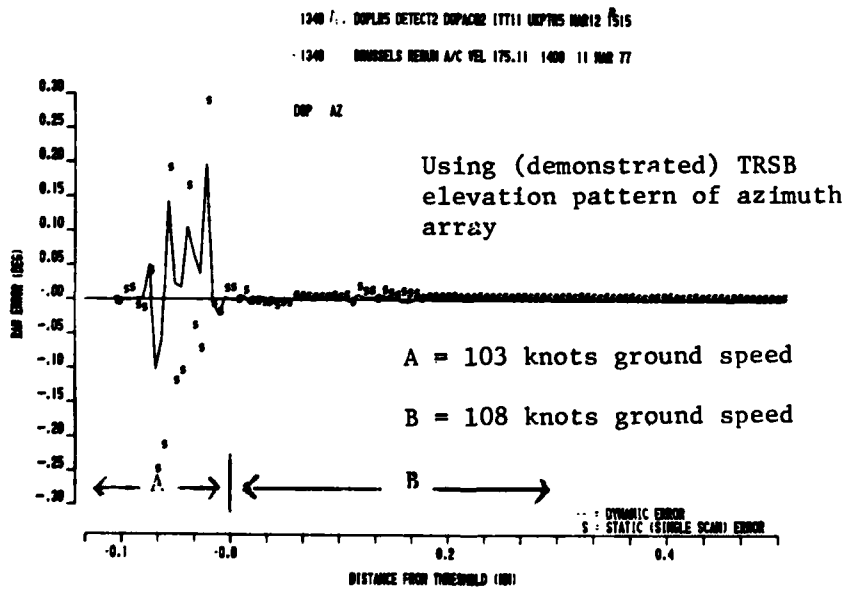

Fig. 6-45. DMLS error for Brussels scenario with threshold height of 50 ft.

TABLE 6-11

SUMMARY RESULTS FOR VARIANTS OF "SYSTEM SENSITIVITY" SCENARIO BASED ON FIGURE 6-42

Approach Velocity Past Threshold (knots)	Threshold Crossing Height (ft.)	Peak M/D Level (dB)	Peak to Peak Angle Error (deg)	
			DMLS	TRSB
108	50	0	<0.01	0.14
103	50	+1	0.02	0.30
103	30	+1	0.02	0.38

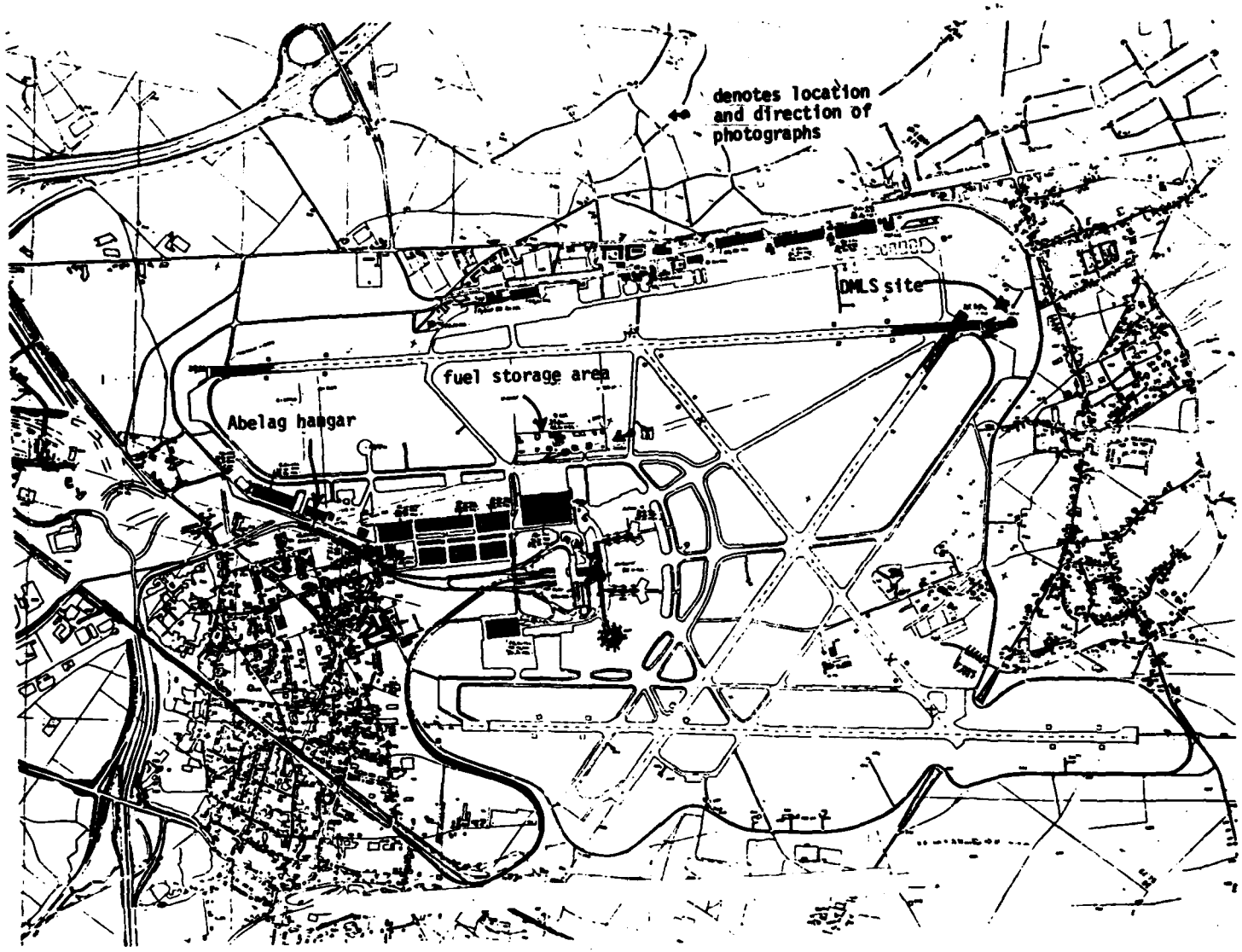

Fig. 6-46. Brussels National Airport.

(a) terrain contours on and off the runway

(b) blockage of the reflection paths by intervening objects

and (c) composition of the building surfaces

using data based on detailed airport maps as well as an on site inspection in June 1977.* Figure 6-46 shows a large scale map of the airport while Fig. 6-47 shows the runway contours.

It was discovered that the original ICAO map (Fig. 6-42) was in error in that building 3 in the scenario (see Fig. 6-43) was planned but not constructed. Therefore, that building was deleted from this scenario. Building 1 in the original scenario was not visible from the azimuth site due to blockage by fuel storage tanks, and building 4 produced negligible multipath in the initial scenario, therefore, these buildings were also deleted from this scenario. Thus, we focused on modeling the reflections from building 2 which corresponds to the Abelag general aviation hangar.

Another important source of data was an onsite inspection and photographs to resolve a number of important details which were not obtainable from maps. Figure 6-48 shows a photograph taken from the fuel storage area of the Abelag hangar which represents the principal multipath threat. The pertinent

---

*The original intent in developing this scenario was to achieve an "airport specific" scenario which could be used for model validation by comparison with DMLS and TRSB field tests. However, some key environmental features were not noted at the time of tests (e.g., hangar door locations, shadowing of the hangars by parked aircraft and the precise flight path). This lack of data coupled with the very low multipath levels (predicted and encountered) resulted in Brussels National Airport being a poor case for quantitative model validation.

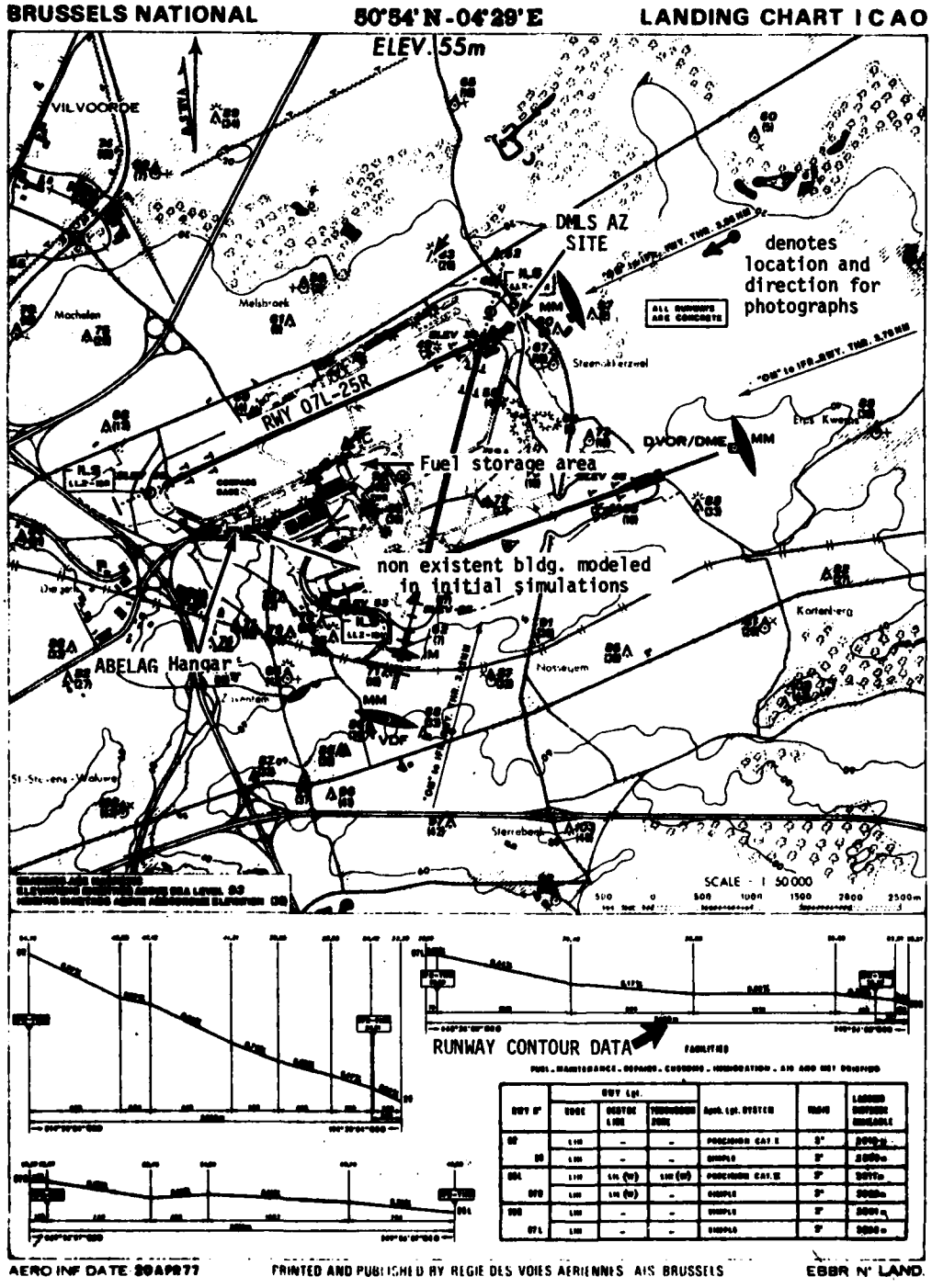

Fig. 6-47. Brussels National landing chart ICAO.

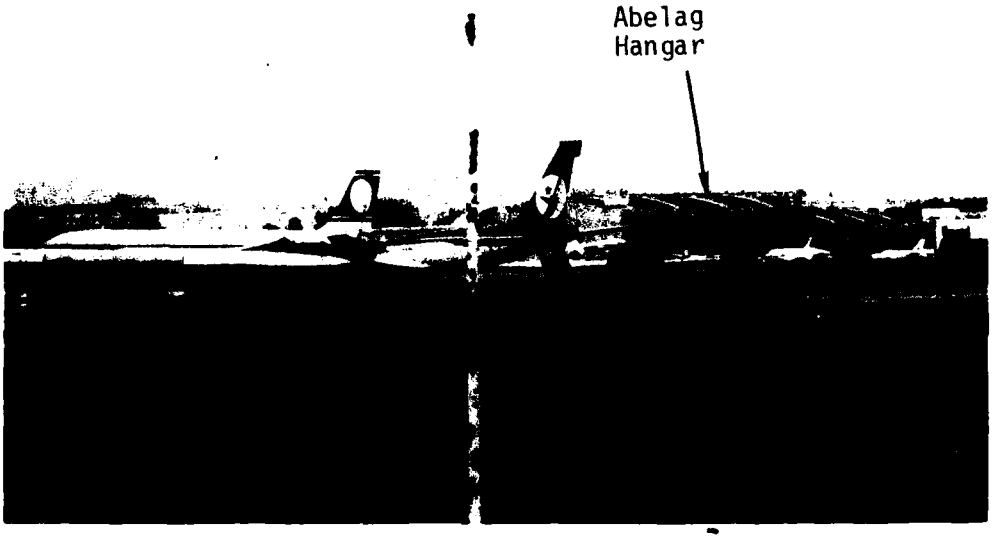

Fig. 6-48. Abelag hangar as seen from fuel storage area.

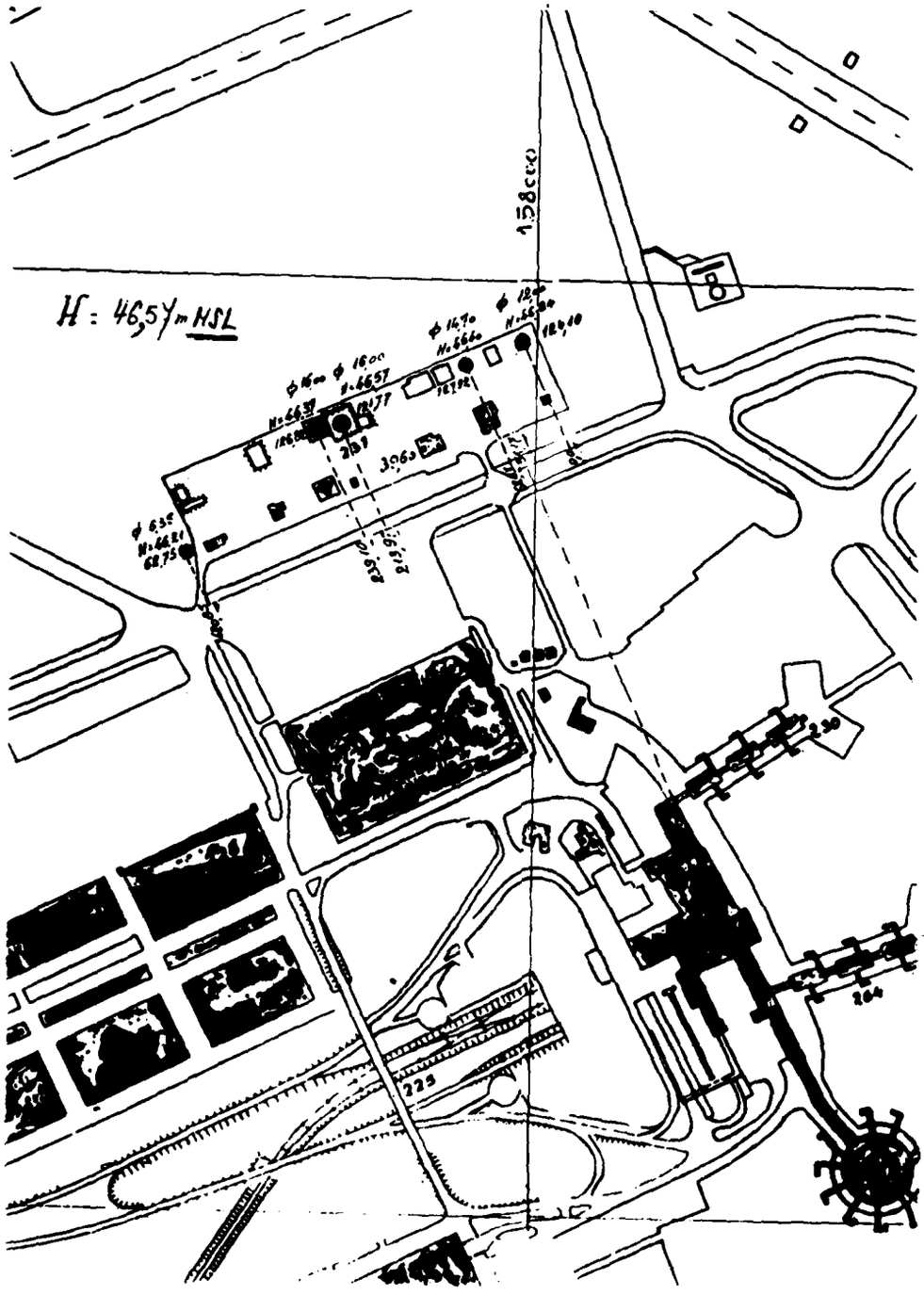

Fig. 6-49. Map of Brussels airport fuel storage area.

reflecting area is the vertical front of the building, the top of which is lower than the building height due to the sloped roof. Also, the hangar doors have a plastic window of approximately 6 foot height at the top.

An extremely important issue which we attempted to resolve was the extent to which the fuel storage area shown in Fig. 6-46 shadows the reflecting hangars so as to reduce the reflected signal levels. Visual inspection with binoculars from the azimuth pad constructed by the UK off the end of runway 25R showed that the line of sight (LOS) from that point to much of the Abelag hangar and the Abelag office building is blocked. However, the large distance (2 miles!) involved made it quite difficult to precisely ascertain the degree of blockage. An attempt was made photographically to resolve this issue using a hand held 200 mm lens on a 35 mm camera, with somewhat ambiguous results.

By close comparison of various photographs using the aircraft tails to provide orientation, we concluded that the LOS to the Esso sign atop the Abelag hangar is not blocked, but that the LOS to the remainder of the hangar is blocked. The white area below the Abelag sign in Fig 6-47 is believed to be due to the light covered buildings and trucks in the fuel storage area.

This blockage assessment was first cross-checked by an alternative estimation procedure which involved photographing the fuel storage area from several angles to estimate map positions and height data. Subsequently a more detailed map of the fuel storage area and an aerial photograph of the pertinent airport surface were obtained from the Brussels airport authorities. These are shown in Fig. 6-49 and 6-50. These latter data were found to agree closely with the earlier photographic estimates of the airport surface positions of the various objects.

Fig. 6-50. Aerial photograph of Brussels National Airport.

Figure 6-51 shows the fuel storage area building and tank locations, wall colors, and heights which were obtained by this procedure. In Fig. 6-52, we show the vertical plan view of the shadowing geometry based on the airport authority's ground height data together with our building height estimates based on photographs. We see that a 15 foot high object at the fuel storage area would block the vertical front of the Abelag hangar, but not the Esso sign atop the hangar. However, a 25 foot high object such as the fuel storage tanks should shadow the entire hangar roof as appears to be the case in Fig.-6-48.

Figure 6-53 shows the computed shadowing profile for the fuel storage area at the fuel storage area. It would have been desirable to quantitatively confirm this by very high quality photographs from the azimuth site, but this was not possible.

A considerable effort was made to develop a method by which the fuel storage area shadowing would be taken into account. The current MLS propagation model does not compute the reflections from a building which is partially shadowed by another building, nor is any experimental data on this available to the best of our knowledge. Since the effect of the shadowing obstacles is to reduce the illumination of the Abelag hangar, it was decided to approximate the shadowing effect as a change in the effective building reflection coefficient, i.e.,

$$\text{effective reflection coefficient} = \text{Fresnel reflection coefficient} \times \text{illumination factor}$$

where the illumination factor = received field at hangar/free space field at hangar. This assumption does yield a proper reflected signal level at the

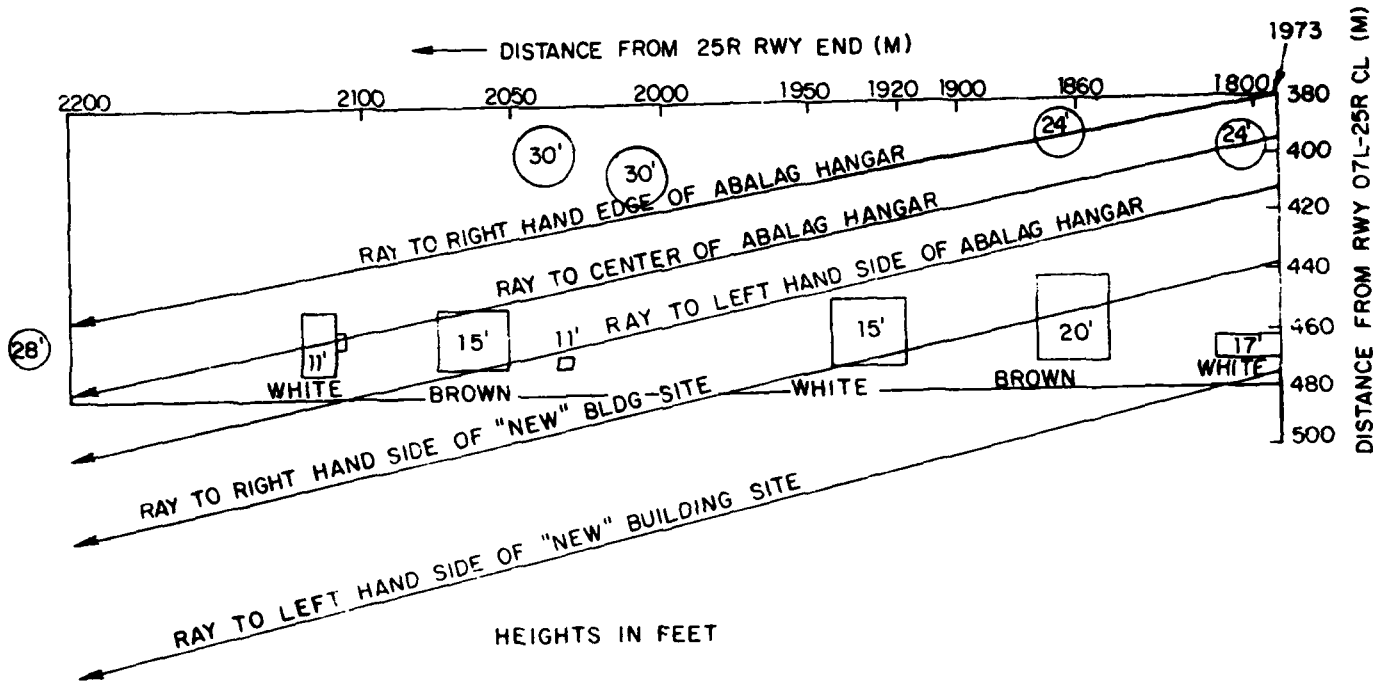

Fig. 6-51. Inferred fuel storage area structure locations and heights.

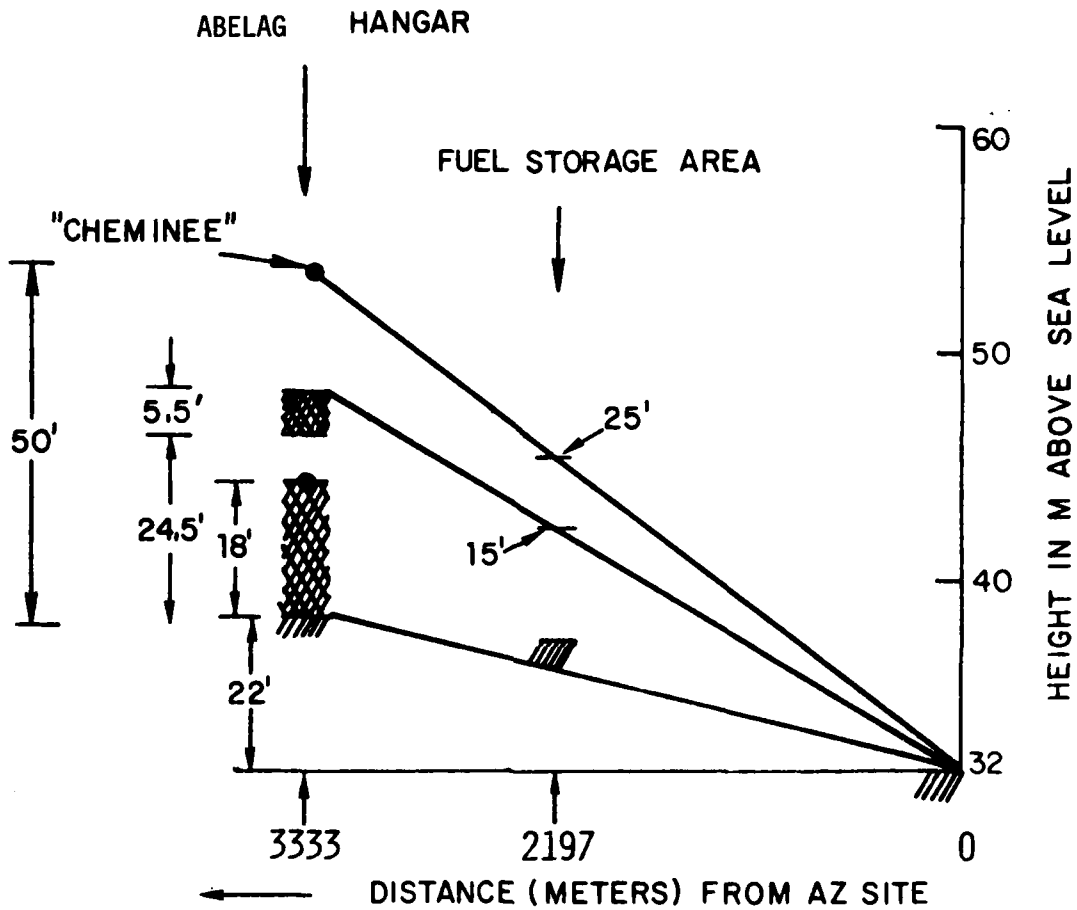

Fig. 6-52. Vertical plan view of Abelag hangar shadowing by fuel storage area structures.

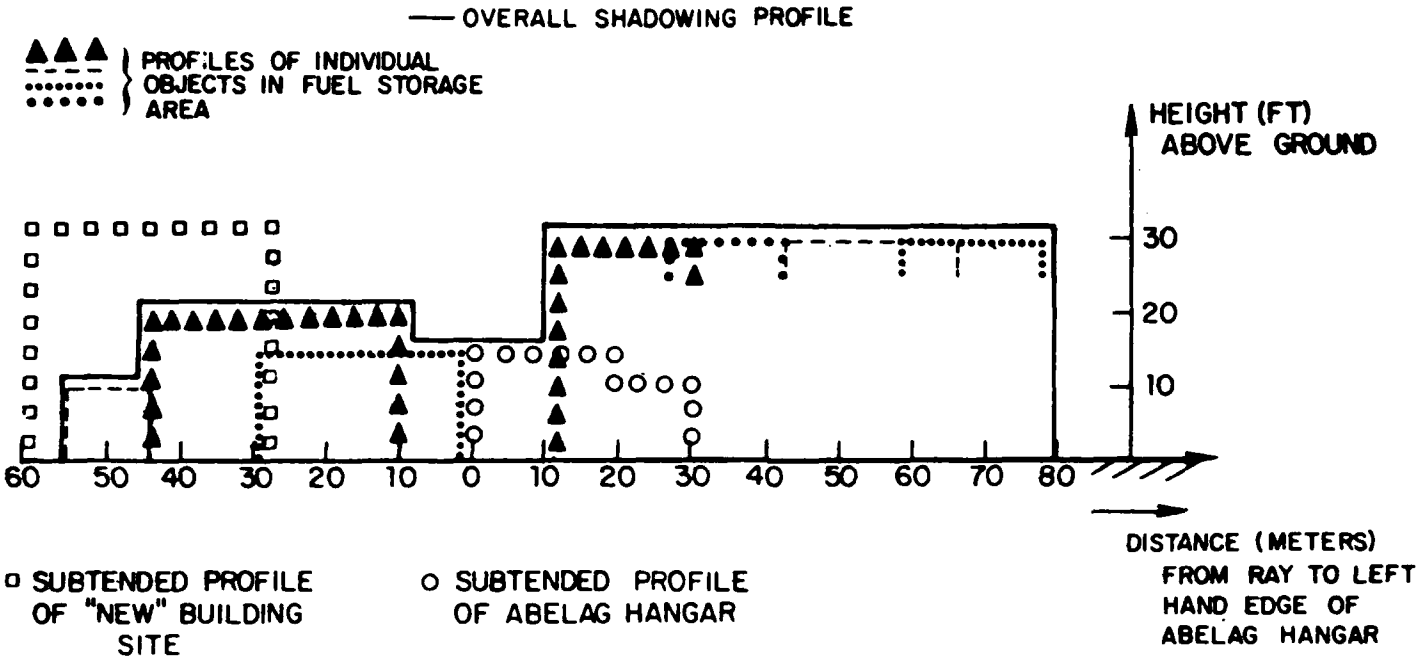

Fig. 6-53. Inferred shadowing profile of fuel storage area.

hangar, but does ignore to a certain extent phase front tilts which also are generated by the shadowing obstacle. To partially incorporate some of the phase front tilt effects, the illumination phase was also computed so that a complex reflection coefficient would be generated.

Table 6-12 shows the computed illumination factors for the Abelag hangar. For purposes of simulation, the building was divided into five plates corresponding to the doors and top edges of the hangar, and an average illumination factor computed for each of these plates. We see that the effect of the shadowing is to reduce the reflected levels by some 6 to 23 dB for various portions of the building. The reduction is largest for the doors. These plate values are also shown in Table 6-12. Plates A, C, and E are the area above the doors while plates B, D, and F are portions of the hangar doors. The assumed effective reflection coefficients for Plates A and C are one-half the values given in Table 6-12.

A distinctive feature of the Brussels environment in early June was the high dense vegetation in the off runway areas. Direct measurements of the reflection coefficient of such vegetation at the incidental angles of interest (below 1°) are not available and no quantitative theoretical models are available. However, experimental measurements at higher angles [137] and qualitative theoretical arguments suggest that the reflection coefficient would be very low. Thus, we modeled such areas as being non-reflectors.

The runway was modeled as a series of flat plates corresponding to the various segments shown in Fig. 6-47. Specific numerical values used were

TABLE 6-12

NORMALIZED ILLUMINATION OF ABELAG BUILDING
AND COMPUTATION PLATES AT BRUSSELS NATIONAL AIRPORT

GROUND HEIGHT ASSUMED TO BE 38.7m ABOVE SEA LEVEL

TABLE FORMAT

X.XXX amplitude

YYY.Y phase in deg

DISTANCE ALONG BUILDING FRONT (FT)

PLASTIC

HEIGHT ABOVE GROUND (FT)	0	36	72	108	144	180	216	252	288	324
5.0	0.203 126.3	0.173 117.0	0.226 95.0	0.129 68.5	0.042 -61.7	0.164 -4.7	0.135 -3.8	0.116 -30.0	0.130 -5.8	0.135 -10.5
10.0	0.233 88.9 (B)	0.210 87.7	0.269 56.9	0.131 42.8 (D)	0.097 -125.2	0.186 -59.4	0.123 -68.6	0.168 -85.9 (F)	0.156 -65.9	0.143 -64.3
15.0	0.282 56.9	0.258 62.1	0.317 27.3	0.132 30.6	0.148 -173.5	0.199 -109.1	0.137 -136.3	0.204 131.6	0.178 -110.0	0.139 -119.6
20.0	0.350 31.5	0.320 39.9	0.371 5.1	0.163 26.5	0.200 144.3	0.208 -154.6	0.182 169.8	0.223 -173.1 (E)	0.192 -161.8	0.147 -176.2
25.0	0.435 12.4 (A)	0.399 21.6	0.435 -10.5	0.205 21.1 (C)	0.259 108.3	0.215 164.3	0.237 129.9	0.235 148.0	0.200 157.3	0.179 134.5
30.0	0.536 -1.1	0.495 7.4	0.514 -20.6	0.282 12.5	0.326 79.1	0.220 127.4				

PLASTIC

Assumed Illumination factor

	PLATE A	B	C	D	E	F
magnitude	.46	.24	.24	.13	.20	.14
angle (deg)	0.0	+61	84	-83	180	-44

plate	distance (m) from end of rwy 25R near end	far end	height (m) above sea level near end	far end
1	0.0	100	32.37	32.97
2	100	350	32.97	33.88
3	1625	2550	33.88	35.48
4	2550	3560	35.48	39.88

*threshold of runway 07L

Figures 6-54 and 6-55 show the scenario airport map and computed azimuth multipath characteristics for a scenario in which the aircraft passed over the threshold at a height of 30 feet on a 2.86° glide slope at 100 knots approach velocity. The building multipath levels are seen to be quite small (i.e., less than -20 dB), with the highest level being associated with the upper portion of the left hangar door.

Figure 6-56 shows the computed TRSB and DMLS error waveforms. Again, both systems have very small errors as expected from the low multipath levels, even though the scalloping frequencies are in a range in which the DMLS reference scalloping error is relatively large.

Several variants on this scenario were also simulated corresponding to various threshold crossing heights and approach velocities. Table 6-13 shows the results for the various cases. In all cases, the M/D levels were quite low so that negligible errors occurred for either system. This scenario shows that there are factors such as terrain contours and reflection blockage by intervening objects which can substantially reduce the multipath levels (and, system errors) at an actual airport and must therefore be considered if one is to accomplish useful predictions of performance on a given flight. By the same token, conducting experiments at an airport which has many potential

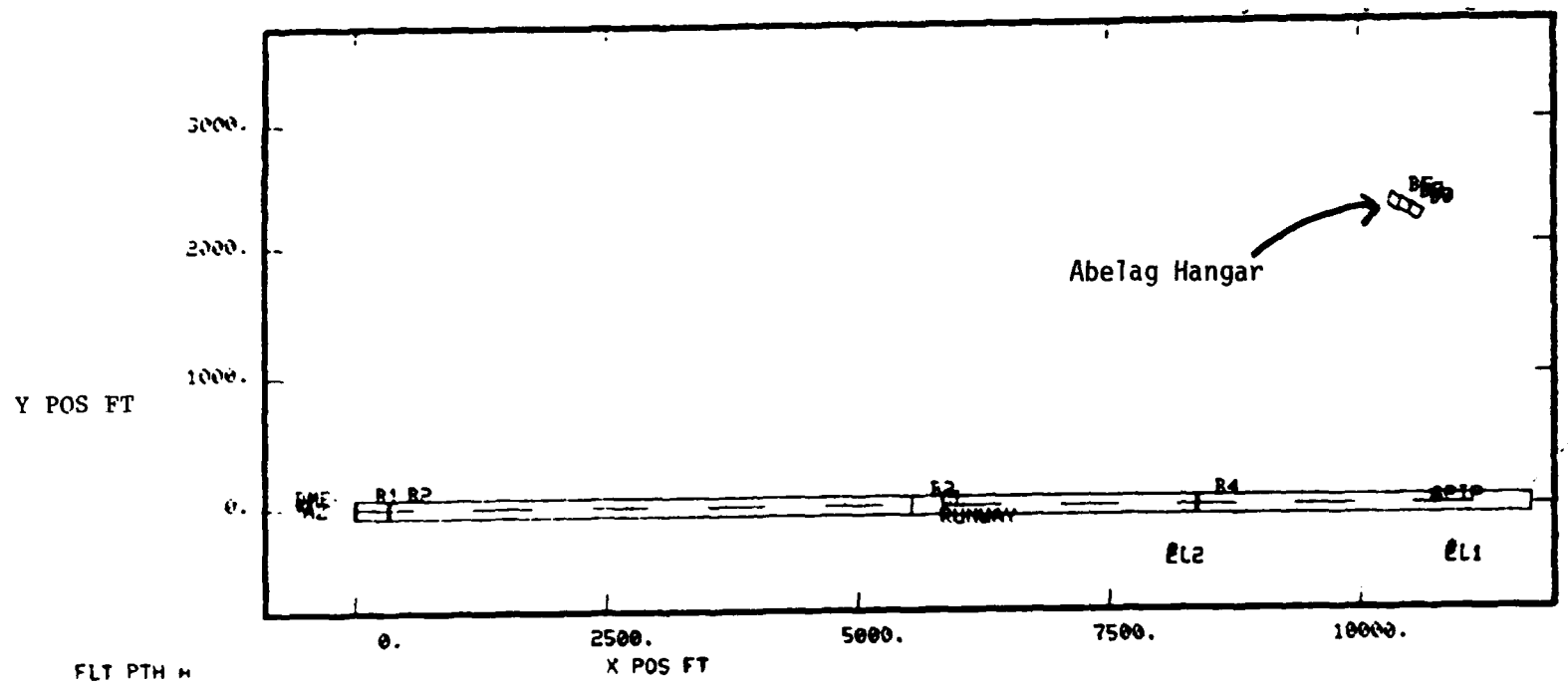

FLT PTH H
AZ SYSTEM

	OBST	RANK	AMP	DIST	RDOP
runway multipath	E1	5	24	34.0	0.
	E2	1	2	204.0	0.
	E3	2	7	3802.6	0.
	E4	3	11	3258.6	0.
hangar multipath	E5	6	26	2068.6	-438.
	E6	4	24	2068.6	-438.
	E7	8	31	1904.0	-419.
	E8	9	31	1870.0	-408.
	E9	10	44	1870.0	-421.
	E0	7	29	1870.0	-421.
	D	0	80	0.0	0.

AMP = - peak M/D level (in dB)

DIST = point of peak M/D = 13679 - x (ft)

RDOP = scalloping frequency (Hz) at point of peak M/D

Fig. 6-54. Airport map for comparative scenario based on June 1977 Brussels airport environment.

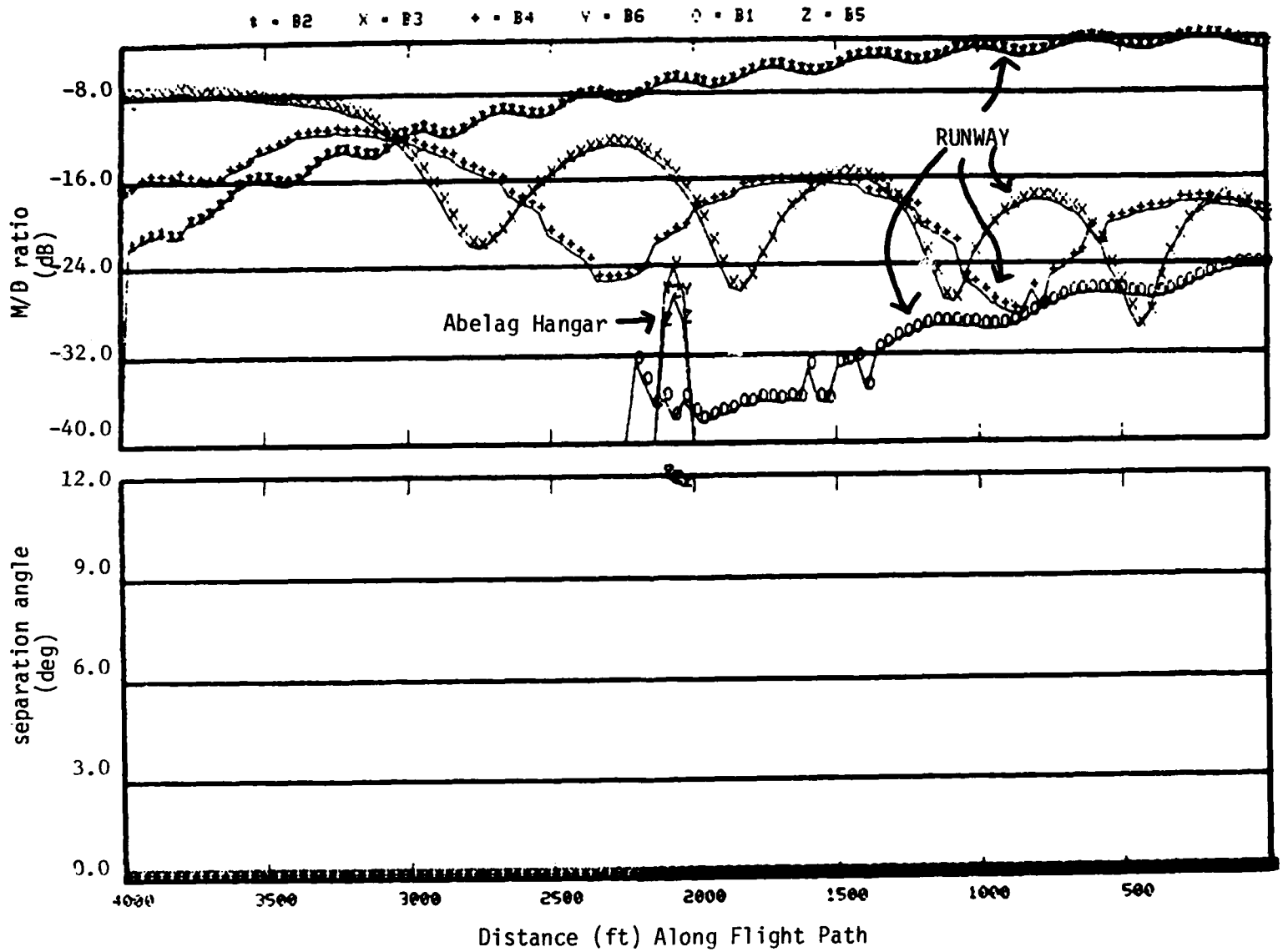

Fig. 6-55. Azimuth multipath diagnostics for comparative scenario of Fig. 6-54.

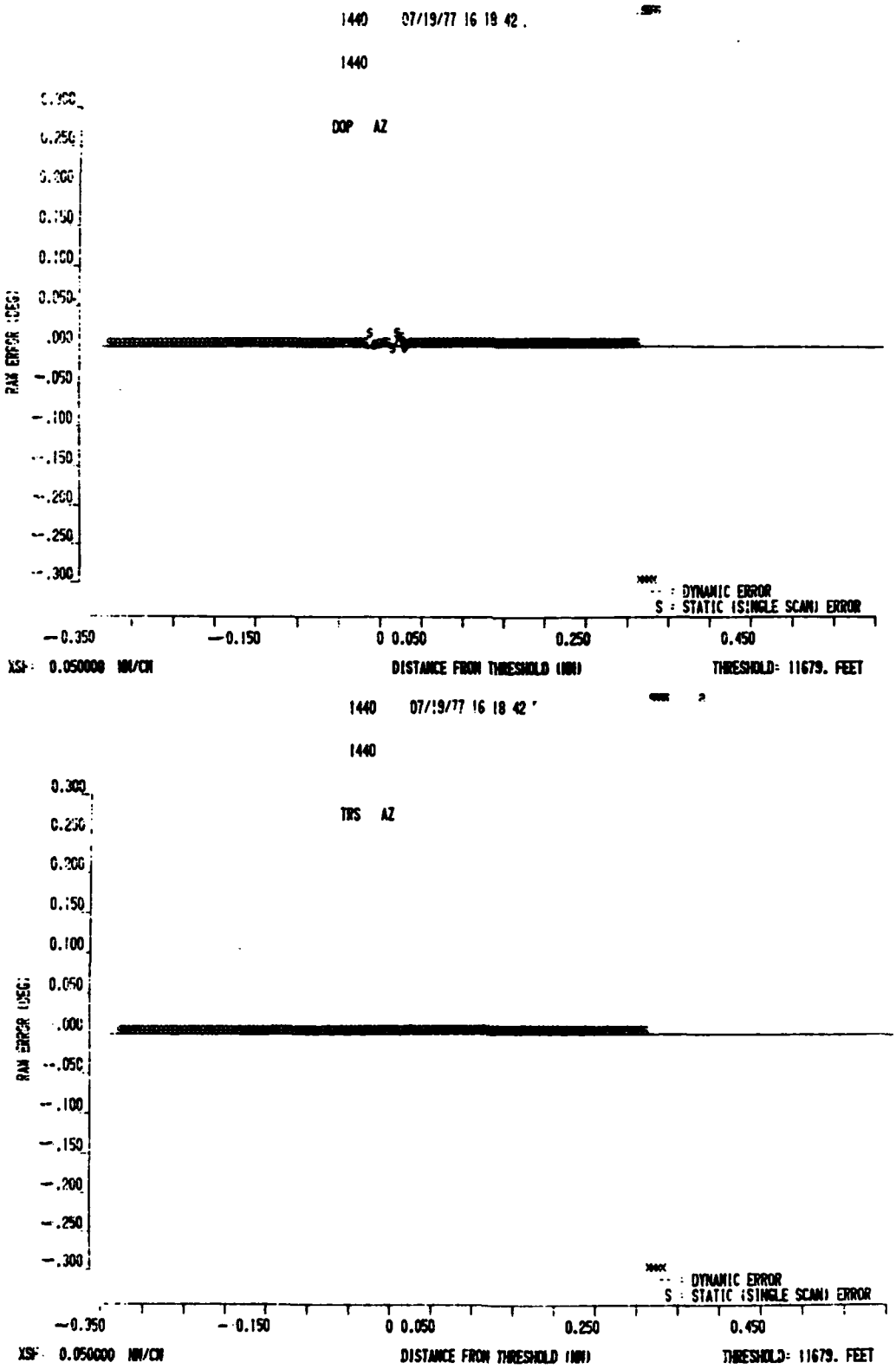

Fig. 6-56. Computed raw errors for comparative scenario of Fig. 6-54.

TABLE 6-13

SUMMARY RESULTS FOR VARIANTS OF SCENARIO BASED ON JUNE 1977 BRUSSELS AIRPORT ENVIRONMENT

Approach Velocity (knots)	Threshold Crossing Height (ft.)	Peak M/D Level* (dB)	Peak to Peak Angle Error (deg) DMLS	Peak to Peak Angle Error (deg) TRSB
100	50	-24	0.01	<0.01
100	30	-21	<0.01	<0.01
150	30	-19	<0.01	<0.01

* Level of largest building reflection path re direct signal.

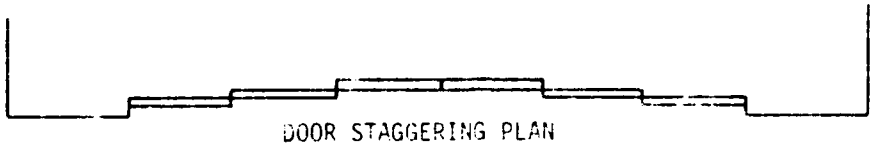

DOOR STAGGERING PLAN
19.4 cm SPACING

DOT No. 1 hangar.

DOOR STAGGERING PLAN

LENGTH = 9 x 25 + 60 = 285' CABLE MAP ⇒ LENGTH = 270'

6 STEEL DOORS SMOOTH WITH REINFORCED GLASS INSET ≈1 cm p-p SURFACE ROUGHNESS
STAGGERED 20.4 cm RAIL TO RAIL

DOT No. 2 Hangar.

6 DOORS STEEL SHEET SMOOTH ≈1 cm peak-to-peak SURFACE ROUGHNESS
STAGGERED 20.5 cm APART ON RAILS

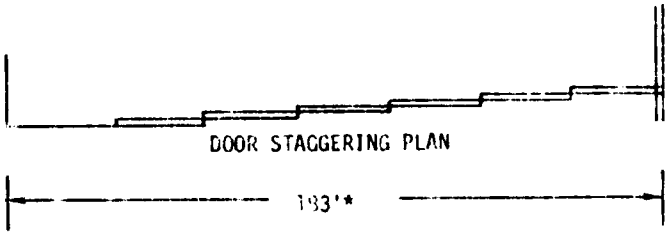

DOOR STAGGERING PLAN

CABLE MAP SHOWS 190' LENGTH

Trans Australian Airlines Hangar #3.

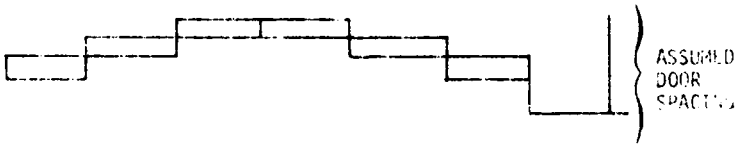

Hangar # 83 (Ansett)

Fig. 6-57. Door spacing of hangars for scenario based on Sydney Airport.

building reflections does not necessarily demonstrate strong multipath immunity unless it is verified that the environment at the time of the test is such that substantive multipath will be encountered.*

3. Comparative Scenario Based on Geometry at Sydney International Airport Runway 07L

Sydney runway 07L has four buildings located near the threshold such that out of beam azimuth multipath with a scalloping rate near 400 Hz is encountered in the flare guidance region. Each of the four building surfaces facing the runways consists of a series of staggered sliding doors with various surface compositions (see Fig. 6-57). This particular configuration offered an opportunity to compare system performance under a circumstance where the net out of beam multipath level is rapidly fluctuating due to reinforcement and cancellation between the various reflected signals.

The airport and flight path models used here were described in Chapter III of Volume I, as were the computed multipath characteristics. For the simulations reported here, a special version of the simulation model was also utilized in which the multipath is recomputed half way through a DMLS azimuth data frame. This permitted us to compare the error with the standard DMLS model in which multipath from each individual scatterer is assumed to be stationary (e.g., have constant amplitude, time delay, separation angle and

---

*The TRSB and DMLS tests at Brussels in summer 1977 did not show any discernable azimuth multipath errors in the threshold region [62].

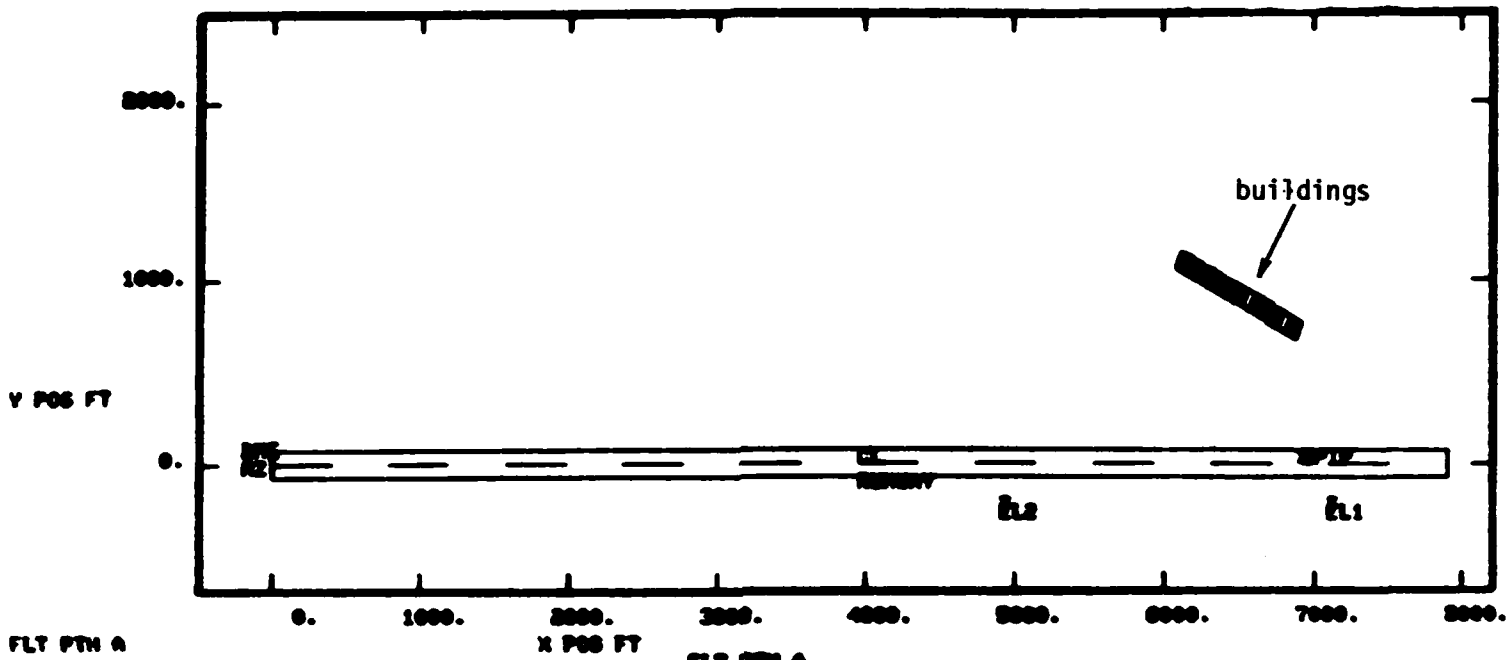

FLT PTH A
AZ SYSTEM

OBST	RANK	M/D(DB)	DIST	RDOP
6	1	-0.2	3019.2	0.
1	14	-4.0	712.	[illegible]
2	[illegible]	-12.1	674.	[illegible]
3	[illegible]	-1.6	674.	[illegible]
4	[illegible]	-4.7	[illegible]	[illegible]
5	[illegible]	-13.7	[illegible]	[illegible]
6	[illegible]	-1.9	[illegible]	[illegible]
7	[illegible]	-14.0	[illegible]	[illegible]
8	[illegible]	-14.1	[illegible]	[illegible]
9	[illegible]	-14.2	[illegible]	[illegible]
10	[illegible]	[illegible]	[illegible]	[illegible]
11	[illegible]	[illegible]	[illegible]	[illegible]
12	[illegible]	[illegible]	[illegible]	[illegible]
13	[illegible]	[illegible]	[illegible]	[illegible]
14	[illegible]	[illegible]	[illegible]	[illegible]
15	[illegible]	[illegible]	[illegible]	[illegible]
16	[illegible]	[illegible]	[illegible]	[illegible]
17	[illegible]	[illegible]	[illegible]	[illegible]
18	[illegible]	[illegible]	[illegible]	[illegible]
19	[illegible]	[illegible]	[illegible]	[illegible]
20	[illegible]	[illegible]	[illegible]	[illegible]
21	[illegible]	[illegible]	[illegible]	[illegible]
22	[illegible]	[illegible]	[illegible]	[illegible]
23	[illegible]	[illegible]	[illegible]	[illegible]
24	[illegible]	[illegible]	[illegible]	[illegible]
25	[illegible]	[illegible]	[illegible]	[illegible]

FLT PTH A
AZ SYSTEM

OBST	RANK	M/D(DB)	DIST	RDOP
[illegible]	[illegible]	[illegible]	[illegible]	[illegible]

AD-A148 524 MLS MULTIPATH STUDIES PHASE 3 VOLUME 3 APPLICATION OF 3/4
MODELS TO MLS ASSES..(U) MASSACHUSETTS INST OF TECH
LEXINGTON LINCOLN LAB J E EVANS ET AL. 08 JUN 81
UNCLASSIFIED ATC-88-VOL-3-PT-2 FAA-RD-79-21-VOL-3-PT2 F/G 17/7 NL

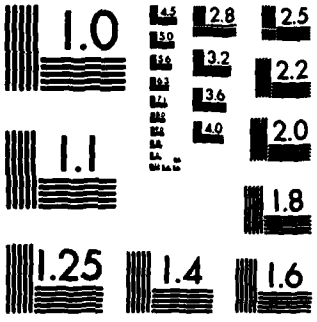

MICROCOPY RESOLUTION TEST CHART
NATIONAL BUREAU OF STANDARDS-1963-A

scalloping frequency) over a data frame (of 30 msec) with one in which the time stationarity is half as long. Appendix A shows that the two models give identical results for reflections from a single large flat homogeneous plate.

Figures 6-58 and 6-59 show the airport map and computed azimuth multipath characteristics using the special version of the propagation model. In a few isolated cases, it can be seen that the multipath level computed at points 15 msec (≈ 6 feet) apart differ (e.g., B28 at ≈ 1230 feet along the flight path), but for the most part the plotted symbols coincide. Figure 6-60 shows the DMLS and TRSB errors using the standard model for TRSB and both DMLS models. We see that the two DMLS models give quite similar errors in terms of peak to peak magnitude and error duration although there are waveform differences. The TRSB dynamic and single scan errors are both low since the multipath is out of beam.*

Simulations with a flight path starting point some 20 feet (≈ 0.1 seconds flight time) prior to the starting point used for the scenario of Figs. 6-58 to 6-60 yielded similar results for the peak to peak error and error region duration, as did simulations with a more detailed runway contour model. It was concluded from these simulations (and, the field data of Vol. I, Chapter III) that the presence of a number of different scattering surfaces with the same nominal scalloping rate does not substantially change the character of DMLS reference scalloping errors.

---

*Australian TRSB flight tests at Sydney showed very low errors in the multipath even though the multipath level occasionally exceeded that of the direct signal [58].

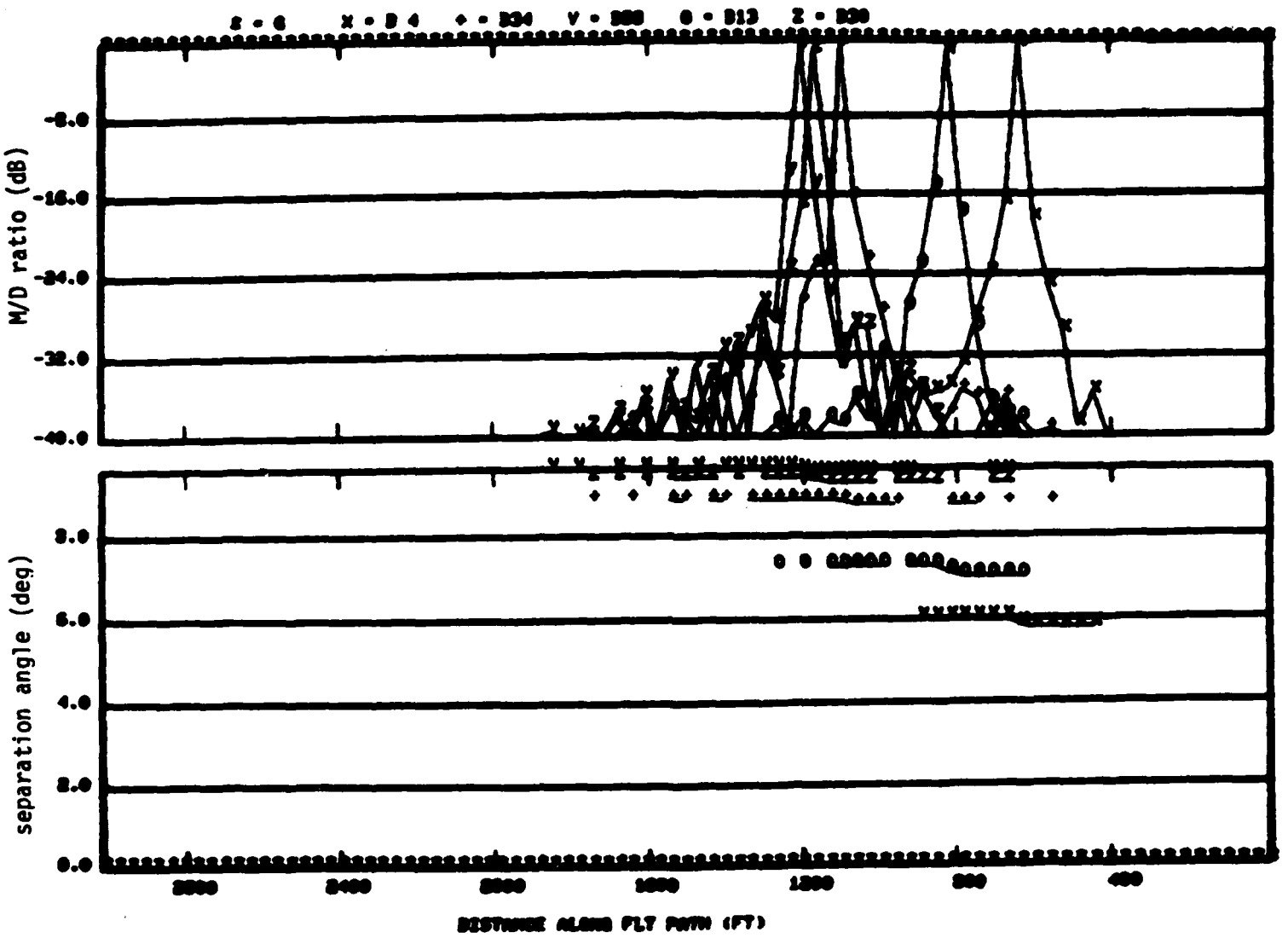

Fig. 6-59. Azimuth multipath diagnostics for scenario of Fig. 6-58.

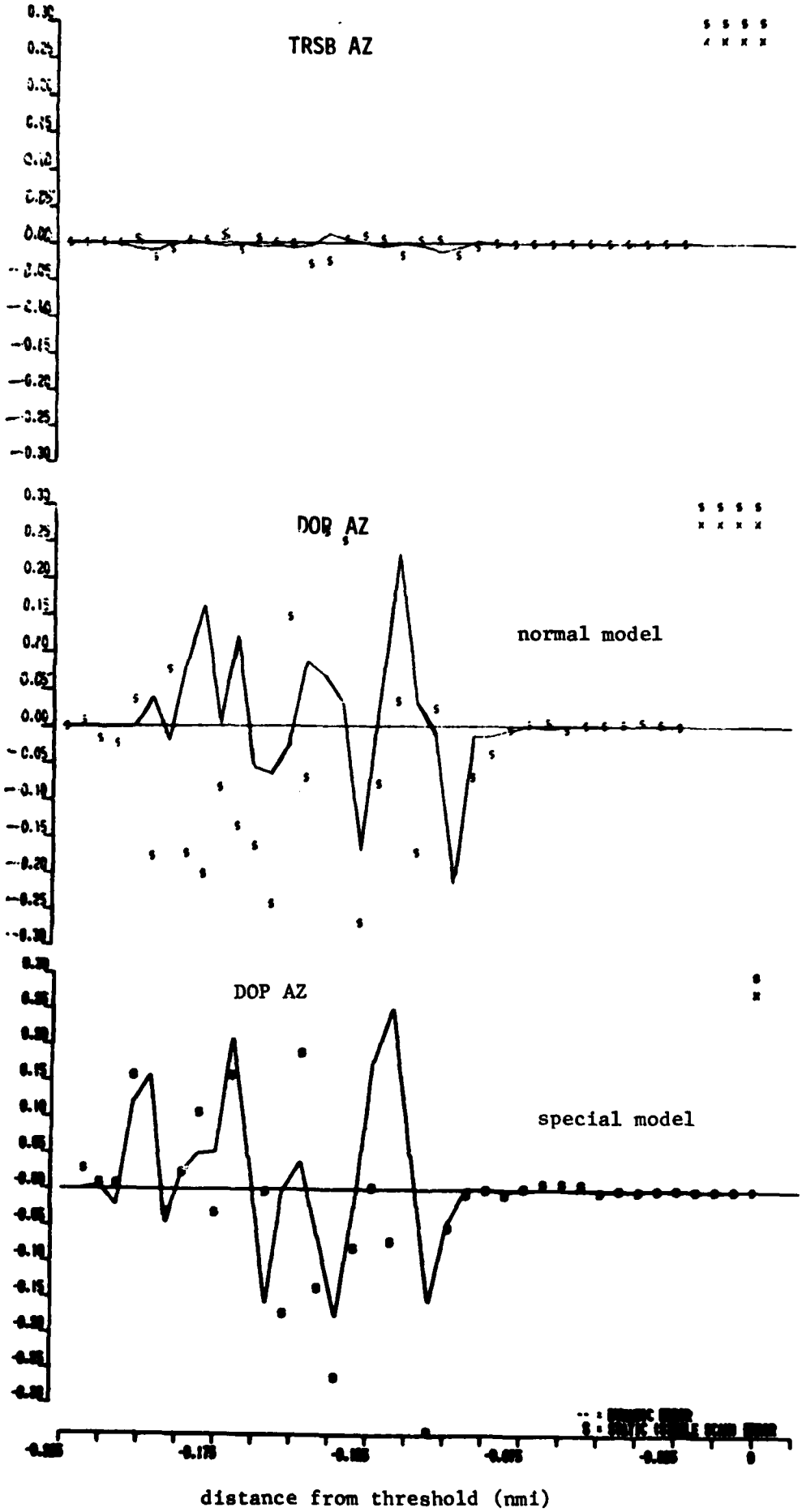

Fig. 6-60. Azimuth error waveforms for "system sensitivity" scenario based on Sydney Airport.

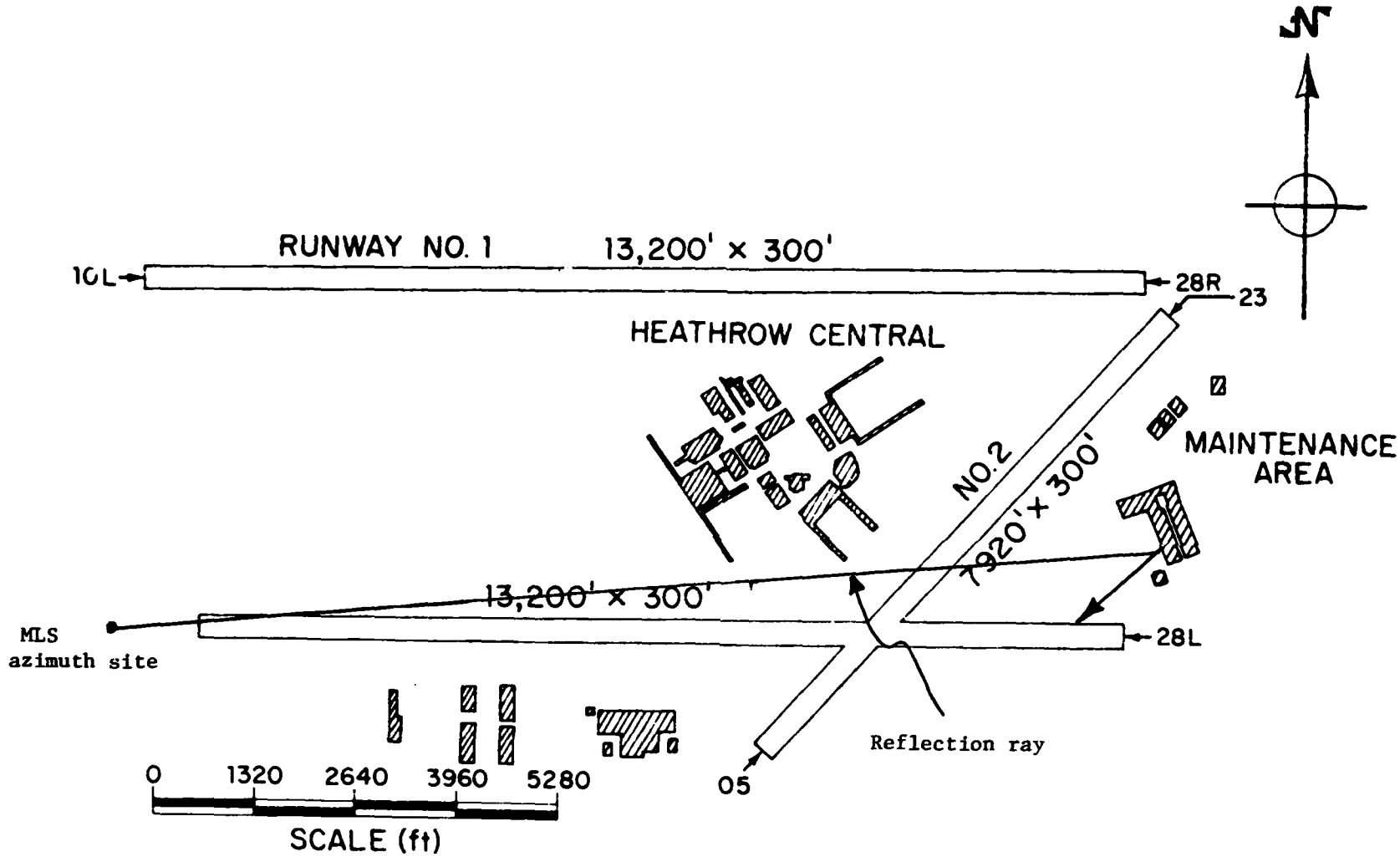

Fig. 6-61. Airport map used to derive array scalloping "system sensitivity" scenario.

4. Array Scalloping Effects Due to a Building

In Fig. 6-61, we show the layout of Heathrow Airport (London) together with reflection rays from a large hangar in the maintenance area assuming that the wall surface scatters like a flat plate. The near edge of the building has an azimuth of approximately 4.1° for an azimuth transmitter sited 1000 ft. beyond the 10R end of the runway. The scalloping rates for azimuth multipath would lie in the region 1200-2000 Hz, depending on the aircraft approach velocity.

This combination of azimuth angle, separation angle and scalloping frequency corresponds to a situation in which array scalloping errors might arise. Therefore a scenario was developed corresponding to the building geometry shown in Fig. 6-61 with the simplifications used for the AWOP comparative simulations.

Figure 6-62 shows the airport representation for the computer simulation. For purposes of the simulation, the building was assumed to be 20 meters high and flat metal. The airplane antenna was assumed to fly down a 20:1 glideslope at a ground speed of 118 knots to a point 160 feet in front of the glide path intercept point and then continue at an eight foot height threafter along the centerline. Figure 6-63 shows the computed multipath characteristics.

Figure 6-64 shows the TRSB and DMLS errors where both systems are utilizing a filled 1° azimuth array. The TRSB single scan and dynamic errors are both seen to be small. The DMLS single scan errors are large; however there is a substantial motion averaging error reduction. It should be noted that the simulation assumed an omnidirectional aircraft antenna. Had a forward

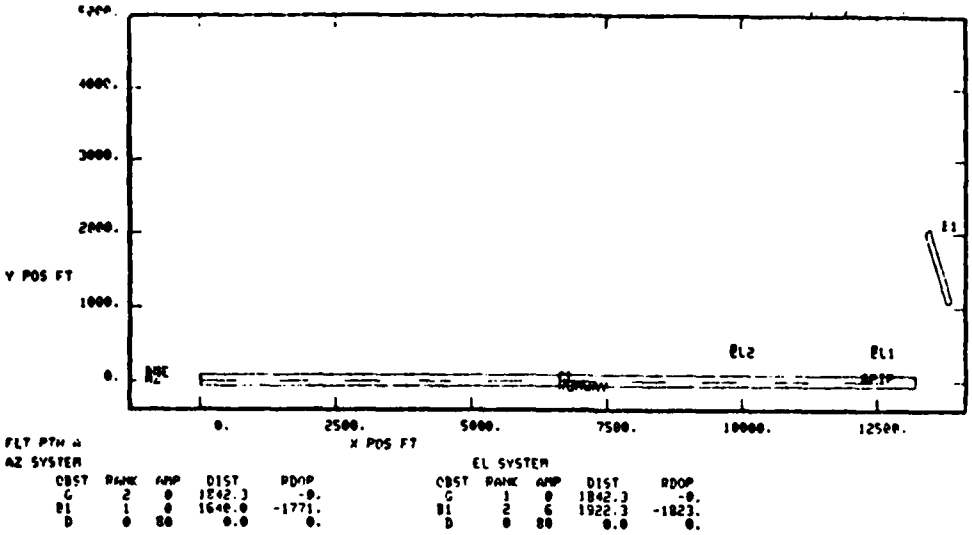

Fig. 6-62. Airport map for array scalloping scenario.

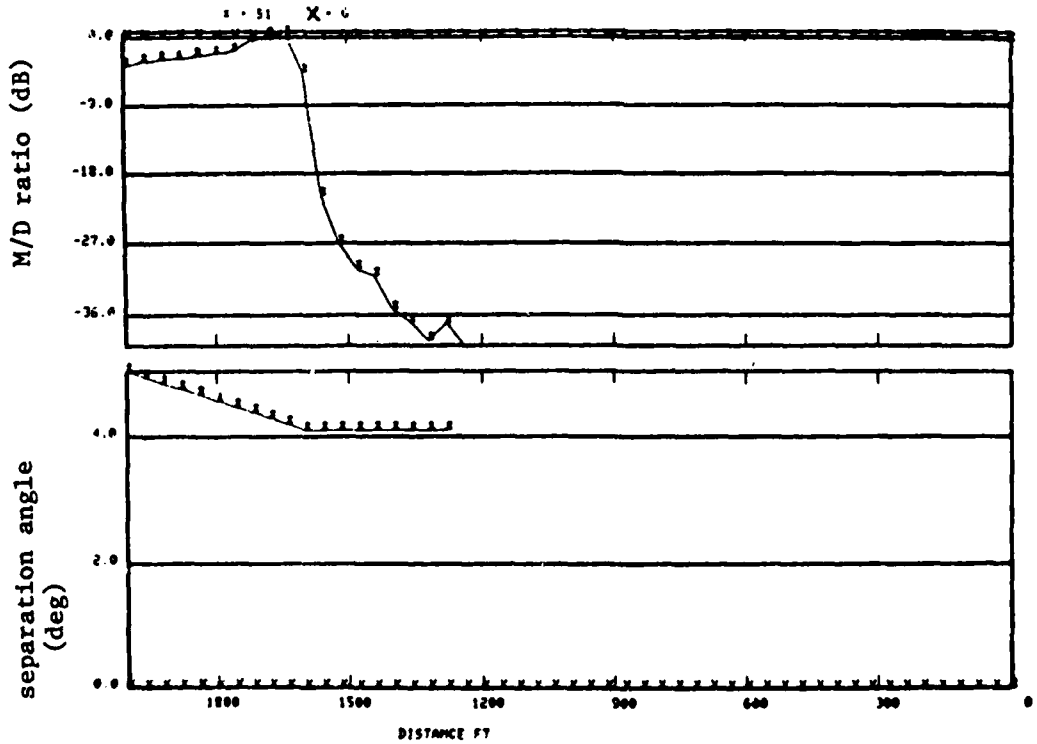

Fig. 6-63. Azimuth multipath characteristics for array scalloping scenario.

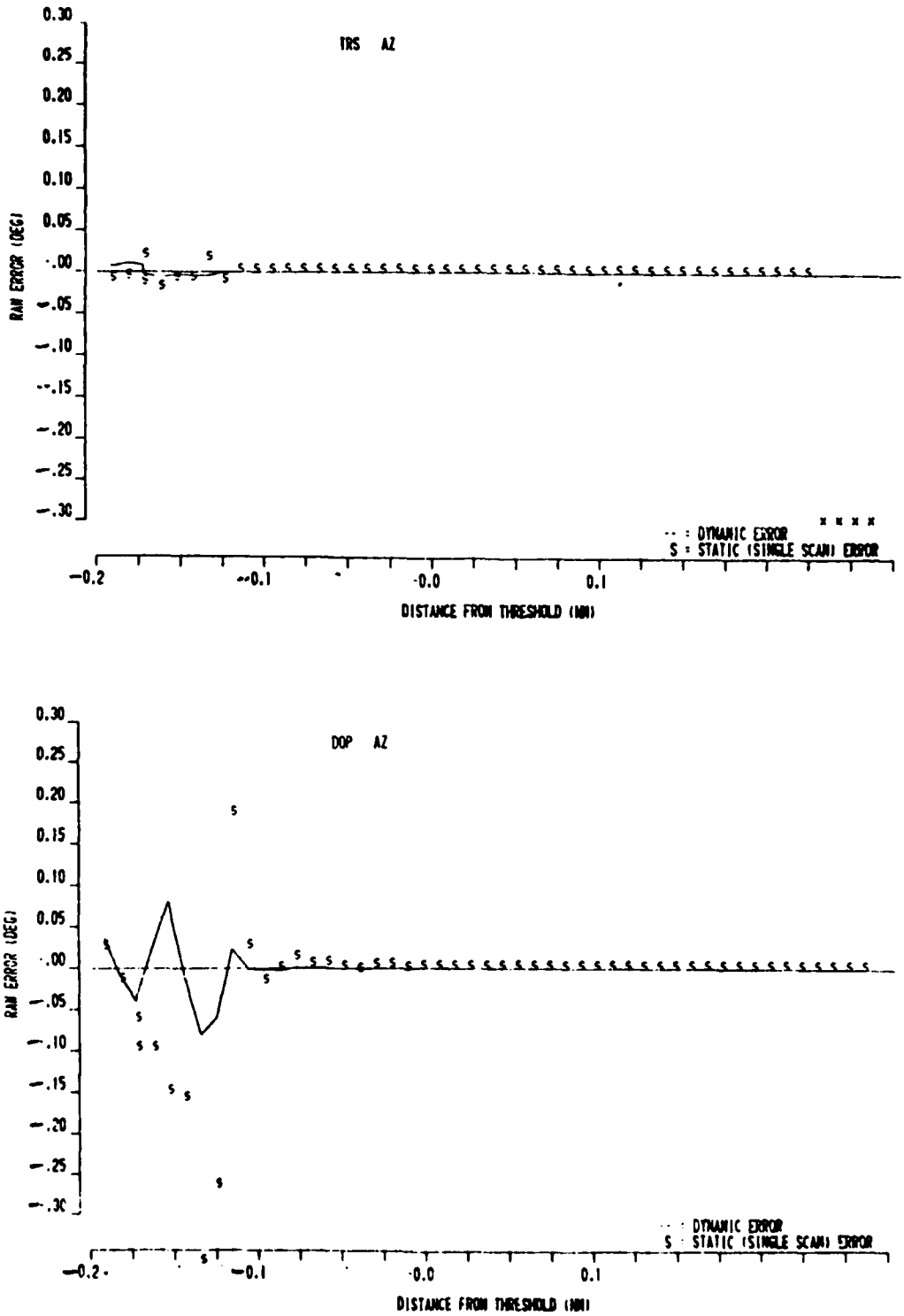

Fig. 6-64. TRSB and DMLS azimuth multipath errors for array scalloping scenario.

looking horn been used as the aircraft antenna, the M/D levels and DMLS error would have been significantly reduced since the multipath is received from the rear sector. This scenario suggests that DMLS array scalloping may not represent as significant a problem as reference scalloping due to the low persistance of the multipath at the motion averaging grating lobe frequencies and the possibility of significantly reducing the M/D level by use of a directional aircraft antenna in the flare region.*

F. Potential Impact of Various DMLS Dynamic Factors on System Implementation

In this chapter, we have analyzed a number of dynamic multipath performance factors unique to the DMLS system which would impact on the capability for system implementation. Time variations in the AGC gain over the period of a DMLS scan were shown to produce sizable variations in the frequency response of the sum and difference filters. These time variations could increase the error by three mechanisms:

(1) the tracker null position may not correspond to the desired position

(2) the mainlobe width (i.e., inbeam region) would increase significantly

and/or

(3) the sidelobe level would rise so as to increase susceptibility to out of beam multipath

Mechanism (1) was found to not be of concern in that the first order changes in sum/difference filter characteristics do not produce a change in tracker null position due to the phase coherent [i.e., IM (Δ/Σ)] processing used.

---

*The likelihood of encountering high level multipath with high scalloping frequencies (e.g., above 1000 Hz) further up the flight path is unlikely due to the geometric constraints.

Similarly the mainlobe widths were found to be little changed. However, the sidelobe levels could increase by 6 dB or more, which would primarily be of concern for the elevation system.

Reference scalloping was analyzed in depth and a detailed study due to ascertain how much error reduction would be achieved by optimizing the scan format sequence. It was determined that the two sequences proposed by the UK ranked quite well in terms of average performance for scalloping frequencies in the range 0-500 Hz although they were relatively poor in performance at a worst case scalloping frequency. Changing the scan format can significantly reduce the errors at a given scalloping frequency, but has certain practical difficulties as a long term solution at a given location since:

(1) aircraft approach velocities and scalloping frequencies for a given flight path and scatterer geometry can vary over an octave (e.g., B707 in still air versus STOL or small propeller aircraft with a head wind), and

(2) new scatterers may be constructed which have geometries leading to worst case scalloping frequencies for the given scan format. Since even with centerline emphasis, reference scalloping errors on final approach could exceed 0.10° for practicable geometries (see scenarios 1 and 3 of this chapter), and off centerline DMLS performance also can be significantly degraded by reference scalloping (see AWOP scenario 5), it was concluded that reference scalloping could create difficulties in long term MLS system implementation at those airports runways (probably less than 15%) where high level azimuth multipath from buildings is encountered.

On the other hand, array scalloping did not appear to be as significant a problem due to the low persistance of poor motion averaging and, the likelihood of significantly reducing the errors if a forward looking antenna were utilized for category III MLS operations.

Lateral diversity was found to be effective at reducing inbeam elevation multipath errors for scatterers (e.g., buildings or aircraft) which have azimuths which are several degrees different from the direct signal azimuth. However, it was not clear that this performance improvement was needed since the DMLS and TRSB performance against reflection elevation multipath was generally adequate in the scenario simulations and in the field tests.

VII. ACQUISITION/VALIDATION (ACQ/VAL) STUDIES

The process of establishing the angular location of the direct signal and validating the correctness of the subsequent track is quite important for the overall MLS integrity, since a highly erroneous position estimate could result if track were to be established on a multipath signal. Out-of-beam azimuth multipath is of the greatest concern in this respect since:

1) Azimuth multipath levels can be significantly increased by ground reflection lobing and/or shadowing effects, whereas the elevation multipath levels are generally lower than that of the direct signal.

2) The large coverage volume in the scanned coordinate means there is a much greater likelihood of encountering significant azimuth multipath at an in-coverage angle which is well removed from that of the direct signal.

3) The azimuth coverge volume generally encompasses a much greater portion of the building complex at the airport.

The nature of the received signal from a multipath source is very similar to that of the direct signal. Consequently, a track established on a strong multipath signal will generally pass the validation tests concerned with tracked signal quality (e.g., angle and signal level consistency), although the angle sense is incorrect.*

Thus, the principal focus in this area was on comparing the capability of the various systems to correctly identify the direct signal in the presence of one or more multipath signals. Acquisition can be thought of as a search in the space of received signals to determine the most likely choice (in a probabilistic sense) of angle for the received direct signal given the past and present received waveforms. Information theoretic considerations (see, e.g., [103]) show that the optimum algorithm in the presence of noise alone is to

---

*Reflected signals are generally not considered to be usable from a flight control viewpoint because the change of indicated angle with changes in aircraft position is reversed from that which arises with valid signals.

maximize the likelihood ratio for the received signals as a function of the direct signal parameters. In the case of additive white Gaussian noise (WGN), the likelihood ratio corresponding to a given signal amplitude is a monotonic function of the output of a (complex) linear filter. Thus, it is conceptually straightforward to compare the likelihood ratios corresponding to each possible direct signal angle.

In the presence of multipath, the optimum processor consists of comparing likelihood ratios corresponding to all possible direct and multipath angles, amplitudes, and phase angles. This optimum algorithm is very complex, and, to the best of our knowledge, has only been attempted in simple cases [138]. Fortunately, in the usual case where the relevant multipath components are at least two beamwidths apart from each other, the noise-only optimum algorithms are very nearly optimum for the range of signal amplitudes encountered.*

Validation has not been characterized well theoretically due to several complicating factors:

(a) "goodness" tests of a given angle track must also consider possible equipment failure

and

(b) the direct and multipath signal amplitudes and angles change as a function of time due to aircraft motion.

In the case of a stationary receiver which ignores the angle track history, the optimal approach is to consider the compound likelihood ratio for all the measurements. For the WGN case and no multipath, this typically reduces to a running summation of the linear filter outputs corresponding to each direct signal angle. When the receiver is allowed to move, summing at a given angle is replaced by a running summation of linear filter outputs corresponding to

---

*Specifically, the likelihood ratio as a function of the angle of a given received component in the vicinity of that component conditional on knowledge of the other component amplitudes, phases, and angles is very similar to the likelihood ratio for the given component in the presence of noise alone.

the various possible aircraft tracks. Since the number of possible tracks becomes very large after relatively short time periods, an "optimum" realization rapidly becomes impractical.

The analysis of acquisition and validation focused on two issues:

(1) The relative direct signal amplitude required to insure that the direct signal is acquired when one or more (lower level) multipath signals are present.

(2) The capability of the reciever to continue tracking an acquired direct signal if a multipath signal of larger amplitude is encountered for a short period of time.

Issue (1) relates to the initial acquisition process, while issue (2) is related to the operational need for providing very high integrity when nearing touchdown.

The following three sections consider ACQ/VAL processing for the TRSB, DLS, and DMLS systems, respectively. The case of TRSB is presented first since the proposed acquisition process is closest in spirit to the optimal system presented above. The DLS discussion is fairly compact, since there have been a number of studies by others on ambiguity resolution in interferometric systems. The proposed DMLS ACQ/VAL process required more extensive analysis, since it utilized some novel algorithms not considered previously in the literature. Section D presents the results of a comparative ACQ/VAL scenario, while Section E summarizes the results.

A. TRSB ACQ/VAL

For scanning beam receivers, the optimum processor for the direct signal in WGN can be closely approximated by filtering the received envelope with a filter matched to the antenna beamshape and determining the time of filter ouptut peak amplitude. Actual TRSB receivers may be viewed as a suboptimum realization in that the video filter is not precisely matched to the received

beam shape. This mismatch is typically in terms of a greater passband than is required. This produces a signal-to-noise (SNR) degradation, but no loss in ability to resolve multiple peaks vis-à-vis that with matched filtering (provided that the ground antenna pattern has low sidelobes). The TRSB coverage region is effectively searched on each scan with an angle grid corresponding to the A/D converter sampling rate (approximately 0.02° for current designs).

Bench tests [92] and our simulations have shown that the current TRSB receivers can successfully establish track on the direct signal as long as its amplitude is at least 1 dB greater than an out-of-beam multipath signal. For multipath levels within 1 dB of the direct signal, no acquisition occurs, while multipath levels within 1 dB of the direct signal will be acquired.

Simulations have shown that similar performance occurs in the presence of several out-of-beam multipath signals, each of which is at least 2 beamwidths removed in angle from any other signal.

Although the TRSB outputs generated on each scan would permit "optimum" track validation, this is not what is done. Rather, the peak amplitude for the tracked signal is compared to the peak amplitude at all "out-of-beam" angles and a counter is incremented or decremented. If the counter decrements to zero, acquisition is restarted. The degradation in performance using this approach is noticeable only when the angle corresponding to an out-of-beam peak greater than the direct signal changes radically between successive scans (e.g., when at low SNR).

Once successful acquisition is completed, the TRSB receivers were shown in field tests to be capable of tracking the direct signal in the presence of short-lived multipath signals which are considerably larger than the direct signal (e.g., 6 dB). The maximum duration for such multipath is a receiver parameter which currently is the lesser of 20 seconds and the time in track.

B. DLS ACQ/VAL

The problem of acquiring the direct signal is simplified somewhat in the DLS system by the time delay discrimination implicit in measurements on a pulse waveform. Multipath with a time delay greater than 1.5 μsec normally would be excluded entirely, while multipath with a shorter duration is effectively attenuated by the factor

$$R_\tau = \exp[-0.227\ (2\tau + \tau^2)] \qquad (7\text{-}1)$$

where τ is the multipath relative time delay in qsec. Figure 7-1 shows contours of R_τ as a function of scatterer location for a case where the receiver is on runway centerline. We see that even in this favorable case,* situations could arise in which the time delay discrimination is very small so that a DLS acquisition algorithm must consider the possibility of large multipath signals.

For a sampled aperture ground derived system such as DLS, the noise only optimum processor corresponds to a multiple beam forming matrix. This could be achieved by hardware [104] or by a software discrete Fourier transform [85]. However, the cost and complexity of achieving this processing in the available computation time evidently were such as to suggest a suboptimum approach based on the small signal suppression properties of a multiple baseline interferometer.

Such systems estimate the direct signal angle by making angle estimates with baselines of increasing length. The angle estimate using the smallest

*The case illustrated is favorable because the receiver is assumed to be along the extended runway centerline. Receivers which are off centerline may encounter reflections from buildings which are quite close to the line of sight.

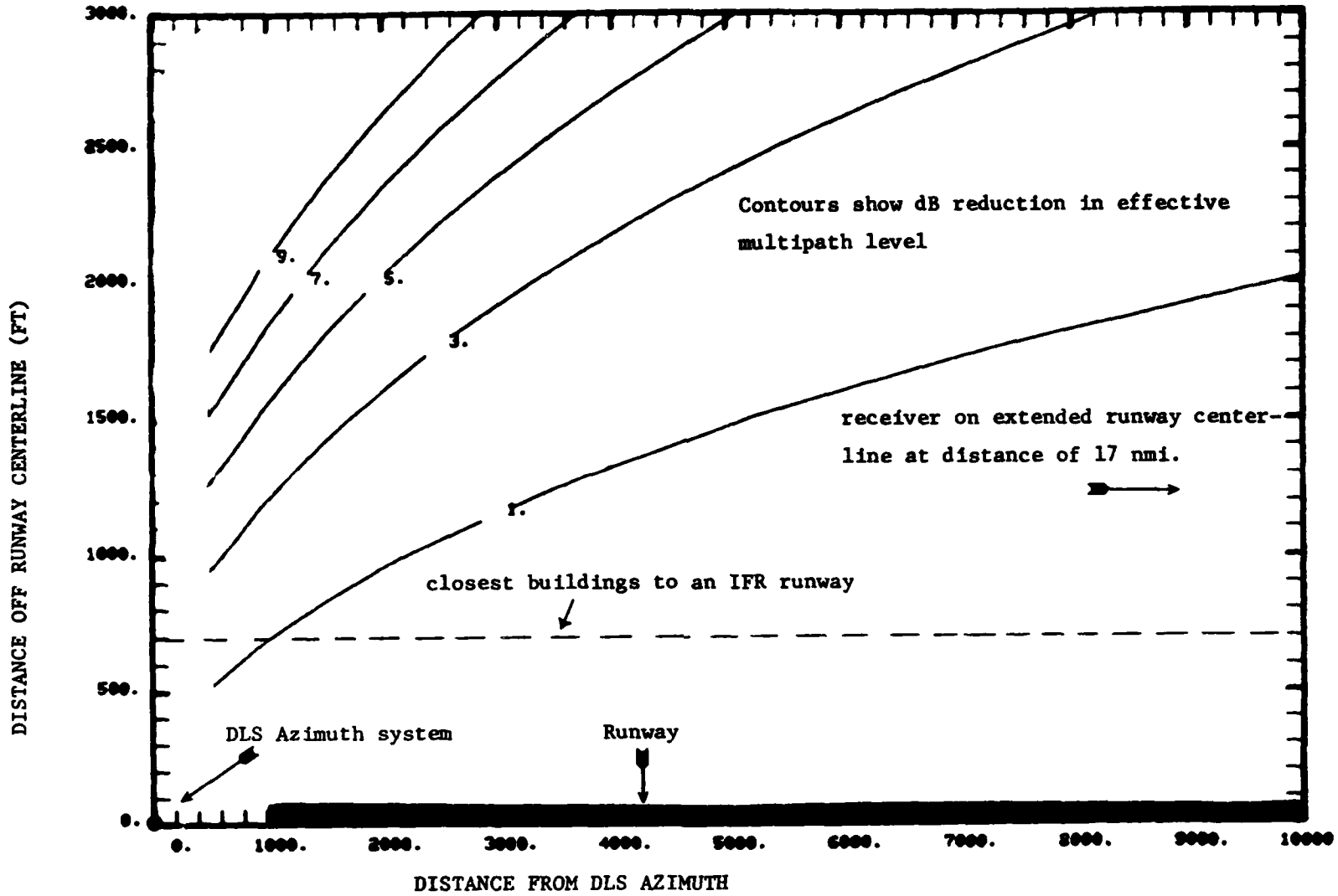

Fig. 7-1. DLS time delay discrimination as a function of scatterer location.

baseline is unambiguous within the coverage volume. The larger baseline angle estimates are ambiguous, but the ambiguity is resolved from the angle estimates using shorter baselines [87]. If out-of-beam multipath causes errors in ambiguity resolution, the resulting angle error is large (e.g., several beamwidths). Thus, the principal focus was on circumstances where ambiguity resolution breakdown occurs.

The likelihood of an error in resolving the ambiguity in the measured phase of a interferometer pair of spacing $\alpha L/\lambda$ from the resolved phase for a pair of spacing L/λ depends on the multipath amplitude, scan angles, and RF phases with respect to the direct signal. Under worst case conditions, it can be shown that errors will not arise if

$$\rho < \sin(\pi/2\alpha) \tag{7-2}$$

where ρ = sum of amplitudes for the various multipath signals. Equation (7-2) shows that the ambiguity resolution stages with large values of α are most vulnerable. The proposed DLS azimuth array consists of an inner circular array with a novel ambiguity resolution scheme and a linear array whose ambiguities are resolved as indicated above. The circular array resolution logic is not readily amendable to analytical treatment such as was used to obtain (7-2). Our simulation experiments have shown that the circular array is most sensitive to these errors, with a minimum single multipath signal amplitude of -7 dB (for multipath approximately 20° removed from the direct signal) being sufficient to cause ambiguity resolution errors.

A more fundamental problem facing DLS in the acquisition/validation area is the lack of any track history in the ground system when making an angle estimate. Since the aircraft interrogation of a DME ground station does not

contain a unique identification code, the DLS system cannot establish a history of previous angle estimates to aid in processing when high multipath levels are encountered. The DLS airborne receiver has a past history of angle estimates which permits the rejection of highly erroneous ground station estimates. Thus, for example, if an out-of-beam multipath signal with relative amplitude $\rho>1$ is encountered during final approach, there could be a total loss of valid angle data with the DLS system. By contrast, systems (such as TRSB or DMLS) with a track memory at the point of angle estimation can continue to estimate the angle of the direct signal if short duration high level multipath is encountered.

C. Doppler ACQ/VAL

For a Doppler receiver, the corresponding noise only "optimum" acquisition consists of a large bank of Doppler filters, one for each possible received Doppler frequency. The receiver is then to choose the largest of these filter outputs. Sampling theory considerations suggest that this could be implemented by a bank of 1 beamwidth wide Doppler filters centered at frequencies 0.5 beamwidths apart, since the output for any other frequency can be obtained by a weighted summation of the equally spaced filter outputs. This approach was not attractive from an airborne cost/complexity viewpoint.

Instead, a suboptimum approach was utilized which trades off SNR, multipath resistance, and acquisition time against equipment complexity by first coarsely estimating the Doppler frequency (by the use of filters which are several beamwidths apart) and then refining that estimate with a second Doppler frequency bank whose filter passbands are 1 beamwidth apart. When only a single signal is present in any given wideband Doppler filter, this coarse/fine approach yields near optimum performance, since the filter outputs

are time smoothed before comparison. In this section, we shall examine the ACQ/VAL procedure proposed by the UK for the digital correlator receiver implementation with particular emphasis on situations where one or more multipath signals are present. The detailed algorithms have already been presented in Sections 3.A.4 and 3.B.3 of Volume II of this report. Figures 3-7 to 3-9 of Volume II, reproduced here as Figs. 7-2 to 7-4, summarize the procedures.

1. Acquisition Algorithm

The initial setting of the tracker frequency is obtained as the result of a two-stage acquisition procedure. Initially, the entire coverage region is divided into a coarse set of "ordinary" frequency "bins," and the filtered detector output on the nth scan $W_n(t)$ (see Eq. (II.3-51)) is correlated with sinusoids and cosinusoids at each of the bin center frequencies $\omega_b(m)$ for an integration time $2T_b$ matched to the bin widths:*

$$C_n(m) = \frac{1}{2T_b} \int_{t_b(m)-T_b}^{t_b(m)+T_b} W_n(t) e^{j\omega_b(m)t} dt, \qquad m = 1, 2, \ldots, \# \text{ bins} \tag{7-3}$$

where

$$2T_b = \frac{2\pi}{\Delta\omega_b} \tag{7-4}$$

$$\Delta\omega_b = \omega_b(m+1) - \omega_b(m) \tag{7-5}$$

---

*The center correlation times $t_b(m)$ vary with bin number across the scan time, as the correlator computational capacity is time-shared among the bins. The values of $t_b(m)$ and of the bin center frequencies are given in Eq. (II.3-64) and Table II.3-2.

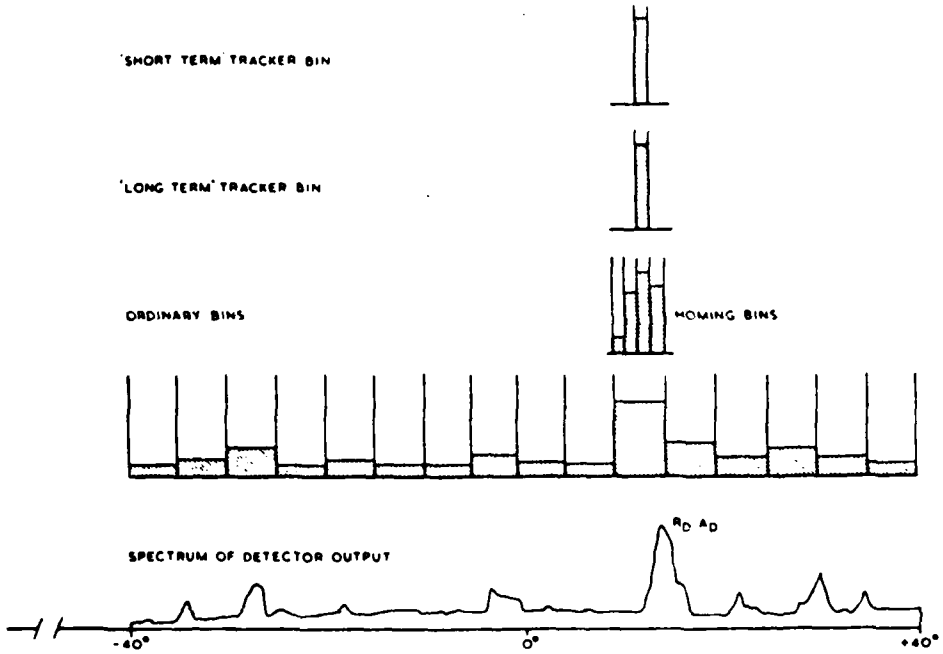

INITIAL ACQUISITION

(a) Coverage sub-divided into 16 bins.

(b) Signal content in each bin measured.

(c) Largest bin or pair of bins gives coarse position by interpolation

FINE ACQUISITION

(a) 4 narrow bins set around coarse position

(b) Process repeated, establishes position within half beamwidth

(c) Set track process to fine position

VALIDATION

(a) Continue measurement of all bins

(b) Confirm that tracked signal corresponds to largest bin position.

CONFIDENCE

(a) Confidence timer (1 sec) incremented when validation is satisfactory, and

(b) tracked signal level is satisfactory compared with its previous history, and

(c) outlier not exceeded,

(d) Otherwise confidence decremented

Fig. 7-2. Summary of DMLS ACQ/VAL (from CAA report [67]).

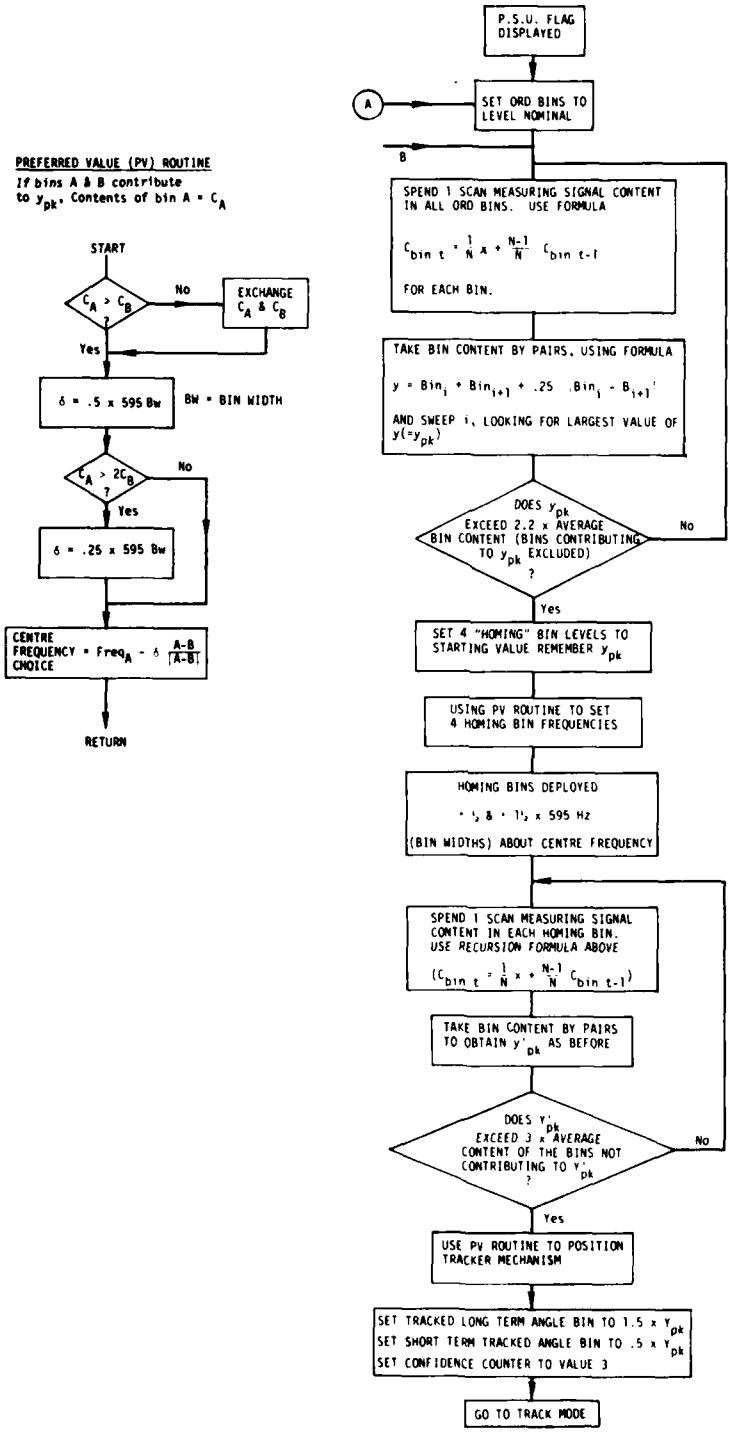

Fig. 7-3. DMLS ACQ/VAL flow chart (from [66]).

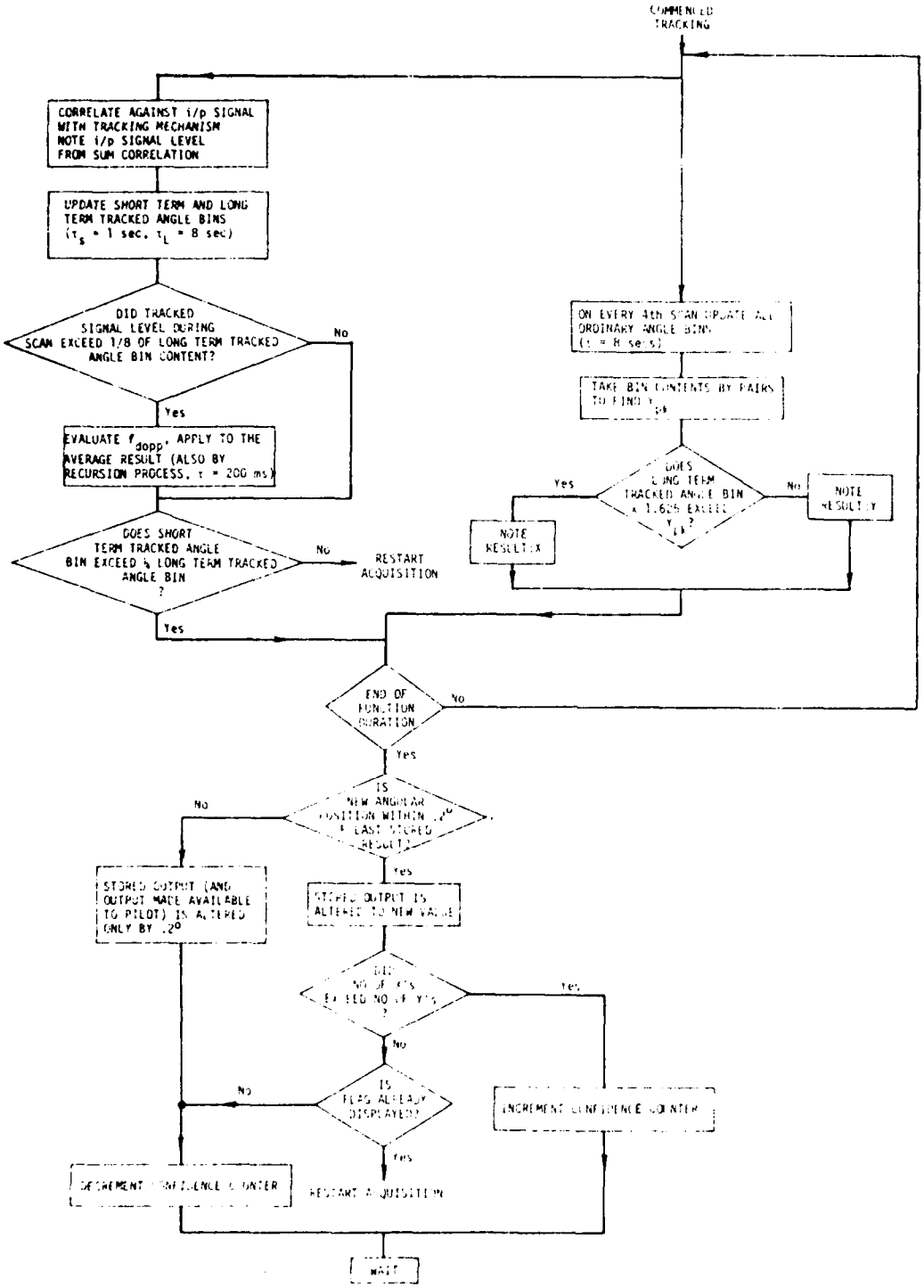

Fig. 7-4. Acquisition/validation for correlation processor.

The complex magnitude* of the correlation output, $C_n(m)$, is passed through a first-order digital filter with a time constant of 5 data frames (1 second) to yiel the bin contents.

The correlation output $C_n(m)$ in response to a single sinusoid at frequency ω, $W_n(t) = \cos(\omega t + \phi)$, is denoted by $X_m(\omega)$ and is calculated as
**

$$X_m(\omega) = \frac{\sin[(\omega_b(m) - \omega)T_b]}{(\omega_b(m) - \omega)T_b} \tag{7-6}$$

Figure 7-5 shows the frequency responses $X_m(\omega)$ for the 16 azimuth coarse bins, plotted as a function of the equivalent signal angle $\theta = \omega/K$, where K is the DMLS coding factor for azimuth. We note that the bin frequency responses at the crossover points are 3.9 dB down from the peak response. This "scallop loss" [54] is quite undesirable from a multipath viewpoint since a multipath signal some 3.8 dB below the direct signal could yield the larger bin contents if the direct signal were located at a crossover point whereas the multipath were at a bin center.

Thus, the DMLS designers utilize a pairwise search of adjacent bins using the algorithm shown in block 3 of Fig. 7-3. The pairwise search metric cannot be represented as the output of a linear filter, i.e., the output for a sum of sinusoids ≠ the sum of the individual outputs. Nevertheless, some insight can be gained by considering the output for a single sinusoid input. The (steady-state) contents of the nth bin pair, $|Y_m(\omega)|$, when the input is a sinusoid at

---

*In both the computer model and the actual receiver, an approximation is used for the complex magnitude function to reduce computation time, see (II.3-67).

**In writing (7-6) we have ignored a complex phase factor, $\exp j[\omega_b(m) - \omega)t_b(m) - \phi]$, as well as an additional term of complex magnitude $|\sin[(\omega_b(m) + \omega)T_b]|$ which is negligibly small for positive ω.

plotted (hexadecimal) number "m" is frequency response for "ord" bin m

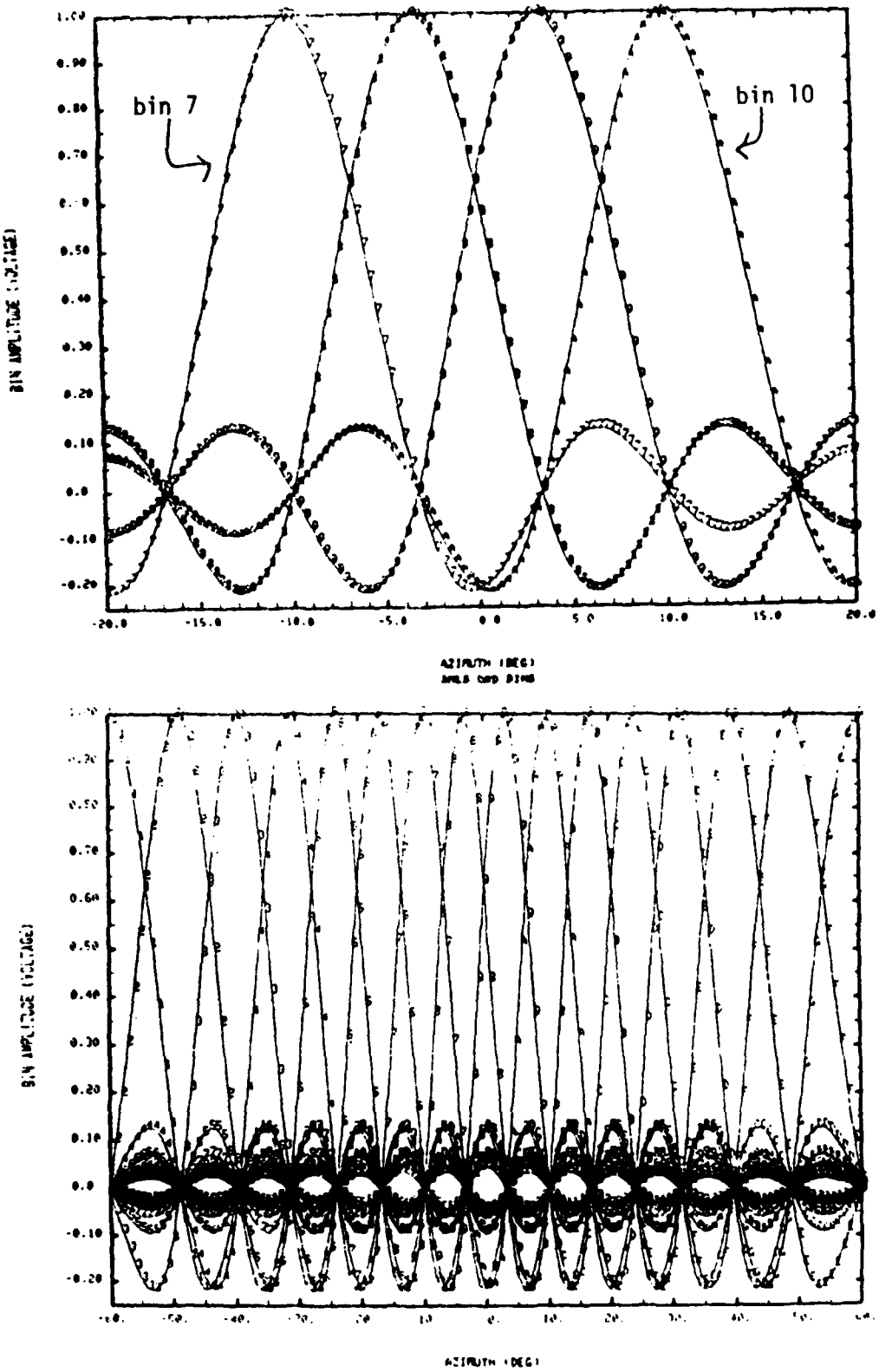

Fig. 7-5. Frequency response characteristic of DMLS "ordinary" acquisition bins.

frequency ω, are calculated from $|X_m(\omega)|$, $|X_{m+1}(\omega)|$ using the pairwise search metric given in (II.3-68),

$$|Y_m(\omega)| = |X_m(\omega)| + |X_{m+1}(\omega)| + \frac{1}{4}\left||X_m(\omega)| - |X_{m+1}(\omega)|\right| \qquad (7\text{-}7)$$

The bin pair responses are plotted in Fig. 7-6. We see that the pairwise outputs are much flatter over the passband (e.g., 0.7 dB peak deviation), but also much wider (13.2° versus 5.9° at the -3 dB points on boresight). The sidelobes are slightly higher (-11.5 dB versus -13.5 dB).

The contents of the largest bin pairs are continually tested against the average contents of the remaining bins. As soon as a suitable excess is built up, the coarse acquisition phase is deemed to be complete and a frequency estimate $\hat{\omega}_b$ is obtained from a coarse interpolation between the center frequencies of the preferred bin pair [see (II.3-71)].

Four homing bins with bin widths equal to one-fourth the coarse bin widths are centered around the coarse frequency estimate $\hat{\omega}_b$. The input signal $W_n(t)$ from each scan is correlated with sinusoids and cosinusoids at each of the homing bin frequencies and the contents of each of the three adjacent bin pairs are computed by the same algorithm used in the coarse search. Eventually an initial setting for the tracker frequency is obtained by interpolating between the center frequencies of the preferred homing bin pair.

The homing bins and adjacent pair combinations have frequency responses identical to that of Figs. 7-5 and 7-6 except that the frequency scale is compressed by a factor of 4, i.e., the "passband" is 4 times smaller. The homing bin search process evidently utilizes the entire processor computational capability since no coarse bin updating takes place while the homing bin search is going on.

(hexadecimal) numeral m denotes output of "ord" bins m and m+1

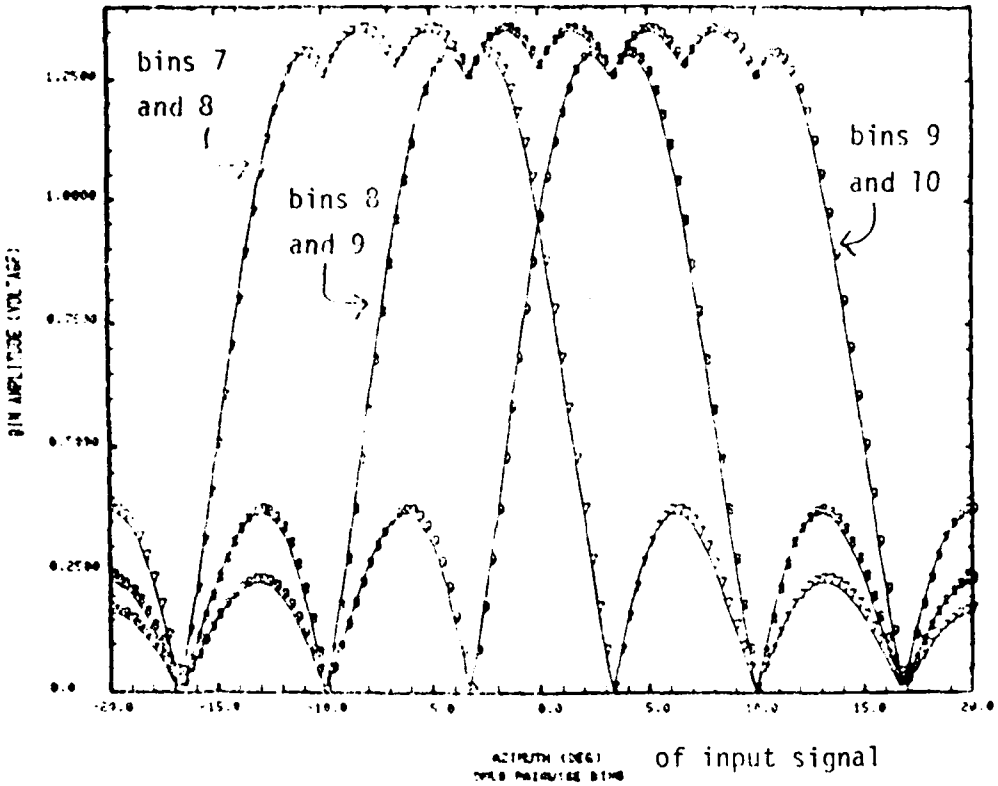

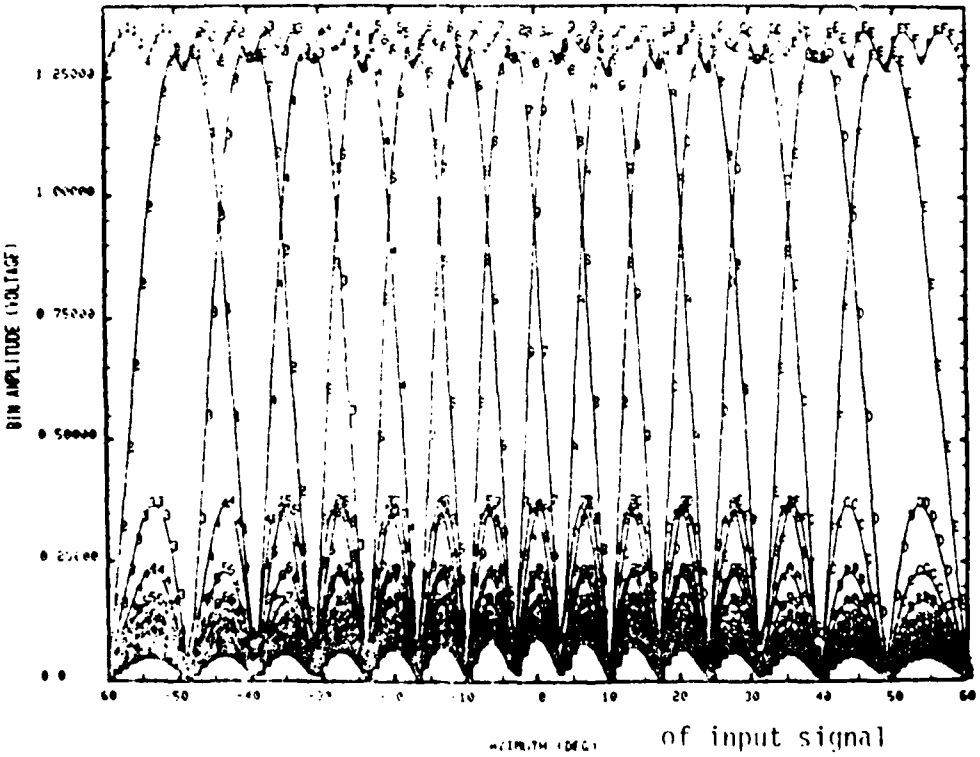

Fig. 7-6. Output of DMLS pairwise "ordinary" bin summations for single input signal.

The coarse frequency estimate $\hat{\omega}_b$ always lies between the center frequencies $\omega_b(m)$, $\omega_b(m+1)$ of the preferred bin pairs; in fact, the interpolation algorithm always produces an estimate in the interval $[\omega_b(m) + \frac{1}{4}\Delta\omega_b, \omega_b(m+1) - \frac{1}{4}\Delta\omega_b]$, where $\Delta\omega_b = \omega_b(m+1) - \omega_b(m)$. The initial tracker setting bears the same relation to the frequencies of the preferred homing bin pair. Thus, the starting tracker frequency is never more than $\frac{1}{4} \times$ homing bin width ($= \frac{1}{16} \times$ coarse bin width $= 0.4°$ on boresight for the 1° azimuth system) outside the interval $[\omega_b(m), \omega_b(m+1)]$. The "pull in" range of the DMLS tracker is approximately 1.5° (= distance to the first sum pattern null). Consequently, if the direct signal is more than ≈ 1.9° outside the interval $[\omega_b(m), \omega_b(m+1)]$, it is unlikely that the tracker will find the direct signal frequency without reacquisition.

Note also that there is no peak-to-peak amplitude comparison tolerancing in either pairwise bin search, i.e., as long as the pairwise search peak is $> K_b\bar{c}$ (where K_b is a constant and $\bar{c}$ = average bin content) a decision is made even though another peak may be very close to the given peak. We mention this because there is, even with the pairwise bin search procedure, a variation in peak level that depends on the (unknown) location of the component with respect to the bin center.

2. Validation Algorithm

The principal validation input from the tracker is the sum correlation value $\Sigma(n)$. This has a frequency response similar to that of the ordinary bins in Fig. 7-5 except that a) the bandwidth is 1 beamwidth and b) the sidelobes are lower (due to Taylor weighting). Three classes of tests occur:

(1) current $|\Sigma(n)| > \frac{1}{8}$ weighted long time average of $|\Sigma(\cdot)|$

(2) short term average $|\Sigma(\cdot)| > \frac{1}{4}$ long term time average $|\Sigma(\cdot)|$

(3) long term time average of $|\Sigma(\cdot)| \times 1.91 >$ coarse bin pairwise search peak.*

A new $\Sigma(n)$ value is determined on each scan n. Failing test (1) causes that scan to be ignored, but the frame will still be accepted as long as one scan passes test (1).

Test (2) is intended to give a "fast dropout" if the tracked signal "disappears". The time required for this to occur depends on the state of the two averages when the tracked signal disappears. If the two averages were equal (corresponding, e.g., to a track which had existed for 8 seconds), the "unlock time" is (approximately) the solution to the equation

$$e^{-t/\tau_s} = 0.25e^{-t/\tau_L} \tag{7-8}$$

where τ_S = time constant for "short term" average

τ_L = time constant for a "long term" average

Substituting $\tau_S = 1$ and $\tau_L = 8$, we find the "fast unlock" time is:

$$t = -\frac{8}{7} \ln 0.25 = 1.6 \text{ seconds} \tag{7-9}$$

The principal test for a larger out of beam signal is accomplished by comparing the "long term" time average of the tracker output to the peak value from the coarse bin pairwise search. Three features of this test deserve special note:

(1) There is no comparison of the frequency corresponding to the coarse bin search peak with the tracked frequency.

(2) The tracker "long term" average is emphasized by some 5.6 dB before the comparison. Some 2.6 dB of the emphasis arises because the pairwise search maximum (see Fig. 7-6) for unity

---

*The original UK documentation (see Fig. 7-4) used 1.625 as the comparison ratio however, during the course of UK/LL discussions concerning the UK receiver for the proposed DMLS US tests in the UK [78] it was learned that 1.91 was the preferred value.

direct signal is 1.35 when the tracker output is 1.0. The remaining 3.0 dB emphasis is intended as a margin against "persistent multipath".

(3) Failing this comparison test with the flag already displayed does not cause reacquisition if the outlier test also fails. Presumably this is done to avoid "nuisance" reacquisition when the SNR is low.*

If the various validation tests are passed, the confidence counter is incremented at the frame end. This counter is set to a value of 3 at the end of fine acquisition; consequently, provided that the ordinary and fine acquisition procedures are completed within a total of 11 scans, the confidence counter can normally achieve a value of 4 by the end of the first frame. If it counts up by 1 each succeeding frame (= 0.2 second interval), it would reach a value of 8 after a total of 5 frames (= 1 second) and then raise the system flag (see Fig. 7-4), allowing the tracked angle estimate to be given credibility and output to the user.

3. Potential Problems with the Proposed DMLS ACQ/VAL Procedure

In this section, we discuss some of the unique** potential problems with the DMLS ACQ/VAL scheme. Our objective is to provide an analytical framework for understanding situations which may cause problems for the DMLS ACQ/VAL algorithms.

a. Initial Acquisition

The most obvious potential problem with the proposed DMLS coarse search procedure is the possibility that several multipath signals, each of which is

---

*E.g., the AWOP WG-A power budget subgroup used a 2σ error of 0.1° to define the minimum angle data SNR. Below this SNR single excursion errors greater than 0.2° should be "common", which in turn would yield outlier test failures.

**e.g., problems that do not arise to the same degree with the TRSB or DLS approaches to ACQ/VAL.

less than the direct signal, may be contained in adjacent coarse bins such that the pairwise search procedure chooses a bin pair containing multipath rather than the direct signal. This was the situation considered in an ACQ/VAL comparative simulation presented at AWOP 6 [79], discussed further in Section D of this chapter. It was shown that certain multipath conditions exist which cause the DMLS acquisition procedure to fail, while producing no corresponding problems for TRSB. The important difference between TRSB and DMLS in this respect is that similar TRSB problems would arise only if separate azimuth multipath sources had angles within a beamwidth of each other.

The acquisition/validation scenario of AWOP WP/322 [79] produced multipath components near the centers of bins 5 and 6 with M/D ratios of approximately -5.0 dB and -3.5 dB at the start of acquisition. A study was undertaken to investigate whether the acquisition failure reported in WP/322 was an *anomalous effect resulting from a rare* conjunction of unfavorable scenario parameters, or whether it demonstrated a more general problem. As expected, it was found that false initial acquisition can be caused by a pair of multipatn components in bins 5 and 6 with M/D ratios similar to the ones considered over a wide range of phase conditions and angle locations within the bins. The results of this study are presented in Section (ii) below.

Additional analysis has shown that a <u>single</u> multipath component whose M/D ratio is < -1 dB can also create significant initial acquisition errors if it is within 2 <u>coarse bin</u> widths* of the direct signal. This phenomenon is quantitatively examined in the next section.

---

*The corresponding statement for TRSB is two <u>beamwidths</u>.

(i) Acquisition Failures Due to a Single Out-of-Beam Multipath Component

The direct signal was located at 0° azimuth which is midway between the coarse bins 8 and 9 (see Fig. 7-5). In the absence of multipath, the 8/9 pair* (see Fig. 7-6) of coarse bins is by far the largest. The homing bins are centered about the direct signal so that the homing bin search yields the direct signal frequency as the initial tracker estimate.

We then considered whether acquisition will be successful in the presence of a single out-of-beam multipath signal whose M/D level is < -1 dB which is located at least 6.6° (i.e., a coarse bin width) away from the direct signal. From the discussion in Section 1.a, it follows that a sufficient condition for failure in this case is that the coarse acquisition choose either the 7/8 or 9/10 pair of coarse bins as opposed to the 8/9 pair (see Fig. 7-6a), because the direct signal is 3.3° outside the intervals $[\omega_b(7), \omega_b(8)]$ and $[\omega_b(9), \omega_b(10)]$.

Due to the symmetry around 0° azimuth it suffices to consider only the cases where the coarse acquisition chooses the 7/8 pair. From the pairwise search equation, we see that this will occur whenever the contents of coarse bin 7 are greater than those of coarse bin 9.** By inspection of the coarse bin frequency responses (see Fig. 7-4a), we see that such an error can arise in two ways:

(1) the multipath is located in bin 7 and sums up with the direct signal sidelobe so as to make the contents of bin 7 greater than those of bin 9 and

(2) the multipath is located near the boundary of coarse bins 9 and 10 and out of phase with the direct signal so that the contents of bin 9 become less than those of bin 7.

---

*I.e., the pair consisting of coarse bins 8 and 9.

**Unless another incorrect bin pair outranks both 7/8 and 8/9.

Since the contents of a single coarse bin are a coherent sum of contributions from the various detected signal components, the minimum multipath level needed to cause an error depends on the relative rf phase between the direct and multipath signals. In Tables 7-1 and 7-2 we summarize the results for minimum M/D levels required to yield a choice of the 7/8 bin pair.

Again, since coarse bin 8 is common to pairs 7/8 and 8/9, an incorrect choice will be made whenever bin 7 is greater than bin 9. Thus, the results in these tables can be explained by reference to Fig. 7-5a. To illustrate, with the multipath at -10°, and 180° relative phase,

contents of bin 7 = $|-\rho - 0.212|$
contents of bin 9 = $|0.637|$
contents of bin 7 are > contents of bin 9 if $\rho > 0.425 = -7.4$ dB

The value quoted in Table 7-1 ($\rho = 0.44 = -7.1$ dB) is slightly conservative because a finite search grid (spacing: $\Delta\rho = 0.01$) was used.

Since the multipath rf phase is unpredictable on the basis of gross flight path/airport geometry details, we conclude that there is a possibility of encountering phase conditions which would cause false acquisition for all of the azimuth angles listed in Tables 7-1 and 7-2. A measure of the likelihood of these multipath phases can be obtained by computing the fraction of uniformly spaced phase samples for which false acquisition occurs, as a function of M/D level; these results are presented in Table 7-3.* The phase

*These fractions are not directly interpretable as acquisition failure probabilities in dynamic situations where nonzero scalloping frequencies cause the multipath rf phases to change from scan to scan. If several scans are needed to complete ordinary acquisition, some phase averaging will occur, tending to diminish those failure probabilities which are $< 1/2$ and to increase those which are $> 1/2$. The magnitude of this effect depends on the interplay of many factors, such as the scan-to-scan phase correlation, the amount by which the M/D level exceeds the false acquisition threshold, and the time constant for updating the ordinary bins, and the rule for declaring ordinary acquisition completed.

TABLE 7-1
MINIMUM M/D OF SINGLE MULTIPATH SIGNAL AT BOUNDARY OF COARSE BINS 9 AND 10 TO YIELD ERRONEOUS ACQUISITION CHOICE OF 7/8 PAIR WHEN MULTIPATH AZIMUTH = +6.6°

MULTIPATH RF PHASE	MINIMUM M/D RATIO (dB)
-150° to +150°	> -1
± 160°	-3.9
± 170°	-4.7
± 180°	-5.0

TABLE 7-2
MINIMUM M/D OF SINGLE MULTIPATH SIGNAL IN COARSE BIN 7 TO YIELD ERRONEOUS COARSE ACQUISITION CHOICE OF 7/8 PAIR

MULTIPATH RF PHASE	MULTIPATH AZIMUTH				
	-12.6°	-11.3°	-10°	-8.7°	-7.3°
0	-0.9 dB	-0.9 dB	-1.3 dB	-1.7 dB	-0.9 dB
± 22.5°	-0.9 dB	-0.9 dB	-1.7 dB	-1.9 dB	-0.9 dB
± 45°	-0.9 dB	-0.9 dB	-1.9 dB	-1.9 dB	-0.9 dB
± 67.5°	-0.9 dB	-2.4 dB	-3.1 dB	-2.9 dB	-1.5 dB
± 90°	-1.3 dB	-3.1 dB	-3.6 dB	-3.3 dB	-1.9 dB
± 112.5°	-3.6 dB	-5.4 dB	-5.4 dB	-4.4 dB	-1.3 dB
± 135°	-4.7 dB	-6.0 dB	-6.0 dB	-4.7 dB	-2.6 dB
± 157.5°	-6.4 dB	-8.0 dB	-7.5 dB	-5.7 dB	-2.2 dB
± 180°	-6.0 dB	-7.5 dB	-7.1 dB	-5.7 dB	*

*The 7/8 pair outranks the 8/9 pair for M/D > -2.5 dB, but the 7/8 pair is never chosen. For -3.3 dB < M/D < -2.4 dB, the largest pair is 9/10. For M/D > -2.4 dB, the 6/7 pair is chosen.

TABLE 7-3
FRACTION OF UNIFORMLY SAMPLED PHASE CONDITIONS CAUSING ERRONEOUS COARSE ACQUISITION SELECTION OF 7/8 PAIR FOR VARIOUS M/D LEVELS OF SINGLE-COMPONENT MULTIPATH AT AZIMUTH ANGLES GIVEN IN TABLES 7-1 AND 7-2

MULTIPATH AZIMUTH	-6 dB	-5 dB	-4 dB	-3 dB	-2 dB	-1 dB
-12.6°	.19	.19	.31	.44	.44	.56
-11.3°	.31	.44	.44	.56	.69	.69
-10.0°	.31	.44	.44	.69	.69	1
-8.7°	0	.19	.44	.56	.69	1
-7.3°	0	0	0	0*	.25*	.62*
+6.6°	0	.03	.08	.14	.14	.14

*See footnote to Table 7-1.

samples were -170° to +180° in 10° steps for multipath azimuth = +6.6°, and -157.5° to +180° in 22.5° steps for the remaining angles.

We see that situations of type (2) in which the multipath at the bin 9/10 border indirectly causes selection of the 7/8 pair are much less likely than situations of type (1). We chose to include them because they have nonzero probability and, when they occur, they pose unique problems to the fine acquisition search (see below). Type (1) conditions causing false coarse acquisition are encountered at reasonable M/D levels for a wide range of phases at all azimuth angles within bin 7.

(ii) Acquisition Failures Due to Two Out-of-Beam Multipath Components in Adjacent Bins

A detailed analysis was carried out for perturbations of the case considered in the AWOP 6 scenario [79]. The direct signal was placed at the bin 8/9 border (i.e., 0° azimuth). A pair of multipath components was placed in bins 5 and 6 with independently varying amplitudes, azimuth angles, and static relative phases, and the DMLS ordinary acquisition algorithm was tested to determine which multipath conditions would cause selection of an incorrect bin pair. Not considered were the fine acquisition procedure, track and loss of track of the multipath, and re-acquisition, because as discussed earlier, an error in the initial bin pair choice is generally sufficient to unduly delay true acquisition.

Tables 7-4 through 7-6 give, as a function of the phases of the multipath components, the minimum equal-amplitude multipath level needed to cause false acquisition, for various multipath azimuth angles within bins 5 and 6. The equal-amplitude constraint has been imposed to make the presentation of results manageable, given the many independent variables considered. The

TABLE 7-4
MINIMUM M/D (DB) OF EQUAL-AMPLITUDE MULTIPATH SIGNALS IN COARSE BINS 5 AND 6 (CENTER OF BIN 5) TO CAUSE FALSE ACQUISITION

ϕ_5, θ_5 = rf Phase (degrees), Azimuth Angle of Multipath Component in Bin
ϕ_6, θ_6 = rf Phase (degrees), Azimuth Angle of Multipath Component in Bin

ϕ_6 \ ϕ_5	-135	-90	-45	0	45	90	135	180	
0	-4.7	-3.3	-1.9	-1.3	-1.9	-3.3	-4.7	-5.4	θ_5 = -23.9°
45	-5	-4.2	-3.1	-1.7	-1.1	-2.2	-3.6	-4.7	(bin 5 center)
90	-4.2	-3.6	-3.1	-1.9	*	-0.9	-2.2	-3.3	
135	-4.2	-3.9	-4.2	-3.6	-3.6	-3.6	-3.9	-3.6	θ_6 = -13.4°
180	-5	-5	-5	-5	-5	-5	-5	-5	(bin 6/7 border)

ϕ_6 \ ϕ_5	-135	-90	-45	0	45	90	135	180	
0	-5.4	-4.4	-3.6	-3.1	-3.6	-4.4	-5.4	-6	θ_5 = -23.9°
45	-6	-5	-4.4	-3.6	-3.1	-3.6	-4.4	-5.4	(bin 5 center)
90	-5	-4.7	-4.2	-3.1	-2.4	-2.6	-3.6	-4.2	
135	-3.6	-3.6	-3.3	-2.9	-1.9	-1.7	-2.9	-2.9	θ_6 = -15.1°
180	-1.9	-2.4	-2.6	-2.6	-2.6	-2.4	-1.9	-1.9	

ϕ_6 \ ϕ_5	-135	-90	-45	0	45	90	135	180	
0	-5.4	-4.7	-4.4	-4.4	-4.4	-4.7	-5.4	-5.4	θ_5 = -23.9°
45	-5.7	-4.7	-5	-4.4	-4.4	-4.4	-5	-5.4	(bin 5 center)
90	-5	-4.4	-4.2	-3.6	-3.6	-3.9	-4.4	-4.7	
135	-4.4	-3.1	-3.3	-2.9	-2.9	-3.3	-3.9	-4.2	θ_6 = -16.8°
180	-3.6	-3.1	-2.6	-2.4	-2.6	-3.1	-3.6	-3.9	(bin 6 center)

ϕ_6 \ ϕ_5	-135	-90	-45	0	45	90	135	180	
0	-3.6	-4.2	-4.7	-4.7	-4.7	-4.2	-3.6	-3.3	θ_5 = -23.9°
45	-3.3	-3.1	-3.9	-4.4	-4.7	-4.7	-4.2	-3.9	(bin 5 center)
90	-3.6	-2.4	-2.6	-3.1	-4.2	-5	-4.7	-4.4	
135	-4.4	-2.2	-1.3	-1.3	-2.6	-4.2	-5	-5	θ_6 = -18.5°
180	-4.4	-3.1	-1.1	*	-1.1	-3.1	-4.4	-5	

ϕ_6 \ ϕ_5	-135	-90	-45	0	45	90	135	180	
0	*	-3.3	-5	-5.4	-5	-3.3	*	*	θ_5 = -23.9°
45	*	*	-3.3	-5	-5.7	-5.4	-3.6	-1.1	(bin 5 center)
90	-1.3	*	*	-3.1	-4.4	-5.7	-5	-4.2	
135	-4.4	*	*	*	-2.9	-4.7	-6	-5.4	θ_6 = -20.3°
180	-4.7	-3.1	*	*	*	-3.1	-4.7	-5.7	(bin 5/6 border)

*Threshold M/D > -0.9 dB

TABLE 7-5
MINIMUM M/D (DB) OF EQUAL-AMPLITUDE MULTIPATH SIGNALS IN COARSE BINS 5 AND 6 (CENTER OF BIN 6) TO CAUSE FALSE ACQUISITION

ϕ_5, θ_5 = rf Phase (degrees), Azimuth Angle of Multipath Component in Bin 5
ϕ_6, θ_6 = rf Phase (degrees), Azimuth Angle of Multipath Component in Bin 6

ϕ_6 \ ϕ_5	-135	-90	-45	0	45	90	135	180	
0	-1.7	-4.4	-6	-6.7	-6	-4.4	-1.7	*	θ_5 = -20.3°
45	*	-1.5	-4.4	-6.4	-6.4	-5.7	-3.9	-1.1	(bin 5/6 border)
90	*	*	*	-3.3	-4.7	-5.7	-5.4	-3.1	
135	-3.1	*	*	*	-2.9	-4.7	-5	-4.7	θ_6 = -16.8°
180	-4.2	-2.9	*	*	*	-2.9	-4.2	-5	(bin 6 center)

ϕ_6 \ ϕ_5	-135	-90	-45	0	45	90	135	180	
0	-3.6	-4.2	-5	-5.4	-5	-4.2	-3.6	-3.6	θ_5 = -22.1°
45	-3.6	-3.6	-4.7	-5.4	-5.4	-5.4	-4.7	-3.6	
90	-3.3	-2.4	-2.6	-3.3	-4.2	-5	-5	-3.9	θ_6 = -16.8°
135	-3.6	-1.9	-1.3	-1.1	-2.6	-3.9	-4.2	-4.2	(bin 6 center)
180	-3.9	-2.9	-1.3	*	-1.3	-2.9	-3.9	-4.4	

ϕ_6 \ ϕ_5	-135	-90	-45	0	45	90	135	180	
0	-5.4	-4.7	-4.4	-4.4	-4.4	-4.7	-5.4	-5.4	θ_5 = -23.9°
45	-5.7	-4.7	-5	-4.4	-4.4	-4.4	-5	-5.4	(bin 5 center)
90	-5	-4.4	-4.2	-3.6	-3.6	-3.9	-4.4	-4.7	
135	-4.4	-3.1	-3.3	-2.9	-2.9	-3.3	-3.9	-4.2	θ_6 = -16.8°
180	-3.6	-3.1	-2.6	-2.4	-2.6	-3.1	-3.6	-3.9	(bin 6 center)

ϕ_6 \ ϕ_5	-135	-90	-45	0	45	90	135	180	
0	-5.7	-4.7	-3.6	-2.9	-3.6	-4.7	-5.7	-6	θ_5 = -25.7°
45	-6	-5	-4.2	-3.1	-2.9	-3.3	-4.4	-5.7	
90	-5	-4.7	-4.2	-2.9	-2.4	-2.9	-3.6	-3.9	θ_6 = -16.8°
135	-3.9	-3.3	-3.9	-3.1	-2.4	-2.4	-2.2	-2.9	(bin 6 center)
180	-2.6	-2.9	-2.6	-2.9	-2.6	-2.9	-2.6	-2.4	

ϕ_6 \ ϕ_5	-135	-90	-45	0	45	90	135	180	
0	-4.7	-3.9	-2.6	-1.7	-2.6	-3.9	-4.7	-5	θ_5 = -27.5°
45	-5.4	-4.4	-3.3	-1.7	-1.5	-2.2	-3.3	-4.7	(bin 4/5 border)
90	-4.4	-4.2	-3.1	-1.9	-1.1	-1.3	-2.4	-2.9	
135	-2.9	-2.9	-3.1	-2.2	-1.5	*	*	-1.5	θ_6 = -16.8°
180	*	-1.7	-1.9	-2.2	-1.9	-1.7	*	*	(bin 6 center)

*Threshold M/D > -0.9 dB.

TABLE 7-6
MINIMUM M/D (DB) OF EQUAL-AMPLITUDE MULTIPATH SIGNALS IN COARSE BINS 5 AND 6 (ONE BIN WIDTH SEPARATION) TO CAUSE FALSE ACQUISITION

ϕ_5, θ_5 = rf Phase (degrees), Azimuth Angle of Multipath Component in Bin 5
ϕ_6, θ_6 = rf Phase (degrees), Azimuth Angle of Multipath Component in Bin 6

ϕ_6 \ ϕ_5	-135	-90	-45	0	45	90	135	180	
0	-1.1	-3.1	-4.2	-4.2	-4.2	-3.1	-1.1	-1.3	θ_5 = -20.3°
45	*	*	-2.4	-4.2	-3.9	-3.6	-2.2	-0.9	(bin 5/6 border)
90	-1.1	-2.9	-3.9	-3.3	-3.9	-3.6	-3.3	-1.1	
135	-2.2	-5	-6.7	-7.1	-5	-3.6	-3.3	-2.9	θ_6 = -13.4°
180	-2.9	-4.7	-6.7	-8	-6.7	-4.7	-2.9	-3.1	(bin 6/7 border)

ϕ_6 \ ϕ_5	-135	-90	-45	0	45	90	135	180	
0	-3.9	-3.9	-4.4	-4.7	-4.4	-3.9	-3.9	-4.4	θ_5 = -22.1°
45	-4.2	-3.9	-4.4	-4.7	-4.4	-4.4	-4.2	-3.9	
90	-3.3	-2.6	-2.9	-2.6	-3.1	-3.9	-4.2	-3.6	θ_6 = -15.1°
135	-3.1	-2.4	-1.3	-1.3	-1.7	-3.1	-3.6	-3.3	
180	-2.6	-1.9	-1.3	-2.4	-1.3	-1.9	-2.6	-3.1	

ϕ_6 \ ϕ_5	-135	-90	-45	0	45	90	135	180	
0	-5.4	-4.7	-4.4	-4.4	-4.4	-4.7	-5.4	-5.4	θ_5 = -23.9°
45	-5.7	-4.7	-5	-4.4	-4.4	-4.4	-5	-5.4	(bin 5 center)
90	-5	-4.4	-4.2	-3.6	-3.6	-3.9	-4.4	-4.7	
135	-4.4	-3.1	-3.3	-2.9	-2.9	-3.3	-3.9	-4.2	θ_6 = -16.8°
180	-3.6	-3.1	-2.6	-2.4	-2.6	-3.1	-3.6	-3.9	(bin 6 center)

ϕ_6 \ ϕ_5	-135	-90	-45	0	45	90	135	180	
0	-4.2	-3.9	-3.9	-3.6	-3.9	-3.9	-4.2	-3.9	θ_5 = -25.7°
45	-3.9	-3.3	-3.3	-3.3	-3.9	-3.9	-3.3	-4.2	
90	-4.2	-2.9	-2.4	-2.4	-3.1	-4.2	-4.2	-3.6	
135	-4.2	-2.6	-1.9	-1.7	-2.2	-3.6	-4.2	-4.2	θ_6 = -18.5°
180	-3.9	-2.6	-1.5	-1.3	-1.5	-2.6	-3.9	-4.2	

ϕ_6 \ ϕ_5	-135	-90	-45	0	45	90	135	180	
0	-1.1	-1.5	-3.1	-3.1	-3.1	-1.5	-1.1	-1.5	θ_5 = -27.5°
45	-1.3	*	-1.1	-3.1	-3.3	-2.6	-1.9	*	(bin 4/5 border)
90	-1.1	*	*	-1.7	-2.6	-3.6	-3.3	-2.6	
135	-2.4	-1.3	*	-0.9	-2.2	-3.6	-3.9	-3.3	θ_6 = -20.3°
180	-3.3	-2.6	-0.9	-0.9	-0.9	-2.6	-3.3	-3.9	(bin 5/6 border)

*Threshold M/D > -0.9 dB.

threshold levels obtained under this constraint are considered representative because they may in general be applied to an average* of the two multipath amplitudes.

In Table 7-4 one multipath signal is located at the center of bin 5 and the other one is swept through bin 6 at increments of 1/4 bin width. In Table 7-5 the position of the bin 5 component is varied while the other component is fixed at the center of bin 6. In Table 7-6 the spacing between the two multipath signals is fixed at one bin width.

The wide variation in the critical M/D level with respect to the rf phase of the multipath signals is due to sidelobe effects. If both multipath components and the direct signal were all positioned at bin centers and thus were noninterfering, the threshold M/D level could be easily obtained analytically by calculating and comparing bin pair contents (according to the algorithm shown in block 3 of Figure 7-4) as follows:

contents of each adjacent multipath bin = ρ
contents of multipath bin pair = 2ρ

contents of direct signal bin = 1
contents of direct signal bin pair = 1.25

$\therefore$ multipath bin pair is chosen if $\rho > 0.625 = -4.1$ dB
where ρ = (voltage) M/D ratio.

For the centerline approach case that we have considered, the direct signal is not at a null of the multipath bin sidelobes and it has a non-negligible phase-dependent effect on the multipath bins' contents. As an

---

*In general, there is a trade-off curve of threshold multipath amplitude pairs (ρ_5, ρ_6) which is convex in most regions of interest. Each line segment tangent to this curve represents a region of constant "average" amplitude, with relative weights determined by its (negative) slope. The weights corresponding to the equal-amplitude point $\rho_5 = \rho_6$ specify an "average" with the property that any (ρ_5, ρ_6) pair within the convexity region averaging higher than the equal-amplitude threshold will cause acquisition failure. For most of the multipath angles considered in the tables, these bounding trade-off weights are roughly equal, except in extreme cases where the false acquisition effect is very asymmetrically dependent upon the two components.

illustration, consider the case of multipath signals at the centers of bins 5 and 6 with phases 180°, 0°, respectively. The relevant bin contents are:

contents of bin 5 = $|-\rho - \frac{2}{7\pi}|$

contents of bin 6 = $\rho + \frac{2}{5\pi}$

contents of bin 5/6 pair = $2\rho + \frac{5}{7\pi}$

contents of bin 8 = contents of bin 9 = $\frac{2}{\pi}$

contents of bin 8/9 pair = $\frac{4}{\pi}$

$\therefore$ multipath bin pair chosen in $\rho > \frac{23}{14\pi} = 0.523 = -5.6$ dB

This exact threshold level is slightly lower than the one quoted in the tables (-5.4 dB) for the same case because a finite multipath amplitude search grid (spacing: $\Delta\rho = 0.02$) was used to generate the tables.

In the opposite extreme case, when the phases of both multipath components are reversed by 180°, the direct signal destructively interferes with the multipath and the bin 5/bin 6 contents become:

contents of bin 5 = $|\rho - \frac{2}{7\pi}|$

contents of bin 6 = $|-\rho + \frac{2}{5\pi}|$

contents of bin 5/6 pair = $2\rho - \frac{23}{35\pi}$ (assuming $\rho > \frac{2}{5\pi}$)

$\therefore$ multipath bin pair chosen if $\rho > \frac{163}{70\pi} = 0.741 = -2.6$ dB

Again, the threshold level determined from the tables (-2.4 dB) is slightly conservative.

When the multipath signals are not located at bin centers, they too contribute to the contents of neighboring bins. The overall phase-dependence of the false acquisition effect tends to be magnified, and so is the complexity of a theoretical analysis. In some cases, bin pairs other than 5/6 or 8/9 are selected. The most graphic example of this effect is shown in the last row of the first sub-table of Table 7-4 (ϕ_6 = 180°, θ_6 = -13.3°,

$\theta_5 = 23.9°$). The bin 6 component is close enough to the direct signal to cause selection of the 7/8 bin pair when its amplitude exceeds -5 dB (compare this with the single component acquisition failure conditions determined earlier in Table 7-1), and this effect is independent of the component in bin 5.

We have chosen to estimate the likelihood of occurrence of damaging phase conditions by computing the fraction of 64 uniformly spaced phase samples (-135° to 180° with 45° spacing, for each multipath component) for which false acquisition occurs, as a function of multipath M/D level. These results are presented in Table 7-7 for the same azimuth angles considered in Tables 7-4, 7-5, and 7-6.* They can be derived from those tables by making use of the equivalence between phase conditions (ϕ_5, ϕ_6) and ($-\phi_5$, ϕ_6).

It is evident from Table 7-7 that placing the multipath signals at adjacent bin centers represents a worst case, on the average. However, it is also clear that the false acquisition effect is not terribly sensitive to the exact location of the multipath angles within a neighborhood of a few degrees. Substantial probability of phase conditions causing acquisition failures exists at reasonable M/D levels for most of the azimuth angle combinations considered in the tables. Furthermore, because of the wider variations with phase for off-bin-center components, there exist certain phase conditions which can result in false acquisition of some off-center components at M/D levels lower than any that can cause trouble in the bin-center case.

The multipath rf phases are unpredictable, because they depend on precise building and aircraft locations (measured in wavelengths). Thus, it can be concluded from the statistical phase study that a significant likelihood of

---

*See footnote in previous section concerning the interpretation of these fractions.

TABLE 7-7

FRACTION OF UNIFORMLY SAMPLED (45° SPACING) PHASE CONDITIONS CAUSING FALSE ACQUISITION FOR VARIOUS M/D LEVELS OF EQUAL-AMPLITUDE MULTIPATH SIGNALS AT AZIMUTH ANGLES GIVEN IN TABLES 7-4, 7-5, AND 7-6

	-6dB	-5dB	-4dB	-3dB	-2dB	-1dB
	0	0.17	0.36	0.73	0.8	0.94
Table 7-4	0.05	0.17	0.36	0.66	0.86	1
Azimuth	0	0.2	0.59	0.89	1	1
Angles	0	0.11	0.5	0.77	0.89	0.98
	0.03	0.28	0.44	0.59	0.63	0.69
	0.11	0.25	0.44	0.56	0.63	0.72
Table 7-5	0	0.2	0.41	0.73	0.86	0.98
Azimuth	0	0.2	0.59	0.89	1	1
Angles	0.05	0.17	0.33	0.61	1	1
	0	0.05	0.2	0.36	0.59	0.89
	0.11	0.17	0.28	0.61	0.8	0.91
Table 7-6	0	0	0.28	0.67	0.84	1
Azimuth	0	0.2	0.59	0.89	1	1
Angles	0	0	0.27	0.7	0.89	1
	0	0	0	0.31	0.5	0.77

acquisition failure exists any time two multipath signals with average amplitude $\gtrsim -4$ dB are simultaneously present within adjacent ordinary bins. The latitude of several degrees in critical azimuth angles encompassed in this condition translates into one of several hundred feet in critical reflector locations. Therefore, it is apparent that there is a substantial range of airport geometries to minute detail in order to discover instances of DMLS acquisition failure.

b. Fine Acquisition

The fine acquisition process involves an angular search in sectors whose width and spacing are about 1 $^1/_2$ beamwidths. Consequently, it is unlikely that gross errors such as those which can arise in the initial acquisition would occur here as long as the initial acquisition estimate was reasonably good. However, there is a potential problem generated by the lack of an on-going coarse search during the fine acquisition. The problem is that if the choice of initial homing frequency was so poor that either no signals (direct or multipath) or two competing multipath signals lie within the homing bins, the fine acquisition process may search indefinitely. Since there is no provision in the algorithm for halting a non-convergent search, it is thus possible after certain types of initial acquisition errors for the receiver to get hung up in a futile homing search that prevents it from correcting its mistake through reacquisition.

From Fig. 7-4 we see that the homing search does not terminate until the average contents of a preferred bin pair exceed the average contents of the remaining bin pair by a factor of 1.2 (= 1.5/1.25) to 1.5. If the homing bins contain no signal, the fine acquisition process must rely on sidelobes of the bin responses to pull in enough signal to converge on the preferred bin

pair. When the signal is far enough from the homing bins that the sidelobe response is relatively flat over the homing bins, or when enough noise is present to equalize the bin contents, the homing search may never terminate. For example, it is easily shown that in the presence of a single signal and no noise, the homing search is strictly non-convergent if the distance between the signal and the center homing frequency is either: 1) exactly 2.5 + n homing bin widths, for some nonnegative integer n (i.e., signal is at a null of the homing bin sidelobes); or 2) greater than 5.452 homing bin widths (1.363 ordinary bin widths).

These conditions do not strictly prevail for the (centerline approach) type (2) acquisition failure cases considered in Section a.(i), but they are borderline. The direct signal lies fortuitously at homing bin sidelobe peaks, 4.0 bin widths away from the center homing frequency. Even so, the fine acquisition process requires a long time to converge (56 to 61 scans for 180° multipath at levels between -5 dB and -0.9 dB) in a static noise-free environment. When noise is present, these convergence times may be indefinitely lengthened. In a dynamic situation, the direct signal may move around while the excessively long homing search is in progress, possibly toward sidelobe nulls or eventually outside the pull-in range of the fine acquisition procedure.

A second type of multipath situation which can cause fine acquisition convergence problems is the one analyzed in section a.(ii), in which two components are present in adjacent ordinary bins. When the multipath levels are high enough that the ordinary acquisition search makes an error, the center homing frequency is generally between the two multipath signals. The homing search is confronted with a signal in or near each of the two outer

homing bins. Thus, if the multipath components are relatively equal in amplitude, the fine acquisition algorithm may never be able to choose between the two outer bin pairs.

As an example, consider the case of two -4 dB multipath components at -23.0° and -17.1° (these angles are displaced from the centers of ordinary bins 5 and 6, respectively, by $1/2$ homing bin width toward the bin 5/6 border). By analysis like that presented in section a.(ii), it can be shown that the ordinary acquisition algorithm chooses the 5/6 border as the center homing frequency for approximately 59% of static phase conditions. Thus, in these cases there are equal-amplitude components at the centers of each of the two outer homing bins. The two outer bin pairs are equivalent (neglecting the effect of the direct signal, which is 10 homing bin widths from the nearest homing bin) and the inner bin pair is inferior to them, so the fine acquisition termination criterion can never be satisfied.

This effect is not critically dependent on the exact symmetry postulated above. For instance, consider varying the relative amplitude of the two multipath components, keeping the "average" amplitude high enough to cause coarse acquisition failure. Then (again neglecting the direct signal) one outer bin pair will eventually be preferred over the other only if the amplitude of the corresponding multipath component exceeds the other by at least a factor of 1.2 (= 1.5/1.25). Therefore, if the coarse acquisition fails, the fine acquisition procedure will be non-convergent as long as the multipath levels differ by no more than ±1.6 dB. If the positions of the multipath components are varied within or just outside the outer homing bins, different ranges (generally phase dependent) of relative multipath levels causing non-convergence are obtained.

All of these convergence problems are exacerbated by a defect in the interpolation scheme (PREFERRED VALUE SUBROUTINE in Fig. 7-5) which is manifest in both the coarse and fine acquisition procedures and which causes the frequency estimates obtained from each to be more granular then intended. Given the proposed DMLS signal normalization, bin update time constants, noise initialization values, and especially the criteria for declaring coarse/fine acquisition complete, it is very unlikely that the contents of one bin of the preferred bin pair will have risen to twice the contents of the other by the time acquisition is finished.

For example, consider the extreme case of a single signal component positioned at a bin center. The contents of all bins except the one containing the signal will remain constant at their (common) initial value, denoted C_o. The contents of the signal bin, denoted C_s, will increase until the acquisition criterion is met, i.e., until

$$C_s + C_o + \tfrac{1}{4}(C_s - C_0) > K_b C_o$$

where $K_b = 2.2$ for ordinary acquisition and $K_b = 3$ for homing. This reduces to

$$C_s > 1.16\ C_o \text{ (ordinary)}$$

$$C_s > 1.8\ C_o \text{ (homing)}$$

So, unless there is significant overshoot on the scan on which acquisition occurs, C_s will never reach the value $2C_o$.

Therefore, the "interpolated" frequency is virtually always at the bin edge midway between the centers of the preferred bin pair. The tracker position determined by the homing search is thus either at an ordinary bin edge or ±1 homing bin width away from an ordinary bin edge. This means, for example, that a direct signal placed at an ordinary bin center will (in the absence of multipath) be tracked initially with an error of one homing bin width.

c. Validation

Several features of the proposed DMLS validation process are a potential source of problems:

(a) Erroneous tracks are not quickly dropped due to the use of slowly decaying averages as a test input. This problem is accentuated by the initialization of the coarse bins to a noise only value and the use of coarse bin peak values to initialize the long term tracked averages.

(b) The comparison of a coarse bin pair peak value to a tracked level without reference to peak location can occasion problems in cases of near beam multipath. (Such problems were observed repeatedly in attempting to replicate the UK static multipath bench tests before it was learned that the UK disabled the ACQ/VAL logic before running bench tests.)

(c) If outlier test failures occur, a failure in the test against out of beam multipath will not cause reacquisition. This is undesirable because an erroneous track might be expected to be quite "noisy" in terms of indicated angle.

On the other hand, the time smoothing of Doppler filter outputs used in the DMLS validation algorithms gives a high level of protection against loss of track due to short duration high level multipath. In particular, when a sequence of "bursts" of high level multipath from objects at azimuths in different coarse bin pairs are encountered in succession, the DMLS receiver would only drop track only if one burst were too long. By contrast, the TRSB receiver could lose track if the duration of all bursts is too long since any out of beam signal greater than the tracked signal will cause the confidence counter to decrement.

Put differently, the DMLS validation logic requires that an out of beam signal both be large <u>and</u> be present at roughly a constant angle to cause a loss of track whereas the proposed TRSB logic requires only that some out of beam signal be large.

D. TRSB/DMLS Comparative Simulation Results

During AWOP discussions of comparative acquisition/validation (ACQ/VAL) performance, it was suggested that the operationally most significant characteristic is the ability to reacquire correctly and promptly (1 sec) if the need should arise when in the final approach and landing phase. To yield some quantitative comparison in this area, the TRSB and DMLS acquisition procedures were tested in a scenario in which the flight profile commences at about 0.4 nautical miles from threshold on the aircraft's final approach. This emulates a situation in which any of a variety of incidents may have caused the receiver to break lock (e.g., momentary interruption of power or other transient fault) and the receiver is forced to reacquire the correct signal.

The origin of the flight path was located within a multipath region in order to challenge both systems' acquisition capabilities in a dynamic situation where the multipath rf phase is rapidly varying. Given the theoretical prediction of potential DMLS acquisition problems in the presence of two simultaneous multipath signals in adjacent ordinary bins, the two-building airport layout shown in Fig. 7-7 was hypothesized.

The comparative simulation was repeated for three different approach velocities so as to more fully probe the effects of the relative rf phase angles sequence in overall ACQ/VAL performance. Detailed descriptions of the simulation results for the three cases are given in Sections 1, 2, and 3 below. Table 7-8 summarizes the TRSB/DMLS behavior for the various approach velocities.

1. Results Presented at AWOP 6 [79]

The assumed airport geometry is shown in Fig. 7-7 and the azimuth multipath diagnostics in Fig. 7-8. The flight profile/building assumptions were as follows:

TABLE 7-8

COMPARISON OF ACQUISITION BEHAVIOR FOR
AWOP 6 WP/322 ACQ/VAL SCENARIO VARIANTS

	Time Outputting Angle of Multipath Signal (secs)		Net Elapsed Time Before Raising Flag on Desired signal track (secs)	
	TRSB	DMLS	TRSB	DMLS
WP/322 scenario (354 knot effective ground speed) (by accident)	0.0	1.8	1.0	4.2
Rerun #1 (118 knot ground speed)	0.0	2.2	1.0	6.4
Rerun #2 (80 knot ground speed)	0.0	0.0+	1.0	7.8

+track was started on multipath, but reference scalloping angle noise generated by direct signal prevented flag from being lifted.

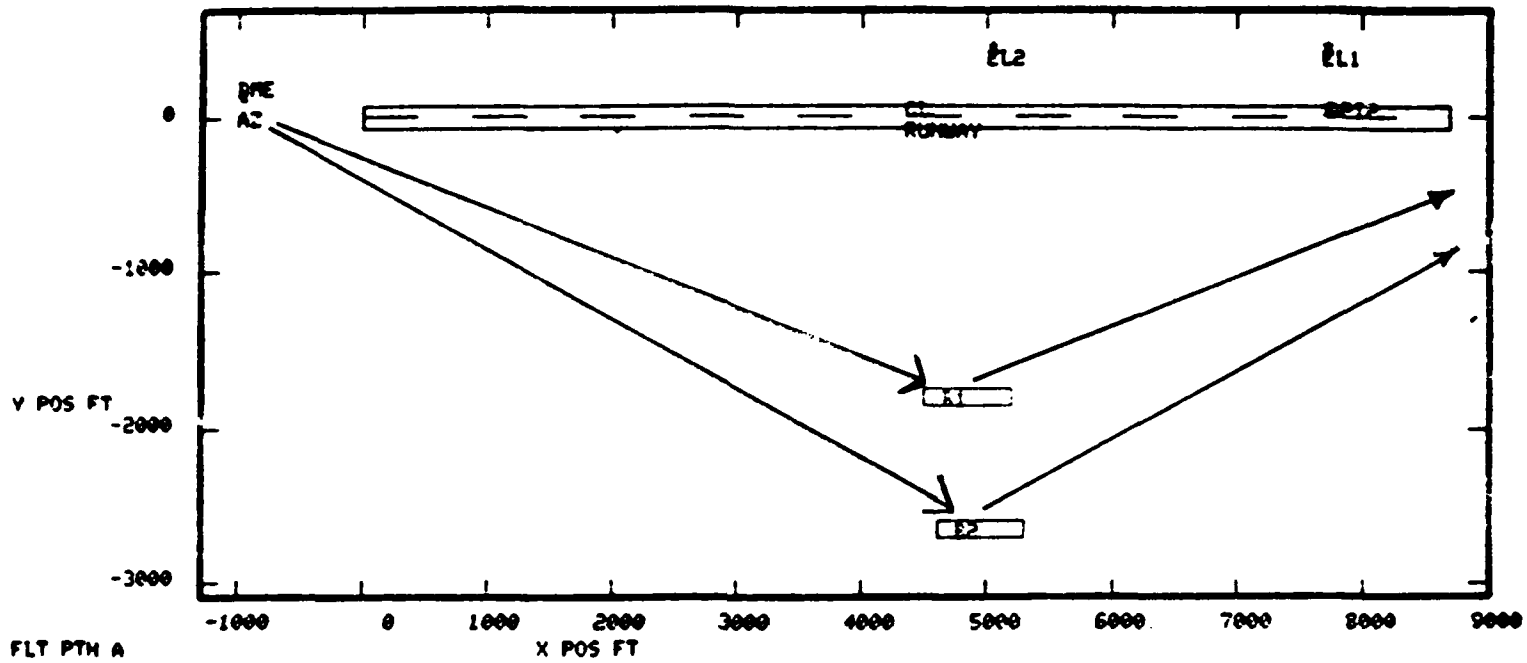

FLT PTH A
AZ SYSTEM

OBST	RANK	AMP	DIST	RDOP
G	1	0	2834 3	0
B1	3	2	0 0	-44
B2	2	2	120 0	-91

RANK = multipath ranking

AMP = maximum M/D ratio (-dB)

RDOP = relative Doppler (Hz) at point of maximum M/D

DIST = distance along flight path (ft) at which maximum M/D occurred = 10531 - x pos (ft)

Fig. 7-7. Airport map for original WP/322 ACQ/VAL scenario.

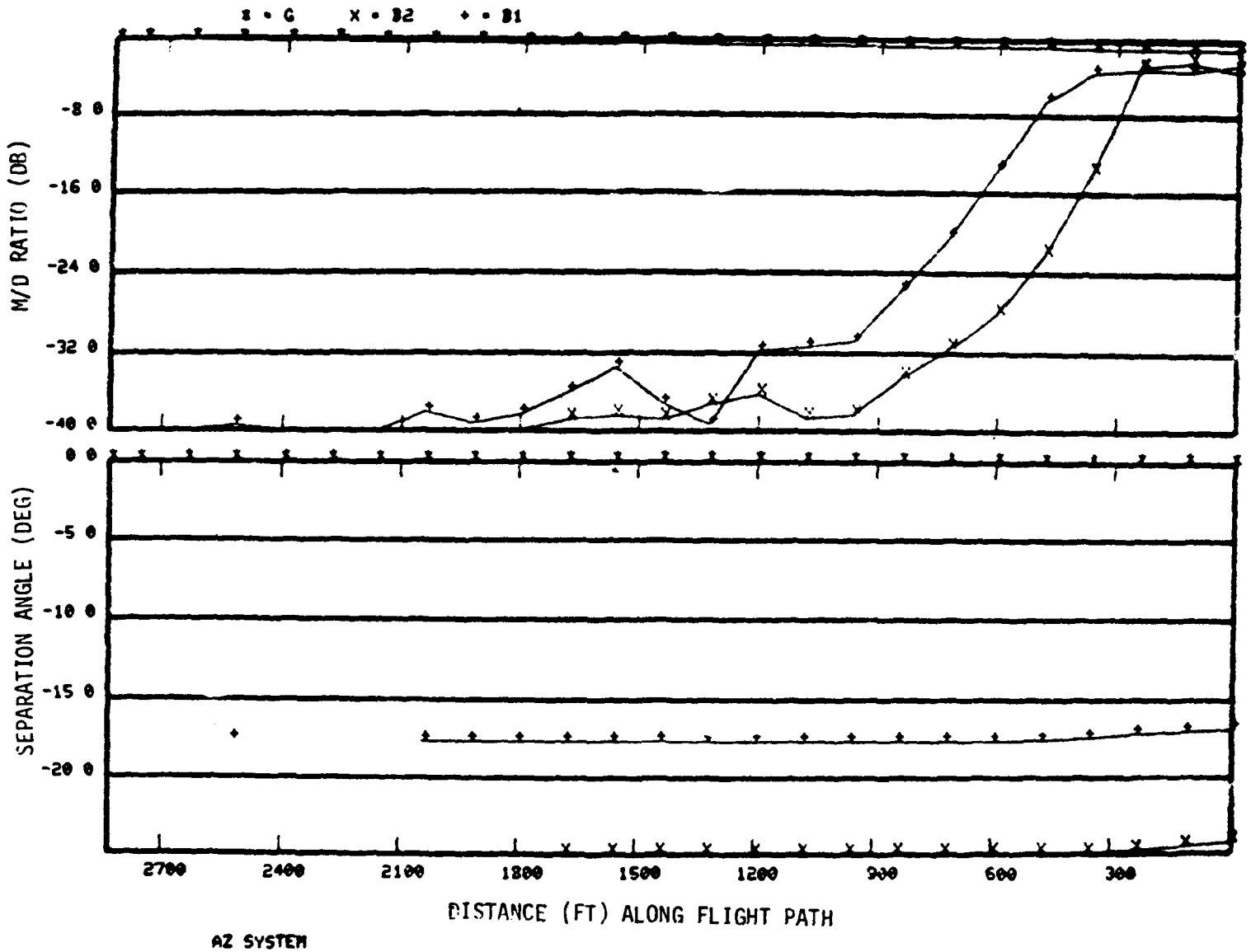

Fig. 7-8. Azimuth multipath characteristics for original WP/322 ACQ/VAL scenario.

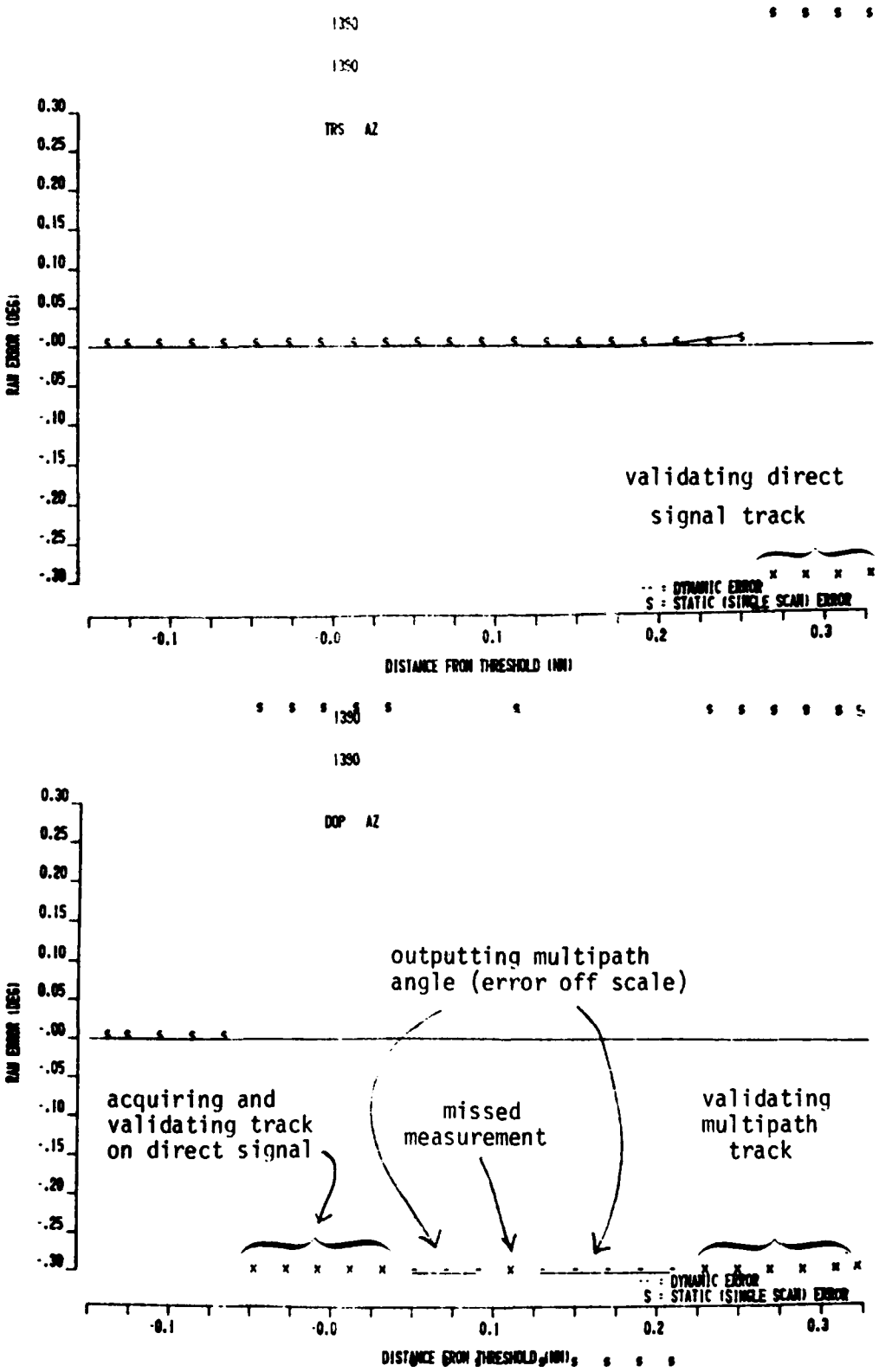

Fig. 7-9. DMLS and TRSB errors for original WP/322 ACQ/VAL scenario.*

* 1st flight path point not plotted in WP/322 for DMLS, due to plotter error.

buildings:	100 feet high with locations shown in Fig. 7-7. The assumed reflection coefficient was -3 dB (= "standard" AWOP assumption). Building locations were such that the multipath falls roughly in the middle of "ORD" bins 5 and 6, respectively.
transmitter:	phase center height was 10 ft. The elevation pattern of the DMLS antenna was identical to that used for TRSB. The proposed reference antenna with centerline emphasis was used for DMLS.
airport terrain:	assumed to be flat with a dielectric constant of 15.0
flight profile:	a 2.75° glideslope from 0.30 nmi before threshold (height = 144 feet) to 1000 feet past threshold (height = 8 feet). Intended to be at a ground speed of 200 ft/sec (= 118 knots); unfortunately, an input data error was made such that multipath and receiver errors were computed every 120 feet along flight path (rather than the 40 feet that was desired). Consequently, the aircraft moved along the flight path as if at 354 knots ground speed.

TRSB acquired the direct signal properly on the first scan and lifted the flag at the end of 1 second. The small TRSB errors in Figs. 7-9 and 7-10 arose from sidelobe multipath effects. The DMLS receiver determined the 5/6 bin pair to be the largest pair on the third scan and made an initial estimate of signal angle to be -20.3° (which does not correspond to either multipath signal). After 23 scans (i.e., in the second frame) the homing bin search yielded an angle estimate of -18.6°, which is close to the multipath signal at -17°. The tracker then proceeded to track that multipath signal for a number of frames. The system flag was raised on the 7th frame and the receiver reported out an indicated position of approximately -17°.

After the flag was raised, data for a number of the individual scans on each frame were discarded (e.g., 6 to 11) as a consequence of test T1 (block 15) in Fig. 7-4. However, this does not cause the confidence counter to decrement. On frame 12, all 12 scans were rejected, thus causing a missed

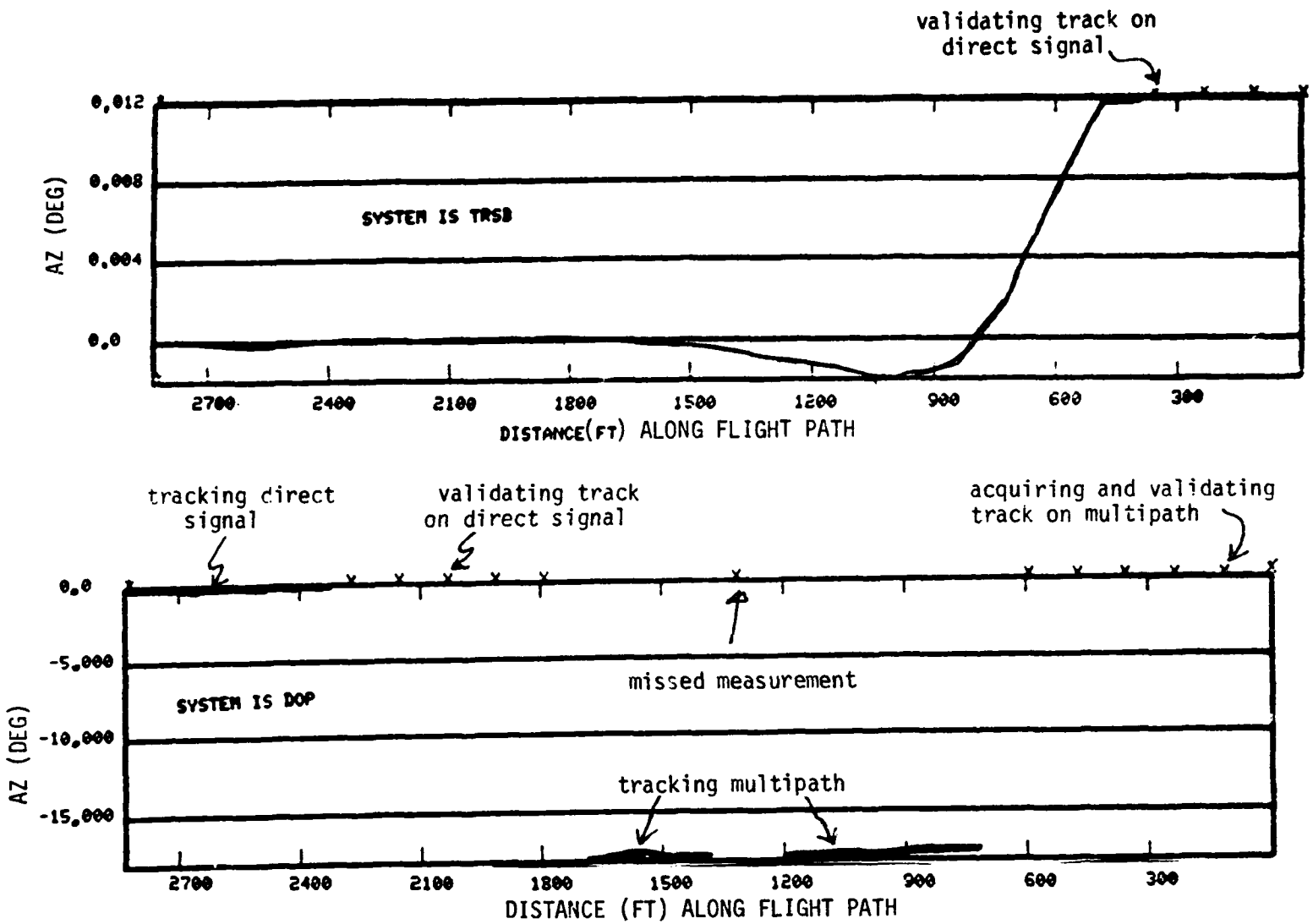

Fig. 7-10. DMLS and TRSB errors for original WP/322 ACQ/VAL scenario.*

* 1st flight path point not plotted in WP/322 for DMLS, due to plotter error.

measurement. On the 14th and 15th frames, the "long term tracked value" was sufficiently less than the pairwise search peak to cause the confidence counter to decrement (test T3 and T5 in Fig. 7-4). However, track was not dropped until the short term/long term test (test T2 in Fig. 7-4) failed on frame 16 (= 3.2 seconds). Figure 7-11 shows the time history of the long and short term averages.

The DMLS receiver then acquired the direct signal on the next frame (2 scans for coarse search, 7 scans for homing) and maintained track for the remainder of the run. The data were output some 4 frames later (= 4.2 seconds total elapsed time) when sufficient validation had been established.

2. Results for WP/322 Scenario with Intended Flight Profile

After the error in flight path computations was identified, the scenario was rerun changing only the spacing increment at which multipath and system errors are computed. The azimuth multipath characteristics are shown in Fig. 7-12 and the system results shown in Fig. 7-13. The TRSB system acquired the direct signal correctly on the first scan and raised the system flag after one second as in the earlier case.

Again, the DMLS system model obtained the 5/6 coarse bin pair as being the largest pair on the third scan, with an initial angle estimate of -20.3°. And, as before, the DMLS "homing" process yielded an initial tracker angle of -18.6° which is close to the multipath signal at -17°. The tracker then proceeded to track the multipath for 26 frames (= 5.2 seconds).

However, the behavior during the multipath tracking period was different in some respects from the initial simulation. During the validation period which follows acquisition the outlier test (test T4 in Fig. 7-2) failed for 5 consecutive frames, thus preventing the acquisition counter from increment-

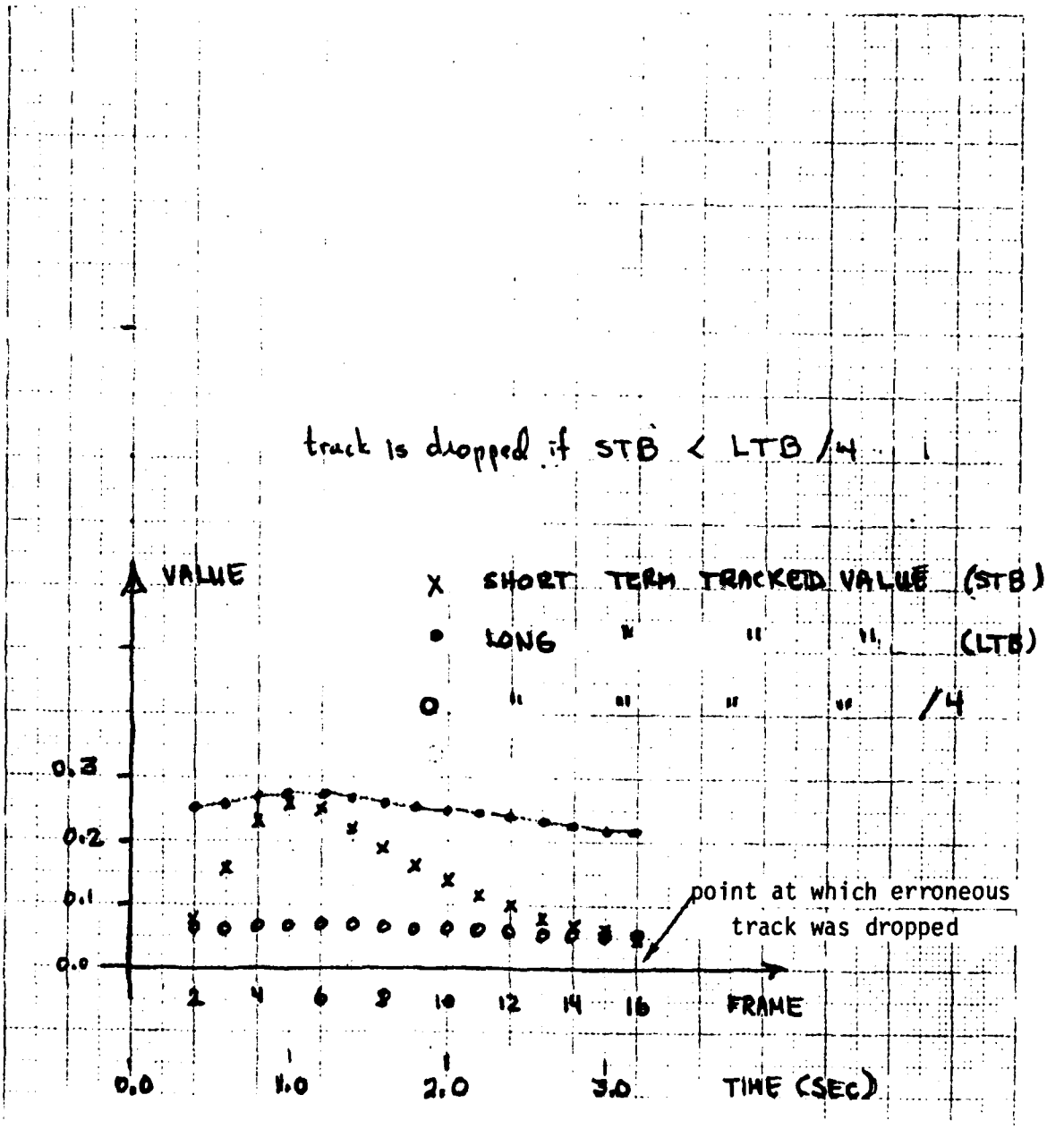

Fig. 7-11. Long and short term tracked averages time history for original WP/322 ACQ/VAL scenario.

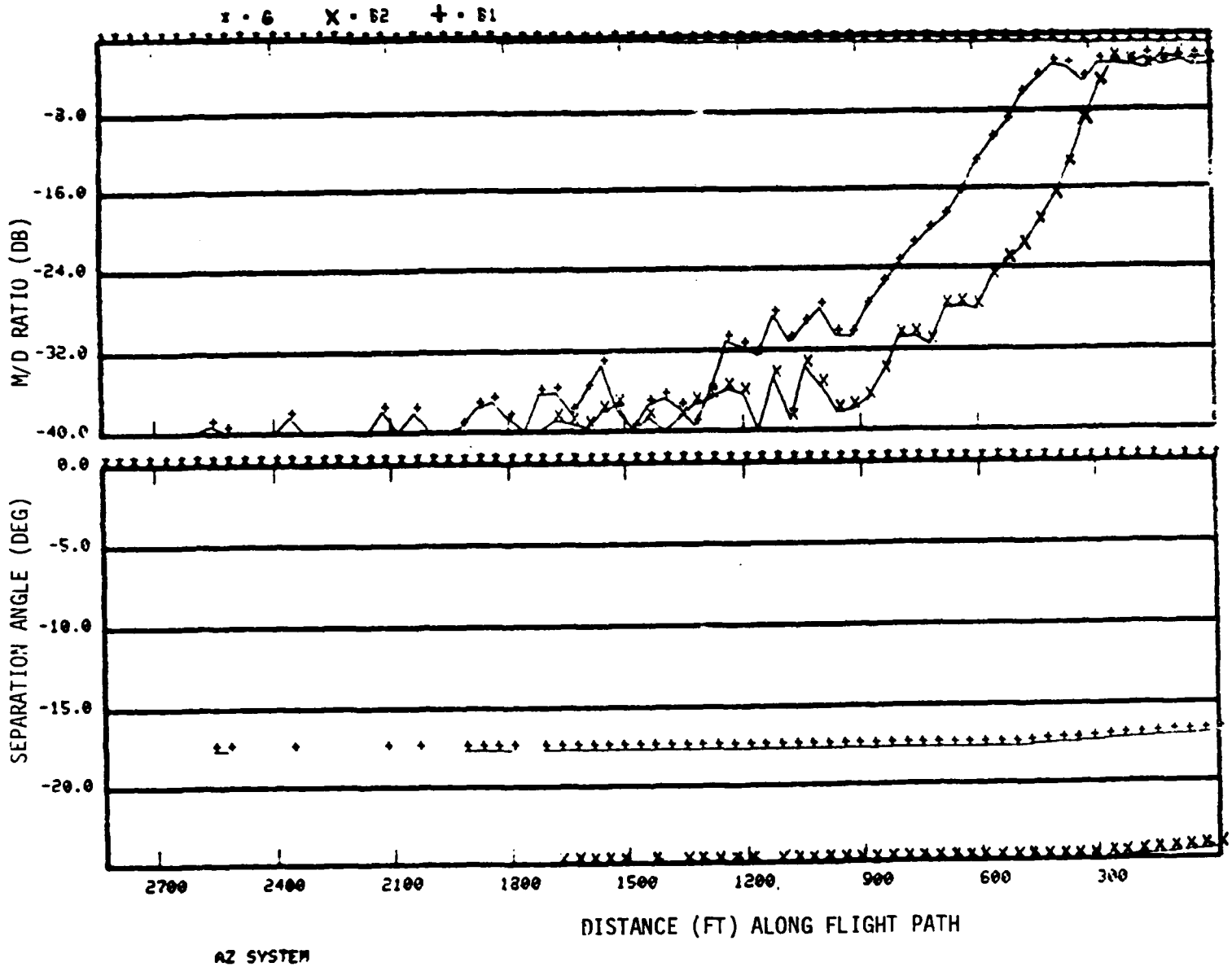

Fig. 7-12. Azimuth multipath characteristics for WP/322 scenario at 118 knots ground speed.

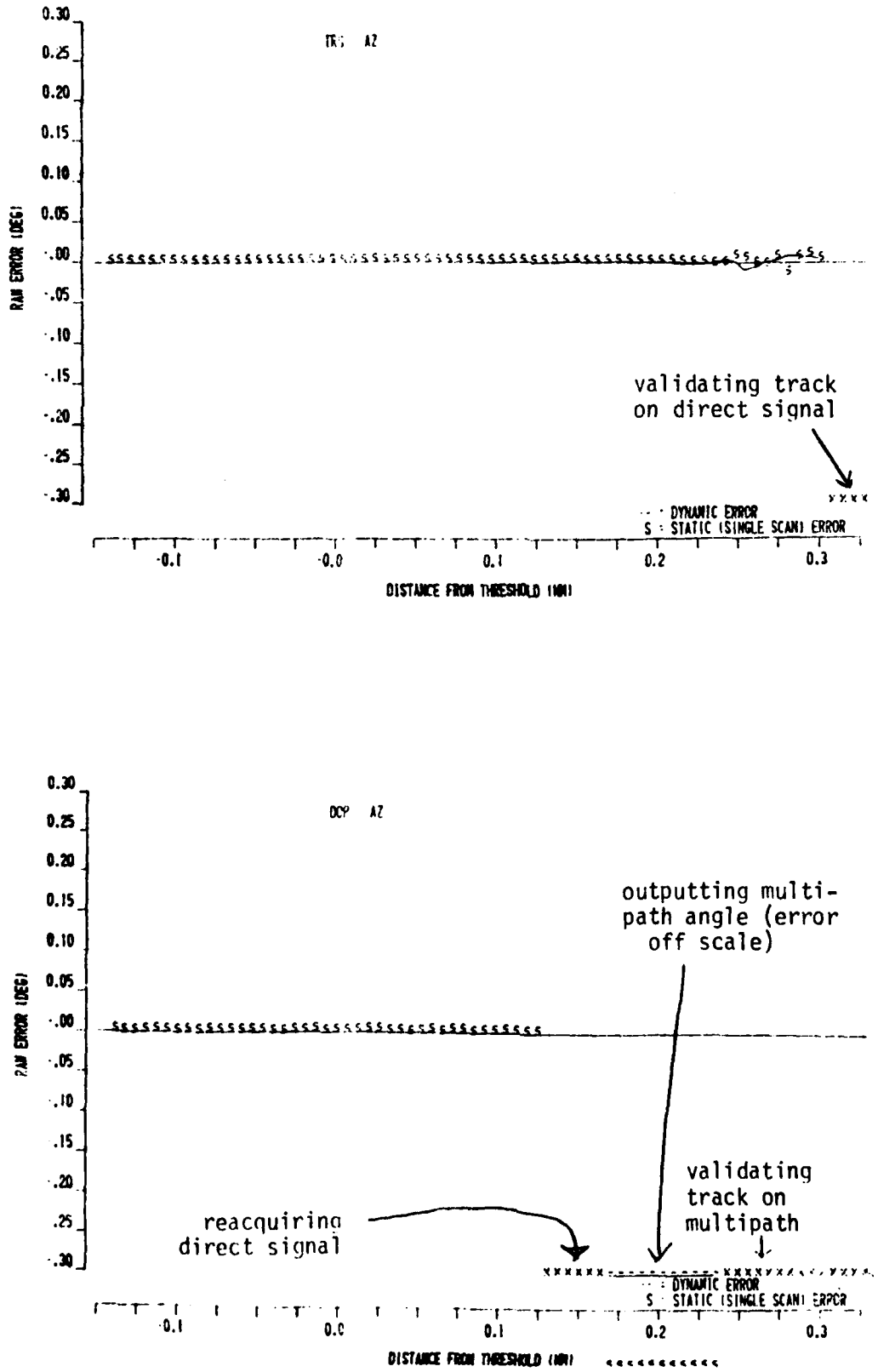

Fig. 7-13. DMLS and TRSB errors for WP/322 scenario at 118 knots ground speed.

ing. This was due to the direct signal causing reference scalloping errors > 0.2° for a track on the multipath. After this 1 second period, the track established and continued on the multipath without incident through frame 20 (= 4.0 seconds).

At this point, the "coarse" bins centered on the direct signal had increased enough to cause the coarse bin peak/long term tracker amplitude test (test T3 in Fig. 7-4) to fail. This resulted in the confidence counter decrementing so that the output was flagged by frame 26 and reacquisition initiated on frame 28. The reacquisition was accomplished within this frame and the flag lifted for a direct signal track on frame 32, some 6.4 seconds after the start of the run.

Figure 7-14 shows the history of the long and short term tracker outputs. We see that the short term average did not decay fast enough to cause reacquisition, because it had built up to a level considerably greater than the long term average when in the multipath region.

3. Results for WP/322 Scenario with 80 Knot Approach Speed

To further examine the role of aircraft ground speed in the ACQ/VAL behavior, the scenario of WP/322 was rerun changing the aircraft velocity to 135 ft/sec and the multipath error spacing increment to 27 feet. The azimuth multipath characteristics are shown in Fig. 7-15 and the system results shown in Fig. 7-16. The TRSB system acquired the direct signal correctly on the first scan and raised the system flag after one second as in the earlier cases.

Again, the DMLS system model obtained the 5/6 coarse bin pair as being the largest pair, this time on the second scan, with an initial angle estimate of -20.3°. And, as before, the DMLS "homing" process yielded on the 2nd frame

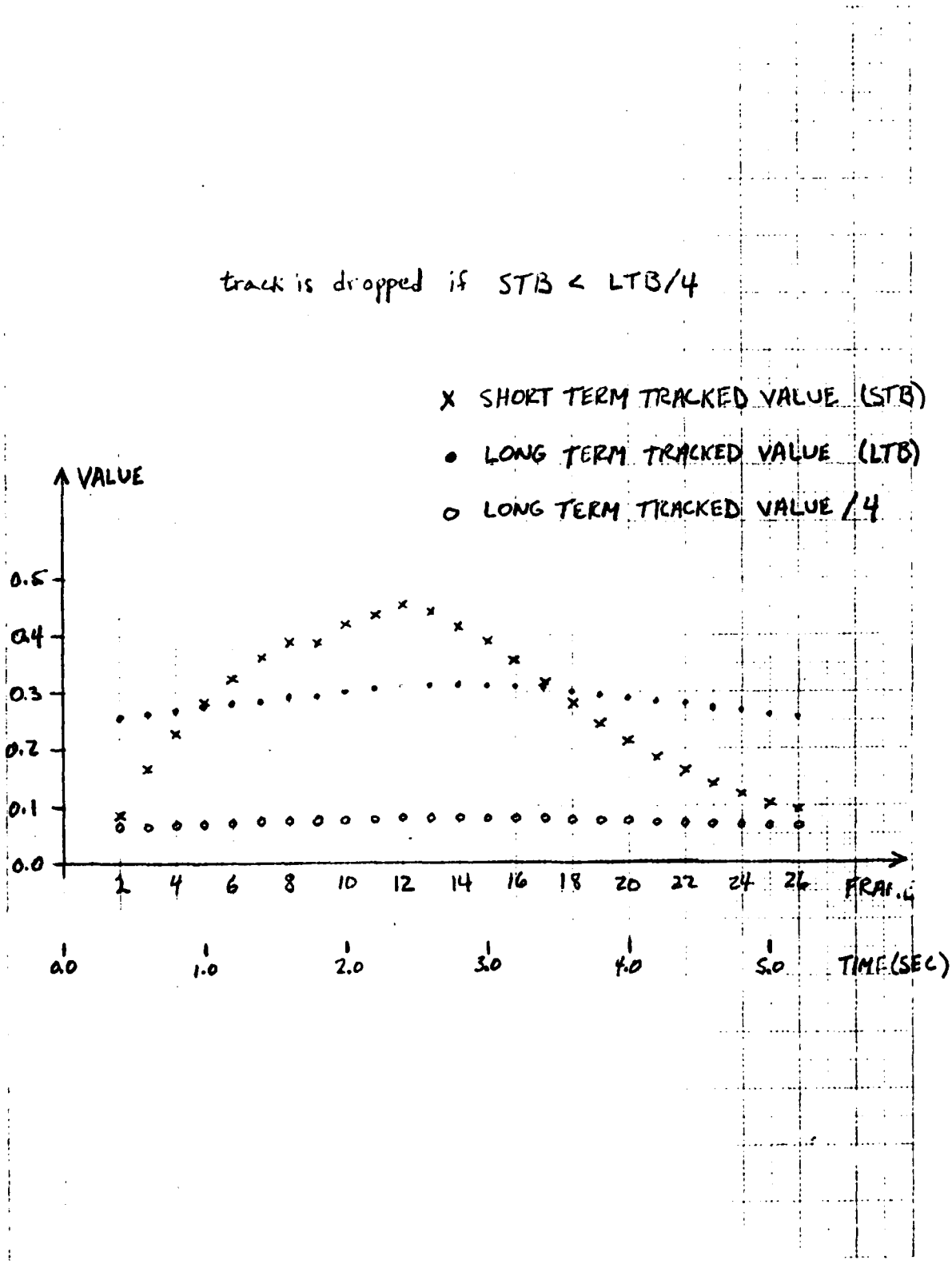

Fig. 7-14. Long and short term tracked averages time history for WP/322 scenario at 118 knots.

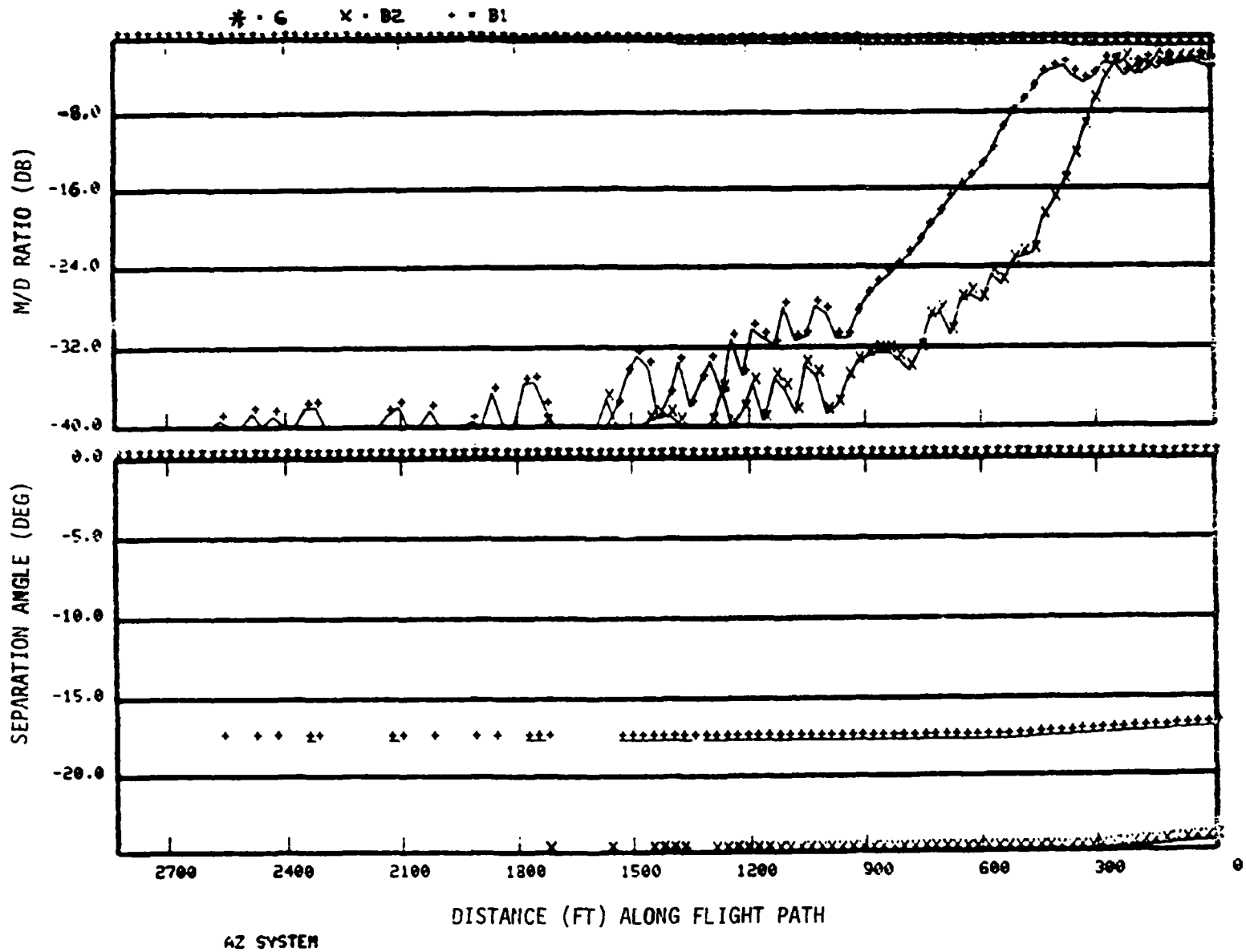

Fig. 7-15. Azimuth multipath characteristics for WP/322 ACQ/VAL scenario at 80 knots.

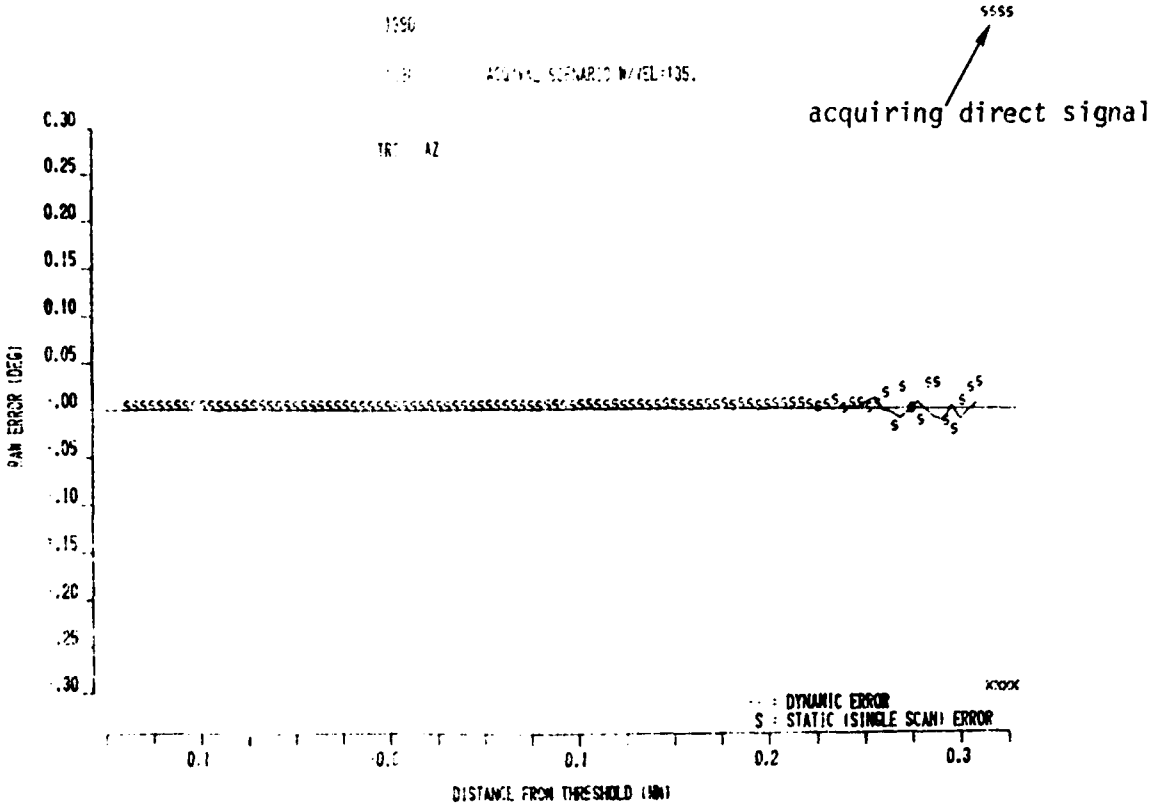

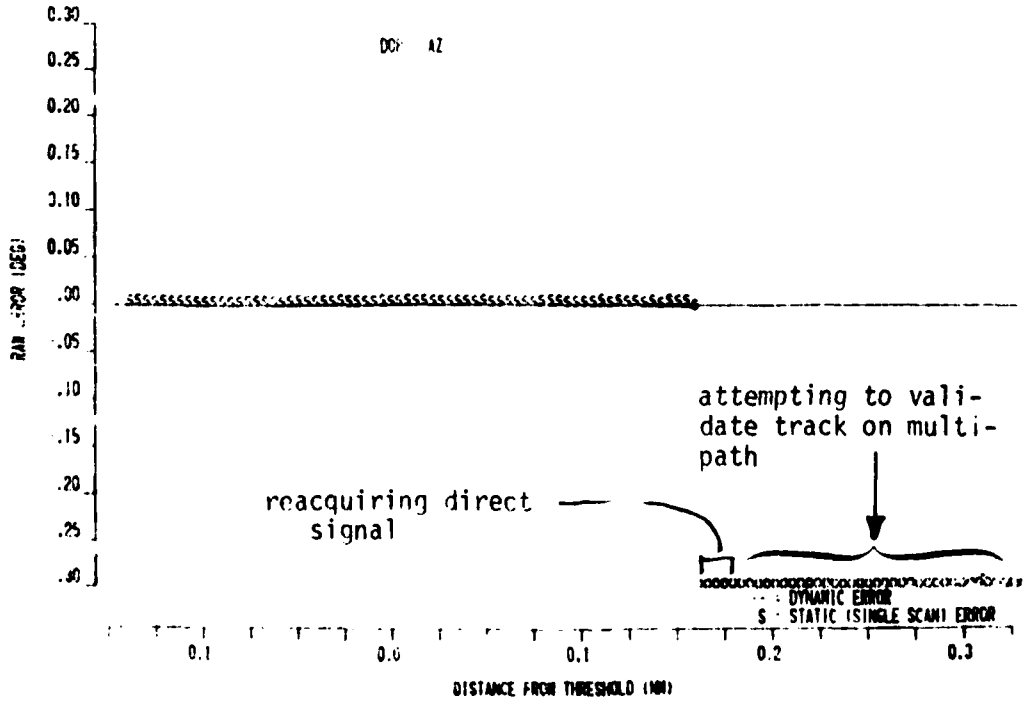

Fig. 7-16. DMLS and TRSB errors for WP/322 ACQ/VAL scenario at 80 knots.

an initial tracker angle of -18.6°. The tracker then proceeded to track the multipath for 31 additional frames (= 6.4 seconds total).

The behavior during the multipath tracking period was different from that for either of the two cases previously considered. During the validation period following acquisition the outlier test (test 14 in Fig. 7-4) failed for all 31 frames, thus preventing the acquisition counter from incrementing. This was due to the direct signal causing reference scalloping errors > 0.2° for a track on the multipath.

From frame 25 onward, the "coarse" bins centered on the direct signal had increased enough to cause the coarse bin peak/long term tracker amplitude test (test T3 in Fig. 7-4) to fail. This would have initiated reacquisition had not the outlier test also been failed (so test T5 in Fig. 7-4 did not occur). On frame 34, the outlier test was passed, allowing test T5 to occur, which started reacquisition. Reacquisition was accomplished in the next frame and the flag lifted for a direct signal track on frame 39, some 7.8 seconds after the start of the run.

Figure 7-17 shows the history of the long and short term tracker outputs. We see that the short term average did not decay fast enough to cause reacquisition, because it had built up to a level considerably greater than the long term average while in the multipath region.

E. Summary

Table 7-9 summarizes the conclusions of the acquisition/validation analysis. It should be emphasized that the initial acquisition performance shown is based on the proposed implementations as opposed to theoretically achievable performance for the generic technique. If the DMLS and DLS techniques were to use an FFT based initial acquisition procedure, their performance on

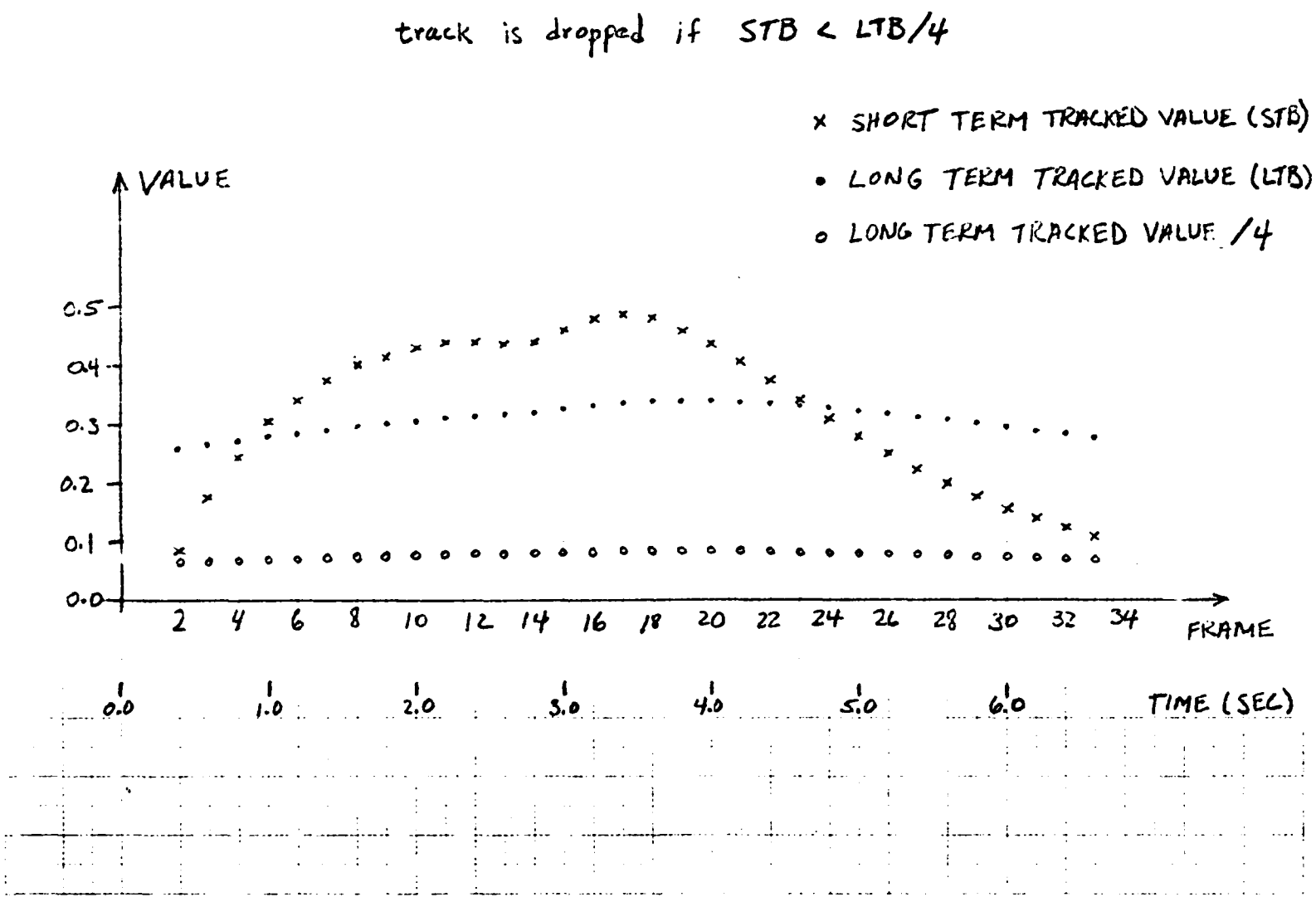

Fig. 7-17. Long and short term tracked averages time history for WP/322 scenario at 80 knots.

TABLE 7-9

COMPARISON OF MLS ACQUISITION/VALIDATION PERFORMANCE

	Minimum Relative Direct Signal Level Required to Insure Proper Initial Acquisition		Tolerable Relative Multipath Levels When Tracking Direct Signal [a]
	Single Multipath Signal	Two Equal Multipath Signals	
DLS	+7	+10	-1
DMLS	+3	+6	+10 [b]
TRSB	+1	+1	+10 [b]

Note a: Multipath duration < smaller of time tracking direct signal and 20 seconds.

Note b: Maximum level determined by sidelobe error effects.

single measurements would be quite similar to that of TRSB. The DLS technique, however, has a slightly greater difficulty in time averaging during initial acquisition since the ground system must make a "hard" decision on each received interrogation as to the correct angle. The differences in capability for maintaining track are, however, related to the overall system concept as opposed to particular implementations.

VIII. SUMMARY AND RECOMMENDATIONS FOR FUTURE STUDIES

A. Summary of Results

In this volume, we have presented the results of a variety of comparative scenarios as well as detailed analyses of certain specific system multipath performance factors which emerged as being important in the scenarios. The specific types of multipath investigated in the scenarios included:

(a) inbeam azimuth multipath:

aircraft reflections
shadowing

(b) out of beam azimuth multipath:

building and aircraft reflections

(c) inbeam elevation multipath

aircraft and building reflections
shadowing

(d) out of beam elevation multipath

reflections from flat terrain and buildings

where the term inbeam refers to scatterers which are angularly within 1.5 standard beamwidths* of the direct signal angle in the function (i.e., azimuth or elevation) coordinate.

The principal conclusions reached from the scenarios and analyses were as follows.

1. The principal <u>inbeam azimuth multipath</u> threat for the various systems was shadowing by intervening objects. Of particular concern was shadowing by aircraft clearing at the runway after landing or taxiing across the runway when shadowing aircraft passes close to the azimuth antenna. Blockage by

---

*a standard beamwidth is approximately λ/L radians where L is the ground aperture size in wavelengths.

small fixed objects (e.g., light posts, monitors, etc.) also can cause discernible errors. These phenomena will have to be considered carefully in siting the MLS at operational airports.

Reflections from aircraft on the taxiways near the runway threshold did not yield discernible errors (e.g., > 0.02°) in any of the scenarios. Since similar results were also obtained in (limited) field tests, it currently appears that such aircraft reflections are not of significant concern.

There was not an appreciable difference in comparative performance for the two C band systems. The analysis and field tests of DLS shadowing performance were less detailed; however, the L band results for AWOP scenario 5 involving building shadowing were comparable to those of the C band system.

2. The principal out of beam azimuth multipath threat to proportional angle guidance is specular reflections from buildings. For the TRSB system, these reflections did not create significant problems as long as a ground antenna with low sidelobes was utilized.

With the proposed DMLS implementation, building reflections with very low scalloping frequencies (e.g., < 20 Hz) could in some circumstances create acquisition problems, but did not yield significant angle errors. These acquisition problems could be remedied by an FFT based narrow band filter initial acquisition algorithm. However, multipath with high scalloping frequencies yielded "reference scalloping" azimuthal errors > 0.05° in both on and off centerline scenarios when significant multipath levels (e.g., > -3 dB) were encountered. The error due to reference scalloping can be quite sensitive on airport geometry, aircraft approach velocity and flight path as well as scan format. Consequently, the DMLS system could be somewhat more diffi-

cult to implement at airports with buildings that yield significant azimuth multipath and, there would be greater sensitivity to multipath from new buildings than would be the case with a TRSB system.

The DLS technique had an intrinsic advantage over the other systems in that the time delay discrimination implicit in the use of a pulse waveform results in lower effective multipath levels than would be the case with CW waveforms. However, several features of the proposed implementation significantly degraded the azimuth multipath performance.

The proposed acquisition algorithm utilizing multiple baseline interferometry could fail with out of beam multipath at lower levels than those required for failure with DMLS or TRSB. These problems were accelerated by the lack of any track memory at the point of angle estimation. This lack of track memory also results in DLS being susceptible to complete loss of valid angle data whenever high level (e.g., > 0 dB M/D ratio) multipath is encountered.

The proposed DLS ground antenna element geometric configuration resulted in a (comparatively) greater likelihood of multipath generated angle errors due to 1) the relatively high sidelobes and 2) errors in converting conical angle estimates to planar estimates using the elevation angle estimate from a horizontal circular array. The effects were most pronounced when the receiver was off centerline.

3. The principal <u>inbeam elevation</u> multipath threats were specular reflections from vertical building walls and shadowing by intervening obstacles. It is anticipated that elevation shadowing by parked or taxiing aircraft will be easy to avoid by operational means than was the case with azimuth systems since aircraft which have landed turn off behind the elevation

antenna. Blockage by small fixed objects (e.g., ILS glideslope monitors) can produce discernible errors on final approach, but there were no substantive system differences in this respect.

Reflections from building walls generated discernible errors in both the comparative scenarios and field tests. The various DMLS and TRSB multipath rejection features (in particular motion averaging) yielded adequate performance (i.e., errors with the AWOP accuracy limits) for the DMLS and TRSB systems in all of the scenarios simulated. The proposed DLS implementation* gave substantially larger errors in several cases, principally due to the wider ground antenna effective beamwidth.

One avenue to reducing the elevation errors due to inbeam specular reflections from vertical surfaces consists of exploiting the differences in azimuth angle between the direct and reflected signals. Both the DMLS and DLS proposals included the notion of phase coherent processing between the signals radiated from (or, received at) pairs of elements in which the two elements lie on the same vertical axis. Normally, the elements all lie on the same vertical axis; however, it is also possible to consider a "vertical diversity" concept in which the element pairs are displayed sideways from one another so that various forms of spatial averaging can be carried out. The simulated DLS implementation included such averaging, while for DMLS lateral diversity was suggested as a growth feature.

Analysis of the DMLS system showed that the performance improvement with lateral diversity was considerably better than that offered by the centerline emphasis of the simulated DMLS and TRSB implementations. However, the effects

---

*following the AWOP assessment, it was reported by the FRG [139] that an alternative DLS implementation could yield significantly improved performance in these cases.

of DMLS lateral diversity on motion averaging improvement and/or protection against terrain reflections from irregular terrain were not fully explored (e.g., by a full simulation). Consequently, it was not possible to fully quantify the utility of lateral diversity for DMLS.

4. The principal out of beam elevation multipath threat considered was specular reflections from flat terrain. Since this threat was carefully considered by all proposers in their system design, it is not surprising that the elevation errors from this source were small in all of the scenarios considered. However, several situations in which terrain reflections could be significant were not considered in the scenarios reported here:

a) Reflections from rough and/or upsloping terrain yielding substantial reflected power near the horizon. In such a case, the multipath separation angle is reduced and, the efficacy of sharply tapered element patterns (e.g. as proposed for DLS and TRSB) is reduced.

b) Mobile small aperture systems (e.g., military tactical) in which a larger elevation beamwidth is used. This both increases the sensitivity to sidelobe multipath and enlarges the inbeam region.

and

c) Flare guidance when the terrain to the side of the runway is not flat.

Our preliminary measurements of irregular terrain reflectivity at L band (Volume I) indicates that the principal reflections can be explained by specular reflections from flat plates of appropriate geometric shape and orientation.

B. Recommendations for Future Studies

The various simulation results and analytical studies and analyses of field data carried out during phase III suggested several areas which merit

further investigation in the context of implementing the TRSB MLS. These include:

(1) Further validation of the near field shadowing model discussed in Volume I with particular emphasis on effects due to "small" objects such as monitor poles and lighting bars since such objects are quite common at MLS azimuth sites.

(2) Field measurements of irregular terrain reflectivity at C band and validation of the propagation model so as to address some of the terain reflection issues discussed in the preceding section.

(3) Examine the multipath sensitivity of the clearance and out of coverage indication (OCI) features for the TRSB azimuth function since many scatterers will be found fairly close to the azimuth array in the angular.

(4) DME multipath effects in the approach and landing region since this subsystem was not examined in detail during the AWOP assessment.

(5) Improved receiver processing with particular emphasis on acquisition/validation algorithms, data averaging/outlier rejection and low angle elevation angle estimation. Several possible avenues of study for the first two topics were discussed in Chapters V and VII of this volume, while the low angle elevation (e.g. flare) processing was not examined in detail as a part of the comparative scenarios.

(6) Detailed studies of the effects of shadowing by taxiing and turning off aircraft on the azimuth system to better quantify the operational constraints which may be required as a function of shadowing aircraft size, distance to the azimuth array, azimuth beamwidth and landing aircraft location.

It should be emphasized that the above list of topics was developed from phase III studies discussed in this report, and do not reflect work accomplished since that time. Several of these areas [in particular, (1), (2) and (3)] have been under active investigation in the time period between the end of the phase III studies and the writing of this report. The results of these investigations will be reported in subsequent reports.

APPENDIX A

COMPARISON OF "STANDARD" AND "SPECIAL" DMLS SIMULATION MODELS FOR A SPATIALLY HOMOGENEOUS BUILDING

The DMLS simulation model described in Volume II of this report assumes that the multipath parameters (amplitudes) from the various individual scatterers are unchanged over the period of a single DMLS angle frame (30 msec for azimuth, 50 msec for elevation) save for the rf phase which increases linearly with time (proportional to the scalloping frequency). On each new frame, all multipath parameters are recomputed for each scatterer.

The "special" DMLS model utilized in Chapter VI assumes that the multipath parameters are unchanged save for rf phase over 1/2 of an angle frame. The multipath paramaters are recomputed for each half of an angle frame as well as for new angle frames.

The two models are expected to give essentially identical results when the multipath characteristics do not vary over a single frame, but may give different results for multipath which has a very rapid spatial variation.

As a check on the multipath computation algorithms and the DMLS programs, simulation results were obtained for a scenario involving a single large flat metallic building for which the multipath would be slowly varying along the flight path.

Figures A-1 and A-2 show the airport map and azimuth multipath using the "special" DMLS model while figure A-3 shows the azimuth multipath diagnostics results using the "standard" DMLS model. Figure A-4 compares the error waveforms. We see that essentially identical results were obtained as expected.

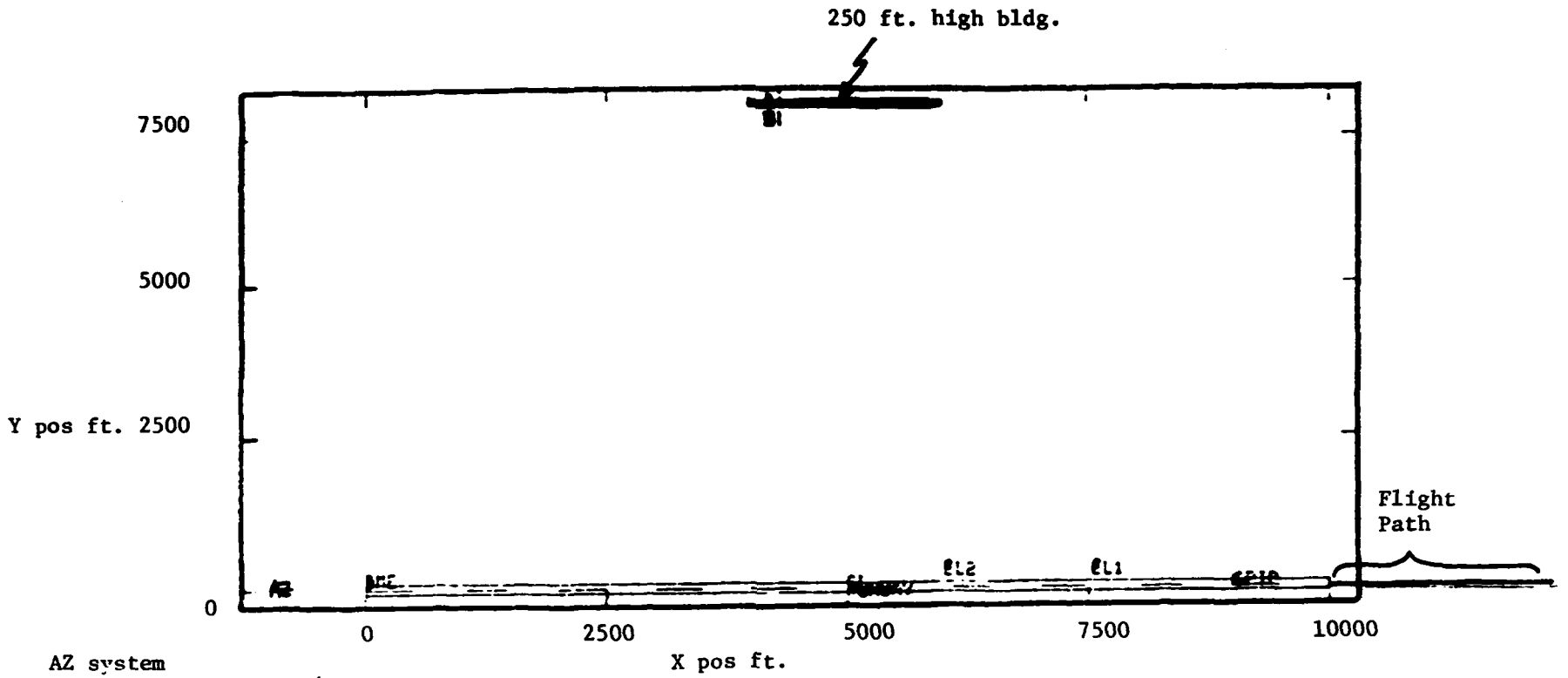

AZ system

OBST	RANK	M/D	DIST	RDOP
B1	1	-6	63.0	-363

Fig. A-1. Airport map for test scenario using "special" DMLS simulation model.

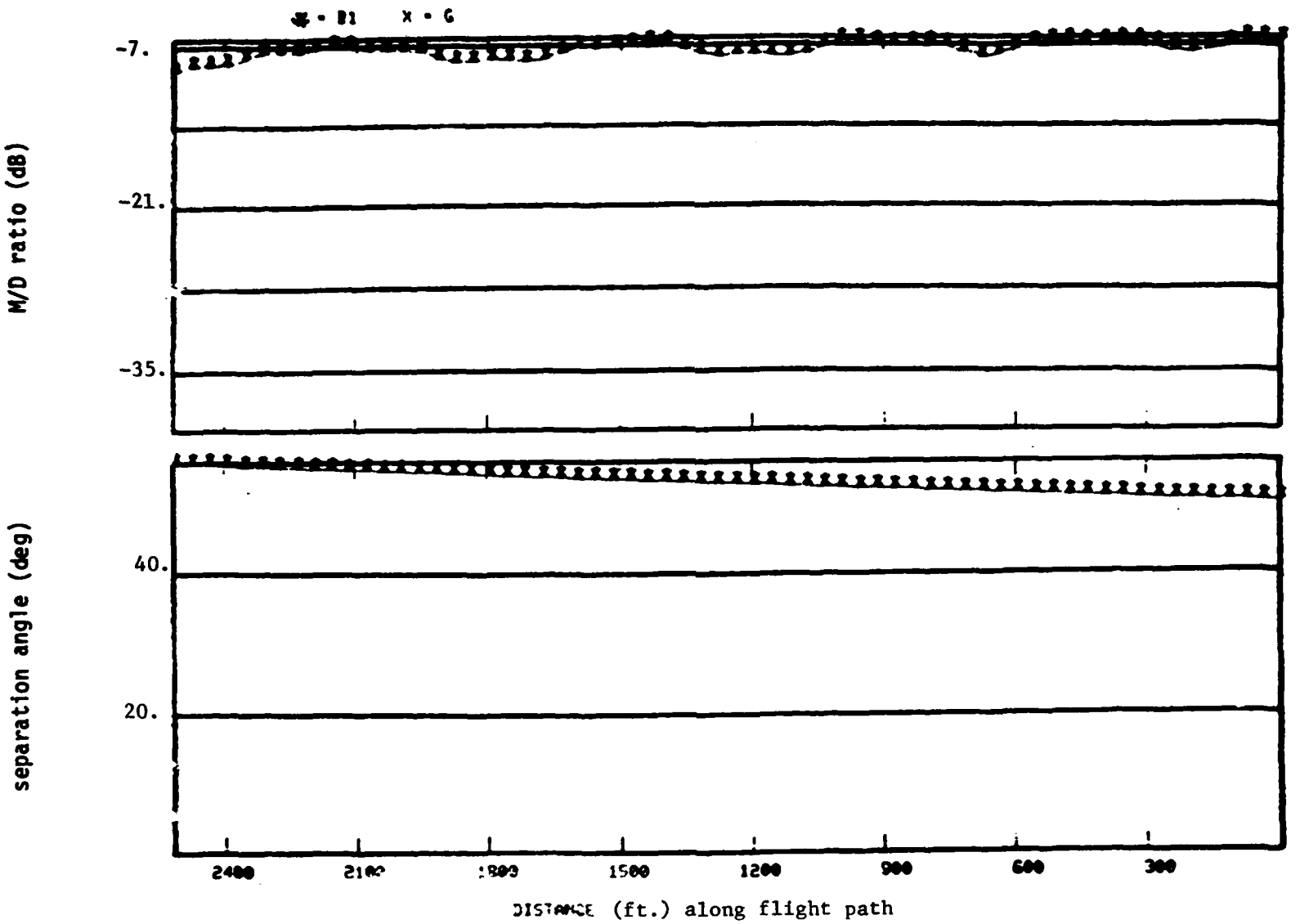

Fig. A-2. Azimuth multipath diagnostics for test scenario using "special" DMLS model.

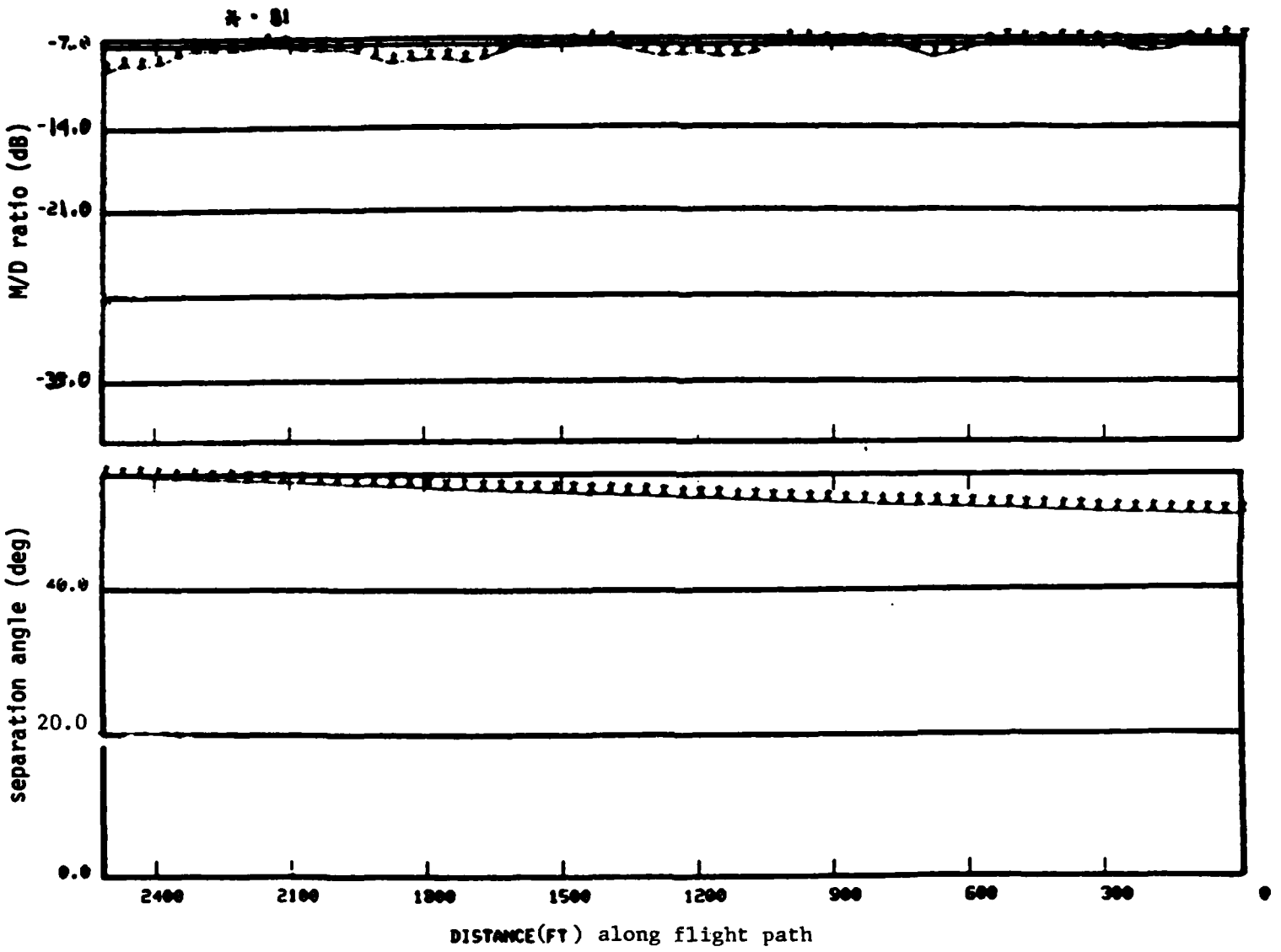

Fig. A-3. Azimuth multipath diagnostics using "standard" DMLS simulation model.

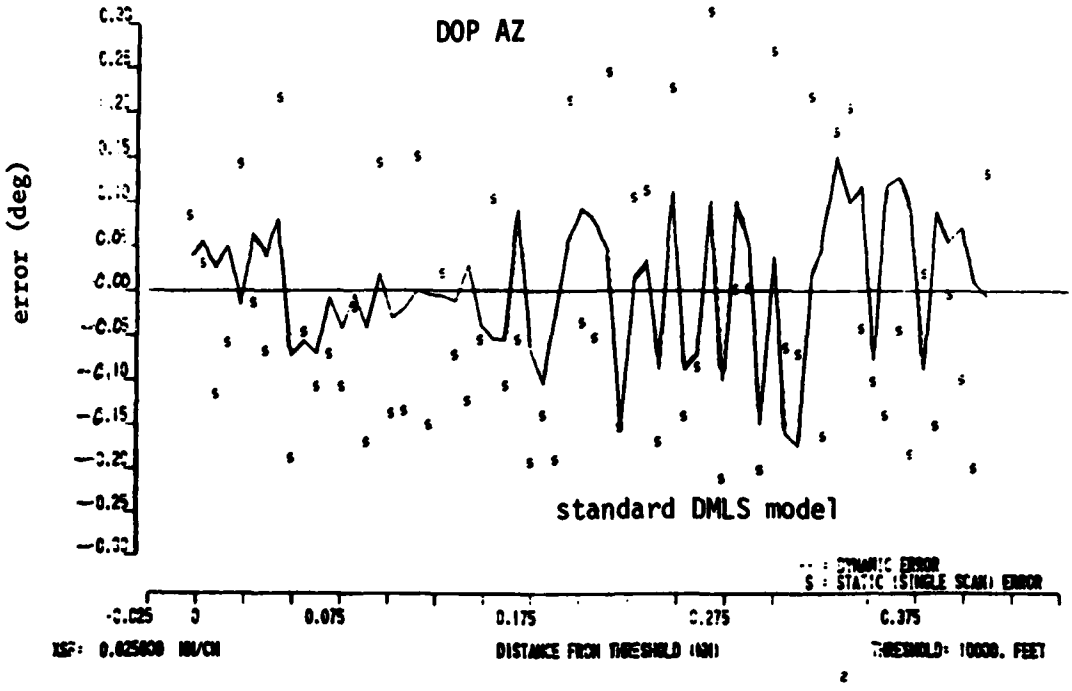

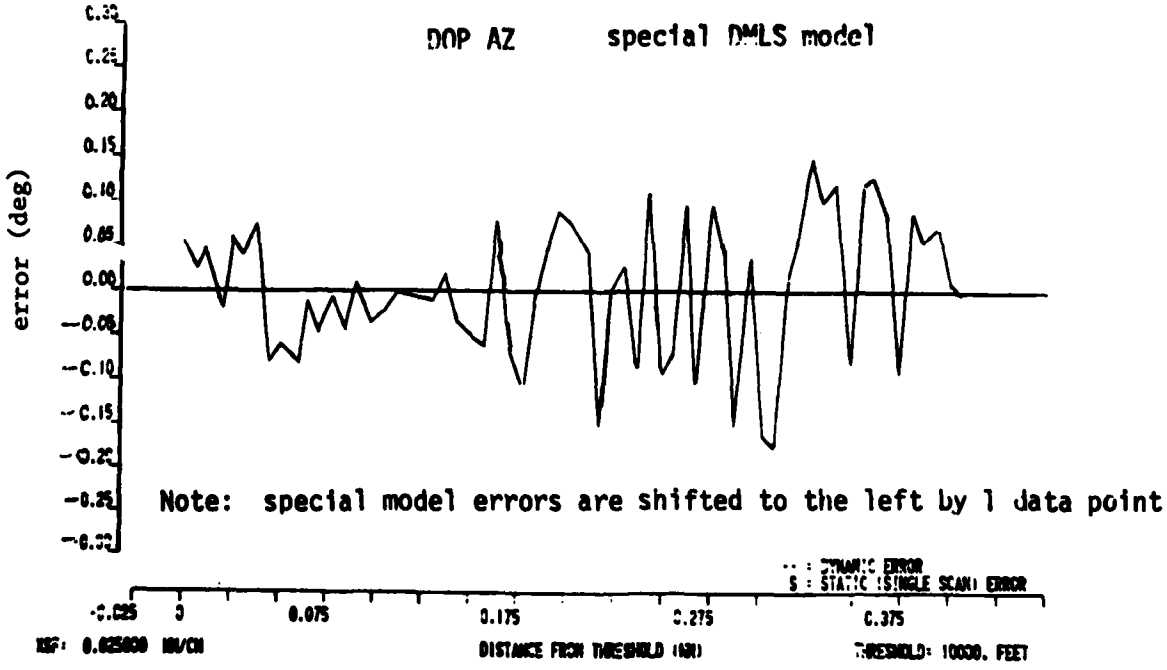

Fig. A-4. Comparison of "standard" and "special" DMLS models for test scenario.

APPENDIX B

SYSTEM IMPLEMENTATIONS SIMULATED

In this section we give a brief description of the specific implementation used in system simulations. More complete descriptions of the simulated systems and the corresponding mathematical models can be found in Volume II of this report.

1. DLS

The DLS multipath control features were summarized in Fig. 1-1. The proposed DLS AZ implementation has a 7λ diameter circular array (as opposed to the 10λ aperture utilized in field tests at Braunschweig) together with a linear array (used as an interferometer) employed when the magnitude of the estimate from the circular array is less than 40°. The baseline for the final estimate is 96.45λ. The 6 elements (see Fig. B-1) at each end of the line array are used as a 5.45λ subarray whose virtual beam pattern is steered toward the azimuth angle as estimated from the innermost elements of these subarrays utilized as a 91λ baseline interferometer.

The elevation antenna employs lateral diversity by dispersing the 30 elements into 5 columns of 6 elements in each column. Figure B-2 illustrates the arrangement of the 30 elements. There are 5 additional elements at the bottom to be used as reference elements in their respective columns. For the final 15λ baseline interferometer estimate, the top and bottom 15 elements are each combined as subarrays whose beam is steered toward the elevation estimate. For the sake of controlling ground reflections, the subarray is never steered below 5.23° elevation.

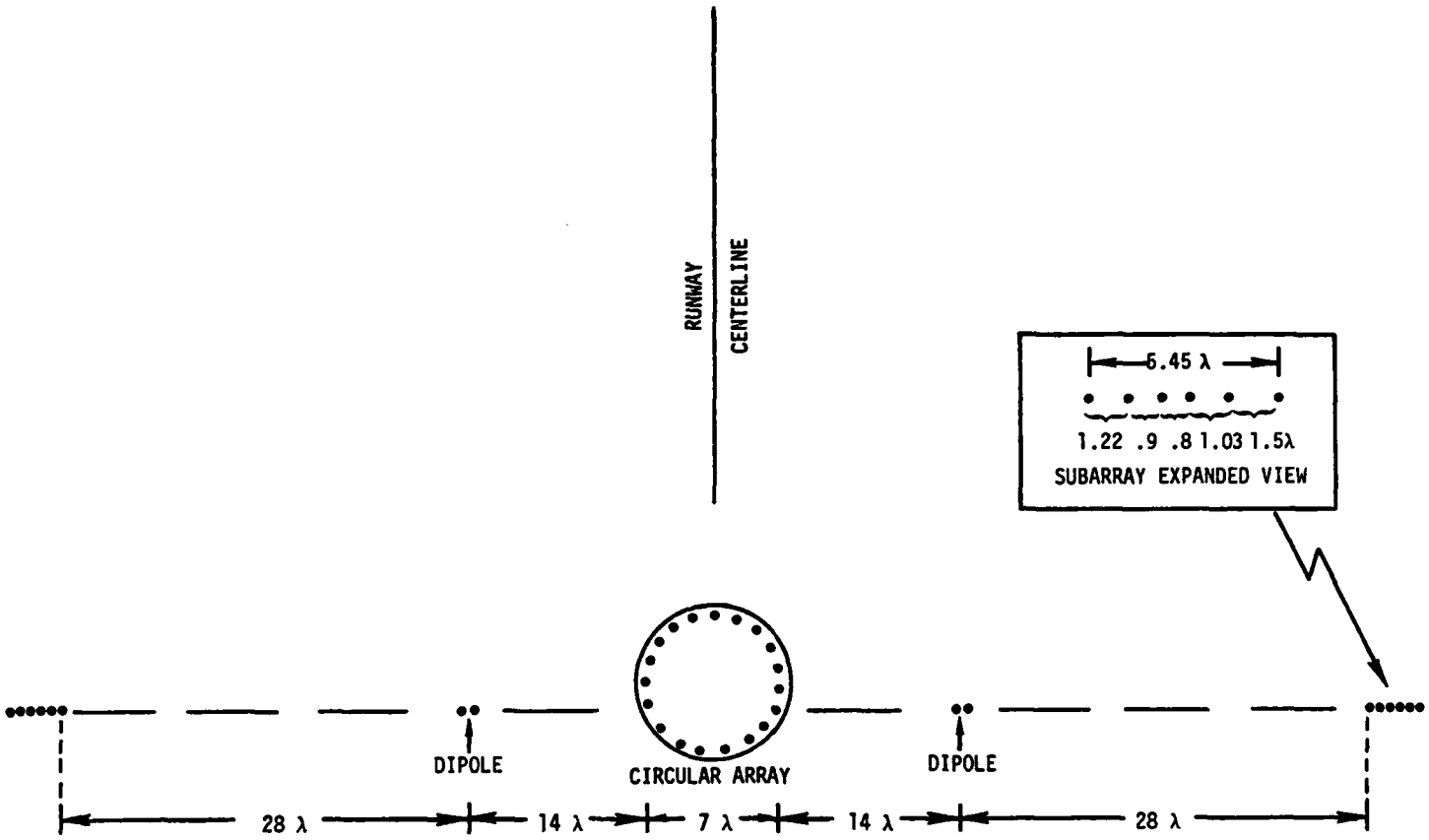

Fig. B-1. DLS azimuth antenna configuration.

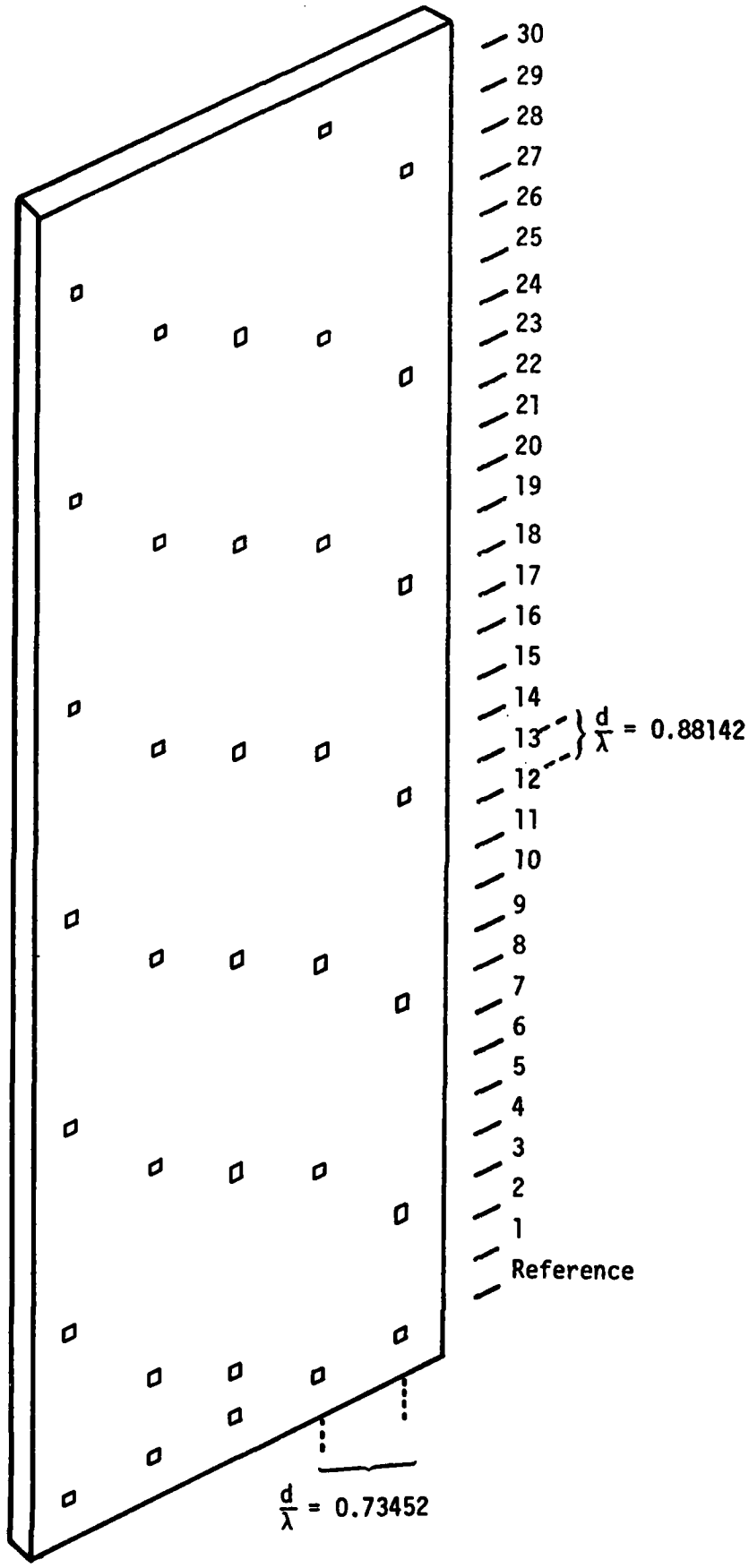

Fig. B-2. DLS lateral diversity EL antenna.

The final ground estimates are transmitted to the aircraft and used as input to a tracker whose output is the estimate utilized for guidance.

2. DMLS

The DMLS multipath combatting features were shown in Fig. 1-2. The specific implementation assumed for the simulation results reported here may be summarized as follows:

a) Signal Format

As described in the U.K. proposal [7], with the scan format $N_s/2$ scans in one direction followed by $N_s/2$ scans in the other direction, where N_s = number of scans in a given data frame (e.g., a "6 x 6" format for azimuth and 20" x 20" format for elevation).

b) Ground Equipment

(1) Azimuth

The "most capable" implementation has a 54λ filled main (commutating) array whose array element patterns are as in the UK proposal [7]. For this implementation, the (fixed) reference array consists of seven main array elements combined to yield a "centerline emphasis" pattern.

The cost reduced 'basic' system implementation is a 54λ commutated reference array in which the main array elements are 1.14λ apart while the two (commutating) reference elements are 0.57λ apart. In this case, the element patterns of the main and reference arrays are identical to those of the 54λ filled main array.

(2) Elevation

A 54λ filled array with fixed reference is used. The array element elevation pattern is as in the UK proposal [7], while the azimuth pattern has a greater gain in the forward direction. The (fixed) reference array elevation pattern is as in [7], while the azimuth pattern has the forward emphasis of the array elements. Lateral diversity is <u>not</u> utilized.

c) Airborne Receiver

The digital correlator processor tracker combines Taylor weighted subinterval correlation results to form "sum" and "difference" patterns. The local oscillator error, ε, on a given scan is taken to be Imag (Δ/Σ) beamwidths.* The local oscillator position on the next scan in the frame is changed by $\varepsilon/2$. A block average of the scan local oscillator frequency plus ε is used to give the local oscillator frequency at the beginning of the next frame as well as the angle estimate for the given frame. The tracker processing is identical for azimuth and elevation (except for the differences in scan duration and number). The acquisition and validation process as well as the AGC circuit described in Volume II is utilized for both functions.

3. TRSB

The TRSB multipath features were summarized in Fig. 1-3. The specific implementation assumed for the simulation results reported here is described in Volume II, its salient features being as follows:

a. Signal Format

As described in US proposal [65].

b. Ground Equipment

(1) Azimuth

The "most capable" implementation uses a 60λ filled phased array with the element patterns shown in the US proposal. The "cost reduced basic" system is a 60λ density tapered phased array using the same elements as in the filled array. Neither coverage control nor power programming (i.e., MCT) is utilized.

---

*The errors ε are truncated to 1 beamwidth.

(2) Elevation

A 60λ COMPACT array is used. The array elements roll off rapidly for elevation angles near the horizon and have "forward direction" emphasis in azimuth. Neither coverage control nor power programming is utilized.

c. Airborne Receiver

The receiver is the "real time" thresholding phase III receiver described in [65] and Volume II. The threshold used is -3 dB and the single scan estimates are smoothed by a digital α-β filter, subjected to the scan outlier test and then output at the scan rate. The single edge processor discussed in [92] is <u>not</u> utilized. The full acquisition/validation process described in volume II is incorporated in the computer simulations.

APPENDIX C

SIMULTANEOUS COMMUTATION IN DMLS ARRAYS

It was suggested by C. Earp [134, 141] and in the DMLS proposal [7] that by movement of both reference and sideband sources, it is possible for a commutated Doppler system to achieve the same resolution with half the aperture that would be required by a "normal" TRSB or Doppler array. If this were the case, then Doppler would have had a significant advantage in MLS applications (e.g., flare and portable tactical systems) where physically large apertures are particularly undesirable.

In this appendix, we analyze the capability of this two source movement scheme to achieve this resolution insofar as in-beam multipath rejection goes. It is concluded that

1) in those cases where the increased resolution is most needed, this scheme will not give better resolution in the sense of in-beam multipath rejection, and

2) with the most recently proposed scheme, there will be a substantial decrease in out-of-beam multipath rejection as well as poorer in-beam multipath performance at high M/D levels.

The remainder of the appendix is organized as follows. In Section 1, we describe the basic notion behind the proposed scheme and give some general theoretical arguments as to why it should not be successful in achieving better resolution. There were no fully detailed descriptions of the commutation approach to be used; consequently we analyze several different possibilities in Sections 2 to 4 under the assumption of no diversity in the orthogonal plane (e.g., no "lateral diversity" for the elevation system). Section 5

presents explicit formulas for the angular errors due to multipath. Section 6 summarizes the results and draws conclusions on the overall multipath performance of the three principal array commutation methods.

1. Overview of Two Source Realization and Expected Performance

The basic train of thought underlying the initial commutated Doppler two source mobility scheme was as follows:

(i) The commutated Doppler technique requires only that a constant relative motion in the scan plane be maintained between the two sources [7].

(ii) The effective resolution beamwidth, BW, of the array can be related to the excess Doppler change

$$\delta\omega = \frac{1}{T}\left[\phi_s(t) - \phi_R(T)\right] - \frac{1}{T}\left[\phi_s(0) - \phi_R(0)\right] - \omega_{os} \qquad \text{(C-1)}$$

by BW ≈ receiver angle change to yield $\delta\omega = 1/T$
where

$\phi_s(t)$ = sideband (commutated array) phase at the receiver

$\phi_R(t)$ = reference (commutated array) phase at the receiver

t = time since the start of a single scan

T = scan duration

ω_{os} = offset frequency between sideband and reference
$= \omega_c - \omega_r$

(iii) With "normal" Doppler processing, only the sideband element moves so that

$$\phi_s(t) - \phi_s(0) \approx 2\pi \frac{vT}{\lambda} \sin\theta + \omega_c T$$
$$= 2\pi \frac{L}{\lambda} \sin\theta + \omega_c T$$

$$\phi_R(t) - \phi_R(0) \approx \omega_r T$$

$$\delta\omega = 2\pi \frac{L}{\lambda} \sin\theta \cdot \frac{1}{T}$$

yielding*

$$BW \approx [2\pi\ (L/\lambda)\ \cos\ \theta]^{-1} \qquad \text{(C-2)}$$

when θ = receiver angle in the function coordinate

(iv) If the reference element also moves during the scan in the opposite direction so the sideband and reference elements interchange positions by the end of scan, then as before

$$\phi_s(T) - \phi_s(0) \approx 2\pi \frac{L}{\lambda} \sin\ \theta + \omega_c T$$

but now

$$\phi_R(T) - \phi_R(0) = 2\pi \frac{(-v)\ T}{\lambda} \sin\ \theta + \omega_r T$$

$$= -2\pi \frac{L}{\lambda} \sin\ \theta + \omega_r T$$

$$\delta\omega = 2\pi\ (2L/\lambda)\ \sin\ \theta \cdot (1/T)$$

and we appear to have

$$BW = [2\pi\ (2L/\lambda)\ \cos\ \theta]^{-1} \qquad \text{(c-3)}$$

Comparing (C-2) and (C-3), it appears that two source mobility has resulted in halving the required aperture to achieve a given resolution. In Fig. C-1, we provide a graphical illustration of the same arguments.

We shall see that the fallacy in the above arguments as far as multipath performance goes is that the <u>multiplicative</u> nature of the Doppler receiver which permits (i) to hold also generates cross products between the multipath and direct signals. These cross products turn out to have frequencies which overlap the desired signal exactly as would be the case with a normal array. And, in both cases, these cross products are the principal error contribution.

More recently, it was suggested [7] that by pseudo randomly moving the two sources around during the scan, the deleterious cross products can be

---

*Equation (C-2) is essentially the resolution of a TRSB phased array.

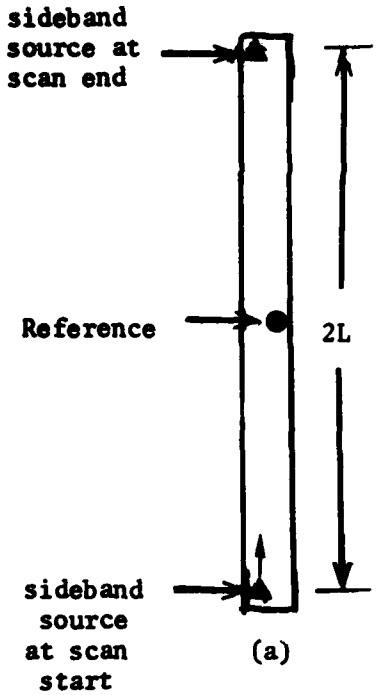

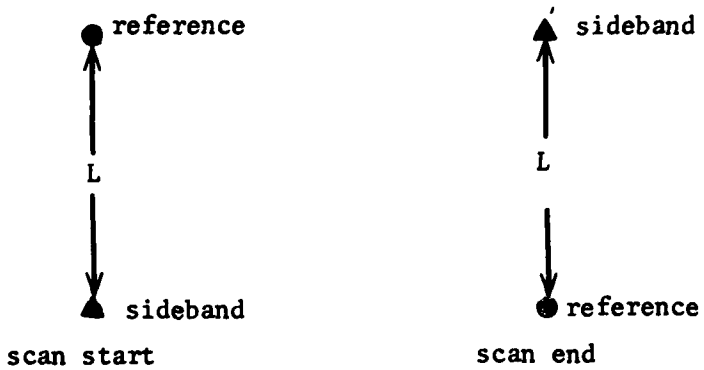

(b) relative locations of sideband and reference sources

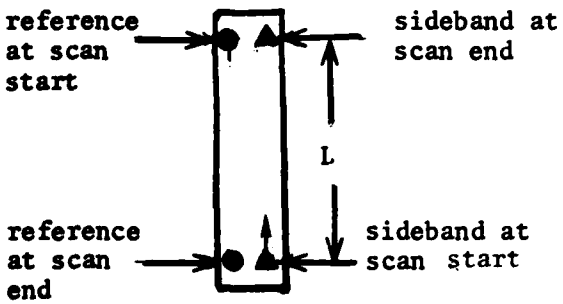

(c) two source movement commutated array

Relative positions of sideband and reference sources at scan start and end are same in both cases ∴ if this is all that matters, effective aperture has been doubled.

Fig. C-1. One argument for increased Doppler resolution via "two source mobility."

decorrelated so that the resolution is doubled. We shall see that for in-beam multipath, the amount of decorrelation is quite small; and that with such a scheme, both in-beam and out-of-beam multipath performances will suffer in certain cases.

Before making a detailed analysis of the performance for various two source mobility mechanizations, it seems appropriate to outline some theoretical arguments as to why such a scheme would not be expected to achieve significantly improved resolution. The train of thought goes as follows:

(1) For a commutated array, the received signal amplitude and phase for each element position provide a complete description of the multipath environment (since given these values, one could, in principle, recreate the entire received waveform),

(2) The time sequence of values obtained at the receiver in (C-1) is identical to the values that would be obtained at the various antenna elements by a ground derived system if the airplane transmitted a signal at the appropriate frequency, as illustrated in Fig. C-2.

(3) Therefore, we can use the well established theory for ground based radar resolution [142] to bound the performance of a Doppler airborne receiver.

(4) The two source mobility, at best, would amount to making measurements at each element on two different frequencies. This could provide improved resolution if the multipath delays are a significant fraction of (1/frequency difference). However, for the UK Doppler format

$\Delta f \sim 84$ kHz

$1/\Delta f \sim 11.9$ μsec

whereas virtually all significant MLS multipath studied to date has delays < 3 μsec. In those cases where increased resolution would be of greatest practical aid (ground reflections for elevation/flare and azimuth in-beam multipath), the multipath time delays would range from 0.1 nsec to 0.3 μsec.

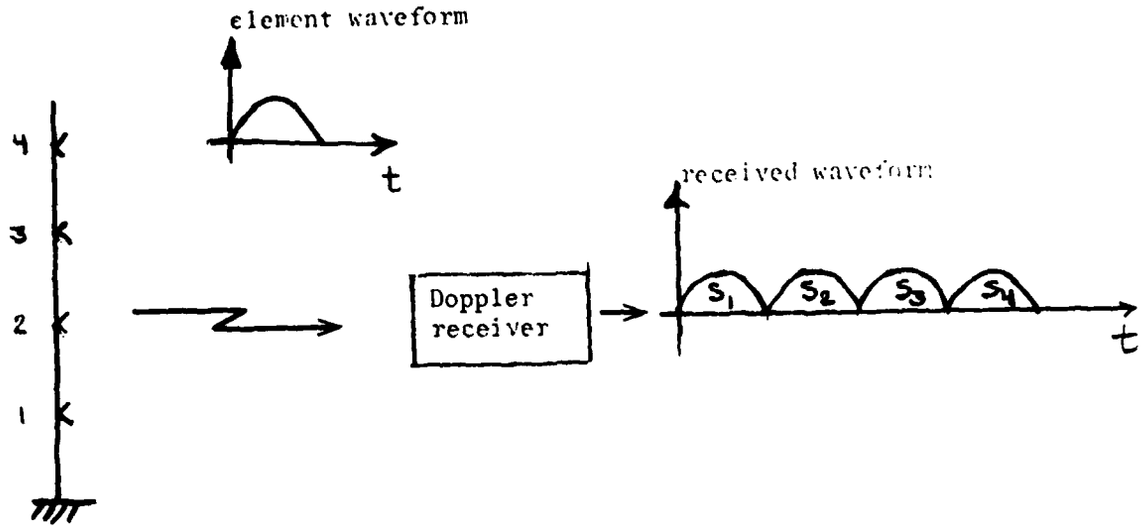

Fig. C-2a. Commutated Doppler array.

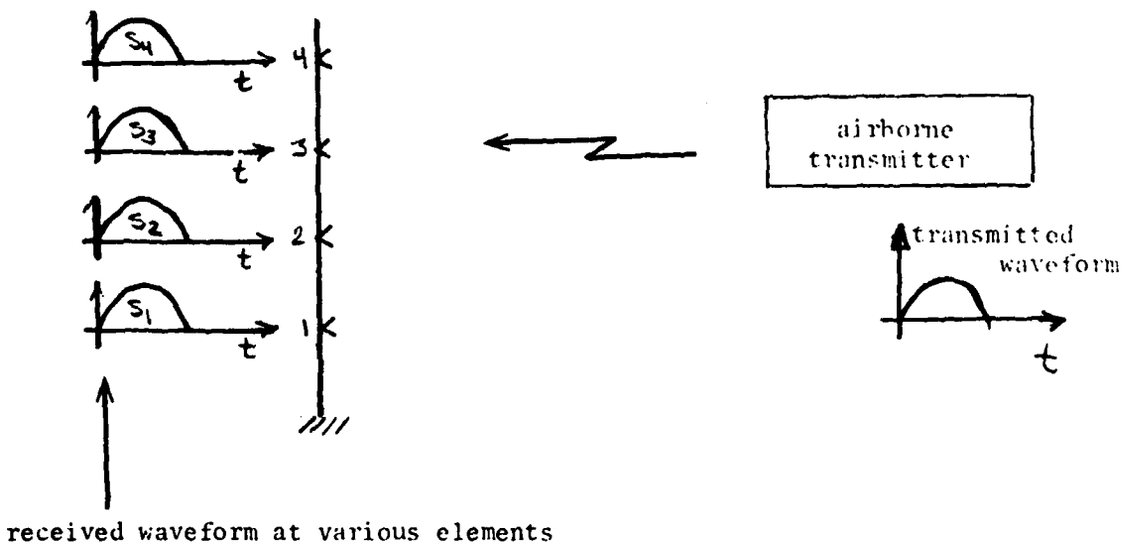

Fig. C-2b. Ground derived system which is dual to commutated Doppler array.

(5) Consequently, if practial Doppler receivers have a resolution close to that of typical ground based radars, it would seem unlikely that the two source scheme would yield a factor of two improvement in resolution.

2. Linear Simultaneous Two Source Movement

In this scheme, at the beginning of the scan, the sideband and reference signals are radiated from opposite ends of the array. During the scan, the sources are uniformly moved toward the opposite ends of the aperture so that by the end of the scan they have interchanged positions as illustrated in Fig. C-3. For simplicity, we consider only a single scan, a motionless receiver, and we will ignore the discrete nature of the commutation process.

The ideas in the analysis are quite simple: we assume the Doppler detector is a squarer followed by a bandpass filter leaving only those components which are near frequency ω_{os}. The multipath and direct components for the sideband and reference signals are represented in complex form to minimize the algebra. We then compare the differential frequency of the various output terms with (1/scan duration) to see if increased resolution has been obtained.

The various received rf signals are as follows:

<u>Sideband (commutated):</u>

direct: $C_D = \exp[j(\omega_c t + kvt \sin \phi_d + \phi_d)]$ (C-4)

multipath: $C_M = \rho \exp[j(\omega_c t + kvt \sin \phi_m + \phi_m)]$ (C-5)

<u>Reference:</u>

direct $R_D = \exp[j(\omega_r t - kvt \sin \theta_d + \tilde{\phi}_d)]$ (C-6)

multipath $R_M = \rho \exp[j(\omega_r t - kvt \sin \theta_m + \tilde{\phi}_m)]$ (C-7)

where ω_c = sideband frequency

ω_r = reference frequency

v = scan velocity

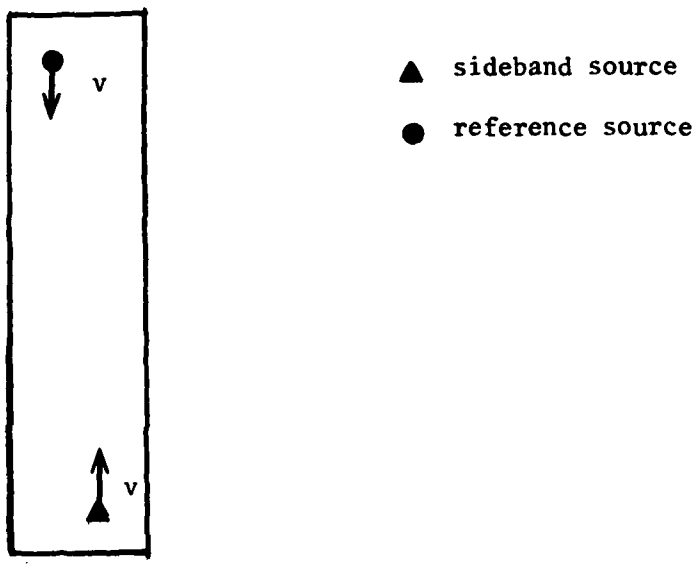

Both sources simultaneously move at velocity v towards opposite end of the array.

Fig. C-3. Simultaneous linear two source movement.

$k = 2\pi/\lambda$

θ_d = direct signal angle (in scan coordinate)

θ_m = multipath signal (in scan coordinate)

ϕ_d, ϕ_m = direct and multipath commutated phases at scan start

$\tilde{\phi}_d$, $\tilde{\phi}_m$ = direct and multipath reference phases at scan start

ρ = M/D (amplitude) ratio

With the above notion, the operation of the detector and bandpass filter can be represented as the product

$$(C_D + C_M)\ (R_D + R_M)^* \tag{C-8}$$

where $(\quad)^*$ denotes conjugation. Carrying out (C-8), we find

desired direct: $C_D R_D^* = \exp[j(\omega_{os}t + 2Kt \sin\theta_d + \phi_d + \tilde{\phi}_d)]$

"ρ^2" multipath: $C_M R_M^* = \rho^2 \exp[j(\omega_{os}t + 2kT \sin\theta_m + \phi_m - \tilde{\phi}_m)]$

cross product 1: $C_D R_M^* = \rho \exp j[\omega_{os}t + Kt(\sin\theta_d + \sin\theta_m) + \phi_d - \tilde{\phi}_m]$

cross product 2: $C_M R_D^* = \rho \exp j[\omega_{os}t + Kt(\sin\theta_M + \sin\theta_d) + \phi_m - \tilde{\phi}_d]$

where $K = (2\pi\ v/\lambda)$

The normalized* frequency separations are by inspection

$$\begin{aligned}\omega_{MM} = \omega_{DD} &= 2K(\sin\theta_m - \sin\theta_d)/(1/T) \\ &= 2\pi\left(\frac{2L}{\lambda}\right)(\sin\theta_d - \sin\theta_m)\end{aligned} \tag{C-9}$$

$$\begin{aligned}\omega_{DM} - \omega_{DD} = \omega_{MD} - \omega_{DD} &= [-2K\sin\theta_d + K(\sin\theta_d + \sin\theta_m)]/(1/T) \\ &= 2\pi\left(\frac{L}{\lambda}\right)(\sin\theta_m - \sin\theta_d)\end{aligned} \tag{C-10}$$

For normal commutated Doppler, v=0 in Eqs. (C-6) and (C-7). This can be shown to yield the normalized frequency separations:

---

*The normalized frequency separation is defined as the difference in radian frequency ÷ (1/T). This is equivalent to 2π x separation angle in beamwidths.

$$f_{MM} - f_{DD} = f_{MD} - f_{DD} = 2\pi \left(\frac{L}{\lambda}\right) (\sin \theta_d - \sin \theta_m) \qquad \text{(C-11)}$$

$$f_{DM} - f_{DD} = 0$$

The term $f_{DM} - f_{DD}$ does not of itself cause any error in a static situation since it has zero separation angle.

Comparing (C-9) and (C-10) to (C-11), we see that this particular two source movement scheme has increased the separation between the $C_D R_D^*$ term and $C_M R_M^*$ terms such that if only the $C_M R_M^*$ term were of concern, we would have achieved the same result as doubling the aperture of a "normal" commutated Doppler array.

However, the most troublesome terms are the $C_D R_M^*$ and $C_M R_D^*$ since they are larger by ρ than the $C_M R_M^*$ term. We see that the separation of these from the direct signal has either not changed or has gotten worse. Consequently, this particular scheme appears to offer little in the way of improved performance.

In Section 5, we show that for small multipath levels, the error performance is fairly similar to that of a "normal" commutated Doppler system. However, for large (e.g., > -6 dB) multipath, large errors can arise with this scheme due to capture by the multipath components.

Additionally, it should be noted that use of this scheme might necessitate some modification of the Doppler channelization if it is necessary to accommodate the first sidelobe of both the sideband and reference signal

spectra, each of which are switched at the normal commutation frequency. (See Section 2.2.2 of Ref. [7] for a discussion of the issues involved).

3. Linear Sequential Two Source Movement

As was the case in the preceding section, the sideband reference signals are radiated from opposite ends of the array. However, during the first part of the scan, only the sideband source moves uniformly toward the opposite end of the array. When it reaches the far end from which the reference source was radiating, it stops. The reference source then moves uniformly to the other end, reaching it at the end of the scan. Thus, as is illustrated in Fig. C-4, the two sources have swapped locations by the end of the scan.

To maintain the same scan velocities and spectrum occupancy, the scan duration must be increased by a factor of two. Although this scheme would appear at first inspection to be essentially identical to that of the previous section, it turns out that a rather different analysis must be used.

Using the complex signal and detector representation of the preceding section, it is easy* to obtain the following results:

1. First half of scan ($0 < t < T$ source at ω_c moves, source at ω_r stationary):

---

*Set v=0 in (C-6) and (C-7) for the first scan half. In the second scan half, set v=0 in (C-4) and (C-5) and recognize that at the start of the second half of the scan,

$$\phi_d = \phi_d + KT \sin \theta_d$$

$$\phi_m = \phi_m + KT \sin \theta_m$$

kvt must be replaced by kv(t-T)

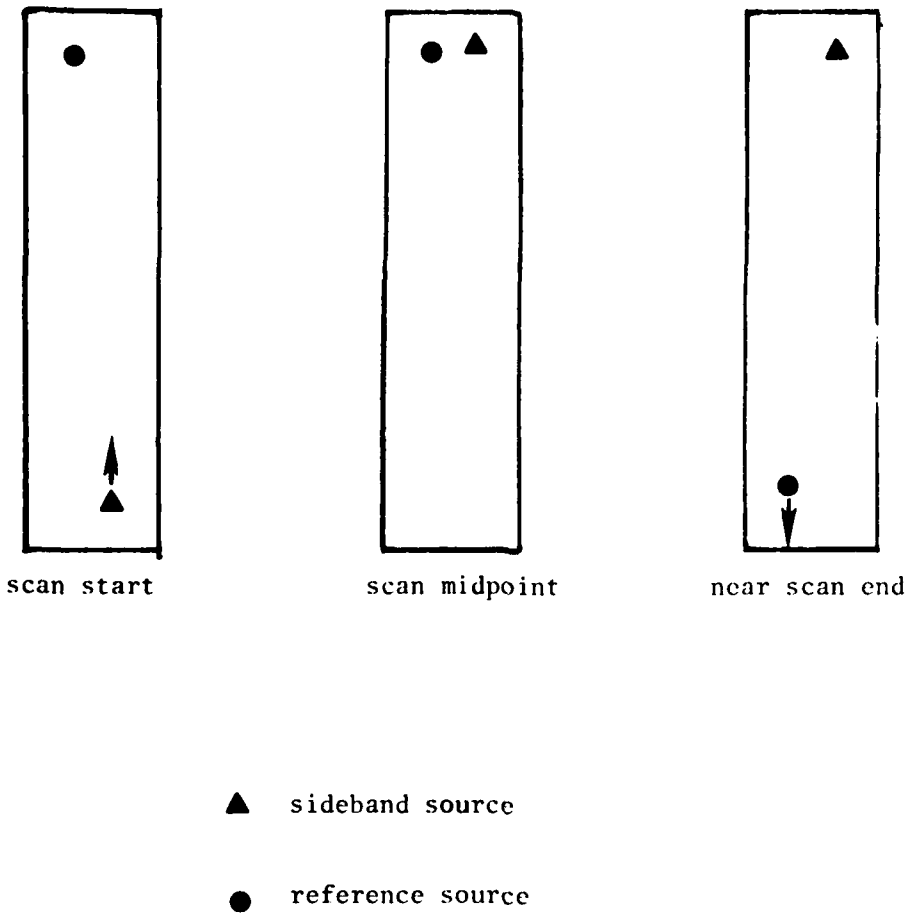

Fig. C-4. Sequential linear two source movement.

AD-A148 524 MLS MULTIPATH STUDIES PHASE 3 VOLUME 3 APPLICATION OF MODELS TO MLS ASSES..(U) MASSACHUSETTS INST OF TECH LEXINGTON LINCOLN LAB J E EVANS ET AL. 08 JUN 81 4/4

UNCLASSIFIED ATC-88-VOL-3-PT-2 FAA-RD-79-21-VOL-3-PT2 F/G 17/7 NL

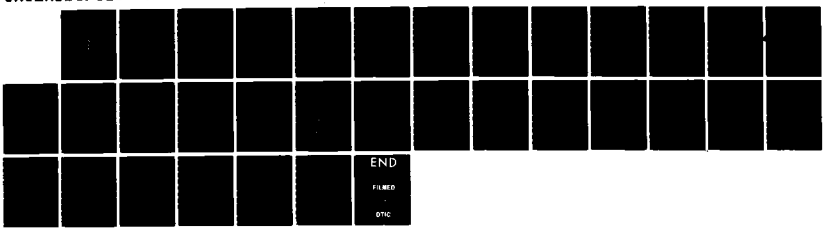

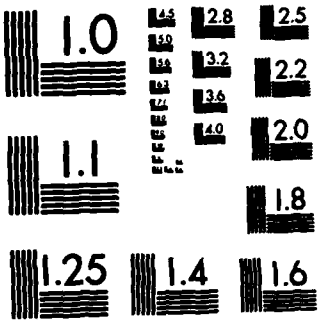

MICROCOPY RESOLUTION TEST CHART
NATIONAL BUREAU OF STANDARDS-1963-A

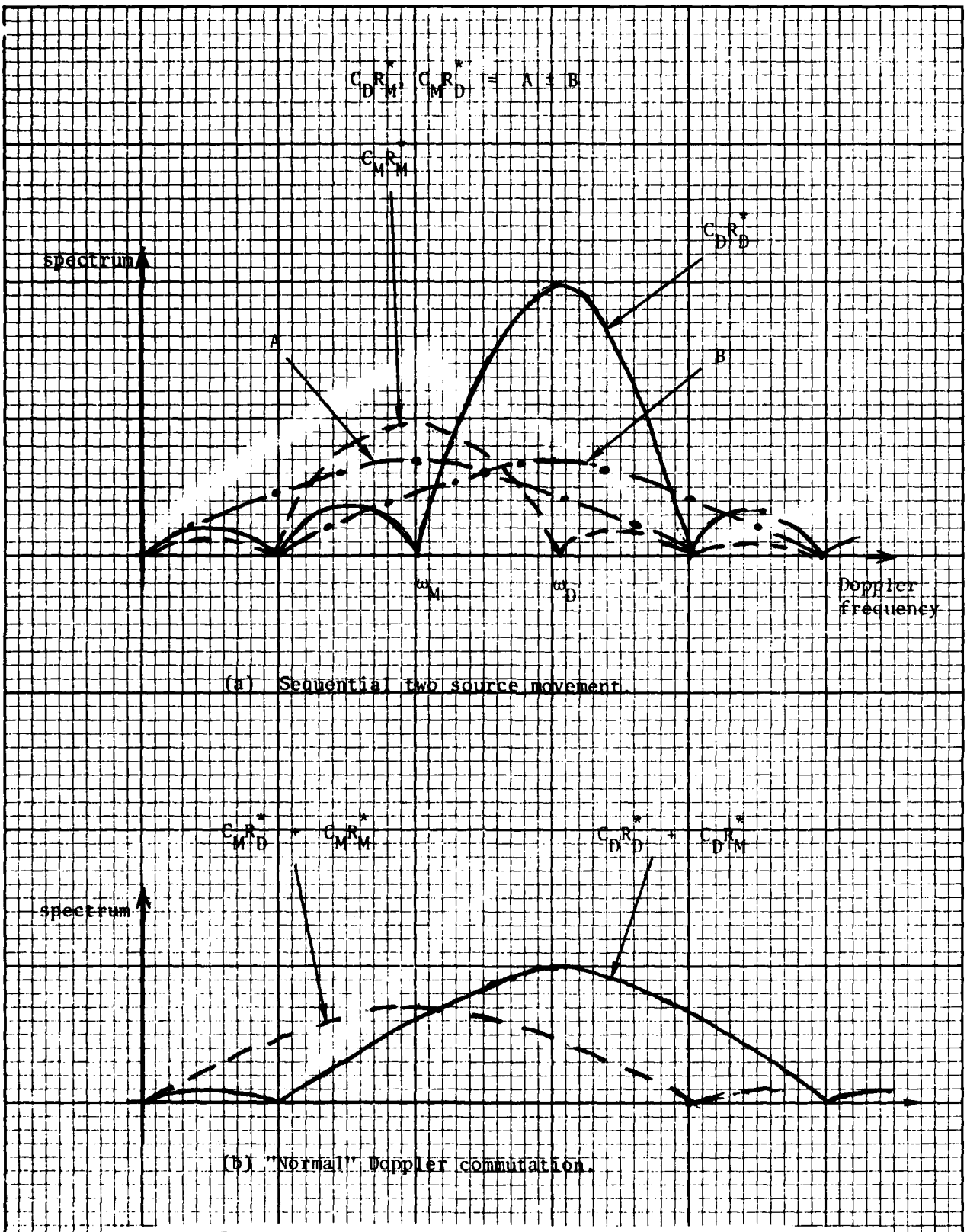

Fig. C-5. Spectra of various Doppler components.

$$C_D R_D^* = \rho \exp j[(\omega_c - \omega_r)t + Kt \sin \theta_d + \phi_d - \tilde{\phi}_d] \quad \text{(C-12)}$$

$$C_D R_M^* = \rho \exp j[(\omega_c - \omega_r)t + Kt \sin \theta_d + \phi_d - \tilde{\phi}_m] \quad \text{(C-13)}$$

$$C_M R_D^* = \rho \exp j[(\omega_c - \omega_r)t + Kt \sin \theta_m + \phi_m - \tilde{\phi}_d] \quad \text{(C-14)}$$

$$C_M R_M^* = \rho^2 \exp j[(\omega_c - \omega_r)t + Kt \sin \theta_m + \phi_m - \tilde{\phi}_m] \quad \text{(C-15)}$$

2. Second half of scan ($T \leq t \leq 2T$, source at ω_r moves, source at ω_c stationary):

$$C_D R_D^* = \exp j[(\omega_c - \omega_r)t + Kt \sin \theta_d + \phi_d - \tilde{\phi}_d] \quad \text{(C-16)}$$

$$C_D R_M^* = \rho \exp j[(\omega_c - \omega_r)t + Kt \sin \theta_m + \phi_d - \tilde{\phi}_m + KT(\sin \theta_d - \sin \theta_m)] \quad \text{(C-17)}$$

$$C_M R_D^* = \rho \exp h[(\omega_c - \omega_r)t + Kt \sin \theta_d + \phi_m - \tilde{\phi}_d + KT(\sin \theta_m - \sin \theta_d)] \quad \text{(C-18)}$$

$$C_M R_M^* = \rho^2 \exp j[(\omega_c - \omega_r)t + Kt \sin \theta_m + \phi_m - \tilde{\phi}_m] \quad \text{(C-19)}$$

The terms $C_D R_D^*$ and $C_M R_M^*$ represent sinusoids which are continuous at t=T with a normalized frequency separation

$$\begin{aligned} f_{DD} - f_{MM} &= K(\sin \theta_d - \sin \theta_m)/(1/2\ T) \\ &= 2\pi(2L/\lambda)\ (\sin \theta_d - \sin \theta_m) \end{aligned} \quad \text{(C-20)}$$

which is identical to (C-11) in the previous section. And, as before, if only these terms were important, then there would be a two-fold increase in apparent resolution.

But, as before, it is the cross terms ($C_D R_M^*$ and $C_M R_D^*$) which are of greatest concern. Here the plot thickens since both terms have an abrupt change in frequency at t=T. Thus, we cannot assign a frequency separation to them as was possible in the earlier section.

Rather, we must look at the spectra of the various terms as is done in Fig. C-5a. In Fig. C-5b, we show the spectra for a "normal" commutated Doppler system. We see that with the two source movement of Fig. C-4, the cross terms have spectra locations and widths that are identical to those of a "normal" commutated Doppler system.

Figure C-5 suggests a small improvement against in-beam multipath if a filter of bandwidth (1/2 T) could be centered on the direct signal, but clearly not a factor of two improvement. However, it is hard from spectral arguments alone to assess the impact of the cross terms at the direct signal Doppler on the overall receiver performance.

Thus, it is instructive to examine the signal waveforms at ω_d and ω_m. These are given by:

	$0 < t < T$	$T < t < 2T$
at $\omega_d = \omega_{os} + K \sin \theta_d$	eq. C-12) + eq. (C-13)	eq. (C-15) + eq. (C-18)
at $\omega_m = \omega_{os} + K \sin \theta_m$	eq. (C-14) + eq. (C-15)	eq. (C-17) + eq. (C-19)

and sketched in Fig. C-6. We see that both waveforms suffer a phase jump at t=T. These waveform discontinuities are similar to those that would occur with two single direction scans of a normal commutated Doppler array. Since with a normal commutated Doppler array increased multipath resolution is generally not obtained by processing sequential same direction scans as one, it would seem unlikely that increased resolution could be obtained with this particular two source movement scheme.

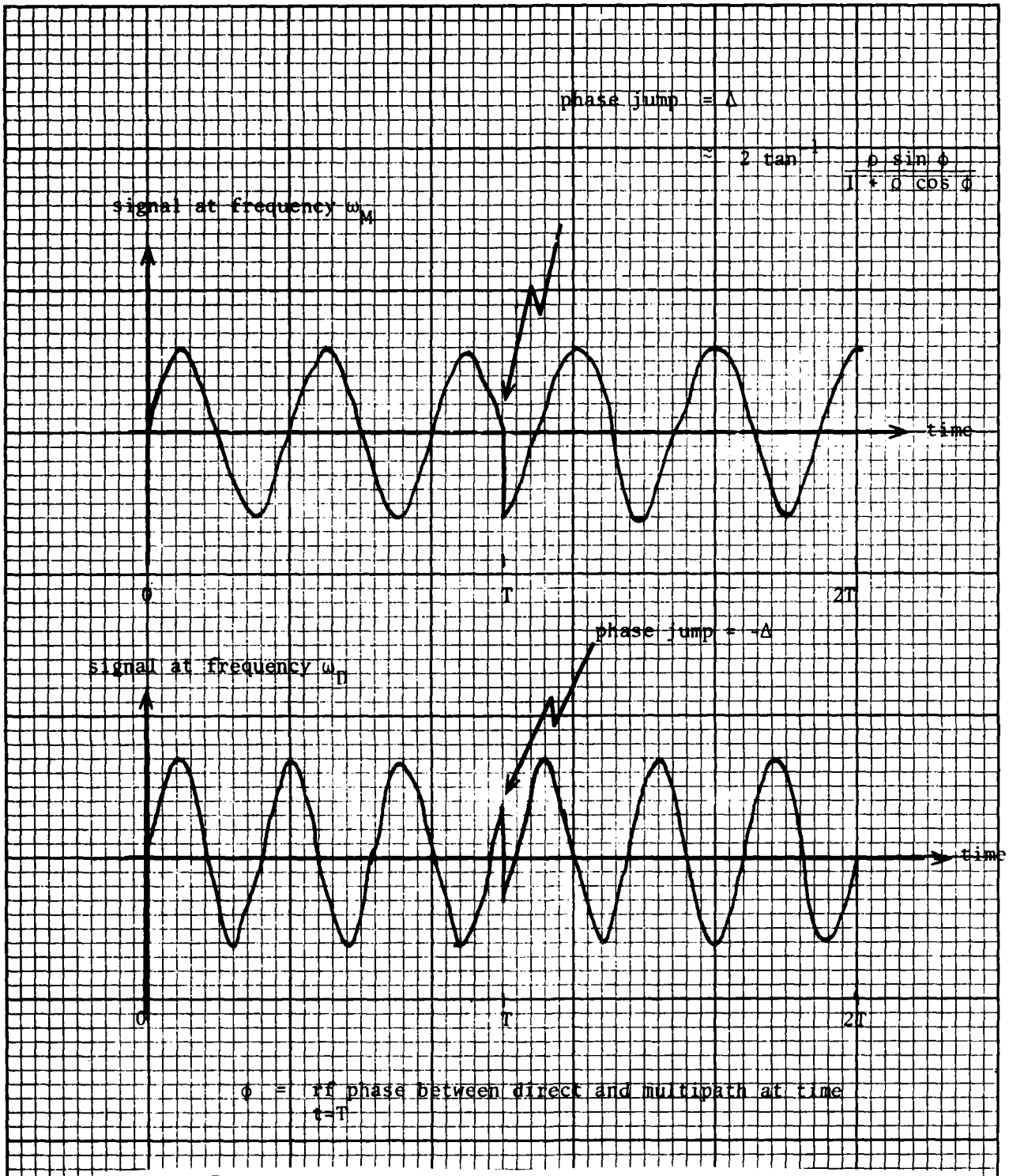

Fig. C-6. Time waveforms with sequential linear two source movement.

4. Randomized Linear Two Source Movement

In the preceding sections, we observed that the multipath cross terms ($C_D R_M^*$ and $C_M R_D^*$) prevented the two source movement schemes from achieving the desired increase in resolution. Evidently, similar conclusions were reached in the UK as well, since the final proposal [7] seemed specifically oriented toward significantly reducing these terms by having the instantaneous center of radiation move around pseudo randomly during the scan.

We have specifically considered the case shown in Fig. C-7 where the two sources move simultaneously toward each other as in Section 3 with the effective center of radiation being changed pseudorandomly on successive commutation steps. The objective of such jumping around is to spread the spectra of the cross terms so that the "in-beam" power is sharply reduced, whereas the direct term ($C_D R_D^*$) and "classical" multipath term ($C_M R_M^*$) are not spread.

A. Signal Model

Since the jumps occur at discrete points in time, we must use a slightly different model for the rf signals. To keep the analysis as simple as possible, we consider the case of "hard" switching between the elements. Then, for source separation $2\ell\delta$ (ℓ an integer, δ the element spacing with the effective center at $m\delta$), we have

$$C_D = \exp j[\omega_c t + k(\ell+m) \sin \theta_d + \alpha_d)] \tag{C-21}$$

$$C_M = \rho \exp j[\omega_c t + k(\ell + m) \sin \theta_m + \alpha_m] \tag{C-22}$$

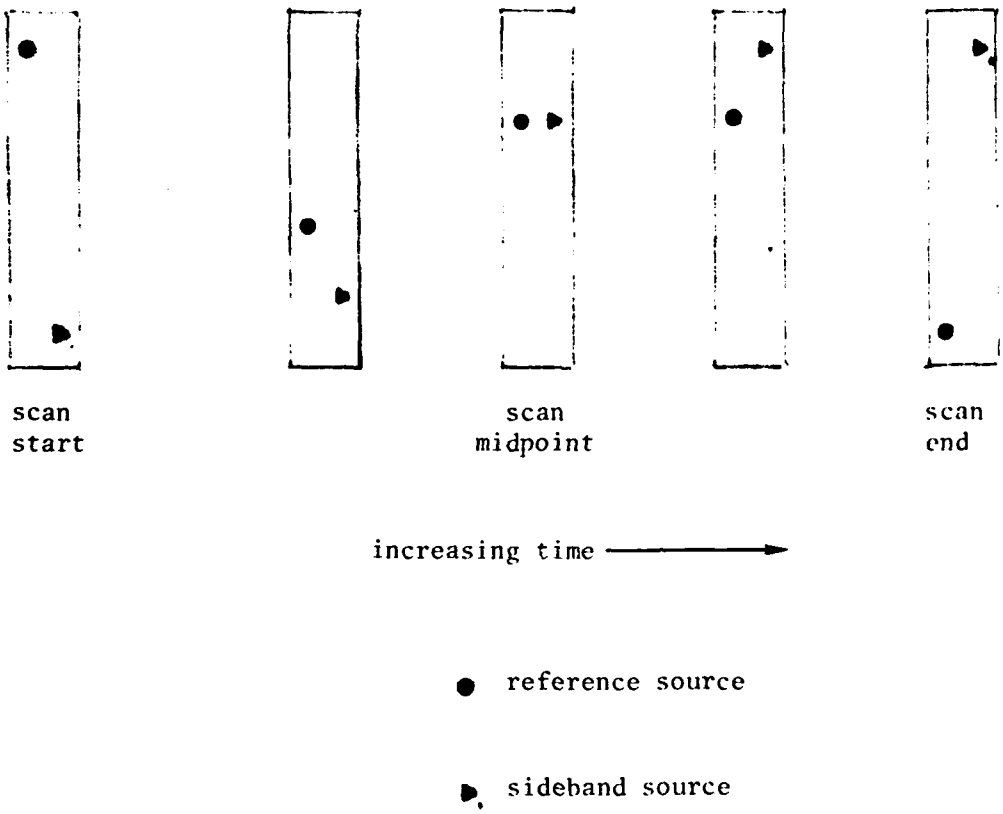

Source separation changes linearly, but instantaneous center location changes pseudorandomly on each commutation step.

Fig. C-7. Reference/sideband source locations in randomized two source movement.

$$R_D = \exp j[\omega_r t + k(m-\ell) \sin \theta_d + \beta_d] \tag{C-23}$$

$$R_m = \rho \exp j[\omega_r t + k(m-\ell) \sin \theta_m + \beta_m] \tag{C-24}$$

where:

α, β = various direct and multipath phases at array center

m = 0 at array center

and the other variables are as defined in Section 3.

We now want to see what happens to the various products when the sideband to reference spacing goes from $2\ell\delta$ with the effective center at $m\delta$ to $(2\ell + 2)\delta$ with the effective center at $\tilde{m}\delta$.*

When the two sources are separated by $2\ell\delta$, we have:

$$C_D R_D^* = \exp j[\omega_c - \omega_r)t + 2k\ell\delta \sin \theta_d + (\alpha_d - \beta_d)]$$

$$C_D R_M^* = \exp j\{(\omega_c - \omega_r\}t + k\delta[\ell(\sin \theta_d + \sin \theta_m) + m(\sin \theta_d - \sin \theta_m)] + \alpha_d - \beta_m\}$$

$$C_M R_D^* = \exp j\{(\omega_c - \omega_r)t + k\delta\{\ell(\sin \theta_d + \sin \theta_m) + m(\sin \theta_m - \sin \theta_d) + \alpha_m - \beta_d\}$$

---

*To yield the scan pattern of Fig. 7, $\ell = K/2\delta$ at the scan start and $+L/2\delta$ at the scan end. The separation changes by 2δ on each commutation step since both elements are assumed to move at an average velocity of $L/T = f_c$ where f_c = commutation frequency.

$$C_M R_M^* = \rho^2 \exp j[\omega_c t + 2k\delta\ell \sin \theta_m + \alpha_m - \beta_m]$$

At a sideband to reference spacing of $(\ell+2)\delta$, the results are as above with m replaced by $\tilde{m}$.

The change in phase of the various product terms between the two spacings is then:

$$C_D R_D^* \text{ phase change: } (\omega_c - \omega_r)\,\Delta T + 2k\delta \sin \theta_d \tag{C-25}$$

$$C_M R_M^* \text{ phase change: } (\omega_c - \omega_r)\,\Delta T + 2k\delta \sin \theta_m \tag{C-26}$$

$$\begin{aligned} C_D R_m^* \text{ phase change: } & (\omega_c - \omega_r)\,\Delta T + k\delta(\sin \theta_d + \sin \theta_d) \\ & + k\delta(\tilde{m}-m)\,(\sin \theta_m - \sin \theta_d) \end{aligned} \tag{C-27}$$

$$\begin{aligned} C_M R_d^* \text{ phase change: } & (\omega_c - \omega_r)\,\Delta T + k\theta(\sin \theta_d + \sin \theta_m) \\ & + k\delta(\tilde{m}-m)\,(\sin \theta_m - \sin \theta_d) \end{aligned} \tag{C-28}$$

where ΔT = time spacing between commutation steps.

The term $(\omega_c - \omega_r)\Delta T$ arises because we evaluate the phase change between the midpoint of the successive commutation steps. The first two phase sequences represent sinusoids at frequencies

$$\omega_{DD} = (\omega_c - \omega_r) + 2k(\delta/T) \sin \theta_d = \omega_{os} + 2K \sin \theta_d$$

$$\omega_{MM} = \omega_{os} + 2K \sin \theta_m$$

just as in Section 3. The last two terms would be equivalent to the frequencies ω_{DM} and ω_{MD} of Section 3 were it not for the phase perturbation terms

$$\pm k\delta(\tilde{m}-m)\ (\sin\theta_m - \sin\theta_d) \qquad \text{(C-29)}$$

These phase perturbation terms (C-29) represent the objective of the randomized source movement since they will spread the spectrum of the $C_D R_M{}^*$ and $C_M R_D{}^*$ terms analogous to that which occurs in lateral diversity.

B. General Nature of Cross Product Spectra and Improvement

Theoretical investigations into multilevel digital phase modulation of a sinusoid have shown [135] that the modulated spectra consist of two terms:

(1) an impulse function representing a sinusoid which is of the same frequency as the unmodulated signal

and

(2) a continuous spectrum which typically has a sin x/x shape centered at the sinusoid frequency with first zeros at the commutation frequency.

The key question as far as improvement goes is how much energy in $C_D R_M{}^*$ and $C_M R_D{}^*$ remains at the frequency $\omega_{os} + K(\sin\theta_d + \sin\theta_m)$; since if there is significant energy at that frequency, this scheme is essentially equivalent to that of Section 2 as far as increased resolution goes.

C. Improvement with Random Choice of Instantaneous Phase Center

The crux of the problem is to determine an appropriate model for the phase jumps as a function of ℓ. If the phase center is moved around pseudorandomly, we can model m as a zero mean integer random variable with uniform distribution* between $\pm M(\ell)$ where

*The case of nonuniform choice of the m values will be discussed subsequently.

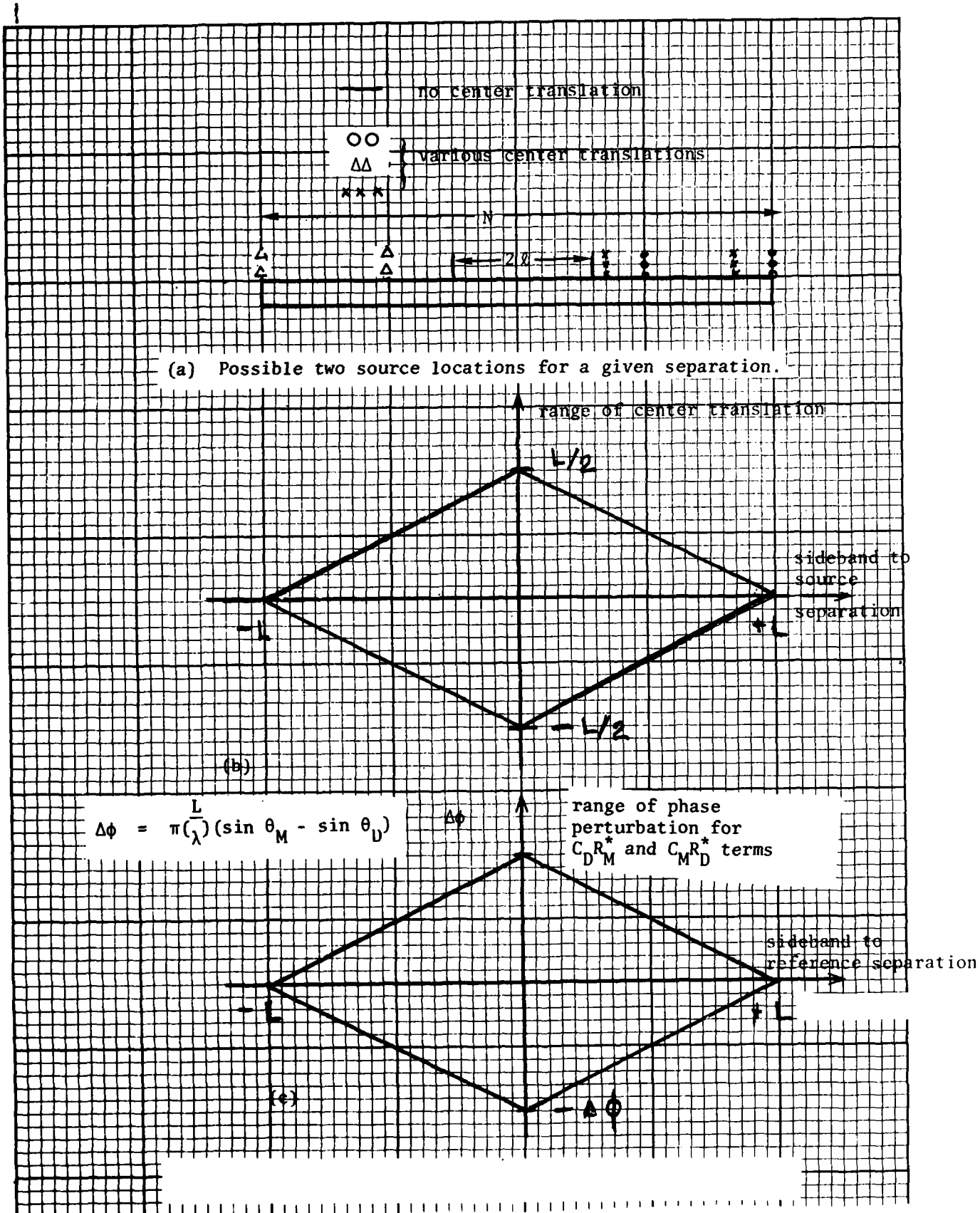

Fig. C-8. Relation of phase perturbations to sideband/reference separation.

$$M(\ell) = N/2 - |\ell| \tag{C-30}$$

To see that this model makes sense, we consider the case of $\ell>0$. As shown in Fig. C-8a, the possible choices for m are the integers from $m = N/2-\ell$ to $-N/2+\ell$.

In Fig. C-8b, we show the range of $\delta M(\ell)$ as a function of ℓ, while Fig. C-8c shows the range of phase perturbations as a function of R. We observe that for in-beam multipath with separation angles of a half beamwidth (i.e., $\sin\theta_m - \sin\theta_d = \lambda/2L$), the median range is $\pi/4$.

Given the probability distribution of the phase perturbations, one can substitute into the formulas of Glance [135] to determine precisely the coherent and incoherent spectra in each case. However, a quite good estimate of the coherent power can be obtained by the simple argument below:

1. We consider the average value of the Fourier coefficient at frequency $\omega_m = \omega_{os} + K(\sin\theta_d + \sin\theta_m)$. For the $C_D R_M^*$ term, this is given by

$$\langle C\rangle = \frac{1}{N} E\left\{ \sum_{\ell=-N/2}^{N/2} C_D R_M^* \, e^{-j[\omega_m t + 2\ell k(\sin\theta_d + \sin\theta_m)]} \right. \tag{C-31}$$

where the expectation is over the phase jumps

$$\Delta\phi(\ell) = k\delta\, m(\ell)\,(\sin\theta_m - \sin\theta_d) \tag{C-32}$$

and $C_D R_M^*$ is evaluated at $t = (N/\ell + \ell + 0.5)\,T/2$.

2. If the phase jumps are independent random variables (the pseudorandom assumption), then by direct substitution it can be shown that

$$\langle C\rangle = \sum_{\ell=-N/2}^{N/2} \frac{1}{N} E[e^{j\Delta\phi(\ell)}]\, e^{j(\alpha_d - \beta_m)} \tag{C-33}$$

The expectation in (C-33) can be evaluated fairly closely by assuming that $\Delta\phi(\ell)$ is a continuous random variable with a symmetrical uniform probability density and peak excursion θ_ℓ. With this assumption, we have

$$E[e^{j\Delta\phi(\ell)}] = \int_{-\theta_\ell}^{\theta_\ell} e^{j\theta}(d\theta/2\theta_\ell)$$

$$= \int_{0}^{\theta_\ell} (\cos\theta)\, d\theta/\theta_\ell \qquad \text{(C-34)}$$

$$= \frac{\sin\theta_\ell}{\theta_\ell}$$

To average over the θ_ℓ, we approximate the θ_ℓ as continuous random variables uniformly distributed from 0 to θ_{max} where

$$\theta_{max} = \frac{2\pi}{\lambda}\left(\frac{L}{N}\right)(N/2)\,(\sin\theta_m - \sin\theta_d) \qquad \text{(C-35)}$$

$$\approx \pi\,\theta_{sep}$$

where θ_{sep} = separation angle between the direct signal and multipath and <u>beamwidths</u>. Thus, we have

$$\langle C\rangle = \frac{1}{\theta_{max}} \int_{0}^{\theta_{max}} \frac{\sin\theta}{\theta}\, d\theta$$

$$= S_i(\theta_{max})/\theta_{max} \qquad \text{(C-36)}$$

where $S_i(\cdot)$ is the sine integral.

For θ_{sep} = 0.7 beamwidths (the worst case separation angle for the UK sine/cosine Doppler processor), $\theta_{max} = 0.7\pi$ and we obtain

$\langle C \rangle = 0.76$ (=-2.2 dB)

For small ρ, this is approximately the error improvement since now both cross terms are offset $K\theta_{sep}$ from the direct component whereas with "normal" commutated array operation, only one component is so offset while the other has zero frequency offset. However, we show in Section 5 that for large multipath levels, the performance using this scheme can, in some cases, be much worse than with a normal array in that the receiver could lock onto the multipath.

By contrast, if one had instead increased the physical aperture twofold, the multipath error for the current UK Doppler processors would be reduced approximately 80% (corresponding to a multipath level reduction of 14 dB).

D. Improvement with "Maximal" Random Change of Instantaneous Phase Center

Rather than shifting the phase center pseudorandomly, one could always attempt to translate the phase center as much as possible between adjacent commutations, e.g.,

$$m(\ell) = (N/2 - \ell)$$

This "maximal shuffle" would (using again continuous approximations to the various discrete phase distributions) yield:

$$E[e^{j\Delta\phi(\ell)}] = \cos\theta_\ell \tag{C-37}$$

and

$$\langle C \rangle = \frac{\sin\theta_{max}}{\theta_{max}} \tag{C-38}$$

Here, the improvement is quite sensitive to the choice of separation angle, e.g.,

$$\langle C \rangle = 0.37 \text{ at } \theta_{sep} = 0.7 \text{ BW}$$
$$= 0.64 \text{ at } \theta_{sep} = 0.5 \text{ BW}$$

Although the "maximal shuffle" provides a greater reduction in the coherent signal than was the case with random choice of phase center, these may be a greater in-beam continuous spectrum component due to the use of only two phase jump values at each commutation step. Quantifying this factor further would require an extension of Glance's closed form results [135] to the case of independent nonidentically distributed phase jumps.

E. Generation of In-Beam Interference from Out-of-Beam Multipath

A significant problem with this last scheme is the generation of in-beam multipath in cases where the multipath would otherwise be out-of-beam. This arises because the $C_D R_M^*$ and $C_M R_D^*$ continuous spectra generated by the phase center translations will have in-beam components even if the other multipath components [at $\omega_{os} + K(\sin \theta_d + \sin \theta_m)$ and $\omega_{os} + 2K \sin \theta_m$] are "out-of-beam." This problem becomes particularly acute in elevation because

1. there is fairly strong out-of-beam multipath (ground specular reflections) fairly close to the direct signal
2. the tracking filter bandwidth spans a significant fraction of the continuous spectra bandwidth.

In Table C-1 below, we estimate the in-beam power for several elevation guidance applications using the UK proposed array spacings [7] for the case of a two beamwidth wide tracking filter and -3 dB ground reflection multipath.

TABLE C-1

"IN-BEAM" POWER FROM CONTINUOUS SPECTRA OF DOPPLER MULTIPATH CROSS TERMS ($C_D R_M^*$, $C_M R_D^*$)

Array Length	Element Spacing	"In-beam" Multipath Power re Direct Power (dB)
60λ	1.7λ	-12.5
30λ	1.7λ	-9.5
15λ	1.7λ	-6.5
90λ flare	3.4λ	-8.2

In generating Table C-1, it was assumed that the continuous spectra of the two terms would be the sum of the individual spectra.

In all cases, this level of in-beam multipath power would probably yield unacceptable errors. The in-beam portion of the front end noise spectrum can be reduced by averaging over successive scans; however, for a fixed two source movement pattern, the continuous spectrum waveforms are unchanged so that no improvement is obtained by multiscan averaging. Changing the movement pattern on successive scans would permit some degree of averaging, but it is not at all clear that the system has enough spatial degrees of freedom to yield the multiple scans averaging improvement which is obtained against front end noise.

5. Doppler Angular Error with "Normal" Scanning and Simultaneous Two Source Scanning

The objective of this section is to obtain analytical expressions for static Doppler errors with "normal" scanning and with the simultaneous two source scanning of Sections 2 and 4. For simplicity, we have based our analysis on a zero crossing counter receiver assuming rectangular filter shapes with no ringing.

By doing so, we can use the phasor diagram arguments used (implicitly or explicitly) by the UK [7], ITT/Gilfillan [13], Hazeltine [11], and in earlier Lincoln studies [28]. In view of the extensive previous use of such phase analysis, it will be assumed here that the reader can fill in the missing details/arguments (Reference [28] contains an exposition of the conceptual arguments as well as references to the other work in this area). The notation here will conform to that of Section 2 unless noted otherwise.

A. "Normal" Commutated Array In-Beam Performance

Here, we assume that

(1) All components ($C_D R_D^*$, $C_M R_D^*$, $C_D R_M^*$, and $C_M R_M^*$) lie in the tracking filter passband.

(2) The multipath time delay is small enough* that

$$\alpha_D = \beta_D$$
$$a_M = \beta_M \qquad \text{(C-39)}$$

(3) The multipath to direct signal rf phase difference at the array center is

$$\phi = \alpha_M - \alpha_D = \beta_M - \beta_D \qquad \text{(C-40)}$$

The problem now is to determine how much the phase of the sinusoid at the direct signal frequency is perturbed at the beginning and end of the scan. If the phase perturbations are $\Delta\phi_s$ and $\Delta\phi_e$, respectively, then the resulting angular error (in radians) is approximately

$$\varepsilon = \frac{\Delta\phi_e - \Delta\phi_s}{2\pi(L/\lambda)\ (\cos\ \theta_d)} \qquad \text{(C-41)}$$

---

*E.g., time delays $\ll 2\pi/\omega_{os} = 11.2$ μsec.

To simplify the expressions and phasor diagrams, it is convenient to represent all vectors relative to the desired signal component ($C_D R_D^*$). This yields:

$$\text{sum signal at direct signal frequency } \underline{\Delta}\ \Sigma_D = (C_D R_D^* + C_D R_M^*)/(C_D R_D^*) = 1 + \rho e^{-j\phi} \qquad \text{(C-42)}$$

$$\text{sum signal at multipath frequency } \underline{\Delta}\ \Sigma_M = (C_M R_D^* + C_M R_M^*)/(C_D R_D^*) = (\rho e^{j\phi} + \rho^2)\ e^{\pm j\Delta\theta} \qquad \text{(C-43)}$$

where $\Delta\theta = \pi \frac{L}{\lambda} (\sin \theta_m - \sin \theta_d) \approx \pi \frac{L}{\lambda} \theta_{sep}$.

The sign in (C-43) is positive at the end of the scan and negative at the scan start. In Fig. C-9, we show the relation of Σ_D, Σ_M, $\Delta\phi_e$, and $\Delta\phi_s$ for several values of ϕ when θ_{sep} is 0.5 beamwidths. The peak angular error is seen to be $\tan^{-1}\rho/[\pi(L/\lambda)]$ occurring at $\phi=0$ and π with zero error occurring at $\phi=\pm\pi/2$. By a similar analysis, it can be shown that the worst case peak error considered over all possible θ_{sep} is $\sin^{-1}\rho/[\pi(1/\lambda)]$. Since $\tan^{-1} x$ and $\sin^{-1} x$ are upper bounded by x, we obtain the well known error bound

$$\varepsilon < \frac{\rho}{\pi} \frac{\lambda}{L} = \frac{\rho}{\pi} \text{ beamwdiths} \qquad \text{(C-44)}$$

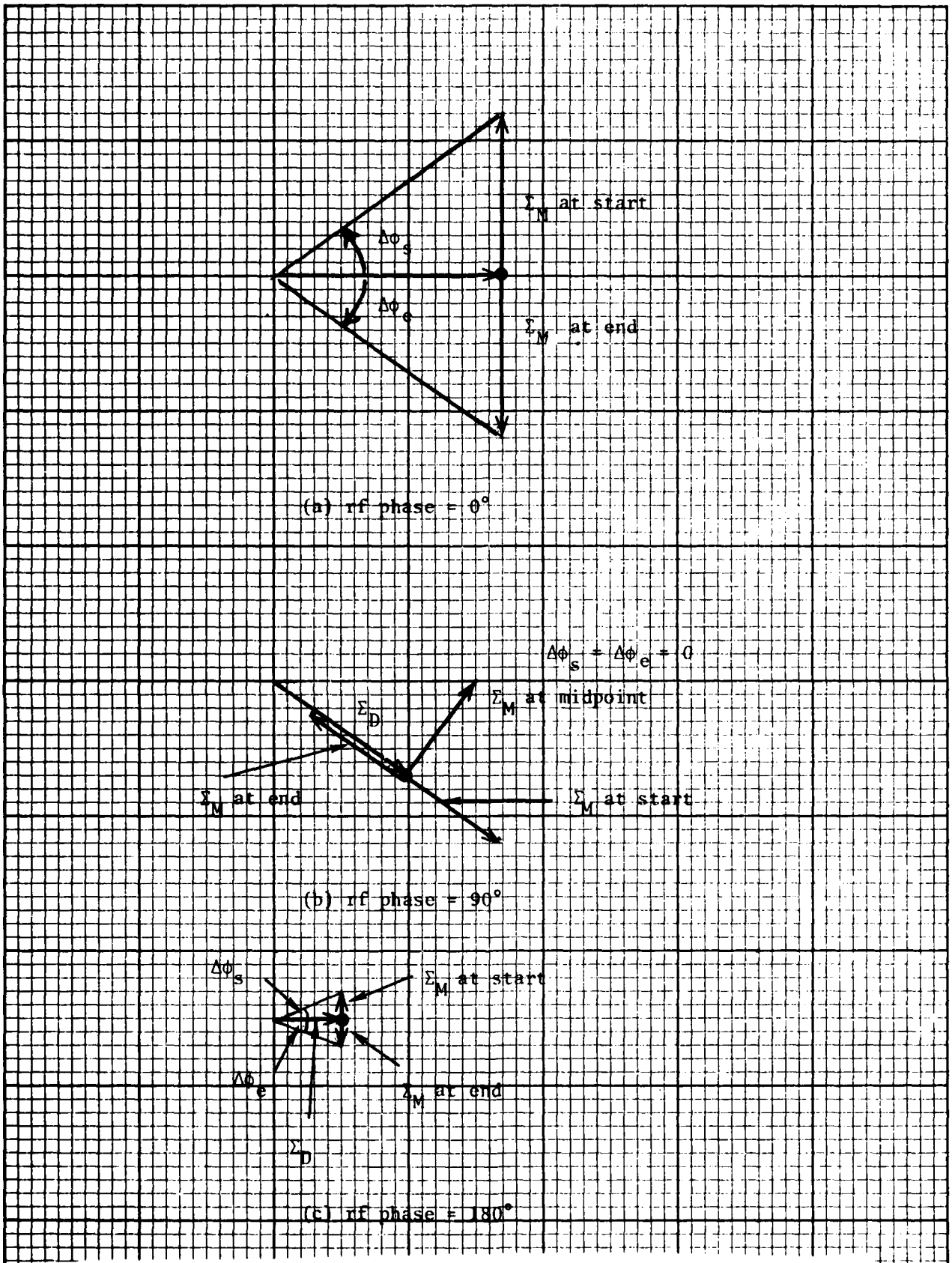

Fig. C-9. Relation of various phasors for "normal" commutated Doppler array at 0.5 BW separation angle.

B. Simultaneous Two Source Scanning

We make the same assumptions as in the previous section except that now only the components $C_D R_D^*$, $C_M R_D^*$, and $C_D R_M^*$ lie within the tracking filter passband. It is argued that this assumption makes sense for a situation in which two source mobility is being used to convert in-beam multipath into an out-of-beam multipath.

Now, the normalized sum signal at the direct frequency is just

$$\Sigma_D = C_D R_D^* / (C_D R_D) = 1 \tag{C-45}$$

while the sum signal at the multipath frequency is

$$\begin{aligned} \Sigma_M &= (C_M R_D^* + C_D R_M^*)/(C_D R_D^*) \\ &= \rho e^{\pm j\Delta\theta}(e^{j\phi} + e^{-j\phi}) \\ &= 2\rho \cos \phi \, e^{\pm j\Delta\theta} \end{aligned} \tag{C-46}$$

In Fig. C-10, we show the relation of Σ_D, Δ_M, $\Delta\phi_c$ and $\Delta\phi_s$ when $\theta_s = 0.5$ beamwidths. The peak error is seen to occur at $\phi=0$ and π, and zero error at $\pm\pi/2$ as is the case with "normal" Doppler scanning.

If $|2 \rho \cos \phi| < 1$, then the angular error is

$$\varepsilon = \frac{2 \tan^{-1} 2\rho \cos \phi}{2\pi(2L/\lambda)} \tag{C-47}$$

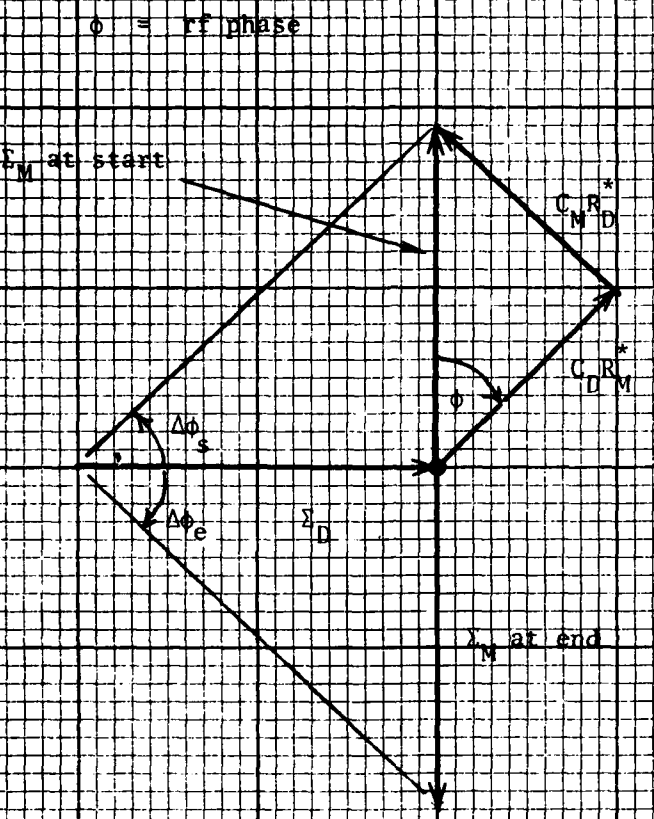

Fig. C-10. Relation of various phasors for simultaneous two source commutation at separation angle = 0.5 beamwidths.

where the factor of 2L comes in because the change of received phase with receiver location is twice that of a normal array. The peak error over all choices of separation angle is

$$\varepsilon = \frac{2 \sin^{-1}(2\rho \cos \phi)}{2\pi(2L/\lambda)} \tag{C-48}$$

Again upper bounding $\tan^{-1} x$ and $\sin^{-1} x$ by x, we obtain the bound

$$\varepsilon < \frac{\rho}{\pi}\frac{\lambda}{L} |\cos \phi| = \frac{\rho}{\pi} |\cos \phi| \text{ beamwidths} \tag{C-49}$$

$$\text{for } 2\rho \, |\cos \phi| < 1$$

which is identical to that of (C-46). Thus, for small M/D levels or fortuitous rf phase difference, the two source movement scheme yields an error essentially identical to that of a "normal" Doppler array.

However, if $2\rho|\cos \phi| > 1$, then the multipath signal will "take over" the zero crossing counter and yield a frequency estimate corresponding to the multipath frequency. This would yield an angular error of

$$\varepsilon \approx \theta_{sep}$$

which, for θ_{sep} = 0.5 - 1.0 beamwidths, would be considered extremely bad. Since the values of ϕ are hardly controllable in any practical situation at C band,it would appear that the two source movement scheme is quite unacceptable in any situations where effective M/D ratios above -6 dB might be encountered.

6. Summary and Conclusions

An analytical investigation was conducted of the proposed methods for commutation of both DMLS sideband and reference sources in the scan plane so as to achieve increased resolution. To yield a manageable analysis we restricted our attention to the static case with a single multipath signal.

Use of a complex signal representation and modeling the detector as a squarer followed by a lowpass filter permitted a compact expression for the input to the Doppler tracking/angle estimation circuits. The analysis then focused on examining the amplitudes and frequencies of the various signals constituting the DMLS angle estimation system input.

It was found that:

(1) The simultaneous two source movement scheme of Section 2 does not provide an increased resolution in that the separation of the most significant multipath components from the direct signal was unchanged from that with a "normal" Doppler array. Additionally, two multipath components have been created at a single frequency where only one existed before, thus introducing a possiblity of the receiver being captured by the multipath.

(2) The sequential two source commutation scheme of Section 3 yields a desired signal spectrum which is narrower by a factor of two than that which occurs with the normal DMLS array. However, the multipath terms of greatest concern have the same spectrum location and width as with a "normal" commutated array. From both spectral overlap arguments and time domain considerations, it appears that no improvement is obtained in this case.

(3) The pseudorandom simultaneous two source movement scheme of Section 4 provides some reduction (e.g., 2-4 dB for a separation angle of 0.5 beamwidths) in the "bad" multipath components that arose with the scheme of Section 2. However, this is at the "price" of generating a low level (but still potentially significant) in-beam multipath component in situations where the multipath would have been out-of-beam with a normal Doppler array.

REFERENCES

1. RTCA SC-117 Final Report, "A New Guidance System for Approach and Landing," RTCA Document DO-148 (Dec. 1970).

2. "National Plan for the Development of the Microwave Landing System," DOT/NASA/DOD Planning Group (July 1971) AD-733268.

3. R.A. Rondini and R.H. McFarland, "Experimental Validation of Boeing 747 ILS Signal Scattering Calculations for Critical Area Determination," FAA SRDS (Jan. 1974) FAA-RD-74-57.

4. "Report of the Seventh Air Navigation Conference," ICAO Doc. 900 4-AN-CONF/7 (April 1972).

5. "Operational Requirements for an Advanced Approach and Landing Guidance System for the Post-1975 Period Prepared by the NATO Industrial Advisory Group (NIAG)," NATO NIAG document NIAG (71) D/1 (March 1971).

6. "The DME-Based-Landing System, DLS," as proposed by the Federal Republic of Germany developed by Standard Elektrik Lorenz AG. and Siemens, AG. (Sept. 1975).

7. "Doppler Microwave Landing Guidance System," proposal submitted by United Kingdom to the International Civil Aviation Organization (Nov. 1975).

8. "Recommendations for Selection of Scanning Beam Technique Using a Time Reference Signal Format for the U.S. Microwave Landing System - Issue Papers and Backup Documentation," Federal Aviation Administration ARD-700 (Jan. 1975).

9. S. Grashoff (chairman) "Report of the Sixth Meeting of the ICAO All-Weather Operations Panel," ICAO Doc. 9200, AWOP/6 (March 1977).

10. T. Breien, "Computer Analysis of MLS in Multipath Environment," IEE Conf. on the Future of All Weather Operations (Nov. 1976).

11. H.A. Wheeler, "Multipath Effects in Doppler MLS," contained in Hazeltine Corp. Report "Microwave Landing System (MLS) Development Plan as proposed by Hazeltine Corp. During the Technique Analysis and Contract Definition Phase of the National MLS Development Program," FAA-RD-73-185 (Sept. 1972).

12. "Microwave Landing System (MLS) Development Plan as Proposed by Texas Instruments, Inc., During the Technique Analysis and Contract Definition Phase of the National MLS Development Program," FAA-RD-74-170 (1 Sept. 1972).

13. ITT/Gilfillan, "Microwave Landing System (MLS) Development Plan as Proposed by ITT/Gilfillan During the Technique Analysis and Contract Definition Phase," FAA-RD-74-118 (Sept. 1972).

14. P. Fombonne, "Position Errors in Microwave Landing Systems," Electronics and Civil Aviation Int. Conf., Paris, France (June 1972).

15. J. Benjamin and G.E.J. Peake, "Contributions to the UK Microwave Landing System Study (Phase 1)," Royal Aircraft Establishment, Tech. Memo RAD 1021 (May 1973).

16. "Interscan," proposal submitted by Australia to International Civil Aviation Organization (December 1975).

17. R. Giles "Study and Test Report on MLS Performance in Shadowing Conditions," ICAO AWOP Paper AWOP/6-BIP.45 (March 1977).

18. B.F. Oreb and J.G. Lucas, "A 1/20th Scale Millimetric Model of the Microwave Landing System," IEE Conf: Future of All Weather Operations (Nov. 1976).

19. L.N. Spinner and V.L. Bencivenga, "Advanced Scanning Beam Guidance System for All Weather Landing," FAA Syst. Res. Dev. Serv., Washington, D.C., RD 68-2 (Feb. 1968), DDC AD-664973.

20. V.L. Bencivenga, "Test and Evaluation of a Portable Scanning Beam Guidance System," (March 1972), FAA-RD-72-16.

21. F.X. Kelly, "Tests of Scanning-Beam Microwave Landing Systems at Difficult Sites," presented at technical seminar "Aviation - A Tool for Economic Development," First International Aerospace Show, Sao Paulo, Brazil (Sept. 1973).

22. Bendix Corp. "Refined Microwave Landing System (MLS) Program Development Plan (Phase III)," (Oct. 1974).

23. Texas Instruments, Inc., "Refined Microwave Landing System (MLS) Development Program Plan," DM74-03-04 (1 Oct. 1974).

24. ITT/Gilfillan, "Five Year MLS Development Program Plan (updated) Microwave Landing System, " MLS-0420 (1 Oct. 1974).

25. Hazeltine Corp., "Refined Microwave Landing System (MLS) Development Program Feasibility Demonstration, Phase II," Report 11009 (1 Oct. 1974).

26. D.A. Shnidman, "The Logan MLS Multipath Experiment," Project Report ATC-55, Lincoln Laboratory, M.I.T. (23 Sept. 1975), DDC AD-A017083, FAA-RD-75-130.

27. D.A. Shnidman, "Airport Survey for MLS Multipath Issues," Project Report ATC-58, Lincoln Laboratory, M.I.T. (15 December 1975), FAA-RD-75-195, DDC AD-A022937/7.

28. J.E. Evans, R. Burchsted, J. Capon, R.S. Orr, D.A. Shnidman, and S.M. Sussman, "MLS Multipath Studies, Volume I: Mathematical Models and Validation; Volume II: Application of Multipath Model to Key MLS Performance Issues," Project Report ATC-63, Lincoln Laboratory, M.I.T. (25 Feb. 1976), FAA-RD-76-3, DDC AD-A023040/9 and DDC AD-A025108/2.

29. J. Capon, "Multipath Parameter Computations for the MLS Simulation Computer Program," Project Report ATC-68, Lincoln Laboratory, M.I.T. (8 April 1976), FAA-RD-76-55, DDC AD-A024350/1.

30. A. Spiridon, "Impact of Obstacle Shadows in Monopulse Azimuth Estimate," Project Report ATC-50, Lincoln Laboratory, M.I.T. (17 July 1975), FAA-RD-75-91, DDC AD-A015139/9.

31. F.L. Frisbie, "Studies of Comparative Shadowing Behavior for DMLS and TRSB," ICAO AWOP Paper AWOP/6-BIP/50 (Feb. 1977).

32. P.S. Demko, "Polarization/Multipath Study," U.S. Army Electro. Command Rep. VL-5-72 (Aug. 1971/June 1972).

33. A.E. Brindley, L.C. Calhoun, and T.N. Patton, (IITRI) "Multipath Environment Evaluation," Air Force Flight Dynamics Laboratory, AFFDL-TR-74-150 (Nov. 1974).

34. ITT Research Institute "A Joint Army/Air Force Investigation of Reflection Coefficient at C and Ku Bands for Vertical, Horizontal, and Circular System Polarizations," AFFDL-TR-76-67 (July 1976).

35. A.E. Brindley, L.E. Calhoun, T.N. Patton, and L. Valcik, "Analysis, Test and Evaluation Support to the USAF Advanced Landing System Program," USAF Flight Dynamics Lab, AFFDL-TR-74-62 (Aug. 1974).

36. E. Bramley and S. Cherry, "Investigation of Microwave Scattering by Tall Buildings," Proc. IEEE, (Aug. 1973).

37. J.G. Lucas and B.F. Oreb, "MLS Modeling Work," Report from Air Navigation Group, School of Electrical Engineering, Univ. of Sydney, Australia, to Australian Dept. of Civil Aviation (1976).

38. B.F. Oreb and J.G. Lucas, "Blocking and Diffraction Due to an ICAO Sheet," personal communication to J. Evans (May 1977).

39. J.E. Evans, D. Karp, R.R. LaFrey, R.J. McAulay, and I.G. Stiglitz, "Experimental Validation of PALM - A System for Precise Aircraft Location," Technical Note 1975-29, Lincoln Laboratory, M.I.T. (29 April 1975), DDC AD-A010112/1.

40. J.E. Evans, "Aperture Sampling Techniques for Precision Direction Finding," paper presented at IEEE Electro 78, Boston, Massachusetts (May 1978).

41. J.E. Evans and S.M. Sussman, "Doppler Azimuth Reference Errors with Out-of-Beam Multipath," ICAO AWOP Working Group A Paper TH.BIP.3 (30 June 1976).

42. T.E. Bernard, "Analytical Studies of Techniques for the Computation of High-Resolution Wavenumber Spectra," Special Report No. 9, Texas Instruments Incorporated, Dallas, Texas (14 May 1969), Project No. VELAT/7701.

43. J. Capon, "High-Resolution Frequency-Wave Number Spectrum Analysis," Proc. IEEE 57, 1408 (1969).

44. N.O. Anderson, "On the Calculations of Filter Coefficients for Maximum Entropy Spectral Analysis," Geophysics 39, 69 (1974).

45. J.P. Burg, "Maximum Entropy Spectral Analysis," Paper presented at the 37th meeting of the Society of Exploration Geophysicists, Oklahoma City, Oklahoma (31 October 1967).

46. R.T. Lacoss, "Data Adaptive Spectral Analysis Methods," Geophysics 56, 661 (1971).

47. R.N. McDonough, "Maximum-Entropy Spatial Processing of Array Data," Geophysics 39, 843 (1974).

48. H.R. Radoski, P.F. Fouger, E.J. Zanalick, "A Comparison of Power Spectral Estimates and Applications of the Maximum Entropy Method," J. Geophy. Res. 80, 619 (1975).

49. T.E. Bernard, "The Maximum Entropy Spectrum and the Burg Technique," Advanced Signal Processing Technical Report No. 1, Texas Instruments Incorporated, Dallas, Texas (25 June 1975), ALEX(03)-TR-75-01.

50. J. Makhoul, "Linear Prediction; A Tutorial Review," Proc. IEEE 63, 561 (1975).

51. T.P. McGarty, "Models of Multipath Propagation Effects in a Ground-to-Air Surveillance System," Technical Note 1974-7, Lincoln Laboratory, M.I.T. (25 February 1974), DDC AD-777241/1.

52. A. Spiridon, "Effects of Local Terrain and Obstacles Upon Near Horizon Gain of L-Band Beacon Antennas," Technical Note 1975-6, Lincoln Laboratory, M.I.T. (17 July 1975), DDC AD-A013732/3.

53. H. Berger and J.E. Evans, "Diversity Techniques for Airborne Communications in the Presence of Ground Reflection Multipath," Technical Note 1972-27, Lincoln Laboratory, M.I.T. (8 September 1972), DDC AD-752249.

54. F. Harris, "On the Use of Windows for Harmonic Analysis with the Discrete Fourier Transform," Proc. IEEE 66, 51 (1978).

55. A. Oppenheim and R. Schafer, Digital Signal Processing (Prentice Hall, New York, L975).

56. A. Brindley, L. Calhoun, T. Patton, and L. Valcik, "Analysis, Test and Evaluation Support to the USAF Advanced Landing System Program Vol. III Part 1 Doppler MLS Guidance Error Data (DOTS Tracking System)," AFFDL-TR-74-62, Vol. III, Part 1 (August 1974).

57. P. Demko, "Propagation Integrity for Microwave Landing Systems," In AGARD Conference Proceedings No. 240 Guidance and Control Design Considerations for Low-Altitude and Terminal-Area Flight (October 1977).

58. "Flight Trials of TRSB/Interscan Equipment at Sydney International Airport, Australia," Paper AWO/78-WP/88 presented by Australia at ICAO AWO Division Meeting. (April 1978).

59. "Tracked Flight Trials of Doppler MLS at Manchester Airport," Paper AWO/78-WP/123 presented by United Kingdom at ICAO AWO division meeting (April 1978).

60. "Tracked Flight Trials of Doppler MLS Azimuth System at Brussels National Airport," Paper AWO/78-WP/12 presented by the United Kingdom at ICAO AWO Division Meeting (January 1977).

61. "Test Results for a Time Reference Scanning Beam (TRSB) 'Basic Narrow' MLS," Paper AWO/78-WO/119, presented by United States at ICAO AWO Division Meeting (April 1978).

62. "DMLS/TRSB Comparative Demonstration Test Results at Brussels National Airport, Brussels, Belgium," Paper AWO/78-WO/141, presented by United States at ICAO AWO Division Meeting (April 1978).

63. DMLS/TRSB Comparative Demonstration Test Results," Paper AWO/78-WP/153 presented by United States at ICAO AWO Division Meeting (April 1978).

64. J.E. Evans and D.A. Shnidman, "Multipath Characteristics of AWOP WG-A Multipath Scenarios," AWOP WG-A Paper TH.BIP/9 also Revision 1 (4 January 1977).

65. "Time Reference Scanning Beam Microwave Landing System," proposal submitted by the United States to the International Civil Aviation Organization (December 1975).

66. R. Butler, (Rappoteur), "Report of the Multipath Subgroup of WG-A Held near Boston, Mass., 11-15 October 1976," L.WP/3 in the report of ICAO AWOP Working Group A, Seventh Meeting, London (Nov. 1-12, 1976).

67. M. Whitney, "UK Presentations and Demonstrations of Doppler MLS Multipath Environments," given at Royal Aircraft Establishment, Bedford, (1 Nov. 1976), CAA Paper 77003 (Feb. 1977).

68. M. Whitney, "DMLS Signal Processing," L.BIP/38 in Report of the Seventh Meeting of ICAO AWOP Working Group A, held in London, U.K. (2-12 Nov. 1976).

69. F. Frisbie, "TRSB Phase III Receiver Functional Description," Paper L.BIP/19 in the report of ICAO AWOP Working Group A, Seventh Meeting, London (Nov. 1976).

70. T. Bohr, "The Proposed DLS Airborne Equipment and DLS System Configuration," L.BIP/42 and L.BIP/43 in Report of ICAO AWOP Working Group A. Seventh Meeting, London (1-12 Nov. 1976).

71. J. Beneke, C. Wightman et al., "Multipath and Performance Tests of TRSB Receivers," FAA-RD-77-66 (March 1977).

72. ICAO All Weather Operations Panel Working Group A, "Report of the Third Meeting Held in Melbourne During the Period 24-28 February 1975" (Feb. 1975).

73. "Validation of Computer Simulation by Comparison with Tests at Operational Airports," Paper AWO/78-WP/135 presented by the United States at ICOA AWO Division meeting (April 1978).

74. "Application and Validation of Computer Simulation to MLS Multipath Performance Assessment," Paper AWO/78-WP/138 presented by the United States at ICAO AWO Division meeting (Jan. 1978).

75. "Performance of Advanced Approach and Landing Systems (AALS)," Electronics Research Laboratory, Univ. of Trondheim, Norwegian Inst. of Tech. (March 1973).

76. "Study of the Radar Reflectivity Characteristics at SSR Frequency of Pilkington 'Insulight' Metallized Glass," Cosser Electronics Limited Report EF/S/055 (Sept. 1973).

77. A. Von Hippel, Dielectric Materials and Applications (Chapman & Hall, Ltd., London, 1954).

78. G. Bailey, Personal Communication (Feb. 1977).

79. F.L. Frisbie, "Comparison of DMLS and TRSB Acquisition/Validation in an Azimuth Multipath Environment," ICAO All Weather Operations Panel Working Paper AWOP-WP/322 (March 1977).

80. B.L. Oreb, "Modeling of the Microwave Landing System (MLS) at 104 GHz," PhD Thesis, Univ. of Sydney, Australia, (1978).

81. G.T. Ruck, D.E. Barrick, W.D. Stuart and C. Krichbaum, Radar Cross Section Handbook, Volume 1 (Plenum, New York, 1970).

82. H. Neugebauer and M. Bachynski, "Diffraction by Smooth Cylindrical Mountains," Proc. IRE 41, 1619 (Sept. 1958).

83. I.M. Hunter, "Some Properties of Air-Derived and Ground-Derived Aircraft Landing Guidance Concepts," J. of British Institute of Navigation (1973).

84. K.D. Eckert, "DME Based System for Enroute/Terminal Navigation, All Weather Landing and Air Traffic Control," in AGARD Conference Proc., No. 240 Guidance and Control Design Considerations for Low-Altitude and Terminal Area Flight (Oct. 1977).

85. L. Armijo, K. Daniel, and W. Labuda, "Application of the FFT to Antenna Array Beamforming," EASCON '74 Conference Proceedings, Washington, D.C. (1974).

86. K. Kohler, "Synthetic Radio Direction Finding with Virtual Antenna Patterns," Electric Comm. 48, 299 (1973).

87. W.B. Kendall, "Unambiguous Accuracy of an Interferometric Angle-Measuring System," IEEE Trans. Space Electronics and Telemetry 11, 67 (June 1965).

88. J. Duncan, "The Effect of Ground Reflections on an Interferometric Direction Finder," IEEE Trans. Aerospace Electron. Systems AES-3, 927 (1967).

89. D.K. Barton, "Multipath Error in a Vertical Interferometer," Proc. IEEE 53, 543 (1965).

90. A. Papoulis, The Fourier Integral and Its Applications (McGraw-Hill, New York, 1962).

91. M.F. Whitney, "Simulation of Phased Array Antenna Systems," Working Paper TH.WP-3 presented at the Hague Meeting of AWOP WG-A (July 1976).

92. J. Beneke et al., "TRSB Multimode Digital Processor," Final Report, Calspan Corporation, Report No. FAA-RD-77 (April 1978).

93. Bendix Corp., "Microwave Landing System, Phase III (Basic Narrow and Small Community Configurations) Final Report, Volume 1," Report No. MLS-BCD-R-2801-1 (June 1978).

94. "Report of the All Weather Operations Division Meeting, 1978," International Civil Aviation Organization, Doc. 9242, AWO/78 (April 1978).

95. F. Frisbie, "Out of Coverage Indication (OCI) and Left/Right Guidance," ICAO AWOP Working Group A Background Information Paper L.BIP/20 (Nov. 1976).

96. Hazeltine Corp., "Cost Minimized Phased Array Circuit Technique (COMPACT)," (1976).

97. J. Sebring and J. Ruth, "MLS Scanning-Beam Antenna Implementation," Microwave J. 41 (1974).

98. F. Pogust, "Microwave Landing Systems,"IEEE Spectrum 15, 30 (1978).

99. R. Kelly, H. Redlein and J. Shagena, "Landing Aircraft Under Poor Conditions," IEEE Spectrum 15, 52 (1978).

100. A. Lopez, "Scanning-Beam Microwave Landing System - Multipath Errors and Antenna Design Philosophy," IEEE Trans Antennas Propag. AP-3, 290 (1977).

101. J. Kuznetsov, "Some Questions Concerning Reduction of Multipath Effect on Microwave Landing System Accuracy," ICAO AWOP 6 Paper WP/305 (1977).

102. F.L. Frisbie, "(Latest) Comparison of DMLS Computer Model with January 1977 DMLS Hybrid Simulator Azimuth Multipath Data," ICAO AWOP 6 Paper BIP/62 (1977).

103. H.L. Van Trees, Detection, Estimation and Modulation Theory Part I (John Wiley & Sons, New York, 1968).

104. M. Skolnik, Introduction to Radar Systems (McGraw-Hill, New York, 1962).

105. D.K. Barton and H.R. Ward, Handbook of Radar Measurement (Prentice-Hall, New Jersey, 1969).

106. L. Jolley, Summation of Series (Dover, New York, 1961).

107. R. J. McAulay, "The Effects of Interference on Monopulse Performance," Technical Note 1973-30, Lincoln Laboratory, M.I.T. (1 August 1973), DDC AD-769336/9.

108. Appendix E in "Report of the Seventh Meeting of ICAO AWOP WG-A held in London, UK, Nov. 1-12, 1976" (Dec. 1976).

109. R. Loh, "Preliminary Crows Landing Acceptance Test Data Analysis," MITRE Technical Report MTR-7617 (March 1978).

110. R. Wade, "Effect of TRSB and DMLS Motion Averaged in/beam Multipath from the Elevation System on the Pitch Axis response of a Modern Transport Aircraft on Final Approach," Smith's Industry Report MLS-SI-RW II [presented by M.F. Whitney as AWOP WG-A Background Information Paper W.BIP/1 (May 1976)].

111. S. Grashoff, "Report of the AWOP Working Group A, Fifth Meeting," Washington, D.C. (May 1976).

112. M. Born and E. Wolf, Principles of Optics, 4th edition (Pergamon, London, 1970).

113. S. Grashoff, "Report of AWOP Working Group A, Fourth Meeting," Braunschweig, West Germany (Jan. 1976).

114. S. Grashoff, "Report of AWOP Working Group A, Sixth Meeting," The Hague, Netherlands (July 1976).

115. T. Hagenberg "Modified AWOP WG-A Multipath Scenarios for Simulation with TRSB,"National Aerospace Laboratory NLR The Netherlands memo VV-77-041 L (July 1977).

116. T. Bohr, "Salzburg Scenario for Multipath Simulation Tests,"AWOP Paper AWOP/6 - BIP/52, (March 1977).

117. ICAO Annex 14 Aerodromes Part IV "Obstruction Restriction, Removal and Marking" (18/9/69).

118. "TRSB Microwave Landing System demonstration program at Tegucigalpa, Honduras," Nat. Aviation Facilities Exp. Center Report FAA-NA-78-XX (Feb. 1978).

119. T. Bohr "Multipath Immunity of MLS in Mountainous Sites,"AWOP WG-A Paper L.WP/4 (Nov. 1976).

120. Inst. fur Angewandte Geodasie (Frankfurt), "Salzburg" Map Series M501 Edition 2 - DMG Number NL 33-1 (1966).

121. A.M. Peterson et al., "Low-angle Radar Tracking" Stanford Research Institute Technical Report JSR 74-7 (Feb. 1976).

122. A.R. Lopez, "Scanning beam Microwave Landing System multipath errors and antenna design philosphy," IEEE Trans. Antennas Propag. AP-25, 290 (1977).

123. R.J. Kelly, "Time Reference Microwave Landing System multipath control techniques," Institute of Navigation 31st Annual Meeting, Washington, D.C. (June 1975).

124. R.J. Kelly and E. LaBerge, "Comparison study of MLS airborne signal processing techniques,"NAECOM '78 Proceedings, Dayton, Ohio (May 1978).

125. R.M. Cox and J.R. Sebring, "MLS - a practical application of microwave technology," IEEE Trans. Microwave Theory Tech. MTT-24 , 964 (1976).

126. M. Whitney, "The vulnerability of TRSB MLS to shadowing effects from runway movements," Paper L.P/44 presented at Nov. 1976 (London) meeting of AWOP WG-A.

127. M. Whitney, "TRSB Shadowing -- A Real Problem," Paper L.WP/71 presented at Nov. 1976 (London) meeting of AWOP WG-A.

128. M. Whitney, "Vulnerability of TRSB MLS to Shadowing Effects (Phase II results)," Paper L.BIP/59 presented at Nov. 1976 (London) meeting of AWOP WG-A.

129. F. Frisbie, "TRSB approach azimuth shadowing by taxiing and over-flying aircraft field tests," Paper L.BIP/48 presented at Nov. 1976 (London) meeting of AWOP WG-A.

130. J.B. Keller, "Geometric Theory of Diffraction," J. Opt. Soc. Am. 52, 116 (1972).

131. H. Redlein and R. Masek, "Doppler scanning landing guidance system development," Proc. Inst. Navig. Nat Air Meeting Conf. (April 1971).

132. J. Benjamin and P. Reich, "A survey of microwave landing guidance problems related to the operational requirements," Proc. Inst. Navig. Nat. Air Meeting Conf. (1971).

133. R. Barratt, "The UK approach to MLS," Microwave J. 19, 19 (1976).

134. C. W. Earp, "Doppler techniques employing two-source mobility," presentation to U.S. MLS Assessment Group (Nov., 1974).

135. B. Glance, "Power spectra of multilevel digital phase-modulated signals," Bell Syst. Tech, J. 50 , 2857 (1971).

136. "The limitations of simulation as an aid to MLS selection," ICAO All Weather Operations Divisional Meeting Working Paper AWO/78-WP/128, (April 1978).

137. E. Sherwood and E. Ginzton, "Reflection coefficients of irregular terrain at 10 cm," Proc. IRE 43 , 877 (1955).

138. R. Birgenheier, "Parameter Estimation of Multiple Signals," PhD dissertation, University of California, Los Angeles, 1972.

139. "Computer simulation results for multipath performance comparison," ICAO All Weather Operations Divisional Meeting Paper AWO/78-WP/100, April 1978).

140. I. White, "Reduction of DMLS Bearing Errors Caused by Reference Fading Part I - Ground Equipment Adjustments and Part II - Airborne Equipment Adjustments," Plessey Company Memos 17/76/N130U and 17/76/N131U (Oct. 1976).

141. C. Earp, "Evolution of the commutated Doppler Microwave Landing System," Landing Guidance, Civil Aviation Authority (UK), 1, (1975).

142. D.K. Barton, Radar Resolution and Multipath Effects (Artech House, Dedham, Massachusetts, 1975).

* U.S. GOVERNMENT PRINTING OFFICE: 1981 700-002/34

END

FILMED

1-85

DTIC